UNIVERSITÉ DE LORRAINE | BIBLIOTHÈQUES UNIVERSITAIRES

AVERTISSEMENT
DROIT D'AUTEUR

Ce document est le fruit d'un long travail approuvé par le jury de soutenance et mis à disposition de l'ensemble de la communauté universitaire élargie.

Il est soumis à la propriété intellectuelle de l'auteur. Ceci implique une obligation de citation et de référencement lors de l'utilisation de ce document. Toute contrefaçon, plagiat ou reproduction illicite encourt une poursuite pénale.

Contact bibliothèque : ddoc-theses-contact@univ-lorraine.fr
(Cette adresse ne permet pas de contacter les auteurs)

Code de la Propriété Intellectuelle. articles L 122. 4
Code de la Propriété Intellectuelle. articles L 335.2- L 335.10

UNIVERSITÉ DE LORRAINE
34 COURS LÉOPOLD — CS 25233
54052 NANCY CEDEX
TÉL : 03 54 50 54 00
CONTACT@UNIV-LORRAINE.FR
WWW.UNIV-LORRAINE.FR

UNIVERSITE DE LORRAINE

Ecole doctorale SIReNa

Centre de Recherches Pétrographiques et Géochimiques

THESE DE DOCTORAT

Docteur de l'Université de Lorraine (spécialité Géosciences)

Par Yafet Gebrewold Birhane

Sous la direction de Raphaël Pik et Nicolas Bellahsen

Volcanic and magmatic organisation of rift segments in Central and Southern Afar at Ocean Continent Transition

Organisation volcanique et magmatique des segments de rift en Afar Central et Sud, à la Transition Océan Continent

Soutenue publiquement le 19 décembre 2025

Directeurs de thèse

Dr. Raphaël Pik, Directeur de recherche CNRS, Centre de Recherches Pétrographiques et Géochimiques

Dr. Nicolas Bellahsen, Professeur Sorbonne Université

Rapporteurs

Dr. Karen Fontijn, Professeur associée, Université Libre de Bruxelles

Dr. Pierre Lahitte, Maitre de Conférence HDR Université Paris-Saclay

Examinateurs

Dr. Sylvie Leroy (***president of the jury***), Directrice de recherche CNRS, Sorbonne Université

Dr. David Jousselin, Maitre de Conférence Université de Lorraine

Invités

Dr. Lydéric France, professeur Université de Lorraine

RÉSUMÉ

La transition entre le rifting continental et l'expansion océanique soulève des questions géodynamiques fondamentales, notamment en ce qui concerne l'initiation de cette expansion magmatique et la formation d'une croûte juvénile. La dépression d'Afar, à l'extrémité nord du système du rift est-africain, présente l'avantage majeur d'exposer des structures d'extension liées à la transition océan-continent, avec des segments de rift magmatiques caractérisés par des morphologies et des styles magmato-tectoniques contrastés. L'objectif de cette thèse est d'identifier la localisation et d'étudier le fonctionnement et la persistance des réservoirs magmatiques dans la croûte afin de mettre en évidence leurs relations et leurs contrôles potentiels avec la segmentation locale de premier et deuxième ordre, ainsi que comprendre l'interaction entre processus magmatiques et tectoniques lors de la génération d'une telle croûte magmatique. L'étude se concentre sur deux segments actifs du rift de la dépression Afar: les segments de Manda Hararo et d'Asal-Ghoubbet. Des orthoimages multispectrales à haute résolution et un modèle numérique d'élévation, une cartographie géologique précise, des investigations sur le terrain, la datation par ^{36}Cl cosmogénique et la géochimie des laves sont combinés pour déterminer la dynamque et l'évolution des événements magmatiques. Les résultats permettent d'identifier et de décrire deux sous-segments de rift axiaux actifs et cohérents au sein du système Manda Hararo. Nous évaluons l'organisation des différentes venues de magmas, leur séjour dans la croûte et leur interaction avec les processus tectoniques. Nous documentons avec précision l'évolution volcanique des segments dans la plage 0 à 35 kyr, y compris les épisodes de rifting les plus récents pour chaque segment: Manda Hararo sous-segment (~1,5 à 3,5 ka), Gumat Mali sous-segment (~0,5 à 2 ka) et Asal-Ghoubbet segment (~0 à 3,5 ka). Les âges d'exposition récents indiquent une recharge périodique des réservoirs magmatiques peu profonds qui alimentent finalement les injections latérales de dykes et les éruptions en surface. Nos résultats révèlent un stockage et un transfert dynamiques du magma organisé au sein de systèmes transcrustaux, où les segments présentent différents styles de rifting. Les variations dans la recharge et la différenciation des réservoirs mettent en évidence des zones de stockage distinctes et des connexions potentielles entre les sous-segments. Ces observations démontrent comment les cycles périodiques de transfert et de différenciation du magma façonnent l'évolution magmatique du rift, avec des implications supplémentaires importantes pour les risques locaux.

ABSTRACT

The transition from continental rifting to oceanic spreading presents fundamental geodynamical questions, particularly concerning the initiation of magmatic spreading and the formation of juvenile crust. The Afar depression, at the northern end of the East African Rift system, presents the key advantage to expose extensional structures related to ocean-continent transition, with magmatic rift segments characterized by contrasted morphologies, and magmato-tectonic styles. The aim of this thesis is to identify the location and investigate the functioning and persistence of magma reservoirs in order to highlight their relationships and potential control with the first- and second-order local segmentation and understand the interplay between magmatic and tectonic processes during the generation of such magmatic crust. The study focuses on two active rift segments of the Afar depression: the Manda Hararo and Asal-Ghoubbet segments. High-resolution multispectral orthoimages and digital elevation models, precise geological mapping, field investigations, cosmogenic ^{36}Cl exposure dating, and lava geochemistry are combined to constrain the timing and evolution of magmatic events. Results allow to identify and describe two active and self-consistent axial rift sub-segments within the Manda Hararo system. We assess the organization of different batches of melts, their residence within the crust, and the interaction of these melts with tectonic processes. We precisely document volcanic evolution of the segments in the range 0 – 35 kyr, including the most recent rifting episodes for each segment: Manda Hararo sub-segment (~1.5 –3.5 ka), Gumat Mali sub-segment (~0.5–2 ka), and Asal-Ghoubbet segment (~0–3.5 ka). The recent exposure ages indicate periodic recharge of shallow magma reservoirs that ultimately feed lateral dyke injections and surface eruptions. Our findings reveal dynamic magma storage and transfer organised within transcrustal systems, where segments exhibit different rifting styles. Variations in reservoir recharge and differentiation highlight distinct storage zones and potential connections between sub-segments. These insights demonstrate how periodic magma transfer and differentiation cycles shape rift magmatic evolution, with additional important implications for local hazards.

ACKNOWLEDGEMENTS

While pursuing this PhD, my family and community faced the difficulties of political instability and ongoing internal conflict. This reality made my journey both demanding and deeply emotional, and I remain profoundly grateful to those who supported and encouraged me throughout these years.

My sincere thanks go to the members of the jury, Karen Funtijn, Pierre Lahitte, Sylvie Leroy, and David Jousselin for dedicating their valuable time during the Christmas season to read my work and evaluate me.

I would like to thank my supervisors, Raphael Pik and Nicolas Bellahsen, for their patience and insight over the course of this project. Over four years of supervision, Raphael has inspired, challenged, and argued with me; he has ultimately too forged and improved my abilities as an earth scientist. I would like to thank Nicolas for the many discussions and for sharing his expertise during the field excursions.

There are many other researchers I would like to acknowledge who have contributed in some way to my research. The training and technical support provided in CEREGE by Irene Schimmelpfennig was invaluable over the course of this project. Lyderic France has been a fantastic mentor and collaborator on the geochemical models, and I thank him for this encouragement and patience during the work on Chapters 3. Likewise, I am grateful to Jessica Flahaut and Simon Daout for their valuable support and guidance with remote sensing work on Chapters 2. I would also like to sincerely thank Christophe Cloquet for the training and technical support provided during chemical preparation and isotope analysis.

This PhD is part of the collaborative research project MAGMAFAR, funded by the French National Research Agency (ANR) and hosted at the CRPG-CNRS. The work performed in this thesis would not be possible without this funding. I would like to thank the members of the MAGMAFAR, Sarah Gommery and Juliette Pin. I would also like to thank all the scientists and staff at the CRPG-CNRS laboratory for their support and for providing a stimulating research environment.

The Department of Earth Sciences at Addis Ababa University provided considerable support both during and after fieldworks. I thank to my former advisors, Gezahegn Yirgu and Dereje Ayalew who have continuously guided and supported me since the very beginning of my academic journey. Beyond their academic mentorship, they have cared for me with the kindness and dedication of a father, and I have always valued our relationship as one of family as much as scholarship. I would also like to thank my colleagues Wegene Talelign and Tsigereda Ayalew from the Department of Geology, College of Natural and Computational Sciences, Hawassa University, for their support and encouragement. I thank the members of the Afar regional government at Semera for their help in the field.

I am grateful to my family, whose understanding, trust, and unconditional support have carried me through this journey. I am profoundly grateful to my father, who has given me both the care of a mother and the guidance of a father; I owe more than words can ever express.

I would also like to thank my friends Abate Assen, Amdemichael Zafu, Bahru Zinaye, Samuel Getachew and Gemechu Bedassa for their companionship and encouragement. In particular, I am grateful to Abate Assen, whose friendship has grown into a bond like family, and whose journey has closely paralleled mine.

Finally, I owe my deepest gratitude to my wife. You left behind your family, and your own studies in Ethiopia to follow me to France. Not for certainty, but for love, for a dream we chose to share. In doing so, you gave up so much, yet gave me everything. Through the long days and late nights of this PhD journey, you have been my unwavering support. Patient in silence, strong in spirit, and always present, even when I was too consumed by work to notice. Your belief in me, when I doubted myself, carried me forward more times than I can count. And now, after three years abroad, our love has grown into something even greater, our daughter. Her smile, her innocence, her very existence is the most beautiful chapter of our story. She is the symbol of everything we have built together with love and resilience. This thesis is not mine alone. It is the result of a shared journey, a shared sacrifice, and a shared dream. Thank you, my love, for your strength, your grace, and your endless support. I dedicate this work, and all that follows, to you and to our daughter, my greatest inspirations.

Contents

Résumé I
Abstract II
Acknowledgements II
Contents IV
List of figures VII
List of tables XI
1. Chapter 1: Introduction 1
1.1 The General context of ocean continent transition 9
1.2 The Afar depression in the evolution of continental rifting 13
1.2.1 The East African Rift 13
1.2.2 Ethiopian volcanic province 20
1.3 The evolution of Afar depression 22
1.4 The Afar rift magmatic segments 26
1.5 Recent magmato-tectonic activities within the Afar magmatic segments 28
1.5.1 The Erta Ale segment 29
1.5.2 The central Afar (Dabbahu-Manda Hararo) segment 31
1.5.3 The Asal-Ghoubbet segment 39
1.6 Thesis Objectives and structures 42
2. Chapter 2: Methods 43
2.1 Remote sensing and Mapping and field observations, sampling 43
2.1.1 Remote sensing data sets 43
2.1.2 Data Processing and Image Analysis Techniques 44
2.1.3 Digital Elevation Model Generation 51
2.2 Cosmogenic Geochronology 52
2.2.1 Sample preparations and Cosmogenic ^{36}Cl analyses 53
2.2.2 Chemical preparation and extraction of cosmogenic ^{36}Cl 53
2.2.3 Cosmogenic ^{36}Cl analyses 55
2.2.4 Calculation of ^{36}Cl cosmogenic exposure ages 56
2.3 Geochemical analysis 57
2.3.1 Quantitative petrographic analysis 58
2.3.2 Major and Trace element analysis 59
2.3.3 Isotope measurement 61
3. Chapter 3: Volcanic activity, magma types and organisation of the Gumat Mali magmatic sub-segment 65

3.1 Geological setting 68
3.2 Materials and methods 70
3.2.1 Remote sensing data sets and processing 70
3.2.2 Digital Surface Model (DSM) generation 71
3.2.3 Geomorphological Mapping 72
3.3 Geochemical analysis 72
3.3.1 In situ-produced ^{36}Cl CRE dating 73
3.3.1.1 Sampling strategy and analytical method 73
3.3.1.2 ^{36}Cl CRE age calculations 75
3.4 Results 75
3.4.1 Chronology of Lava Flows 75
3.4.2 Field observations, geological Map and associated volcanic history 77
3.4.2.1 Oldest Volcanic Products 78
3.4.2.2 Recent Historical Volcanic Products 79
3.4.3 Lava geochemistry 86
3.5 Discussion 93
3.5.1 Nature of the mantle source components 93
3.5.2 Plumbing system and general organisation of the magmatic sub-segment 98
3.5.3 Volcanological risk assessment 102
4. Chapter 4: Detailed architecture of the magmatic sub-segments in centeral Afar 104
4.1 Materials and methods 107
4.1.1 Geological mapping and sampling 107
4.1.2 Sampling details 107
4.2 Results 110
4.2.1 Chronology of Lava Flows 110
4.2.2 Geological Map and Volcanic history 111
4.2.3 Lava Geochemistry 120
4.2.3.1 Major and trace element compositions 120
4.2.3.2 Sr, Nd and Pb isotopes 123
4.3 Discussion 130
4.3.1 Magma types 130
4.3.2 Differentiation of magmas and crustal processes 131
4.3.3 Spatial and temporal organisation of the central Afar active sub-segments 132
4.3.4 The ocean continental transition in central Afar 135

5. Chapter 5: the magmatic cyles of the Asal-Ghoubbet rift segmentnt.....137
5.1 Geological setting 140
5.2 Materials and methods 142
5.2.1 Remote sensing and Geological Mapping.....142
5.2.2 Geochemical data analysis and corrections.....142
5.2.2.1 Bulk-rock measurements 142
5.2.2.2 Plagioclase Accumulation Correction 143
5.2.3 In situ-produced ^{36}Cl Cosmic Ray Exposure (CRE) dating.....144
5.2.3.1 Sampling strategy and Physical preparation.....144
5.2.3.2 Chemical preparation and ^{36}Cl measurements.....145
5.2.3.3 Topographic-shielding corrections 146
5.2.3.4 ^{36}Cl CRE age calculations 147
5.3 Results.....148
5.3.1 Chronology of Lava Flows.....148
5.3.2 Relative Chronology of Lava Flows 149
5.3.3 Field investigations, geological map and associated magmatic history.....150
5.3.3.1 Recent aerial volcanic products of various axial centres.....151
5.3.4 Major and trace elements 161
5.4 Discussion.....166
5.4.1 Magma differentiation and system replenishment 166
5.4.2 Mantle source of magmas 169
6. Chapter 6: Conclusions and Future Perspectives 172
6.1 Magmatic functioning of the Gumat Mali sub-segment.....173
6.2 Magmatic functioning of Asal-Ghoubbet rift system 174
6.3 Organisation of the Central Afar magmatic sub-segments.....175
6.4. Future Perspectives …….…….…… 178
References.....178
Appendix I (Chapter 2) 203
Appendix II (Chapter 3).....208
Appendix III (Chapter 4) 218
Appendix IV (Chapter 5) 231
Appendix V (Conference abstracts).....240
Résumé étendu en Français ……. 244

LIST OF FIGURES

Figure 1.1: Schematic representation illustrating the cyclic stages for opening and closing of ocean basins 2

Figure 1.2: Schematic illustrations of three end-member modes of lithospheric extension 4

Figure 1.3: Conceptual models illustrating the mechanisms of lithospheric extension 5

Figure 1.4: Schematic model of the temporal evolution of continental rifts 6

Figure 1.5: Conceptual model of magmatic systems in Ethiopian rift. 8

Figure 1.6: Schematic model of the two types of passive continental margins. 11

Figure 1.7: Diagram showing characteristic properties of two end member types of rifted continental margins. 12

Figure 1.8: Map illustrating the magmatic activity in East Africa. 15

Figure 1.9: Seismic tomographic image illustrating the LLVP beneath Africa 16

Figure 1.10: a) Cartoon depiction of melt generation processes within the Eastern Branch of the East African Rift System 19

Figure 1.11: Spatially heterogeneous nature of the mantle upwelling beneath Afar 20

Figure 1.12: Geological map of the rift systems 21

Figure 1.13: A) Topography and bathymetry of the Horn of Africa 22

Figure 1.14: Map show the distribution of rocks during the development of the rift 25

Figure 1.15: Magmatic segments of the Afar depression and schematic cross sections of the three most active magmatic segments. 28

Figure 1.16: Architecture of the Erta Ale magmatic plumbing systems. 30

Figure 1.17: Compilation of documentation on the DMH rifting episodes available in the literature.. 33

Figure 1.18: Location of subaerial spreading centres and comparison of the rifting episodes in the Afar region with Iceland. 35

Figure 1.19: Schematic illustration of magmatic cycles and the evolution of the DMH rift segment. 37

Figure 1.20: Architecture of the central Afar magmatic plumbing systems. 38

Figure 1.21: Architecture of the Asal magmatic plumbing systems. 41

Figure 2.1: RGB band combinations computed from Sentinel-2. 46

Figure 2.2: Principal Component Analysis (PCA) generated from Sentinel-2 47

Figure 2.3: A zoomed view of selected areas in the PCA image used for mapping the diversity of lava flow fields in central Afar. 48

Figure 2.4: Decorrelation stretch (DCS) image after enhancement using low-pass filtering computed from Sentinel-2 49

Figure 2.5: Minimum Distance Classification (MDC) applied to the Sentinel-2 DCS image.. 50

Figure 2.6: Zoomed views of selected areas highlighting lava flow fields and volcanic structures. 51

Figure 2.7: Photo shows the AMS ASTER instrument at CEREGE. 56

Figure 2.8: Evolution of cosmogenic ^{36}Cl concentration through time 57

Figure 2.9: Quantitative petrographic analysis of lava samples from Central Afar using Minimum Distance Classification 61

Figure 2.10: Instruments used for isotope measurment 64

Figure 3.1: Geological map of Afar 67

Figure 3.2: Geological map of magmatic rift segments in Central Afar. 70

Figure 3.3: Detailed map of Gumat Mali magmatic sub-segment. 81

Figure 3.4: Schematic cross sections illustrating the topographic influence of the fissural eruptions. 82

Figure 3.5: Field photograph of the volcanological features and associated lava flow fields. 83

Figure 3.6: Field photos (right) and carton (left) shows the volcanic stratigraphy constructed at the main crater (Teleke Loma). 84

Figure 3.7: Location, photographs and ^{36}Cl CRE ages of the various lava flow fields. 85

Figure 3.8: Total Alkali–Silica (TAS) diagrams.. 89

Figure 3.9: A major element Harker diagrams show variations in major oxides of erupted lavas. 90

Figure 3.10: Variations in trace elements between the erupted lavas. 91

Figure 3.11: Multi-element variation diagram and Rare Earth Element (REE) patterns of the lava series. 92

Figure 3.12: Trace element pattern showing the result of mass balance mixing. 97

Figure 3.13: (Sm/Yb)N vs. (La/Sm)N and (Sm/Yb)N vs. (Ba/Th)N of the Gumat Mali samples. 100

Figure 3.14: Temporal volution of magma composition during the most recent magmatic phases at Gumat Mali sub-segment. 101

Figure 4.1: Geological map of Afar 106

Figure 4.2: Geological map of central Afar. 109

Figure 4.3: Map of the central Afar sub-segments. 114

Figure 4.4: Cross-section map of the central Afar sub-segments. 115

Figure 4.5: Field photographs shows volcanological features and associated lava flow fields in the central Afar sub-segments. 117

Figure 4.6: Field photographs and ^{36}Cl CRE ages of representative lava flows. 120

Figure 4.7: Total Alkali vs. Silica, wt% (TAS) classification diagram for lavas from central Afar sub-segments.. 124

Figure 4.8: Major element Harker diagrams show variations in major oxides vs MgO among the lavas from central Afar. 125

Figure 4.9: Variations in trace elements vs MgO of lavas from central Afar.....126

Figure 4.10: Multi-element variation diagram and Rare Earth Element (REE) patterns of the lava series. 128

Figure 4.11: Trace element ratios of lavas from central Afar.....127

Figure 4.12: Isotopic composition the central Afar sub-segments.....129

Figure 4.13: Summary compilation of cosmogenic ^{36}Cl age versus degree of differentiation of lavas 132

Figure 4.14: Schematic cartoon depicting magma plumbing system organization in central Afar active sub-segments 136

Figure 5.1: Geological map shows the main active magmatic segments of the Afar depression 139

Figure 5.2: High resolution Ms orthoimage shows the very recent lava flow fields along the axial volcanic centres of Asal-Ghoubbet rift. 148

Figure 5.3: Detailed map of the axial volcanic centres of the Asal-Ghoubbet rift. 155

Figure 5.4: Topographic architecture of the axial volcanic centres of the Asal-Ghoubbet rift. 156

Figure 5.5: Locations, field photographs, and ^{36}Cl CRE ages of various lava flow fields at the axial rift volcanic centres. 158

Figure 5.6: Field photographs shows key volcanological features and associated lava flow fields within the axial volcanic centres. 159

Figure 5.7: TAS (Total Alkali vs. Silica, wt%) classification diagram for lavas from Asal-Ghoubbet segment.. 162

Figure 5.8: Variations in major elements vs MgO among lava samples. 163

Figure 5.9: Variations in trace elements between the lava samples. 164

Figure 5.10: Multi-element variation diagram and Rare Earth Element (REE) patterns of the lava series. 165

Figure 5.11: Magma replenishment and differentiation through time at the Asal-Ghoubbet rift segment. 168

Figure 5.12: Evolution of magma composition during the 1978 Ardukoba rifting episode. 169

Figure 5.13: (Tb/Yb)N vs. (La/Sm)N of the Asal-Goubet segment samples. 170

Figure A2.1: The Workflow adopted to map lava flows and volcanic structures using Landsat 8 OLI and Sentinel-2 MSI datasets. 205

Figure A2.2: Physical preparation of lava samples for cosmogenic ^{36}Cl measurements. 206

Figure A2.3: Graphical illustration of AMS measurements of the $^{36}Cl/^{35}Cl$ and $^{35}Cl/^{37}Cl$ ratios for lava samples from the central Afar and Asal rift. 207

Figure S3.1: Major and trace elements variations of the lava series. 216
Figure S3.2: Multi-spectral orthoimages shows the main volcanic features. 217
Figure S4.1: Major and trace elements variations of the central Afar lava series 230
Figure S5.1: Locations and field photographs of the volcanic features and ^{36}Cl CRE ages…... 239
Figure S5.2: Major and trace elements variations of the Asal-Ghoubbet lava series in the binary diagrams. 239

LIST OF TABLES

Table 3.1: Locations and description of lava flow samples used for ^{36}Cl dating. 74

Table 3.2: ^{36}Cl CRE age of the Lava flows. 76

Table 4.1: Locations and descriptions of lava surface samples used for ^{36}Cl dating. 108

Table 4.2: ^{36}Cl CRE ages of the Lava flows.. 116

Table 5.1: Locations and description of lava flow samples used for ^{36}Cl CRE dating. 145

Table 5.2: Analytical ^{36}Cl data and ^{36}Cl CRE ages of the lava flows at the Asal-Ghoubbet rift volcanic centres. 154

Table 2.1: Summary of remote sensing datasets 203

Table 2.2: Characteristic of spectral band of Landsat 8 (USGS) and Sentinel-2 (ESA) 203

Table 2.3: Comparison of visual estimates from hand specimen and Minimum Distance classification. 204

Table S3.1: Major (in wt.%) and trace element (in ppm) concentrations in bulk rock samples before chemical treatment. 208

Table S3.2: Concentrations of the target element oxides, measured in splits taken from the samples after the chemical pre-treatment (acid etching). 213

Table S3.3: Trace element composition of host minerals in the most primitive Afar samples. 214

Table S3.4: The trace element compositions after mass balance mixing. 214

Table S4.1: Major (in wt.%) and trace element (in ppm) concentrations in bulk rock samples before chemical treatment. 218

Table S4.2: Sr, Nd, and Pb Isotopic compositions of lava flows from central Afar sub-segments 229

Table S5.1: Major (in wt.%) and trace element (in ppm) concentrations in bulk rock samples after corrections for Plageoclase accumulation. 231

Table S5.2: Concentrations of the ^{36}Cl target elements, measured in splits taken from the samples after the chemical pre-treatment. 235

Table S5.3: Interpolated ages for the Lava surface samples at the Asal-Ghoubbet rift segment. 235

Table S5.4: Bulk rock composition of the Aphyric lava flows and olivine-hosted melt inclusions of the axial zone of Asal rift. 236

Chapter 1

1. Introduction

The Wilson Cycle is a fundamental concept to the theory of plate tectonics (Wilson, 1966; Burke, 2011), which describes the concept of repeated opening and closing of ocean basins along the same plate boundaries (Figure 1.1). It represents a key concept in the assembly and breakup of continents. This cycle comprises six stages (Wilson et al., 2019): (1) embryonic rifting, where mantle upwelling, lithospheric thinning, and localized magmatism initiate continental breakup; 2) young passive margin marked by the onset of seafloor spreading and production of Mid-Ocean Ridge Basalts (MORB) at narrow oceanic basins; 3) the formation of large oceanic basins by continental drift (Mature Ocean); (4) declining oceans, where subduction begins and arc-related magmatism develops; (5)the subsequent closure of oceanic basins through oceanic lithosphere subduction (Terminal Ocean); and (6) continent-continent collision and closure of the oceanic basin and formation of Suture Zone. These orogenic sutures are zones of weakness that then reopen into ocean basins. Mantle dynamics and the resulting magmatism play a fundamental role in the different stages of the cycle and in the transitions between these stages (Burke, 2011). Convective circulation within of the Earth's mantle drive the movements of tectonic plates. Mantle downwelling promotes continental aggregation and acts as a major driving force during the convergent phases of the Wilson cycle. In contrast, the divergent phases are associated with mantle upwellings that initiate lithospheric stretching and rifting (Figure 1.1). Magmatism is an inherent expression of these geodynamic phases throughout the cycle.

Extension controls continental breakup, ultimately leading to the formation of new oceanic crust along mid-ocean ridges. Two principal models have been proposed to explain the mechanisms of lithospheric extension (e.g, Lister and Davis, 1989; Buck, 1991; Ebinger, 2005; Rosenbaum et al., 2008). The first is the mechanical stretching model (Figure 1.2), which treats rifting as the response of the lithosphere to purely tectonic forces (Dunbar and Sawyer, 1989; Mckenzie & Jackson, 1983; Rosenbaum et al., 2008). In this framework, the brittle upper lithosphere accommodates deformation by faulting, while the lower lithosphere responds by ductile flow. Lithospheric flexure is an important component of this process, with the degree of bending controlled by crustal thickness, lithospheric strength, and the prevailing thermal regime (Kusznir & Karner, 1985). Depending on lithospheric rheology, extensional stresses may be distributed across broad zones, localized onto single normal faults, or focused along

low-angle detachment faults (Buck, 1993; C. Ebinger, 2005). Such variations strongly influence the morphology of the resulting rift system. A key limitation of this model, however, lies in the magnitude of the forces required to initiate rupture: while a thinned lithosphere may yield to relatively weak extensional stresses (Forsyth & Uyedaf, 1975; Solomon et al., 1980), a thick lithosphere demands stresses far greater than those plausibly available from plate boundary forces such as slab pull (Hopper and Buck, 1993; Kusznir and Park, 1987).

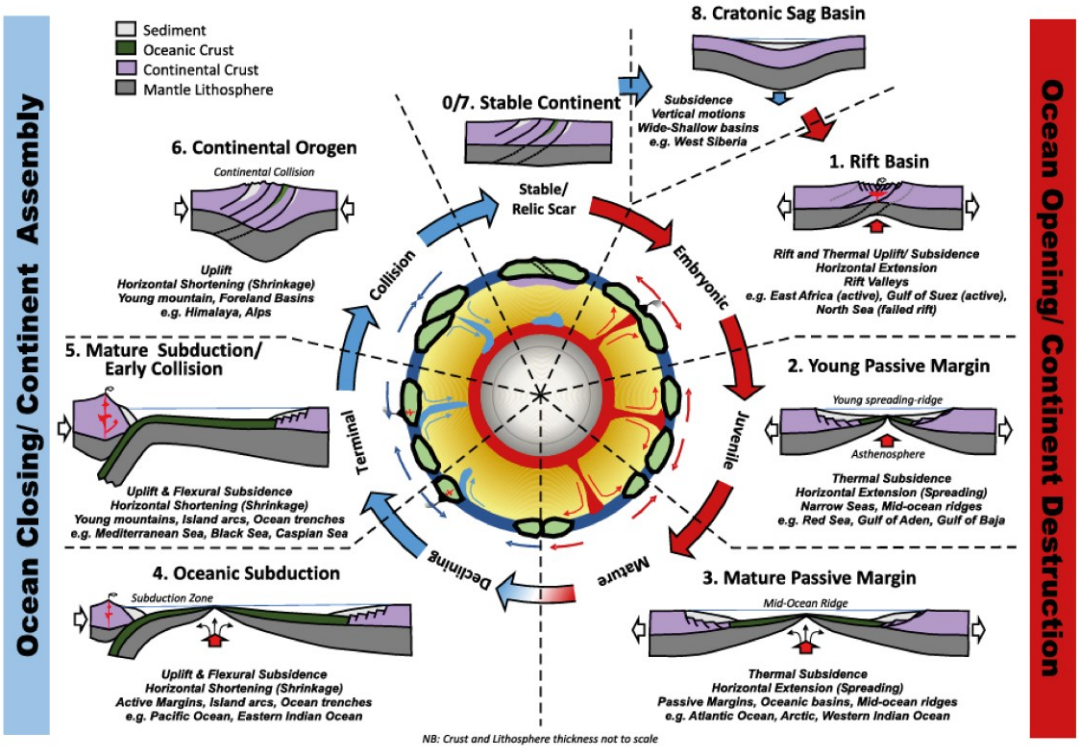

Figure 1.1: *Schematic representation illustrating the cyclic stages for opening and closing of ocean basins (After Wilson et al., 2019).*

This limitation led to the development of the second model (Figure 1.3), the magma-assisted extension model, in which rifting is driven not only by tectonic stresses but also by magmatic processes (C. Ebinger, 2005). In this scenario, extension is accommodated jointly by normal faulting and the emplacement of dikes. Magmatic dike intrusion enables lithospheric rupture under much lower stresses than required for purely mechanical faulting, because dikes transfer magma upward and effectively weaken the lithosphere (Buck, 2006). Whereas tectonic faulting produces large-scale subsidence and rift-basin formation, dike injection primarily adds new material without significant vertical deformation, redistributing stresses within the crust and upper lithosphere (Figure 1.3).

At the crustal scale, these two processes of faulting and magmatism interact in varying proportions as rifting progresses. Early stages of continental extension are often dominated by large border faults and limited volcanism (Figure 1.4 A), while the transition toward breakup is marked by increased dike intrusion and the organization of the rift into discrete magmatic segments (Figure 1.4 B). When the continental break-up reaches completion, and the rift-to-ridge transition is complete, all magmatism occurs within the ridge axis, and is fuelled by melting from a passively upwelling asthenosphere (Figure 1.4 C).

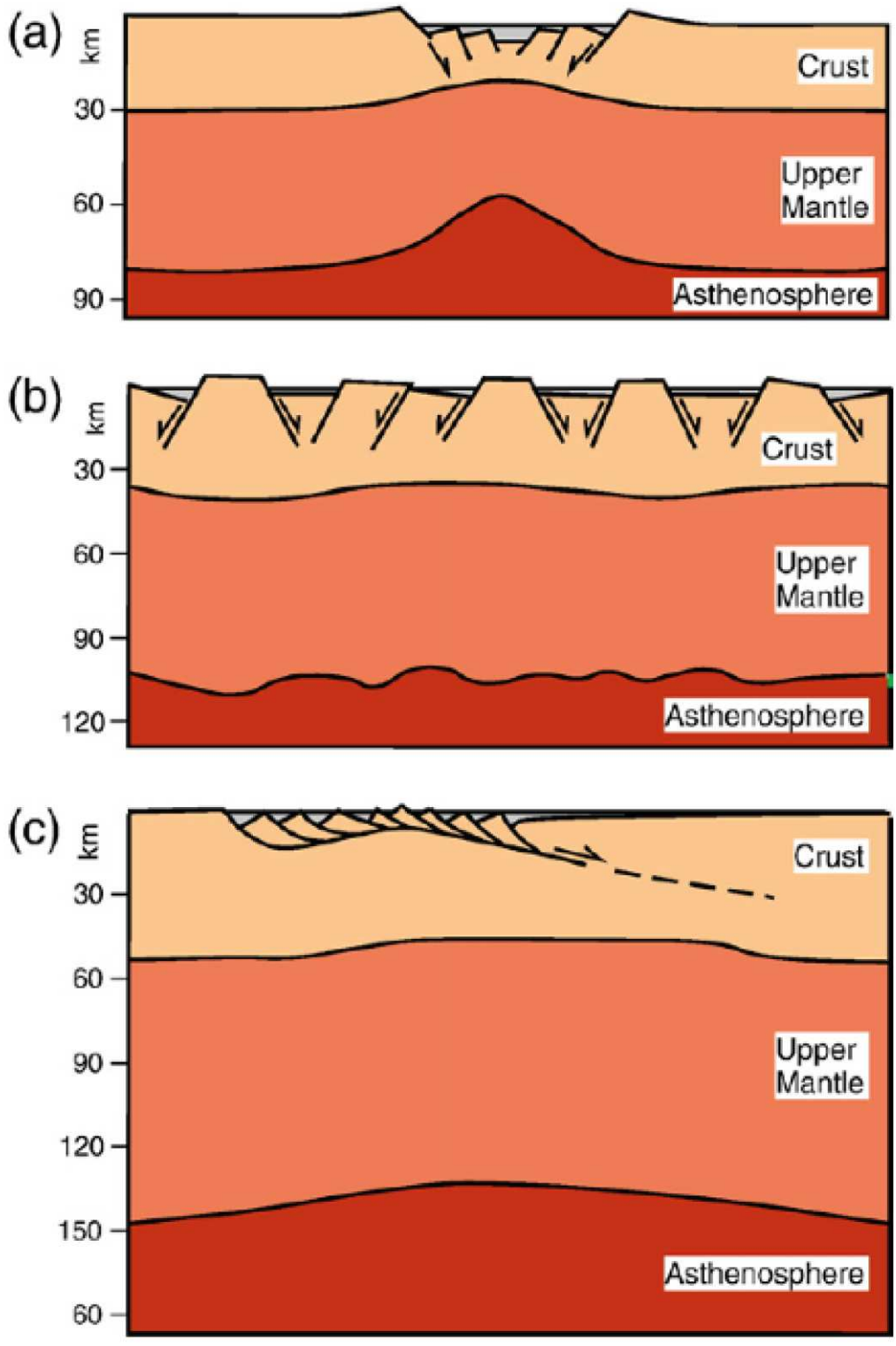

Figure 1.2: *Schematic illustrations of three end-member modes of lithospheric extension (Rosenbaum et al., 2008). (a) narrow rift (b) wide rift. (c) core complex mode of extension.*

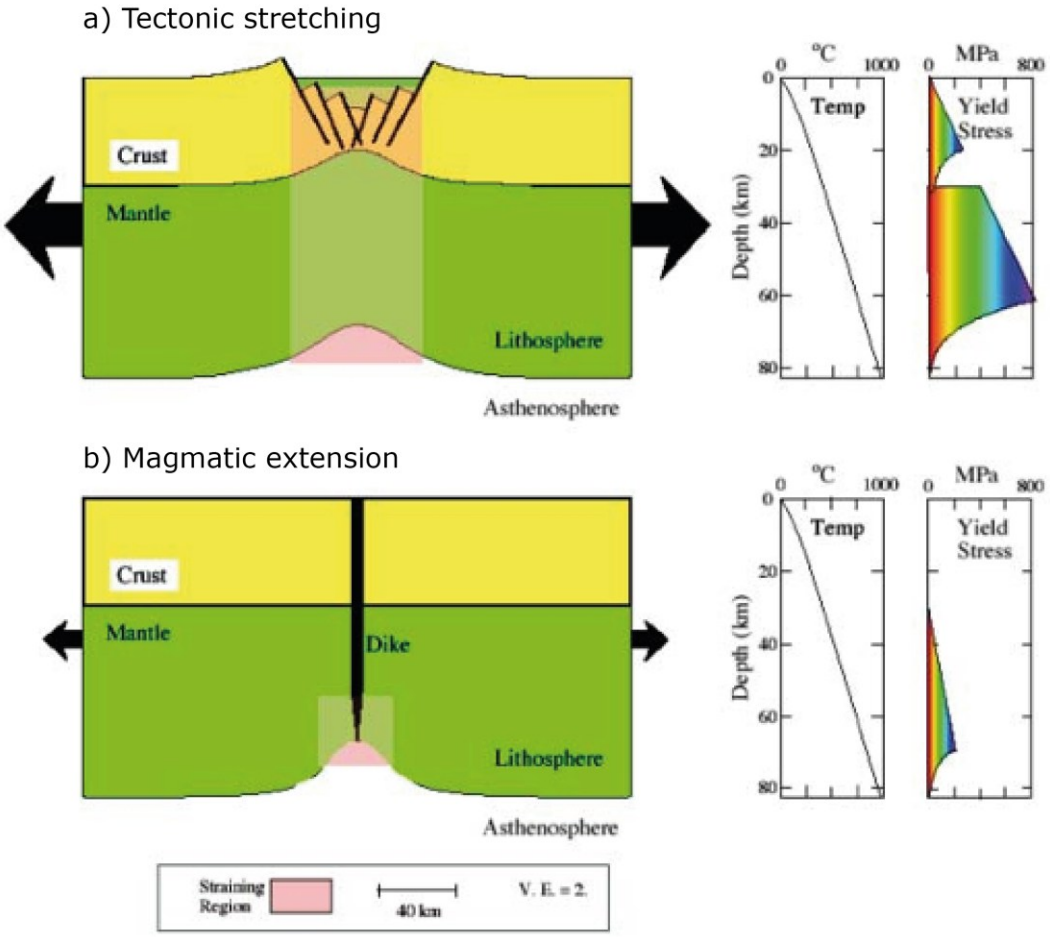

Figure 1.3: *Conceptual models illustrating the mechanisms of lithospheric extension (Buck, 2006). a) extension is accommodated by the detachment of normal faults in brittle layers of the lithosphere and*

by ductile flow in the lower lithosphere. b) stress reduction and focusing are facilitated by dike intrusion.

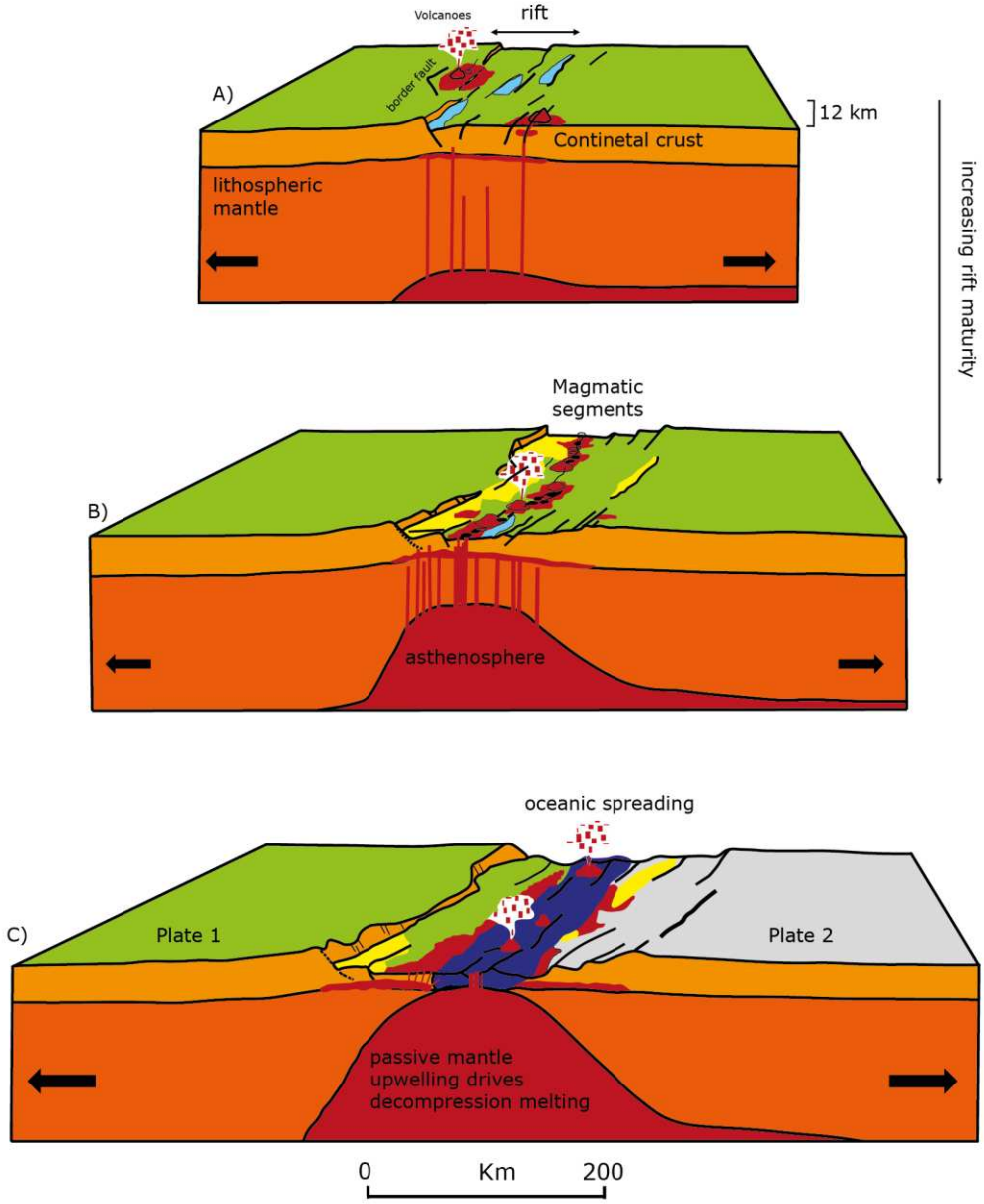

Figure 1.4: *Schematic model of the temporal evolution of continental rifts (redrawn after Ebinger, 2005). A) Early- stage rifting: Extension is accommodated by large border faults forming graben and half-graben structures. Lithospheric thinning allows asthenospheric upwelling, which transfers heat and may trigger partial melting by decompression. Resulting melts can reach the surface, with volcanism concentrated along border faults (e.g., southern East African rift system). B) Mature continental rifting: The rift matures over time; the lithosphere undergoes further thinning through faulting and ductile flow at depth. Progressive asthenospheric upwelling enhances partial melting,*

weakening the lithosphere. Magmatism and deformation become concentrated within axial zone of the magmatic segments, and extension is mainly accommodated by repeated dike intrusions (e.g., Main Ethiopian Rift and Afar). C) Sea-floor spreading: continental breakup reaches completion, and the new oceanic crust is created. Magmatism is focused along the ridge axis and is sustained by melting of passively upwelling asthenosphere (e.g., Gulf of Aden).

Magmatic systems in the Ethiopian rifts at different stages of their evolution (MER and Afar) have been studied in a comparative way (e.g., Hutchison et al., 2018; Biggs et al., 2021). As rifting proceeds from early (MER) to more advanced stages (Afar), magmatic systems evolve from relatively melt-rich, stable, and simple plumbing architectures to more crystal-rich, dynamic, multi-reservoir systems (Figure 1.5). In the MER, silicic magmas are highly evolved (especially peralkaline rhyolites), produced by protracted fractional crystallization of basaltic parental melts, often with minimal crustal assimilation; magma residence times are relatively long and the storage tends to be in sill-like lenses or mush zones in the mid to lower crust (Hutchison et al., 2018). In the northern Afar, magmatism is thought to be dominated by shallow basaltic reservoirs, frequent dyking, and plumbing architectures analogous to observations from spreading centres at mid-ocean ridges (Field et al., 2012; Biggs et al., 2021). However, recent petrological and isotopic data of the Erta Ale volcano (J. Pin et al., 2024) support a more complex magmatic plumbing system, showing protracted fractional differentiation in both shallow and deeper reservoirs, involvement of evolved, crystal-rich mush zones, and longer storage times not expressed at the volcanic surface.

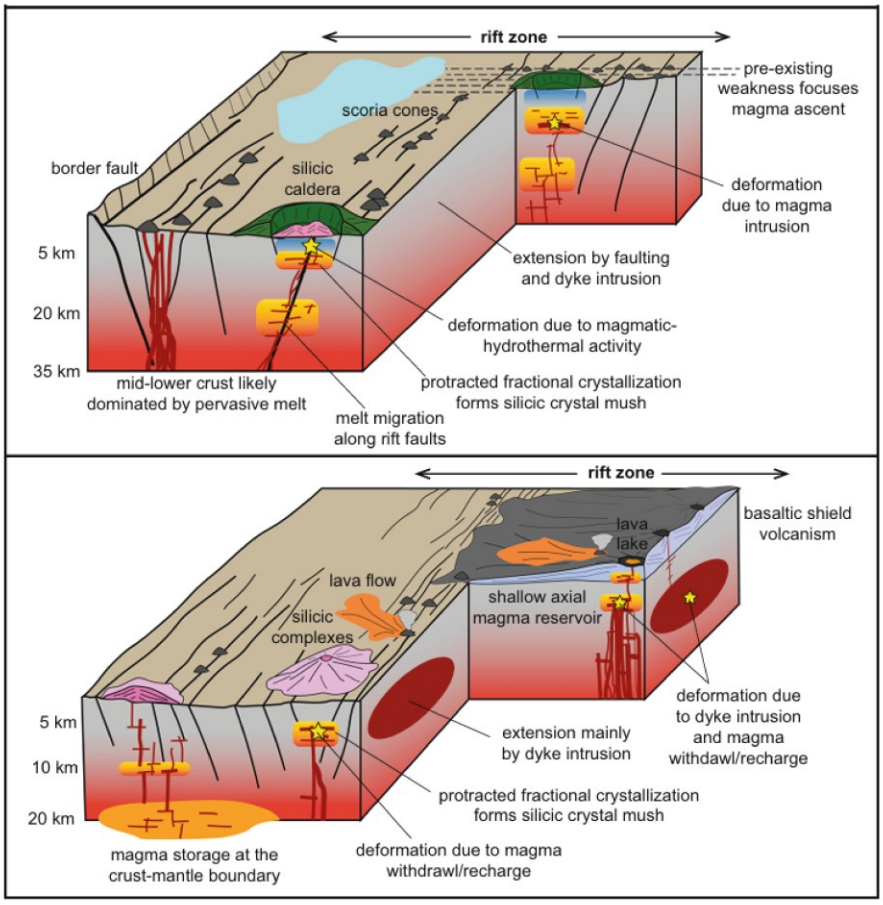

Figure 1.5: *Conceptual model of magmatic systems in Ethiopian rift at different stages of their evolution (Biggs et al., 2021). Magmatic architecture in the MER (top) and Magmatic architecture in the Afar rift segments (bottom), with the Manda Hararo segment in the foreground, and the Erta Ale segment in the background.*

Repeated dike injections are considered the fundamental driver of oceanic spreading (Hayward and Ebinger, 1996; Ebinger, 2005; Bialas et al., 2010; Wright et al., 2012). During such episodes, magma is transported from crustal reservoirs to the surface through fissures, where it intrudes as dikes and sometimes erupts. Direct observations of this process at mid-ocean ridges are rare because most occur beneath several km of seawater. A notable example is the 1993 dike injection at the Juan de Fuca Ridge (Dziak et al., 1995; Fox et al., 1995). Continental rift zones, however, have provided key opportunities to study dike emplacement at the surface. Well-documented examples include the Krafla rifting episode (1975-1984), the seismic crisis and associated Bardarbunga caldera collapse (2014), and the inflation-deflation cycles at the Svartsengi volcanic system (2023-2024) in Iceland; the Ardoukoba eruption (1978) in Djibouti; and the Dabbahu-Manda Hararo rifting episode (2005-2010) in Afar. These events, combined with advances in geophysical monitoring have provided crucial insights into how magmatic processes facilitate continental break-up. The general purpose of this thesis is anchored in this

general framework and reasoning of magmato-tectonic interactions during the late stages of continental breakup, on the example of the Afar depression (Ethiopia).

1.1 The general context of ocean-continent transition and the MAGMAFAR goals

At continental margins, the lithosphere is progressively thinned and stretched until complete rupture, allowing the formation of new oceanic crust. Two types of passive margins can be distinguished (Figure 1.6), depending on whether they are magma-poor or magma-rich (e.g., Franke, 2013; Peron-Pinvidic et al., 2019). These rifted margins develop during the final stages of extension, when continental breakup is imminent or has just occurred. While the processes that initiate rifting are observable at continental rifting in some active places on Earth, the final stages leading to breakup and the formation of new oceanic crust are only well illustrated by fossil context on ocean margins imaged by geophysics, making sampling and their petrological/geochemical investigation difficult.

Uniform extension of the lithosphere (McKenzie, 1978) explains some basic properties of magma-poor rifted margins but fails to explain other important characteristics (Huismans and Beaumont, 2011; Huismans and Beaumont, 2014; Lu and Huismans, 2021). To address this, Huismans and Beaumont (2011) proposed that crustal stretching can occur in a decoupled manner between the upper and lower lithospheres rather than occurring uniformly. Building on this work, Huismans and Beaumont (2014) identified two end-member styles of rifted continental margins (Figure 1.7), controlled by depth-dependent extension with contrasting styles of lithospheric breakup. In type I margins (e.g., the Iberia-Newfoundland conjugates), upper lithosphere breakup occurs while the lower lithosphere is still necking, whereas in Type II margins (e.g., central South Atlantic) the upper lithosphere extends over a wide region resulting in distributed necking and thinning, leading to breakup significantly later than the lower lithosphere. The tectonically active Afar rift system is the best location globally in which to study magmatic rift development and processes of the ocean-continent transition. Currently, the lower crust of Afar is being stretched while the upper crust remains largely intact (Hammond et al., 2012), consistent with Type II extension.

The Ocean-Continent Transition (OCT) marks the boundary between rifted domains and the oceanic lithosphere. The geologic processes in this domain are mostly active during the late syn-rift phase. Defining this phase, however, is complex due to the variety of rift styles, and geophysical data, though greatly improved in recent decades, still have limited resolution for

imaging structures at large depth along and across the passive margins. In magma-poor margins (Figure 1.7 a), the OCT is characterized by hyperthinned crust (usually around 10 km), abnormal heat fluxes, gravity anomalies, exhumed mantle and/or intruded distal margin. Mantle exhumation is thought to be associated with the absence of mantle melting by decompression and occurs after the completion of continental break up (Huismans and Beaumont, 2011; Huismans and Beaumont, 2014; Picazo et al., 2016; Lu and Huismans, 2021). In magma-rich margins (Figure 1.7 b), the OCT is less well described especially because the upper crust is covered by thick volcanic flows (Seaward Dipping Reflectors (SDRs). Consequently, the nature and the deformation of the crust below these units cannot be studied by direct observations, except in exhumed margins (e.g., Greenland) where a transitional crust is characterized by intrusions and underplating of magma during rifting (Geoffroy, 2005).

The OCT is one of the noteworthy events in global geodynamics. This striking phenomenon brings about fundamental changes in various parameters such as the transition from rift to drift, the mantle source of magmas, the nature of the lithosphere, and the architecture of magmatic plumbing systems. Despite their importance for the Earth geodynamics, the processes that govern the initiation of oceanic spreading and the associated production of juvenile magmatic crust remain first order open questions. Global models linking the striking different morphologies, the variable igneous parameters (magma budgets, compositional variations related to source and crustal processes), and the contrasted tectonic activity of the different types of Mid Ocean Ridges or magmatic rifts have been explained by quantitative modelling, bathymetric, and petrologic studies (Buck et al., 2005; Cannat et al., 2019; Carbotte et al., 2006; C. J. Ebinger & Casey, 2001). However, few quantitative constraints exist on: (i) how do magmatic and tectonic processes control the styles and morphologies of magmatic segments? what are the parameters responsible for the characteristics of proto, steady-state spreading processes? (ii) why and how do stable magma production and organized/focussed transfer to the crust start and led to break-up?

The ANR-funded MAGMAFAR project is designed to address these questions by investigating the unique active system of the Afar rift. The project integrates several work packages to develop a quantified evolutionary model of magmatic OCT and associated processes. This thesis contributes to the MAGMAFAR project by focusing on the detailed architecture of active magmatic segments along the axial zone of the rift.

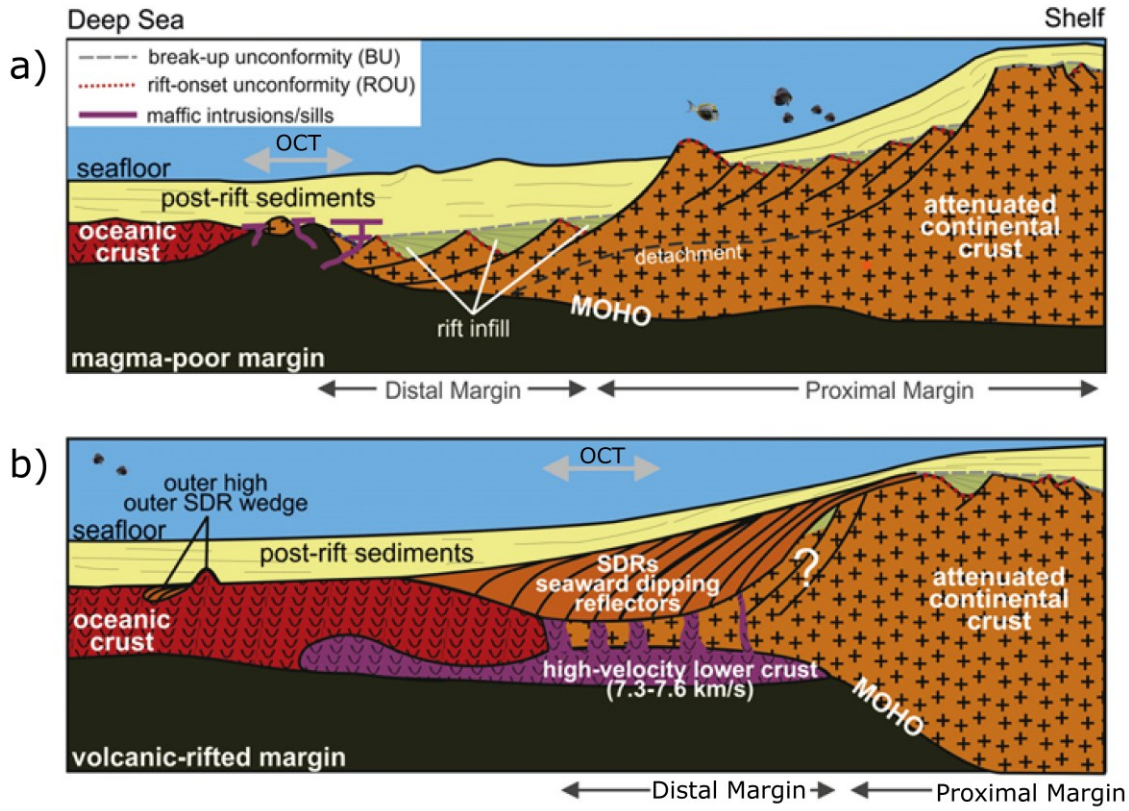

Figure 1.6: *Schematic model of the two types of passive continental margins (Franke, 2013). a) The magma-poor margin is defined by a wide area of highly attenuated continental crust where the upper crust is deformed by deep-reaching listric faults that may sole out on a common detachment surface, the proximal margin. In the distal margin the listric faults may cut across the entire crust leading to a detachment at the Moho discontinuity. Further seaward extensional allochthones may be situated on exhumed mantle before relatively thin oceanic crust is reached. b) Magma-rich margins show a comparably narrow proximal margin with considerable crustal thinning over a short distance, thick wedges of syn-rift volcanic flows manifest in seismic reflection data as SDRs, and wide high-velocity (Vp > 7.3 km/s) lower-crust seaboard of the continental rifted margin. The oceanic crust is comparably thick at those margins, especially close to the OCT.*

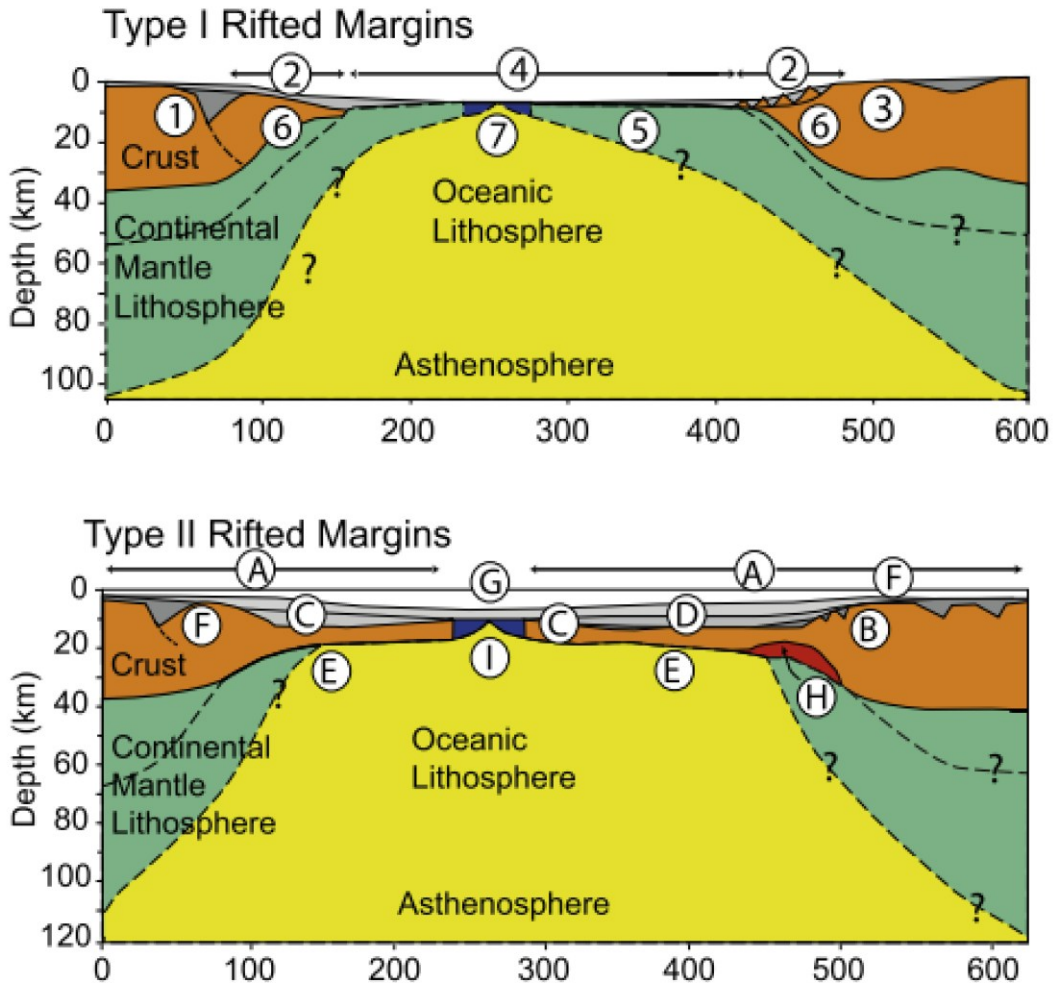

Figure 1.7: *Diagram showing characteristic properties of two end member types of rifted continental margins (after Huismans and Beaumont, 2014). The top panel shows depth-dependent extension with strong crust bonded to mantle (Type I Margins) marked by 1) development of major basin forming faults/shears that penetrate into the crust possibly rooting in the lower crust; 2) formation of narrow transitional regions (<100 km wide) where the continental crust thins abruptly; 3) Asymmetric geometry and uplift of rift flanks; 4) breakup of the crust before breakup of the mantle lithosphere; 5) exhumation and exposure of serpentinized continental mantle lithosphere in the OCT); 6) relatively little surface magmatism during rifting; 7) oceanic crust that is initially thin, and late stage establishment of a magmatic ocean spreading centre. The bottom panel shows depth-dependent extension with weak lower crust (type II margins) marked by A) ultra-wide (>350 km) regions of very thin continental crust, with little evidence for a lower crustal layer; B) faulted early syn-rift sedimentary basins; C) undeformed late syn-rift sediments; D) sediments deposited under demonstrated shallow marine; E) replacement of continental mantle lithosphere by hot asthenosphere beneath large regions of the margin; F) lack of mechanical flexural flank uplifts of the crust; G) no clear evidence of exposed exhumed mantle lithosphere; H) limited magmatism during rifting, with lower crustal seismic layers*

with velocities consistent with magmatic underplating, and SDRs; I) a mature magmatic mid-oceanic ridge established system soon after crustal breakup and normal thickness oceanic crust.

1.2 The Afar depression in the evolution of continental rifting

1.2.1 The East African Rift

The East African Rift System (EARS) is the archetypical active continental rift, extending over 3,000 km from the Afar region in the north to Mozambique in the south. It accommodates the divergence between the Somalian and Nubian plates and comprises a series of rift basins, fault zones, and volcanoes (Figure 1.8). As one of the world's largest continental tectonic structures, the EARS preserves the transition from continental rifting to oceanic spreading, offering a rare opportunity to study the full progression of this process. The system consists of distinct, diachronous segments: some magmatically active, such as the eastern branch, and others largely amagmatic, such as the western branch. To the north, it connects with the Red Sea and Gulf of Aden mid-ocean ridges, marking the transition toward oceanic opening. Rifting in East Africa is strongly influenced by magmatism, often localized along pre-existing lithospheric weaknesses. The rift flanks are defined by high plateaus, such as the Ethiopia-Yemen domes, which rise above 4,000 m. These elevated regions formed through both extensive volcanic activity between 45 and 22 Ma, linked to the opening of the Red Sea and Gulf of Aden (Wolfenden et al., 2005), and rift- or dome-related topographic uplift (Pik et al., 2003, 2008; Wichura et al., 2011; Sembroni et al., 2016).

Modern satellite geodesy and GPS studies show that rift opening rates vary widely along the East African Rift. In Ethiopia, present-day extension occurs at rates of ~4–6 mm/yr, generally oriented E–W to NNE–SSW, and decreases southward to ~2 mm/yr in the MER (Fernandes et al., 2004; Déprez et al., 2013; Saria et al., 2014; Birhanu et al., 2016), but can reach up ~20 mm/yr in Afar (McClusky et al., 2010; Pagli et al., 2014). These spatial variations reflect complex tectonic dynamics controlled by rift geometry/stage and inherited lithospheric structures. The development of several segments of the East African Rift was facilitated by the reactivation of Neoproterozoic orogenic suture zones (e.g., Corti et al., 2007; Schmidt et al., 2023), consistent with Wilson's (1966) theory.

Volcanism in the East African Rift occurred through multiple distinct episodes (Rooney, 2017, 2020a, 2020b, 2020c, and references therein). The initial Eocene phase (45-34 Ma) was dominated by basaltic eruptions in southern Ethiopia and northern Kenya. This was followed by the Oligocene flood basalt event (~33.9-27 Ma), which emplaced 1-2 km thick sequences

of voluminous trap lavas across northwestern Ethiopia and Yemen, representing one of the largest Cenozoic volcanic sequences worldwide. During the early Miocene (~26.9-22 Ma), a less voluminous but widespread basaltic resurgence occurred, with a notable pulse at 24–23 Ma. The middle Miocene (12-9 Ma) marked a return to large-scale basaltic volcanism, particularly in the Turkana Trough and the North Kenya Rift. This phase is primarily a basaltic event of limited duration (approximately 1 to 2 My), after which the expression of magmatism became largely localized. This phase is associated with the onset of extension in the MER around 11 My ago, with the initiation of steeply dipping boundary faults generally associated with eruptive volcanic centers, and a progressive focusing of the deformation zone (Ebinger and Casey, 2001). Between 9 and 5-4 Ma, volcanism became spatially and temporally variable, with persistent basaltic eruptions along rift margins and the Yerer-Tullu Wellel volcano-tectonic lineament, later advanced and concentrated on central volcanoes. The Stratoid phase (5-1 Ma) produced voluminous lava fields, beginning with fissural basaltic outpourings that evolved into low-flux eruptions in Turkana and the MER. Since ~1.8 Ma, magmatism and faulting become even more localized to magmatic segments approximately 20 km wide and 60 km long, marked by aligned eruptive centers, fissures, and focused faults (Ebinger and Casey, 2001). The most recent Axial phase (0.5 Ma-present) is defined by small-volume basaltic flows, chains of tuff cones, and large central silicic edifices, with activity largely restricted to axial or marginal grabens.

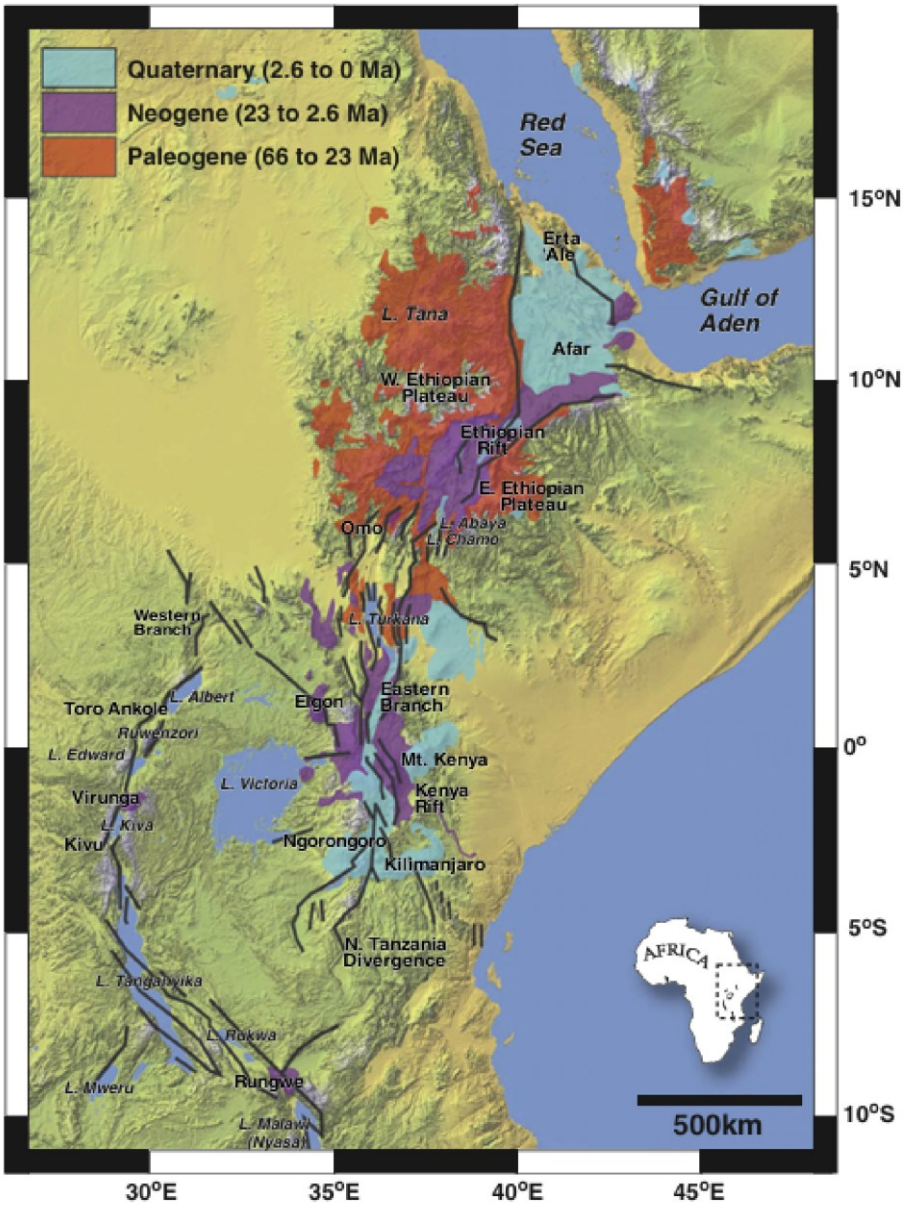

Figure 1.8: Map illustrating the magmatic activity in east Africa (after Rooney, 2017).

Geophysical data provide evidence for a mantle plume involvement in the generation of magmatism across east African. Seismic and tomographic studies have imaged a large low-velocity province (LLVP) beneath Africa (Figure 1.9), often termed the African superplume, linked to anomalous uplift across the East African superswell (Nyblade and Robinson, 1994; Bastow et al., 2005; Bastow et al., 2010; Hammond et al., 2011; Hansen et al., 2012; Hammond et al., 2014; French & Romanowicz, 2015). This structure likely supplied the thermal and

compositional anomalies driving volcanism and topographic uplift in Ethiopia since the Oligocene (Kendall et al., 2006).

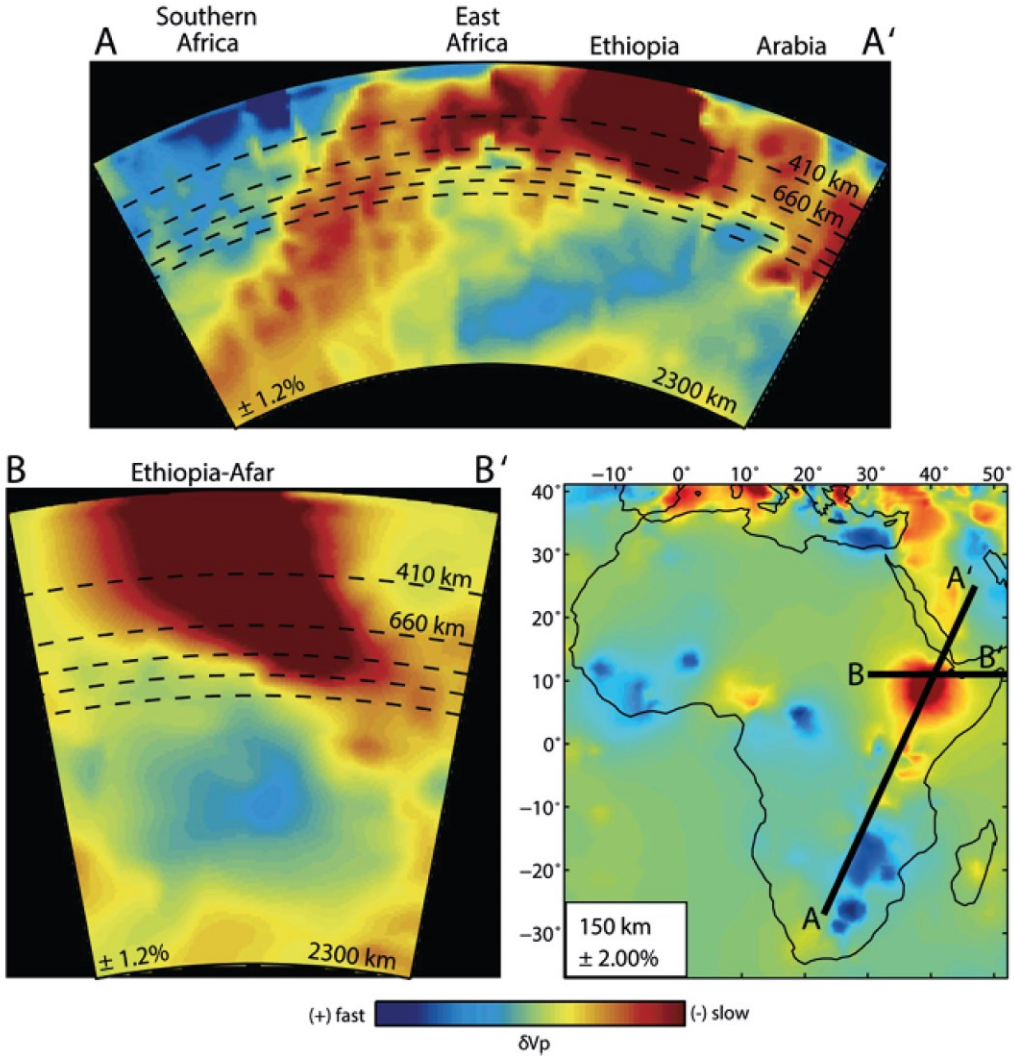

Figure 1.9: *Seismic tomographic image illustrating the LLVP beneath Africa (Hansen et al., 2012). Cross-sectional view of the P-wave tomography model along profiles A-A' (top) and B-B' (bottom), highlighting the low-velocity features in the African and Arabian mantle. Dashed lines mark the 410 and 660 km discontinuities as well as depths of 800, 900, and 1000 km.*

The involvement of a mantle plume in the generation of East African magmatism is also supported by geochemical data. The first isotopic evidence regarding the mantle source of the East African Rift was provided by (Schilling, 1973), who demonstrated that the East African Rift lavas exhibit isotopic compositions distinct from typical mid-ocean ridge basalts (MORB). Instead, they showed enriched mantle signatures, which Schilling interpreted as evidence for a

mantle plume contribution beneath East Africa. Geochemical data, particularly isotopic compositions, indicate that the MER and Afar lavas are derived from a mantle source distinct from typical Mid-Ocean Ridge Basalt (MORB) mantle source (Rogers, 2006). Specifically, $^{3}He/^{4}He$ isotope ratios of Afar flood basalts exhibit a primitive high ^{3}He mantle source typical of plume-influenced settings (Marty et al., 1996; Pik et al., 2006).

There is ongoing debate as to whether magmatism across EARS originates from a single plume or from multiple upwellings. Some models invoke a single, channelized plume (Ebinger and Sleep, 1998). However, geochemical differences between the diachronous segments (e.g., Ethiopia and Kenya rift) suggest contributions from more than one mantle source (Furman et al., 2006; Rogers, 2006). These divergent views may be reconciled through two distinct mantle plumes; the first order being the deep-seated anomaly arising from the African LLVP; the second order being secondary plumes upwelling from the larger-scale primary anomaly at upper mantle-transition zone depths (Pik et al., 2006). Rooney et al. (2012), suggested that the East African Rift magmatism reflects interaction among three components: the Afar plume, the sub-continental lithospheric mantle, and depleted upper mantle. While plume-derived material which resembles the mantle reservoir "C" component described by (Hanan and Graham, 1996), contributes significantly to the magmatism, the mantle source has been polluted by incorporation of metasomatized lithospheric mantle and recycled continental components. The mixing of these end members accounts for the heterogeneous geochemical signatures observed across the rift. However, basaltic rocks from the Afar and MER define two geographically and, to a lesser extent, geochemically distinct groups (Castillo et. al., 2020). These lava groups are inconsistent with the commonly held view that there is a distinct Afar mantle plume at the northern end of the rift system, and that the plume influence systematically decreases away from its center. Castillo et al. (2020) challenged the mantle source model proposed by Rooney et al. (2012), arguing instead that the high $^{3}He/^{4}He$ basalts from these groups reflect a dominant contribution from the African Superplume. They suggested that this deep mantle source, rather than significant lithospheric contamination or simple plume-asthenosphere mixing, plays a major role in generating East African Rift magmatism. Watts et al. (2025) proposed that beneath Afar there is a single, asymmetric, but chemically and spatially heterogeneous mantle upwelling (Figure 1.11). The variability in melt composition and abundance across the three rift arms is controlled by rifting rate and lithospheric thickness. Faster, thinner rifts (e.g., the Red Sea Rift) show more channelized flow and higher compositional variability, while slower, thicker lithosphere rifts (e.g., MER) display shorter-scale heterogeneity.

Primitive lavas within the EARS have been classified into six magma types (Rooney, 2020d). The generation of these magmas is largely the result of either: (i) melting of easily fusible compositions located within the lithospheric mantle due to thermobaric perturbations of the lithosphere, or (ii) melting of the convecting upper mantle due to decompression caused by thinning of the plate during extension (Figure 1.10). Type I magmas are defined primarily from flood basalts erupted during the Eocene and Oligocene. The origin of these lavas is associated with a mantle plume. Type II magmas are typically encountered during the initial stages of lithospheric destabilization (Rooney, 2020a, 2020b, 2020d). These magma types are typically the first erupted within the Southern Kenya Rift, subsequently transition to mixed source melts, and then eventually to melts derived from the convecting upper mantle. The potential origin for these magmas is thought to be within the sub-lithosphere (Rooney et al., 2014; Furman et al., 2016; Natali et al., 2016; Rooney, 2017). Type III magmas, ubiquitous within the EARS, are found throughout the well-developed rifts in Afar, MER, and Northern Kenya Rift, where lithospheric mantle reservoirs currently have limited contribution to erupted lavas (Figure 1.10). The origin of these lavas has been hypothesized within the lithospheric mantle as a mixture of plume, depleted mantle, and African lithosphere (Rooney, 2017; Rooney et al., 2012). Type IV magmas are a hybrid of melts derived from the source of Type II and Type III magmas and may be formed when asthenosphere-derived Type III magmas interact with and destabilize existing lithospheric mantle metasomes (Figure 1.10 b). Its type locality is in the modern magmatism occurring in parts of the Turkana Depression. Type V magmas are typified by one of the major magmatic trends within the Western Branch of the EARS. The origin of these lavas has been described as melts derived from a phlogopite-bearing lithospheric mantle metasome (Furman & Graham, 1999). Type VI magmas are characterized by extreme depletion in the most incompatible trace elements (Figure 1.9 b), have unradiogenic Pb isotopes, and radiogenic $^{143}Nd/^{144}Nd$. These lava types are found only within the Afar Depression, and even then only in lavas that are less than 5 Ma. The genesis of such lavas has been proposed as melting of a depleted component 'intrinsic' to the Afar plume (Barrat et al., 2003; Daoud et al., 2010; Rooney et al., 2023).

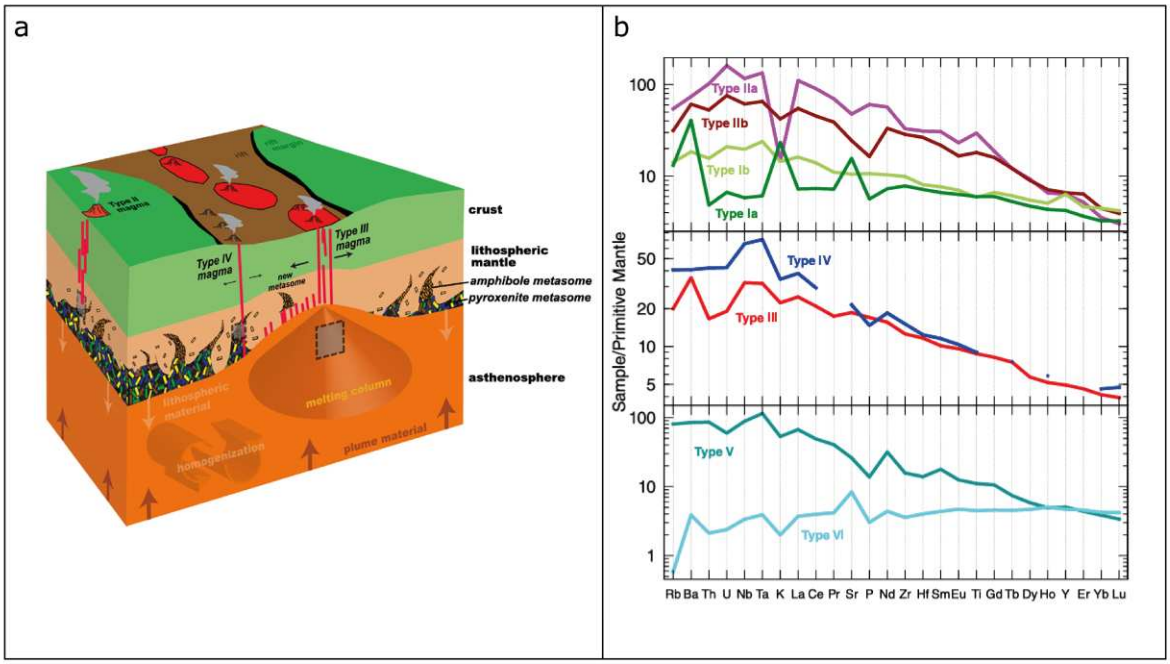

Figure 1.10: *a) Cartoon depiction of melt generation processes within the Eastern Branch of the East African Rift System (after Rooney, 2020d). b) Primitive mantle normalized diagram (Sun and McDonough, 1989) showing the different magma types identified in East Africa (after Rooney, 2020d).*

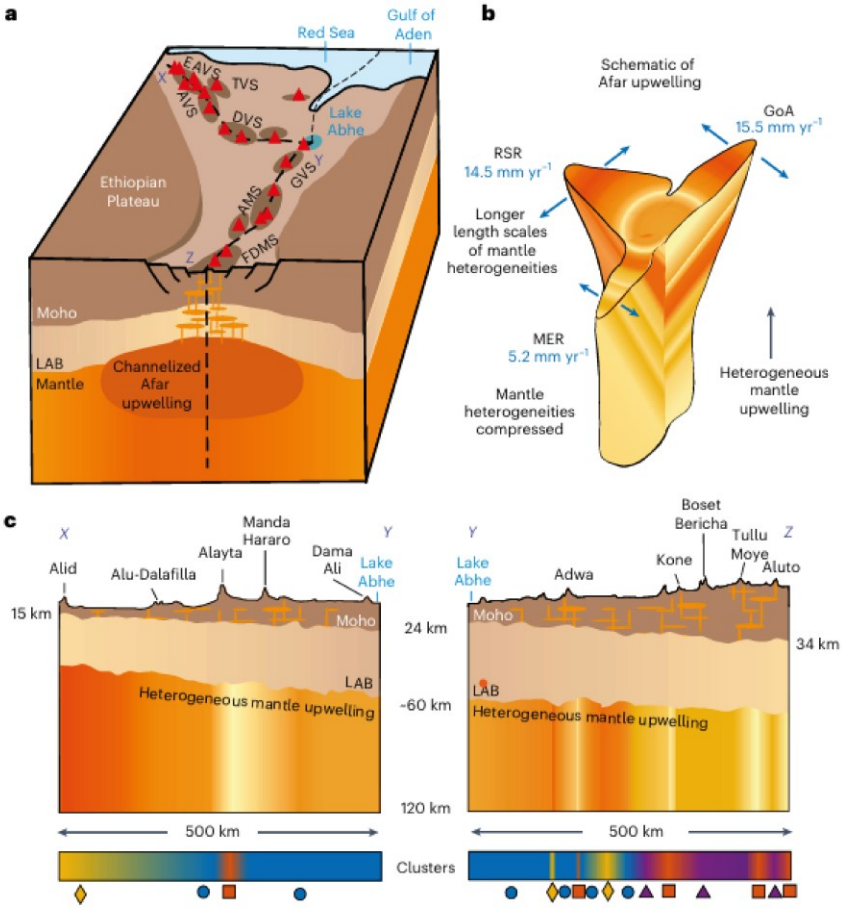

Figure 1.11: *Spatially heterogeneous nature of the mantle upwelling beneath Afar (Watts et. al., 2025). a) the rifts across Afar and the mantle upwelling being channelized by the rift. The lines of section X-Y-Z are those shown in panel c. Volcanic segments are shown and labelled. b) the Afar upwelling showing the dimensions of channelized flow along the three rifts (dashed lines). c) cross sections along the red sea rift (RSR) (line section X-Y) and MER (Y-Z) showing the distribution of chemical heterogeneities within the upwelling. The depths of distinct features, including the lithosphere asthenosphere boundary (LAB), are not shown to scale.*

1.2.2 Ethiopian volcanic province

The Afar Depression forms a key node in the evolution of the Ethiopian volcanic province, where deep mantle upwelling, lithospheric extension, and magmatic processes are intimately coupled during the OCT. This region extends across Ethiopia, Eritrea, and the Republic of Djibouti, and marks the boundary between the Somali, Nubian, and Arabian plates. It is a triple junction of the rift-rift-rift type. This depression is an arid region covering approximately 200,000 km² bounded by a complex system of major border faults and stretched and flexure

zones (Wolfenden et al., 2005), which form the escarpments and topographic margins of the Ethiopian Plateaus to the west and south (Figure 1.12).

The long-term plume-rift interactions in Afar control segment-scale volcanism and influence the evolution of rifting. Rifting in this region initiated with the arrival of the Afar plume around 30 Ma ago (White & McKenzie, 1989; Marty et al., 1996; Morgan, 1972; Pik et al., 2006; Bastow et al., 2008), producing voluminous flood basalts across the Ethiopian plateau (Hofmann et al., 1997), followed by the development of a rift-ridge-ridge triple junction linking the MER to the Red Sea, and Gulf of Aden oceanic ridges (Figure 1.12).

Seismic profiles have been used to infer the crustal structure of the Afar region. Crustal thickness beneath the Ethiopian Highlands can reach up to 45 km. In contrast, within the Afar Depression, total crustal thickness ranges from 20 to 26 km in the central and southern areas, decreasing to only 15-16 km beneath the Erta Ale region (Makris & Ginzburg, 1987). This pronounced thinning in northern Afar is accompanied by large volumes of basaltic eruptions since the Quaternary (Figure 1.13; Bastow & Keir, 2011; Keir et al., 2011).

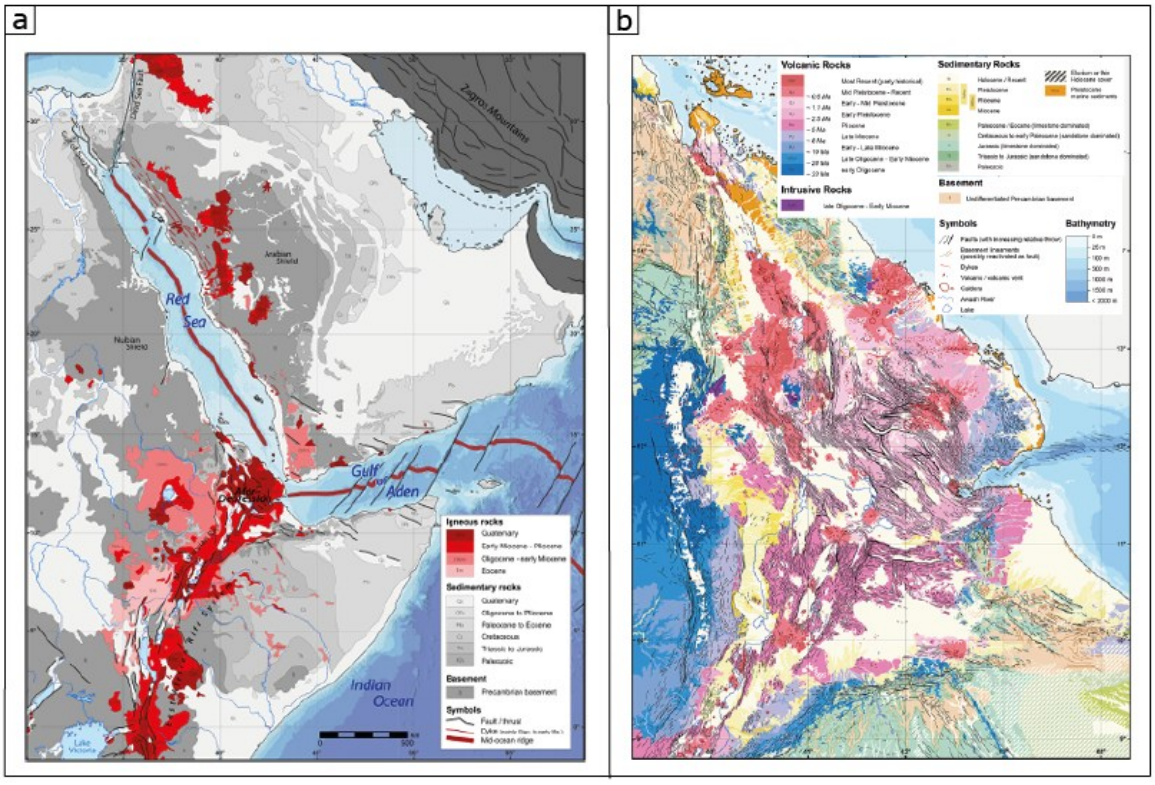

Figure 1.12: *Geological map of the rift systems (after Rime et al., 2023). a) map illustrating the extent and chronology of volcanic rocks of the Afro-Arabian system. b) geological map of the Afar depression*

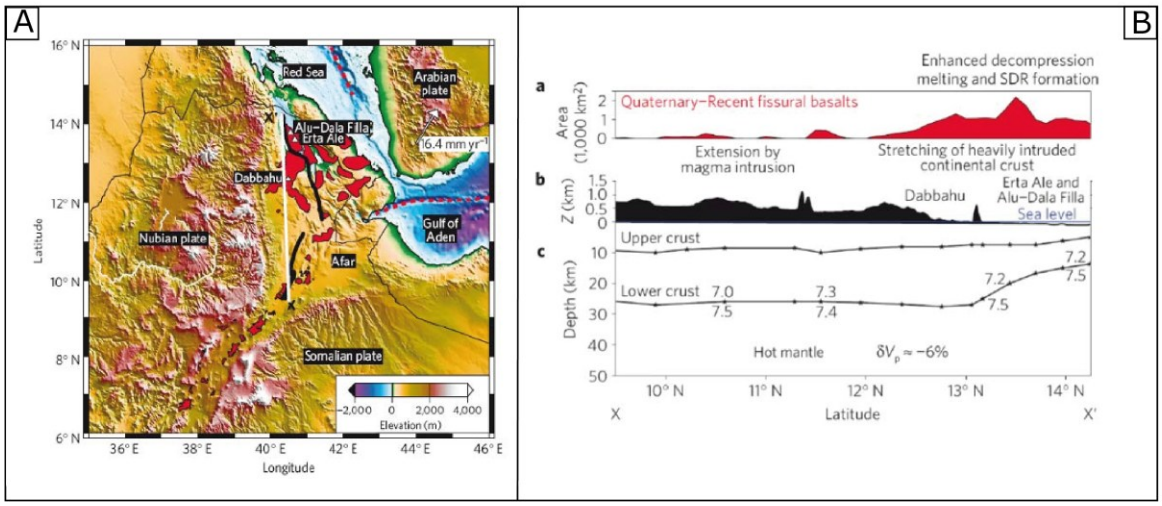

Figure 1.13: *A) Topography and bathymetry of the Horn of Africa (after Bastow and Keir, 2011). Black lines indicate the location of seismic profiles used to constrain crustal thickness in B. white triangles mark the position of volcanoes, red areas correspond to Quaternary to recent volcanism, and the white line highlights the X-X' profile shown in the B. B) spatial distribution of volcanism in Ethiopia (a) variations in the volume of Quaternary to recent volcanism along profile X-X', highlighting the sharp increase in volcanism toward northern Afar and its negative correlation with topography; (b) crustal thicknesses inferred from seismic velocities, plotted in (c), showing an almost constant thickness of the upper crust and a sudden thinning toward northern Afar, coinciding with the peak of Quaternary volcanism and the lowest elevations in the region.*

1.3 The evolution of Afar depression

The Afar Depression is a region where the African LLSVP extends to relatively shallow depths (Figure 1.9), giving rise to what is referred to as the Afar plume. Here, rifting occurred diachronously with the onset of the Gulf of Aden Rift at ~ 35 Ma (Leroy et al., 2010; Pik et al., 2013), the Red Sea Rift at ~23 Ma (Szymanski et al., 2016), and the Main Ethiopian Rift at ~11 Ma (Wolfenden et al., 2004). Afar is a mature continental rift where extension is accommodated by both tectonic and magmatic processes. Rifting started 29-25 Ma ago (Wolfenden et al., 2005), and has been characterized in western Afar by a magmatic wide rift stage (Stab et al., 2016), until significant thinning of the lithosphere (6-5 Ma ago) prepared for the subsequent extrusion of the widespread and voluminous Magmatism.

Magmatism in the Afar Depression can be subdivided into several major episodes (Figure 1.14; Varet, 2018; Rooney, 2020; Rime et al., 2023). Before the Miocene (24 Ma ago), the region

formed part of a single broad continental shelf, with the earliest evidence of extension marked by the opening of the Gulf of Aden at 30 Ma. During the early to middle Miocene (24-15 Ma), crustal uplift accompanied the formation of the Red Sea and East African rift systems. This stage was characterized by intense magmatism, including the emplacement of the Affara Dara pluton, and the opening of the Red Sea at around 14 Ma.

From 15-3.9 Ma, rifting continued with the emplacement of the Dahla Series (Figure 1.14 A) and the development of marginal rift basins. Volcanism became more widespread and progressively migrated toward the rift interior, while the chemical composition of the lavas evolved toward more primitive signatures. Key volcanic products of this period include the Adolei basalts and Mabla rhyolites. Concurrently, the Danakil Ridge, mainly composed of earlier formations (Precambrian basement and Mesozoic cover), experienced significant uplift without undergoing any major internal deformation, while oceanic crust began forming in the Gulf of Aden between 8 and 4 Ma.

The most voluminous phase of magmatism occurred during the eruption of the Afar Stratoid Series between 3.8 and 1 Ma (Figure 1.14 B). Large volumes of fissural basaltic flows, with more than 55,000 km² and reaching thicknesses of over 1 km, covered the depression (Geological Map of Central and Southern Afar, 1975; Lahitte et al., 2003b; Stab et al., 2016; Varet, 2018; Rime et al., 2023). This magmatic pulse coincided with the opening of the Gulf of Tadjourah at 3 Ma, representing the inland propagation of the Aden Ridge and the onset of proto-oceanic spreading. During this phase, the Danakil Block was uplifted and became a distinct tectonic unit, acting as a structural barrier between the Red Sea and Afar.

Recent studies highlighted how continental flood basalt provinces evolve toward axial magmatic segments during rift maturation (Alene et al., 2017; Rooney et al., 2023; Tortelli et al., 2022, 2025). The transition from the Stratoid to the Gulf Series in Afar depicted a fundamental change in rift magmatism. The Stratoid flood basalts, emplaced at approximately ~3.8 My, were voluminous and broadly distributed across southern and central Afar, reflecting diffuse strain and melting of a mixed mantle source including plume, depleted mantle, and metasomatized lithosphere (Alene et al., 2017; Rooney et al., 2023). In contrast, the Gulf Series (~1.1-0.6 Ma) was less voluminous but more spatially localized marking the onset of axial-style magmatism, with geochemical evidence for a more homogeneous mantle contribution and shallower, higher-degree partial melting (Rooney et al., 2023). This transition reflects a progressive focusing of extension and lithospheric thinning, which in turn shallowed the melting column, increased the degree of partial melting, and confined eruptions to narrower

rift zones. Tortelli et al. (2022, 2025), suggested that these changes can be explained by tectonic localization of strain rather than variations in mantle plume input.

Since ~0.4 Ma, magmatism in Afar has become increasingly focused along the axes of discrete rift segments, marking the current axial phase of rift evolution (Figure 1.14 C). These axial segments display significant contrasts in the volume of recent magmatic activity. The northern Afar (Erta Ale) segment is characterized by significantly higher recent melt supply (magmatic topography) compared to the central (Dabbahu-Manda Hararo) and the southern (Asal-Ghoubbet) segments, where magmatism has been comparatively less voluminous (Figure 1.15 B). An open question that follows is: how did magmatism evolve from the Gulf Series into the fully axial phase of magmatic rift segments, and what processes controlled this transition? why does the locus of the highest-volume magmatism in the present-day axial phase lie in northern Afar, while the earlier voluminous Stratoid and Gulf Series volcanism was concentrated in southern and central Afar? Understanding this transition and spatial shift in magmatic productivity is key to resolving how mantle supply, lithospheric structure, and rift kinematics interact to reorganize magmatism during the final steps toward continental break up.

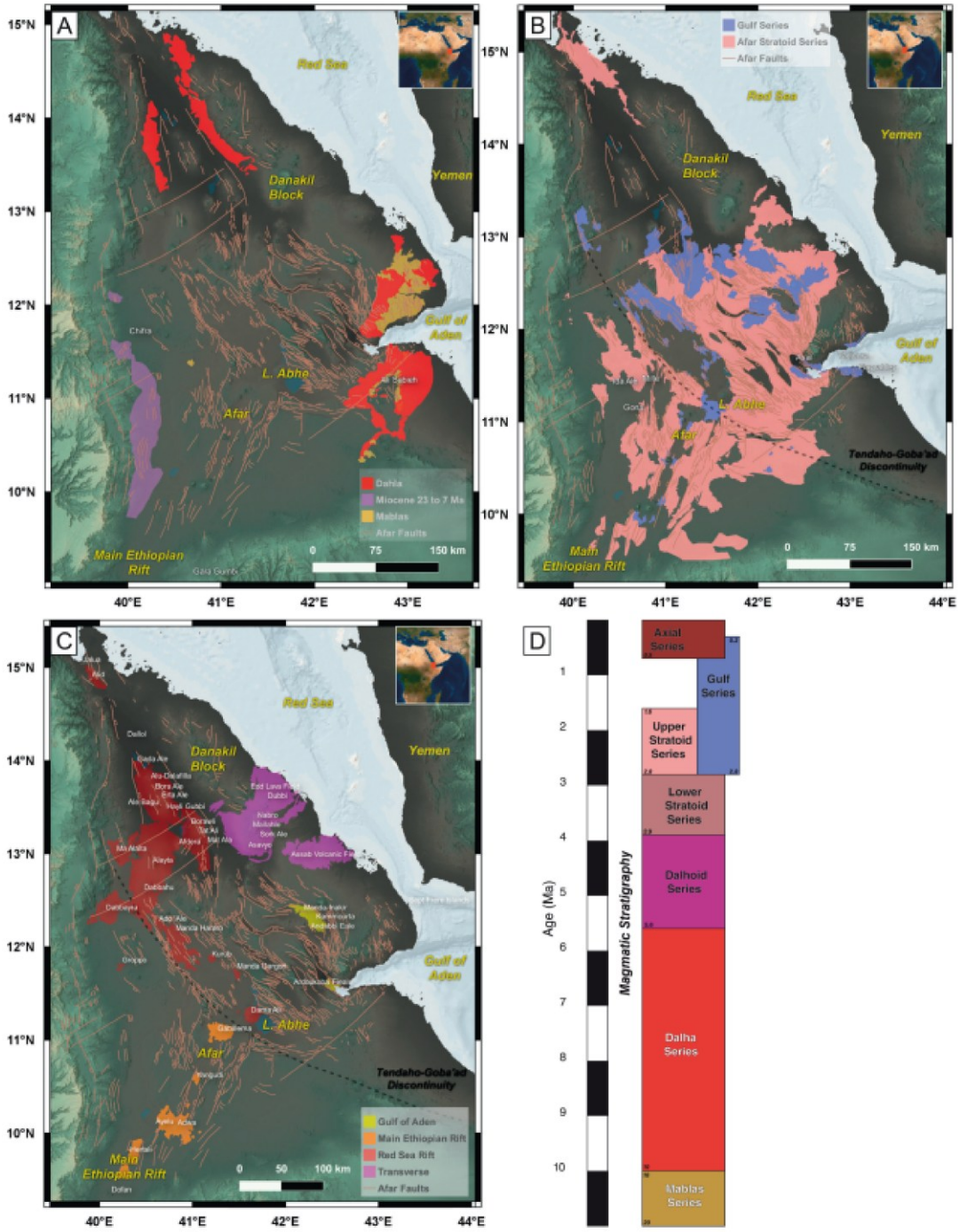

Figure 1.14: Maps from Rooney (2020b), based on the work of Stab et al. (2016), the Afar geological map (Geological map of central and southern Afar, 1975), and the geological map of Djibouti (Geological map of the Republic of Djibouti, 2015) showing the distribution of rock units during the development of the rift during: (A) the Miocene; (B) the Afar Stratoid Series and the Gulf Series; (C) the Axial phase. Volcano names and locations shown in white are taken from the Smithsonian database.

(D) Stratigraphic column after Rooney (2020b) showing the magmatic units. Small italicized numbers represent the approximate age limits of each unit in millions of years.

1.4 The Afar rift magmatic segments

The magmatic, structural and crustal variations of the along axis rift segmentation from the MER to northern Afar (Figure 1.15) is thought to represent various stages (maturity levels) of extensional processes (Buck et al., 2006; Bastow et al., 2008; Ebinger and Casey, 2001; Keir et al., 2013; Rooney et al., 2014) or alternatively different styles of rifting (Stab et al., 2016; Rime et al., 2023). Complete continental break-up has not yet occurred in the Afar, resulting in a stretched and heavily intruded crust (Bastow & Keir, 2011; Hammond et al., 2011; Keir et al., 2013; Stab et al., 2016). Highly differentiated melts from Central Afar were associated with important upper continental crust contamination until 4 Ma ago, while this upper crust contamination is absent since then (Ayalew et al., 2019), suggesting that the Afar crust is now mainly magmatic (Hutchison et al., 2018). In this geodynamic framework, breakup of the continent occurs by the interplay between structural and rheological changes in the lithosphere due to mechanical deformation, heating, and magmatism, with increasing proportions of extension accommodated by magma intrusion and dyking processes.

From the onset of the axial phase to the present, rifting in Afar has been focused along en-echelon magmatic rift segments (MRS), where divergence is accommodated at a rate equivalent to slow spreading centers (~15 mm/yr; Doubre et al., 2007; McClusky et al., 2010). These MRS are typically 60-100 km long and 20-40 km wide but exhibit contrasted characteristics regarding faulting and volcanism. From North to South, the Erta Ale, the Dabbahu-Manda Hararo, and the Asal-Ghoubbet rift segments display typical morphologies which vary from a prominent axial ridge to an axial depression (Figure 1.15 B). This raises the question why rifting is expressed differently in each of the Afar rift segments. Afar is often considered the most mature part of the East African Rift, and differences in rifting modes between its segments can be interpreted as variations in maturity level, or rifting style. The volume of Quaternary recent fissural volcanism and crustal thickness have been used to argue that Erta Ale segment represents the final stage of break-up process (Bastow and Keir, 2011; Keir et al., 2013). This segment experienced an abrupt increase in extensional strain accommodated by ductile stretching compared to the southern Dabbahu-Manda Hararo segments which are still principally accommodating extension by magmatic intrusion. Protracted heating and weakening of the plate from previous localized magma intrusions are

invoked for this change in extension mechanism, accompanied by a switch from an intrusion dominated magmatic system to an extrusion dominated one, which both combined will generate typical SDRs. This model however can be challenged by the fact that previous voluminous magmatic episodes linked to continuous channelling of the Afar plume have been emplaced southward in central Afar (Stab et al., 2016). Thus, central Afar apparently experienced higher intrusions and potential weakening of the crust than Northern Afar. In addition, evidence of significant Plio-Quaternary volcanic episodes are lacking along the margins of this narrow northern segment (Le Gall et al., 2018). This model of typical final stage of extension at Erta Ale is also difficult to reconcile with the case of the southernmost Asal-Goubbet segment. The Asal-Goubbet segment is located on a terminal position close to the adjoining active spreading ridge (Gulf of Aden), and experienced important recent crustal thinning (Doubre et al., 2007; Geoffroy, 2005), but it displays opposed morphology and magmato-tectonic characteristics, in contrast to the Erta Ale segment (Figure 1.15 B; Geoffroy et al., 2014; Manighetti et al., 2001; Pinzuti et al., 2013). Thus, rather than simply considering the various Afar segments as representing different stages of rift evolution (Bastow & Keir, 2011; Ebinger and Casey, 2001) or ridge propagation (Manighetti et al., 2001), it has been recently proposed that their characteristics could be derived from different styles of rifting (Stab et al., 2016; Rime et al., 2023) principally controlled by the availability of magmas and the long-term interplay between the continental lithosphere and the underlying Afar plume.

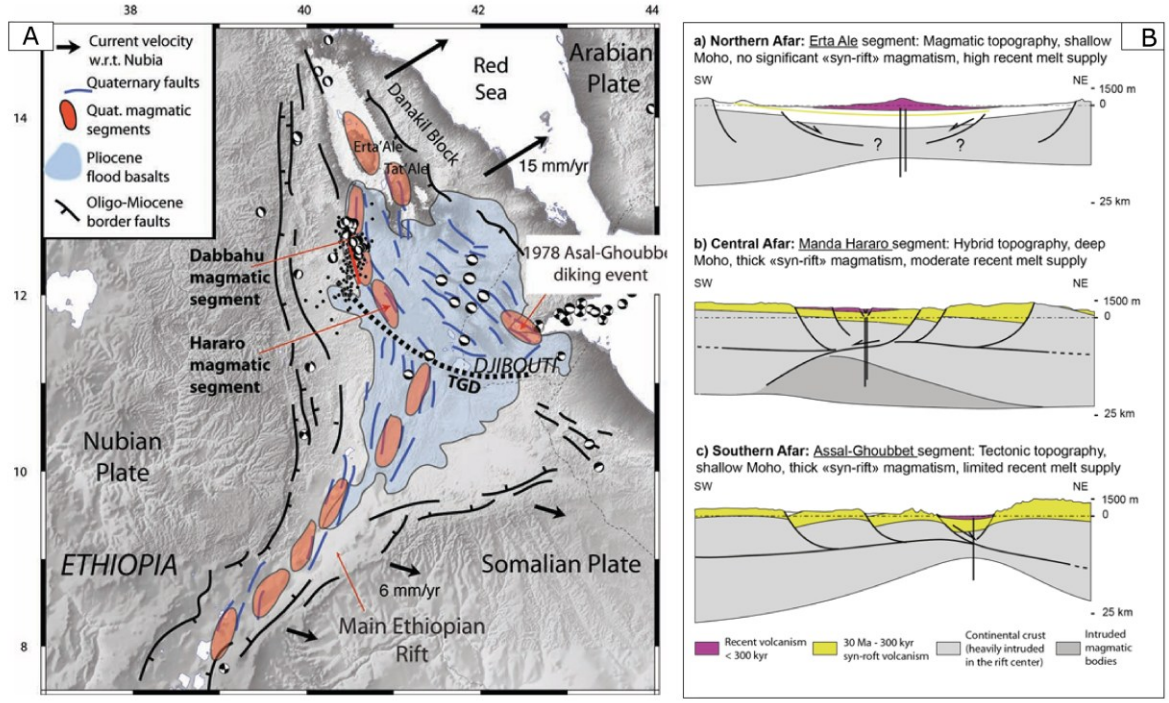

Figure 1.15: *A) Magmatic segments of the Afar depression (After Ebinger et. al., 2008). B) schematic cross sections of the three most active magmatic segments in Afar illustrating their different styles, as well as their contrasted long-term and recent magmatic activity. Horizontal and vertical crustal scales are identical. The vertical scale for topography is different.*

1.5 Recent magmato-tectonic activities within the Afar magmatic segments

The Afar Depression has been the site of multiple recent magmato-tectonic events, each associated with distinct rift segments discribed above. These segments illustrate varying expressions of active rifting and magmatism. The geophysical data and related studies provide key constraints for the description and understanding of the magmatic segments. Recent geophysical documentation of the most recent magmatic and rifting events along the Erta Ale and Dabahhu segments reveals important details about the architecture and operation of plumbing systems, highlighting contrasts in the shape and depth of magma reservoirs (Field et al., 2012a; Pagli et al., 2012; Xu et al., 2017; Moore et al., 2019). Possible interconnections between the adjacent Dabbahu and Manda Hararo segments have also been reported (Illsley-Kemp et al, 2018). In Central Afar, geophysical studies show an unexpected crustal stress field and seismic anisotropy oriented perpendicular to rift axis (Illsley-Kemp et al., 2017). They also point to diverging interpretations of how divergence is accommodated, and how this relates to

the long-term history and evolution of its magmatic segments (Doubre et al., 2017; Pagli et al., 2018).

Comparing these Afar events to globally active rift systems, particularly the Icelandic rift zones, reveals striking parallels in the style and mechanisms of rift propagation. The Dabbahu-Manda Hararo rifting episode bears strong similarity to the 1975-1984 Krafla rifting episode in northern Iceland, which also involved episodic dyke intrusions, ground deformation, and fissural eruptions (Einarsson and Brandsdottir 1980; Ebinger et al., 2010). More recently, the 2021-2024 fissural eruptions near Grindavik on the Reykjanes Peninsula have shown a similar dynamic, with repeated magma intrusions, minor eruptions, and rapid surface deformation (Greenfield et al., 2022; Pedersen et al., 2023). Below is described the detailed sequence of recent magmato-tectonic events within the three most active Afar magmatic segments.

1.5.1 The Erta Ale segment

The Erta Ale segment is a NNW-trending rift segment considered a southward en-echelon propagation of the Red Sea Ridge (Tazieff et al, 1972; Manighetti et al., 1998). It extends 95 km in length and 42 km in width, with tectonic extension occurring at ~13 mm/yr (McClusky et al., 2010; Pagli et al., 2014). This geodynamic setting makes Erta Ale a natural continuation of the Red Sea opening, where volcanism is closely linked to lithospheric thinning. Volcanic activity is dominated by persistent effusive eruptions and long-lived lava lakes, particularly at Erta Ale volcano, which has been active for decades (Barberi and Varet, 1977). While most erupted lavas are basaltic with little variation (Field et al., 2012b; Watts et al., 2020, 2023), the full Erta Ale range shows a complete differentiation series from basalt to rhyolite (Barberi & Varet, 1970; Barrat et al., 1998), with the oldest rocks dated at 1.2 ± 0.5 Ma (barberi, 1972).

Geophysical, petrological, and geochemical studies have provided insights into the architecture of the Erta Ale magmatic plumbing system and the evolution of its magmas (Figure 1.16). The persistence of the lava lake indicates that the edifice is primarily sustained by intrusions and a reservoir located at very shallow depths (Figure 1.16 a; Field et al., 2012b; Oppenheimer & Francis, 1997). Seismic studies reveal shallow magma lenses at 1-5 km depth (Figure 1.16 c; Moore et al., 2019; Pagli et al., 2012; Xu et al., 2020), feeding eruptions via dike intrusions. Such shallow storage has been used to argue for an oceanic character of the Erta Ale segment (Moore et al., 2019), though this architecture is typically associated with fast-spreading ridges (Macleod and Yaouancq, 2000). In contrast, the current spreading rate is closer to slow to ultra-slow ridges (McClusky et al., 2010). Some authors interpret the high magma fluxes as evidence

of final asthenospheric decompression linked to final thinning, related to late-stage continental breakup (Figure 16 b; Hutchison et al., 2018; Bastow and Keir, 2011; Keir et al., 2013). Recent petrological and isotopic data suggest a more complex transcrustal plumbing system. Watts et al. (2023) proposed a multi-level, partly interconnected magmatic network, where melts rise from plume-fed mantle sources, experience limited deep-crustal assimilation, and mainly differentiate in shallow sill-like reservoirs before eruption (Figure 1.16 d). A thicker transcrustal magmatic system, where protracted differentiation from basalt to trachyte-rhyolite occurs via fractional crystallization and reactive porous flow in mush-rich reservoirs (Figure 1.16 e) is however documented and suggested by (Pin et al., 2024).

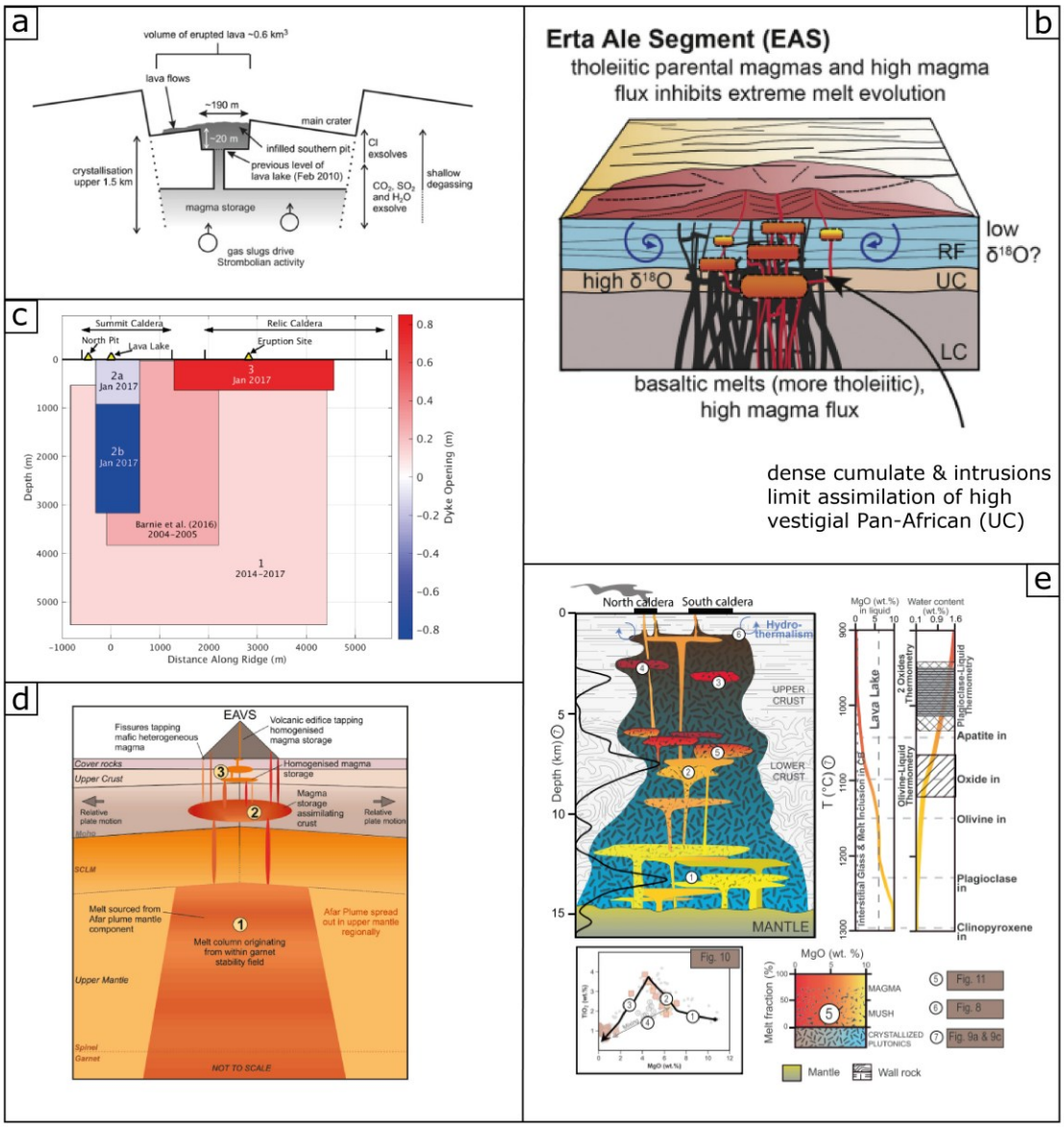

Figure 1.16: *Architecture of the Erta Ale magmatic plumbing systems. a) Schematic of the Erta Ale shallow plumbing system in November 2010 based on integrated ground and satellite observations and*

petrology (after Field et al., 2012). b) Schematic summarizing crustal structures of the Erta Ale and petrological constraints on magmagenesis (after Hutchison et al., 2018). c) Rift-perpendicular cross-sectional view of dike structures during the 2017 eruption from radar data (after Moore et al., 2019). d) Schematic diagram showing the generation of the volcanic rocks within the Erta Ale volcanic system (after Watts et al., 2023). e) Schematic model of the plumbing system architecture at Erta Ale Volcano (after Pin et al., 2024).

1.5.2 The central Afar (Dabbahu-Manda Hararo) segment

The active Dabbahu-Manda Hararo (DHM) segment in central Afar extends from the Dabbahu stratovolcano to the Semara plain. It extends 100 km in length and 20 km in width and can be divided into two sub-segments: the northern Dabbahu segment and the southern Manda Hararo segment (Figure 1.15 A). The transition between northern and the southern subsegment is marked by a westward offset of approximately 10 km at the Ado-Ale Gommoyta, a dissected, silicic central volcanic complex (AGVC; Lahitte et al., 2003a). The entire segment is characterized by a fissural basaltic floor dissected by a system of normal faults, oriented NNW-SSE in the northern part of the segment and NW-SE in the south (Figure 1.17 A). This study focuses on the less-documented southern Manda Hararo segment.

One of the best studied periods of activity in the Afar region was in 2005-2010 at the DMH segment, which was the first sub-aerial rifting episode ever recorded in the region. This rifting crisis began on 14 September 2005 with a series of 4.7 magnitude of earthquakes recorded between the Dabbahu and Gabho volcanoes (Figure 1.17A). On 26 September, a 500 m long, 60 m deep north-south oriented fissure opened on the flanks of Dabbahu, ejecting ash. Between 2006 and 2010, a sequence of 13 smaller dykes was intruded along the rift from the segment centre, all smaller volume than the 2005 intrusion. Three of these smaller dykes (in 2007, 2009, and 2010) breached the surface, erupting basaltic lavas (Ferguson et al., 2010). Multiple geophysical observations and related studies closely monitored the rifting episode, allowing for detailed modelling of intrusions and providing new insights into the interplay between tectonic and magmatic processes throughout the rifting sequence.

The 2005 mega-dyke, up to 10 m thick and ~65 km long, intruded the upper 10 km of the crust, triggering intense seismicity, a silicic eruption, fault reactivation, ~2 m of uplift along the rift

flanks, and ~3 m subsidence at the rift axis (Ayele et al., 2007; Yirgu et al., 2006; Grandin et al., 2009; J. V. Rowland, Baker et al., 2007b; Wright et al., 2006). The eruption occurred at the off-axis Gabho volcano, triggered by the injection of basaltic magma into a silicic reservoir (Wright et al., 2006). Seismicity first detected at Dabbahu and Gabho marked magma arrival, triggering the Gabho eruption and destabilizing the axial chamber, which partially drained into the mega-dyke. The volume of magma was estimated at ~2.5 km³ (Ayele et al., 2007; Wright et al., 2006).

InSAR data linked the open volume created during intrusion to deflation in the feeding reservoirs, though deformation at Dabbahu and Gabho alone could not explain the full dyke volume. Additional deflation farther south indicated a third, major reservoir beneath the central segment, where the rift intersects the Ado'Ale complex. About 80% of the dyke magma originated from this central source, and the remaining ~20% was supplied by the Dabbahu and Gabho reservoirs (Figure 1.17 D; Ebinger et al., 2010; Keir et al., 2009; Calais et al., 2006; Wright et al., 2006).

The intrusion reactivated numerous faults within a 1-2 km wide corridor, accommodating displacements of ~0.5-3 m (Grandin et al., 2009). Although it did not reach the surface, the dyke produced 5-8 m of horizontal opening at 3-10 km depth. Deformation across the rift included ~2 m uplift on the rift shoulders and ~1 m subsidence in the axial zone above the dyke. The dyke intruded beneath the elevated eastern rift shoulder (Figure 1.17 B), in contrast to models predicting emplacement along the lower rift axis (e.g., Buck, 2004).

The initial mega dyke was followed by a sequence of smaller dyke intrusions, injected during the 2006-2010 period. These earlier intrusions are mostly without significant surface volcanism. Three dikes reached the surface and produced fissural eruptions. The first two eruptions (2007 and 2009) occurred at the south of the axial caldera, about 10 km south of the Ado-Ale Gommoyta Volcanic Complex, and the 2010 eruption took place on the eastern flank of the axial caldera (Figure 1.17 A). The emitted volumes were very small: between 0.05 and 0.25 km³ (Ferguson et al., 2010; Grandin et al., 2010a; Hamling et al., 2009; Keir et al., 2009). Geodetic models estimated the partitioning between extruded and intruded material at 1:180 (Figure 1.18 D; Ferguson et al., 2010). The evolution of these intrusions during emplacement were closely monitored with microseismic data, which have provided opportunities for measuring the Earth's response to the major stress change associated with rifting. Although some dikes propagated northward or southward (Figure 1.17 C), all originated from the same reservoir, a common source: the axial magma chamber (Grandin et al., 2010b; Grandin et al.,

2011). Unlike the 2005 injection, these dikes were emplaced along the rift axis, with small deflation recorded at Dabbahu and Gabho. In contrast, the axial magma chamber of the segment continuously recorded deflation/inflation cycles corresponding to each recharge and subsequent drainage of the chamber These cycles, observed during the Dabbahu rifting crisis, are comparable to those documented in previous rifting episodes, most notably at Krafla in Iceland (Figure 1.18 C; Wright et al., 2012). Once the initial deflation occurred, triggered by the injection of the first mega dike, the magma chamber gradually began to refill, trending back toward the pre-rupture pressure conditions. This return to equilibrium was not continuous, as each subsequent dike injection was accompanied by renewed deflation. The persistence of dike intrusions indicates that the initial injection did not fully relieve the accumulated stresses. Instead, successive smaller dike intrusions progressively released the remaining stress, even as tectonic stresses began to accumulate again.

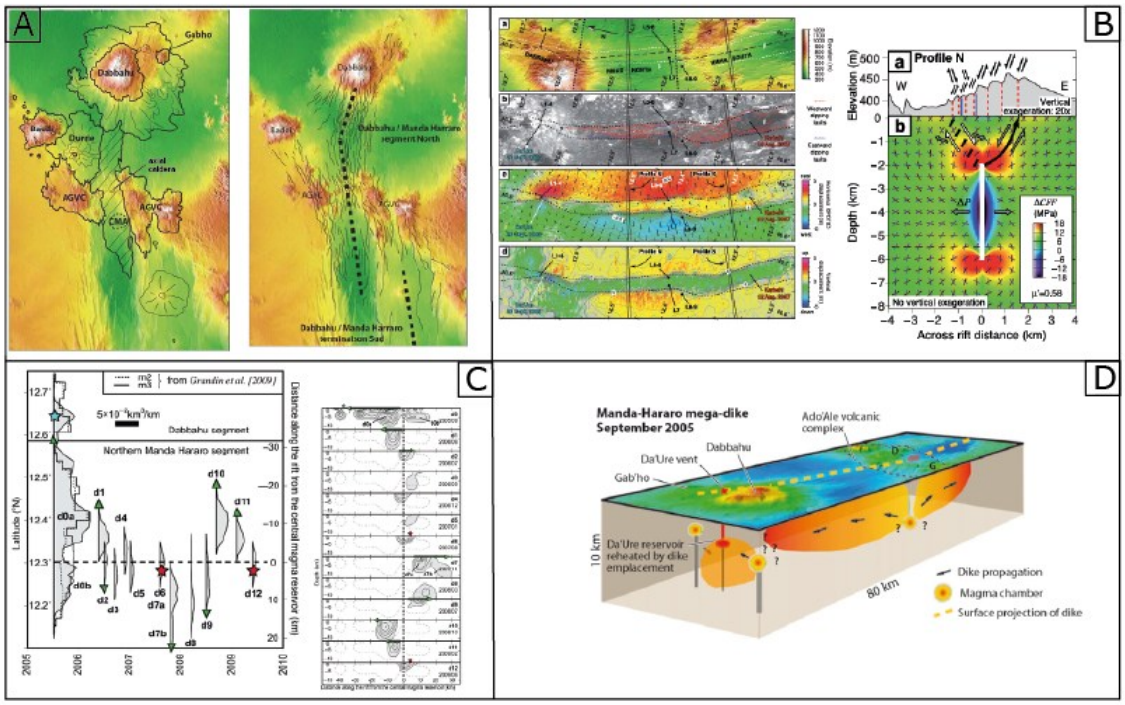

Figure 1.17: *Compilation of documentation on the DMH rifting episodes available in the literature. A) Volcano-tectonic features of the DMH segment (after Medynski et. al., 2015). The left-hand panel shows the extent of volcanic products issued from the volcanic complexes, and the right-hand panel shows the main faults that structure the rift segment. A clear change in fault orientation can be observed between the axial magma chamber (CMA) and Dabbahu. Similarly, there are two fault families oriented towards Badi: one connecting with the AGVC, and the other linking with Dabbahu. B) Distribution of the deformation associated with the injection of the 2005 mega dyke (after Grandin et al., 2009). The left-hand panel shows the reactivated faults after the main rifting event (red = west-dipping, light blue =*

east-dipping, with the high proportion of west-dipping faults); and the resulting horizontal and vertical displacements. The right-hand panel presents a cross-section of the stress fields induced by the dyke and the motion of the reactivated faults (section line in black on the elevation profile). The dyke intruded beneath the rift shoulder rather than along the rift axis, an unusual configuration compared with theoretical models. C) Distribution of dykes intruded during the 2005-2009 period (After Grandin et al., 2010). The left-hand panel shows distribution of dykes as a function of time and latitude. The dykes d1 to d12, which followed the injection of the 2005 mega dyke (d0), are smaller in volume by comparison. The dotted line represents the axial magma chamber. Dyke propagation directions are indicated by green arrows. For d6 and d12, basaltic fissure eruptions are associated with the intrusions. A third eruption occurred in 2010 during the injection of a thirteenth dyke. The right-hand panel shows locations of the 13 dykes intruded between 2005 and 2009 as a function of depth and distance along the rift from the central magma reservoir (dashed vertical line). D) Schematic illustrating the magmatic reservoirs involved in the 2005 dyke intrusion (after Ebinger et al., 2010). To the north, the off-axis magmatic reservoirs beneath the Gabho complex and the Dabbahu complex, and to the south, the axial magma chambers are shown.

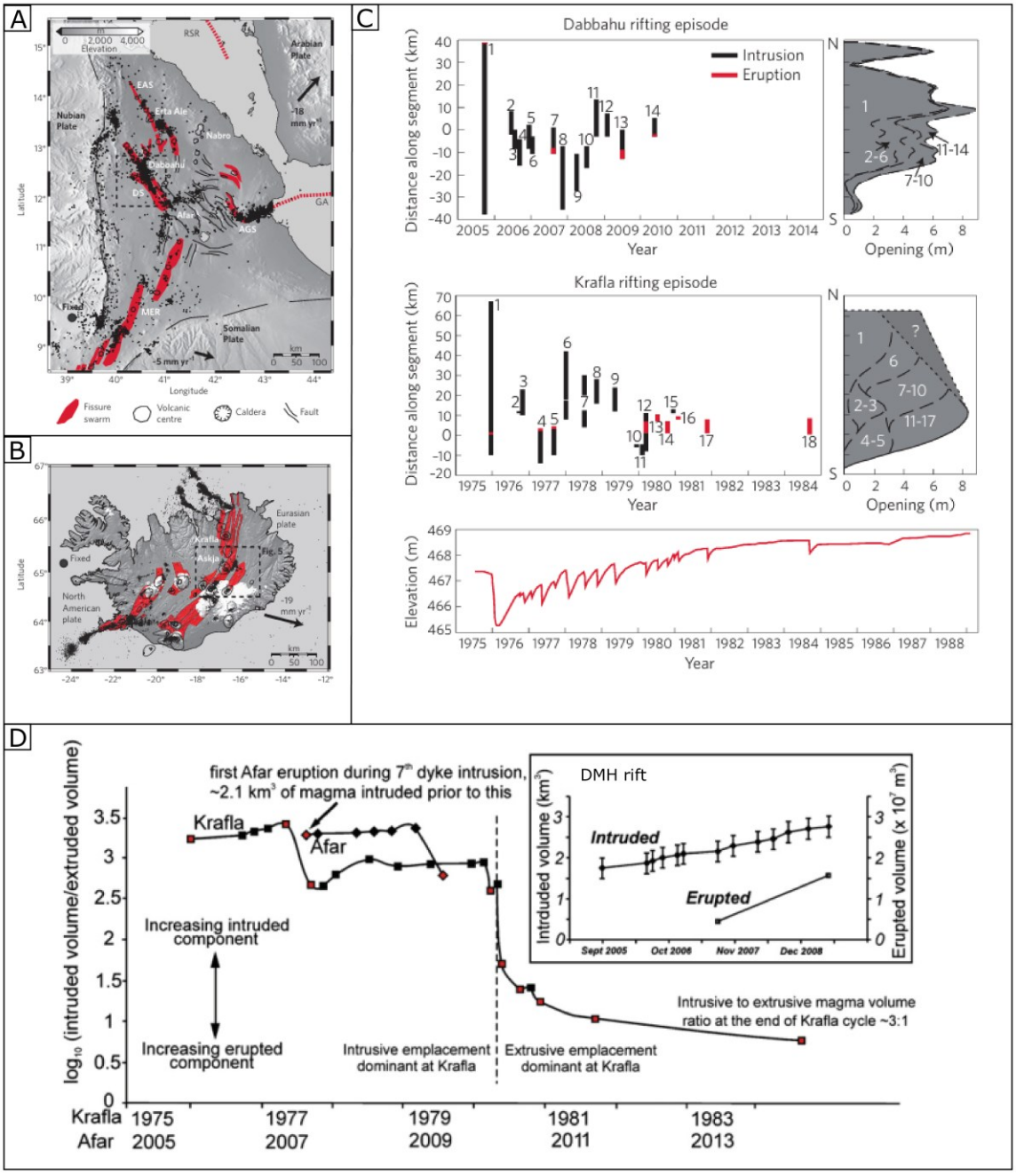

Figure 1.18: *Location of subaerial spreading centres and comparison of the rifting episodes (after Wright et al., 2012). A) Tectonic map of the Afar region. B) Tectonic map of Iceland. C) Summary of Dabbahu and Krafla rifting episodes. Location of dyke intrusions as a function of time are shown in black lines and eruptive fissures are indicated in red. D) Temporal trend of cumulative intrusive to extrusive magma volume ratios during the Krafla and the DMH rifting cycles (after Ferguson et al., 2010). The erupted scale is ×100 the intruded for the DMH rift.*

The 2005-2010 volcano-tectonic crisis sparked extensive multidisciplinary research, which has provided a foundation for understanding active rifting processes, magmatic systems, large scale

magmatic segmentation, and the development of rift topography (Figure 1.19 and 1.20). Three slowly evolving magma reservoirs at Dabbahu-Gabho area were detected from InSAR data (Figure 1.20 c; Grandin et al., 2010c). In the Dabbahu segment, distinct magmatic cycles each of 20-40 kyr duration have been distinguished using combination of structural investigations, field mapping, geochemical analysis and cosmogenic ^{3}He exposure dating of lava surfaces (Medynski et al., 2013). These cycles are marked by alternating phases of high and low magma supply, and strongly influenced rift morphology. Periods of abundant magma masked faulting by resurfacing the rift floor, while reduced magma supply allowed faulting to dominate topographic development (Figure 1.19 a). The interaction of multiple magma reservoirs, including those at the segment center and at Dabbahu volcano, controls both rift segmentation and the construction of rift topography. Two distinct magma reservoirs, well-separated in time and space have been identified in the Dabbahu segment (Figure 1.19 b; Medynski et al., 2015). The neo-volcanic activities and development of axial graben is mainly controlled by the location and activity of these crustal magmatic reservoirs (Figure 1.20 a; Medynski et al., 2016). Isotopic and oxygen data from Hutchison et al. (2018) revealed a magmatic system beneath the Manda Hararo Rift Segment (MHRS) that is characterized by limited crustal assimilation, with magma evolution dominated by fractional crystallisation of basaltic parents, and substantial storage of crystal cumulates that account for at least 16–30% of the crustal volume generated by extension (Figure 1.20 b). The magmatic systems architecture of the central Afar rift prior to the localized volcanism has been suggested from mineral chemistry (Tortelli et al., 2024). During the transition from the Upper Stratoid Series (US; 2.6-1.1 Ma) to the Central Afar Gulf Series (CAG; 1.1-0.6 Ma), the magmatic system underwent a marked shift: the US stage was characterized by melt-dominated, relatively homogeneous, moderately zoned magma storage at ~10-18 km depth, ascending more directly to surface, while the CAG stage was characterized by smaller, crystal-rich, interconnected reservoirs, with more frequent mixing and recharge events, and more complex textural evidence of mush and multi-level storage (Figure 1.20 d).

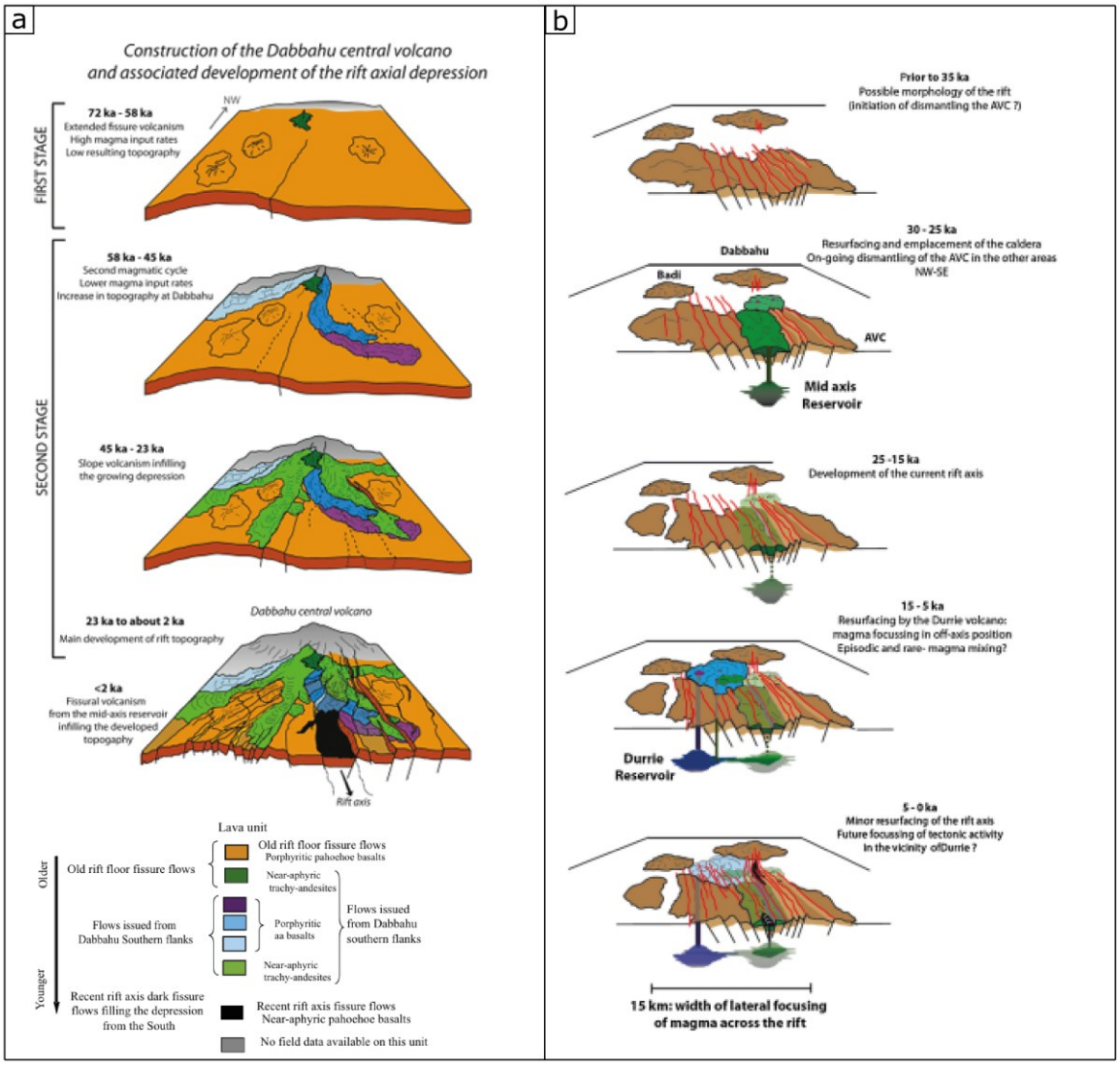

Figure 1.19: *a) Schematic illustration of magmatic cycles from 72 ka to the present, showing their interplay and correlation during the morphological evolution of the northern DMH rift (After Medynski et.al., 2013). b) Schematic illustrating the evolution of the DMH rift over the past 30 ka (after Medynski et.al., 2015). Evolution of magma reservoirs through time has been suggested to relay magmatic activity from the axis to the western flank, indicating a possible rift-jump.*

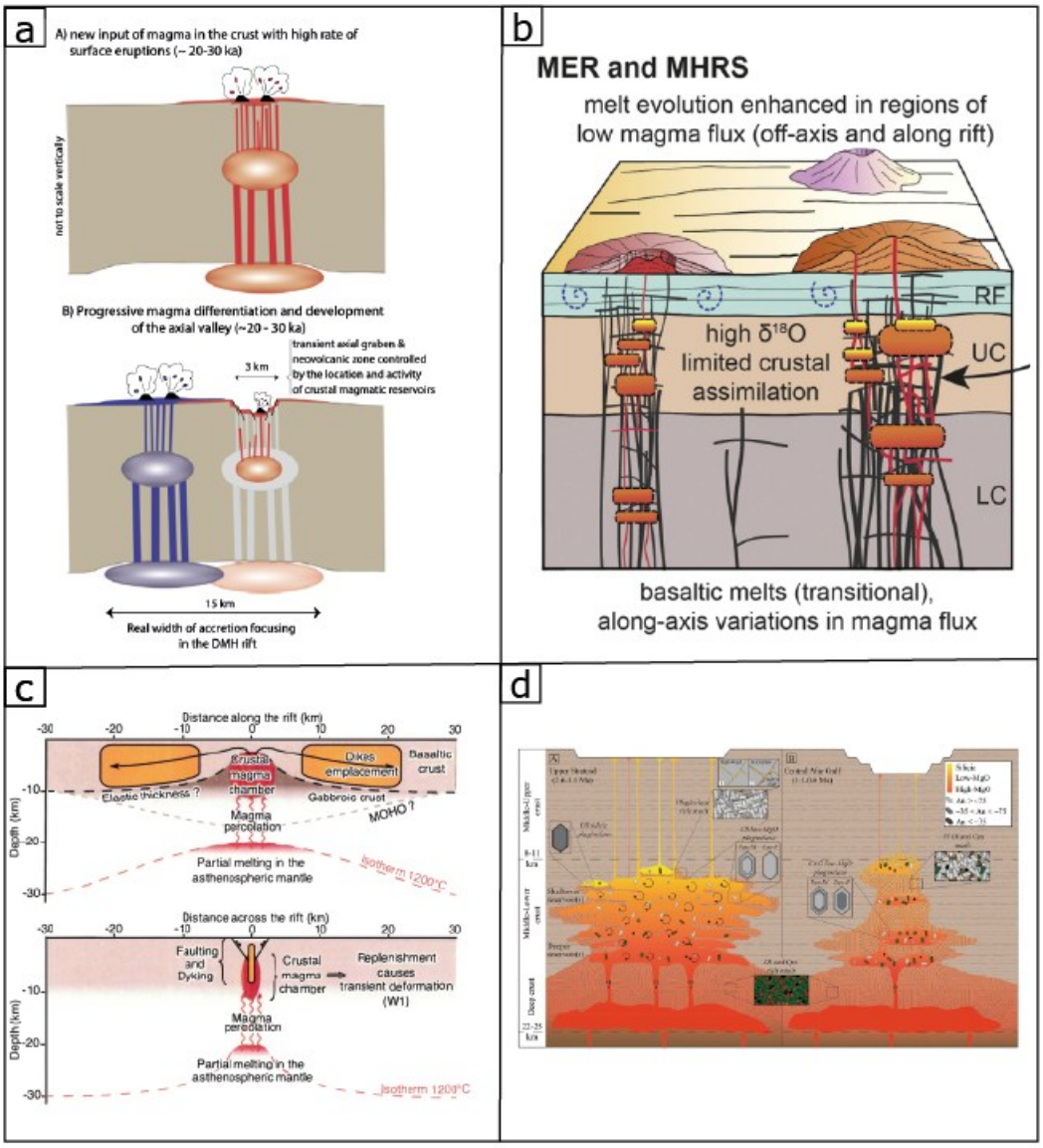

Figure 1.20: *Architecture of the central Afar magmatic plumbing systems. a) Schematic illustrating the role of magmatic reservoirs during the evolution of the DMH rift (after Medynski et. al., 2016). b) Schematic summarizing crustal structures of the Manda Hararo rift segment and petrological constraints on magmagenesis (Hutchison et al., 2018). Grey colours represent intrusive melts while orange rectangles represent cumulate bodies. Blue spirals reflect hydrothermal circulation that generates low δ18O crust. RF = rift fill (i.e., lavas and sedimentary cover); UC= upper crust; LC= lower crust. Intermediate-mature continental rift zones (e.g., MER and MHRS) promote extreme melt evolution since parental basalts are transitional in composition and local magmatic flux is low. c) Schematic illustrating lithological and mechanical structure of the DMH rift (after Grandin et al., 2010c). Magma is episodically distributed along the segment by repeated lateral dike injections,*

inducing a sudden deflation of the axial magma reservoir. d) Schematic model depicting the magmatic system of US and CAG series (after Tortelli et. al., 2024).

1.5.3 The Asal-Ghoubbet segment

The Asal segment located at the southern end of the Afar Depression, oriented NW-SE, and represents the inland propagation of the Aden Ridge (Manighetti et al., 1998). Extension is accommodated through successive detachments linked to surface faults (Geoffroy et al., 2014), at a rate of ~15 mm/yr perpendicular to the rift axis (Ruegg and Kasser, 1987). Its surface morphology and its position as a direct continuation of the Gulf of Aden oceanic ridge, suggest that it behaves as a slow-spreading ridge (Leroy et al., 2012). The segment includes a 4 km-wide, 12 km-long axial trench bounded by Lake Asal to the northwest (157 m below sea level) and the Gulf of Ghoubbet to the southeast, and the Fieale volcano occupies a central position between these two zones (De Chabalier and Avouac, 1994).

Volcanic products in this region are dominated by basaltic lavas containing centimeter-scale plagioclase phenocrysts, commonly bytownite, with abundant magmatic inclusions (Pinzuti et al., 2013). Rhyolitic products occur on the outer rift margins, marking the onset of rifting around 1 Ma (Le Gall et al., 2018). Deformation later focused along the Asal-Ghoubbet axis (Manighetti et al., 1998; Doubre et al., 2007b; Le Gall et al., 2018). Early volcanism within the axial zone included phreatomagmatic activity driven by magma-water interaction, forming tuff cones, pyroclastic deposits, and reworked hyaloclastites dated to 100-300 ka (De Chabalier & Avouac, 1994; Manighetti et al., 1998).

The most recent eruption occurred during the 1978 Ardoukoba rifting episode (Abdallah et al., 1979), a well-documented case of magma-assisted rifting. It was triggered by dyke injection, accompanied by a seismic swarm and faulting (Ruegg et al, 1979; Doubre et al., 2007). This rifting episode allowed one of the first direct measurements of significant tectonic plate movement where geodetic measurements showed ~2 m of horizontal extension and up to 70 cm of subsidence across the rift (Ruegg et al, 1979). The eruption began on November 7, 1978, one day after the onset of seismic activity, and lasted until November 14 (Allard et al, 1979). Initially, three scoria cones developed along parallel fractures, before activity focused on the Ardoukoba cone, which grew to ~40 m in height. Lava fountains propagated southeastward along the fissure, and eruption ended with a sudden decrease in the number of lava fountains on November 14.

Geophysical and related geochemical studies reveal a complex magmatic plumbing system beneath the segment (Figure 1.21). A shallow reservoir with 2-3 km lateral extent is inferred below the Fieale edifice at depth greater than 5 km (Figure 1.21 a; Doubre et al., 2007b; Pham Van et al, 1981; Smittarello, D. et al., 2016). Normal faults reach depths of 2-3 km, matching seismic hypocenter depths (Doubre et al., 2007b). Two deeper interfaces have been also recognized: one at 8-12 km, interpreted as the Moho (Ruegg and Kasser, 1987; Sandvol et al., 1998), and another at ~23 km, proposed by others as the true Moho (Dugda & Nyblade, 2006), consistent with regional crustal thinning observed throughout the Afar Depression. Geodetic modeling from InSAR data has suggested a kilometer-scale lens at ~17 km (La Rosa et al., 2024). The lithosphere–asthenosphere boundary is estimated at ~40 and 80 km depth along the rift axis (Figure 1.21 c; Pinzuti et al., 2013). Petrological evidence suggested involvement of multiple magma reservoirs or the mobilization of different parts of a heterogeneous magmatic reservoir during the 1978 Ardoukoba (Figure 1.21 b; Vigier et al., 1999). More recently, a magmatic plumbing system extending to ~23 km depth during the 1978 eruption has been proposed (Figure 1.21 d; Pin et al 2025 in revision), with shallow evolved magma feeding the initial phase before deeper, hotter primitive magma was tapped, indicating a vertically integrated transcrustal system. This study focuses on the most recent magmatic activity of the axial phase.

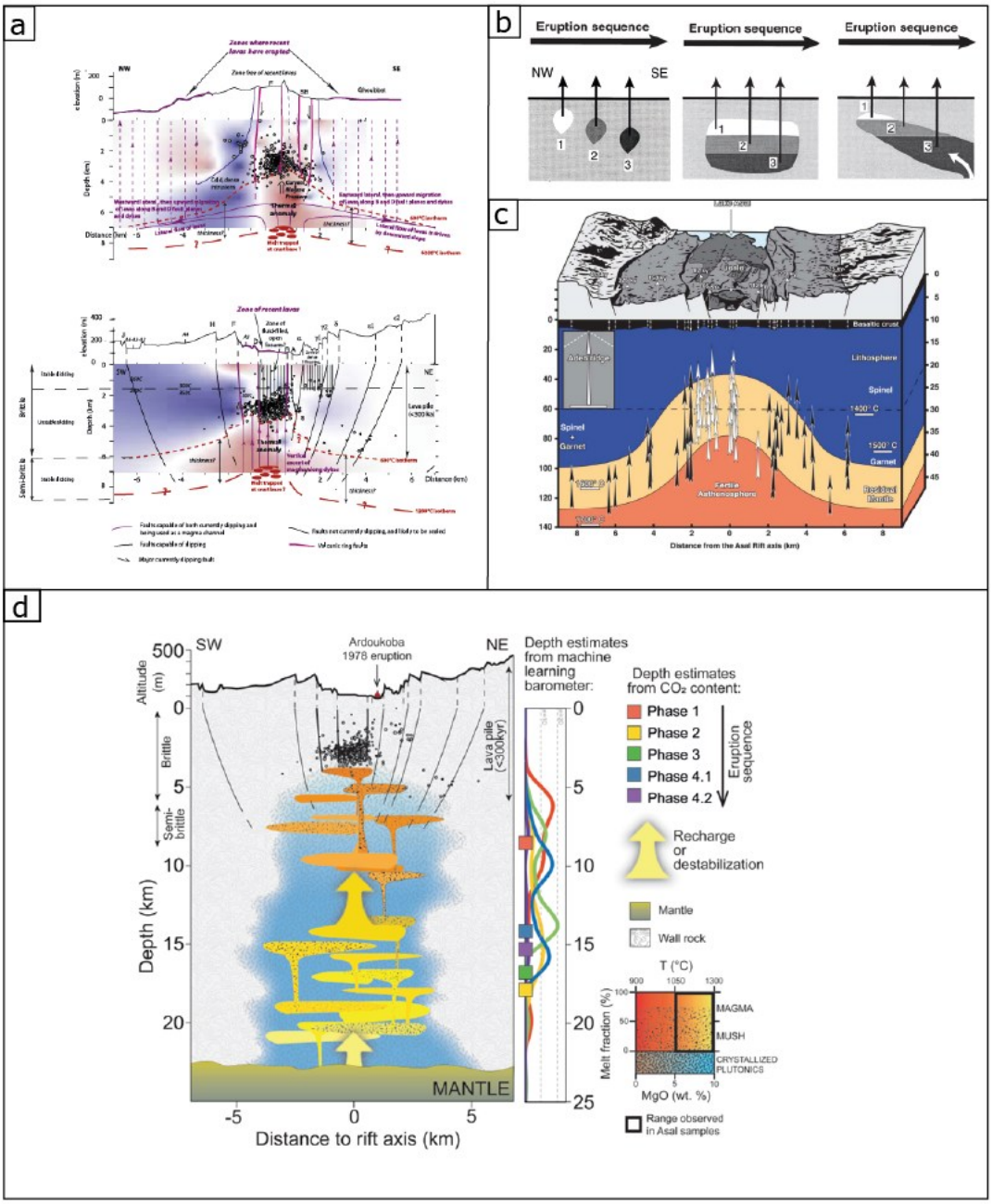

Figure 1.21: *Architecture of the Asal magmatic plumbing systems. a) The crustal structure of the Asal-Ghoubbet rift segment (after Doubre et al., 2007). b) Schematic drawings of the structures of the magma reservoirs during the 1978 Ardoukoba eruption (after Vigier et al., 1999). c) Melting regime across the Asal Rift (after Pinzuti et al., 2013). d) The plumbing system architecture at Ardoukoba volcano (after Pin et al.,2025 in revision).*

1.6 Thesis Objectives and structures

Active magmatic segments in the Afar depression present various morphologies, crustal thicknesses, and magma production rates which offer the opportunity to study both mantle and crustal processes. These rift segments from North to South, display typical morphologies which vary from a prominent axial ridge to an axial depression. This raises the question why rifting is expressed differently in each of the Afar rift segments? Afar is often considered the most mature part of the East African Rift, and differences in rifting modes between its segments can be interpreted as variations in maturity level, or rifting style. In all existing models proposed to explain and interpret this rift system and its contrasted segments, the role and behaviour of magmas appear to be a fundamental key parameter. Many hypotheses and models have been recently proposed, sometimes opposed, sometimes provocative, sometimes contradictory, often resulting from data that do not document the system at the same time and space scales. They however all led to the same findings that we still need to understand precisely: (1) how are magmas generated? (2) how are they transferred to the crust? (3) how do they interact and are controlled by other forcing parameters (in particular, the mechanical behavior of the lithosphere)? There are also open questions regarding the transition and spatial shift in magmatic productivity within these rift segments. (4) how did magmatism evolve from the Gulf Series into the fully axial phase, and what processes controlled this transition? (5) why does the locus of the highest-volume magmatism in the present-day axial phase lie in northern Afar, while the earlier voluminous Stratoid and Gulf Series volcanism was concentrated in southern and central Afar?

To address these questions, this study investigates the two active rift segments of the Afar depression: the Manda Hararo and Asal-Ghoubbet segments, in order to understand the various potential controls and causes of magmatic accretion. The study focuses on identifying the location, and then investigating the functioning and persistence of magma reservoirs, in order to precisely determine the vertical and lateral organisation of the plumbing systems, their potential interconnections, how they interplay with extension processes, and how they potentially control large-scale segmentation. To achieve these main and specific objectives, complementary approaches of (i) remote sensing, (ii) field investigations, (iii) precise geological mapping, (iv) cosmogenic ^{36}Cl exposure dating, and (v) lava geochemistry are employed.

The thesis is organized into six chapters, complemented by appendices that contain the complete dataset generated and used in this study. Following the introductory and methodology

chapters, the remaining chapters are self-contained and presented in the format of research articles. References for all cited works and the list of appendices are provided at the end of the thesis, after Chapter six.

Chapter 1: highlights the general scientific background, the research questions and defines the objectives of this thesis.

Chapter 2: summarises the remote sensing techniques, fieldwork, and sample preparations, and provides a detailed description of the analytical techniques and instrumentation used to generate the data presented in the thesis.

Chapter 3: presents the field observations, geomorphological mapping, cosmogenic chronology of lava flows, and geochemistry of the Gumat Mali magmatic sub-segment, and discusses volcanic activity, magma types and general organisation of the segment.

Chapter 4: presents the field observations, geomorphological mapping, cosmogenic chronology of lava flows, and geochemistry of the Manda Haro sub-segment. It also details the architecture of the central Afar sub-segments through a discussion of the magma types, processes, and magmatic interactions within the trans-crustal plumbing system.

Chapter 5: Presents the last 10 ka volcanic history of the Asal-Ghoubbet rift sub-segments. This study integrates high resolution cosmogenic exposure ages with lava geochemistry to reconstruct the magmatic cycles within the axial zone of the Asal rift.

Chapter 6: summarises the thesis, and places the findings into wider context, highlighting potential directions for future research.

Chapter 2

2. Methods

This PhD-thesis combines complementary approaches of (i) precise and comprehensive mapping of volcanic structures and basaltic lava flows using remote sensing and field investigations, (ii) cosmogenic exposure dating (^{36}Cl) of volcanic surfaces, and (iii) composition of volcanic products (major and trace elements, and isotope geochemistry), to constrain the temporal frame and the dynamics of magmatic processes. This quantitative approach is focused on the central Afar and Asal magmatic rift segments. A detailed description of the methods used in the thesis is presented below, including the rationale for its selection and the procedures followed.

2.1 Remote sensing and field investigations

Multispectral imagery records reflected or emitted electromagnetic energy, with each material exhibiting a characteristic absorption and reflection pattern (Corradino et al., 2019). In volcanic terrains, the spectral reflectance of lava flows is particularly significant in the visible (VIS, ~400-700 nm) and near-infrared (NIR, ~700-1,300 nm) regions of the spectrum (Aufaristama et al., 2018). Remote-sensing based geological mapping, uses these spectral properties to identify lava flow fields, determine their flow directions, and locate associated volcanic vents.

2.1.1 Remote sensing data sets

To delineate the extents of lava fields and map the diversity of volcanic units within the magmatic sub-segments of the central Afar, three types of satellite imagery were used: Landsat 8 OLI level 2, Sentinel-2A MSI, and high-resolution stereo images from the AIRBUS DS Pleiades mission. Landsat 8, the eighth satellite in the American Landsat program, carries two sensors onboard: the Operational Land Imager (OLI) and Thermal Infrared Sensor (TIRS). OLI provides nine spectral bands at 30 m resolution (Bands 1-7 and 9), with Band 8 (panchromatic) at 15 m. Bands 2-7 are suitable for distinguishing lithologies and delineating structures. TIRS bands 10 and 11, collected at 100 m resolution, provide surface temperature information. One Landsat 8 OLI scene ((LC08_L2SP_167052_20211029_20211108_02_T1), Path 167/Row 052) with minimal cloud cover was accessed from the image courtesy of the US Geological Survey Earth Resources Observation and Science Centre (http://earthexplorer.usgs.gov) in GeoTIFF format, representing terrain-corrected Level 2 data. Details on the instrument, data

type, and scene ID for Landsat 8 are summarized in Table A2.1, Appendix, and the spectral bands are summarized in Table A2.2, Appendix.

The Sentinel-2 Multispectral Instrument (MSI), part of the Copernicus Program, acquires optical imagery in 13 spectral bands ranging from 0.433 µm to 2.194 µm, with three spatial resolutions: 10 m (bands 2, 3, 4, 8), 20 m (bands 5, 6, 7, 8a, 11, 12), and 60 m (bands 1, 9, 10). For lava flow mapping, high-resolution bands were used: Band 2 (Blue, 0.494 µm), Band 3 (Green, 0.560 µm), Band 4 (Red, 0.665 µm), and Band 8 (NIR, 0.834 µm). Two Sentinel-2 MSI scenes, free-accessed from the European Copernicus Program, were used alongside Landsat 8 images. The instrument, data type, and scene IDs are also summarized in Table A2.1, Appendix, while the spectral and resolution characteristics of the bands are provided in Table A2.2, Appendix. All datasets were downloaded in GeoTIFF format, representing systematically terrain-corrected Level 2 data.

High-resolution Pleiades stereo imagery was used to complement the moderate-resolution Landsat and Sentinel-2 data. For Central Afar, nineteen stereo pairs of panchromatic and multispectral images, covering a total area of 4,535 km², were provided by the Incitation à l'utilisation scientifique des images Spot (ISIS) program from Centre national d'études spatiales (CNES) (https://dinamis.teledetection.fr), and two multispectral Pleiades stereo pairs in black and front images were freely acquired from French national service platform, Form@ter for Asal rift. ForM@Ter data portal is a solid earth cluster within the Data Terra framework that provides access to very-high-resolution imagery and on-demand stereoscopic processing services (https://www.theia-land.fr/en/blog/product/dsm-opt-digital-surface-modeling-using-pleiades-stereo-tri-stereo-imagery/). The panchromatic channel has a spatial resolution of ~0.7 m (480-830 nm), while the multispectral bands (Blue, Green, Red, NIR) have a resolution of ~2.8 m. These images offer a wide radiometric range, providing good contrast over low-relief areas, which improves the identification of lava flow surfaces and volcanic structures compared to other datasets (Gleyzes et al., 2012; Palaseanu-Lovejoy et al., 2019; Bisson et al., 2021).

2.1.2 Data Processing and Image Analysis Techniques

Remote sensing data were processed using ENVI® software through a sequence of interactive techniques (Figure A2.1, in Appendix). Pre-processing was performed prior to the main image analysis steps to ensure the data were suitable for interpretation. These procedures included layer stacking and image subsetting. The selected Landsat 8 and Sentinel-2 images were cropped to the area surrounding the lava flows of interest, which optimized processing

efficiency and improved classification accuracy by reducing the number of pixels evaluated. For visualization, three spectral bands were selected from each dataset to generate false-color composites. Form Landsat 8 dataset, the RGB 7-4-1 composite was found to be most effective in highlighting recent lava flow fields, particularly those associated with the Volcanic centers (Figure 2.6C). For Sentinel-2, the RGB 4-3-2 composite provided enhanced discrimination of volcanic and tectonic structures, including calderas, fissures, and spatter cones, as well as recent lava flow fields (Figure 2.1). The higher spatial resolution of Sentinel-2 (10 m pixel bands) proved especially better and valuable information for delineating lava flow fields and identifying small-scale volcanic and tectonic features (Figure 2.6A).

Principal Component Analysis (PCA) was applied to the Sentinel-2 imagery (Figure 2.2). PCA is a linear transformation that reorganizes the variance of a multi-band image into a new set of uncorrelated image bands, referred to as principal components (PCs). The transformation rotates the data onto orthogonal axes, maximizing variance along the first components (Unglert et al., 2016). This enhances spectral contrasts and produces images that improve visual analysis of volcanic features, particularly the identification and delineation of lava flow fields (Lillesand et al., 2015). In the northern part of the study area (Figure 2.3C), PCA enabled the mapping of the boundary between younger lava fields and the older basalts (white polygons), blocks of old basalts enclosed within younger lava flows (yellow polygons), and very recent lava flows (black polygons). The PCA also revealed structurally controlled fissural lava flow fields extending northward from a caldera system (Figure 2.3A; see also Figure 2.1). In the southern part of the study area (Figure 2.3B), PCA improved the delineation of lava flow boundaries, while in the western part (Figure 2.3D) it highlighted lava flows associated with a caldera system that appear to be fault controlled.

Decorrelation stretch (DCS) was applied to the Sentinel-2 image (Figure 2.4) to enhance the visual distinction of lava flow units. DCS is a transformation technique that reduces the correlation between spectral bands, thereby highlighting subtle variations that may not be apparent in standard composites (Gillespie et al., 1986). This method is commonly used to produce false-color images and improve the interpretability of geological features. In this study, DCS enabled precise mapping of lava flow boundaries (Figure 2.6B), providing an important validation of the flow delineations obtained from the RGB composites and PCA results.

Pixel-based image classification was applied to both Landsat 8 OLI and Sentinel-2 datasets to distinguish lava flows and related volcanic vents. Among the classification approaches, the Minimum Distance Classification (MDC) was used, which is a supervised method where pixels are assigned to the class whose mean spectral signature is closest in digital parameter space (Richards, 1999; Head et al., 2013). Training samples, or regions of interest (ROIs), were defined to represent different lava flows and other geological units and features. These ROIs were selected based on RGB composites, PCA and DCS visualizations, and supported by existing geological maps from the literature. Statistical properties of the ROIs were carefully evaluated, and classification parameters were set, including the maximum standard deviation from the mean and the maximum distance error. The final classification image (Figure 2.5) successfully captured various sub-layers within lava flow fields that shows variations in lava morphology (Figure 2.6D).

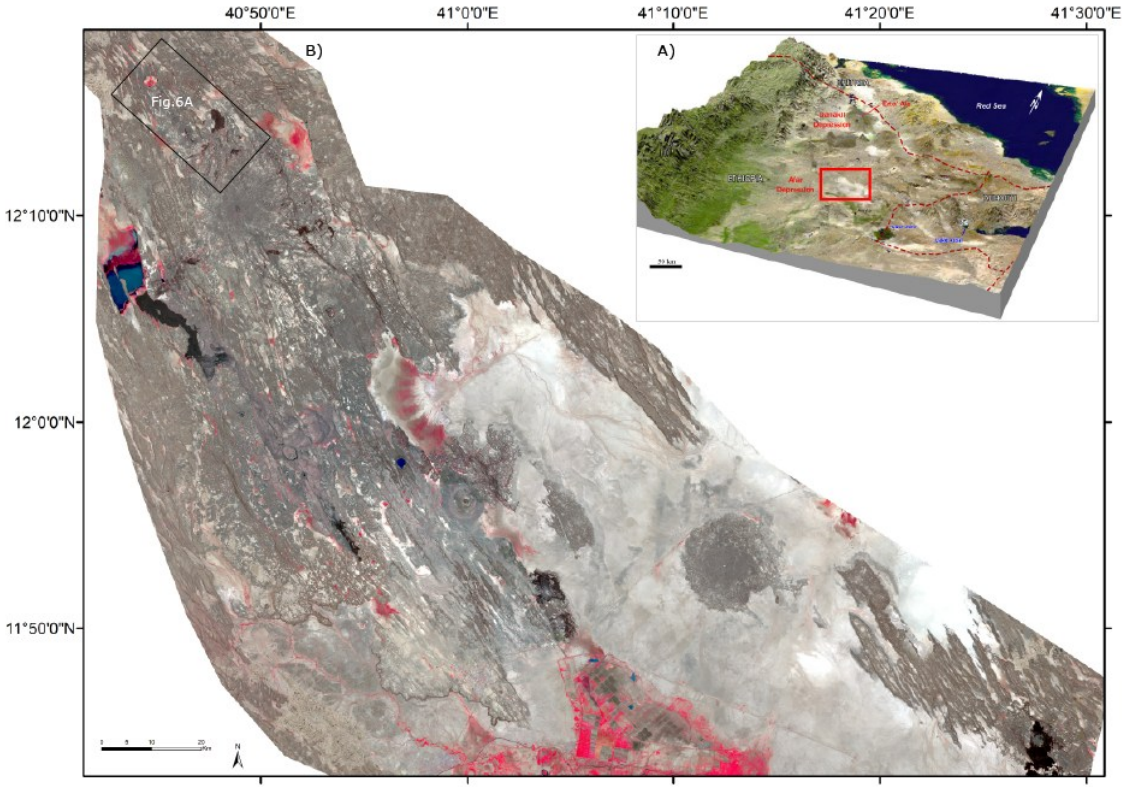

Figure 2.1: *RGB band combinations computed from Sentinel-2. (A) inset map showing the location of the study area: a perspective view of central Afar generated by draping a Landsat image over a digital elevation model (source: Wikipedia). (B) Sentinel-2 RGB 4-3-2 composite.*

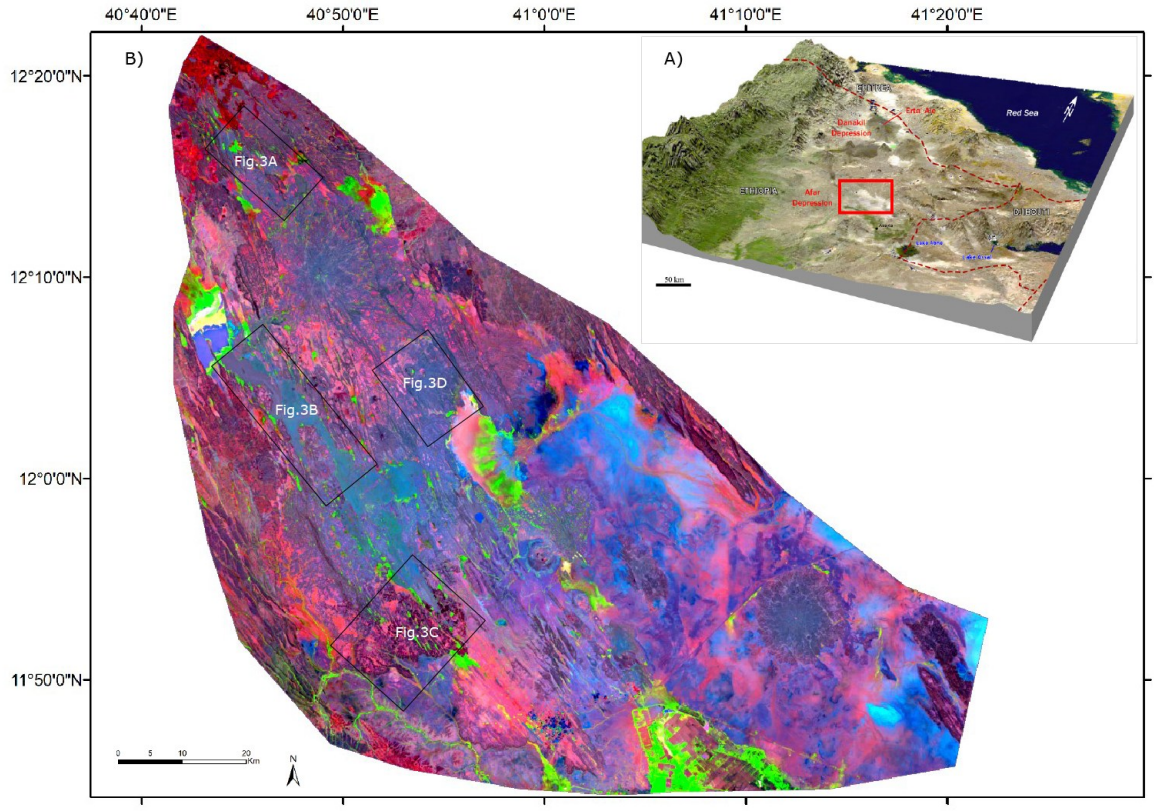

Figure 2.2: *Principal Component Analysis (PCA) generated from Sentinel-2 imagery. (A) inset map showing the location of the study area: a perspective view of central Afar generated by draping a Landsat image over a digital elevation model (source: Wikipedia). (B) PCA image after enhancement using low-pass filtering, applied for detailed mapping of the diversity and delineation of flow extents in central Afar. A zoomed view of selected areas is provided in Figure 2.3.*

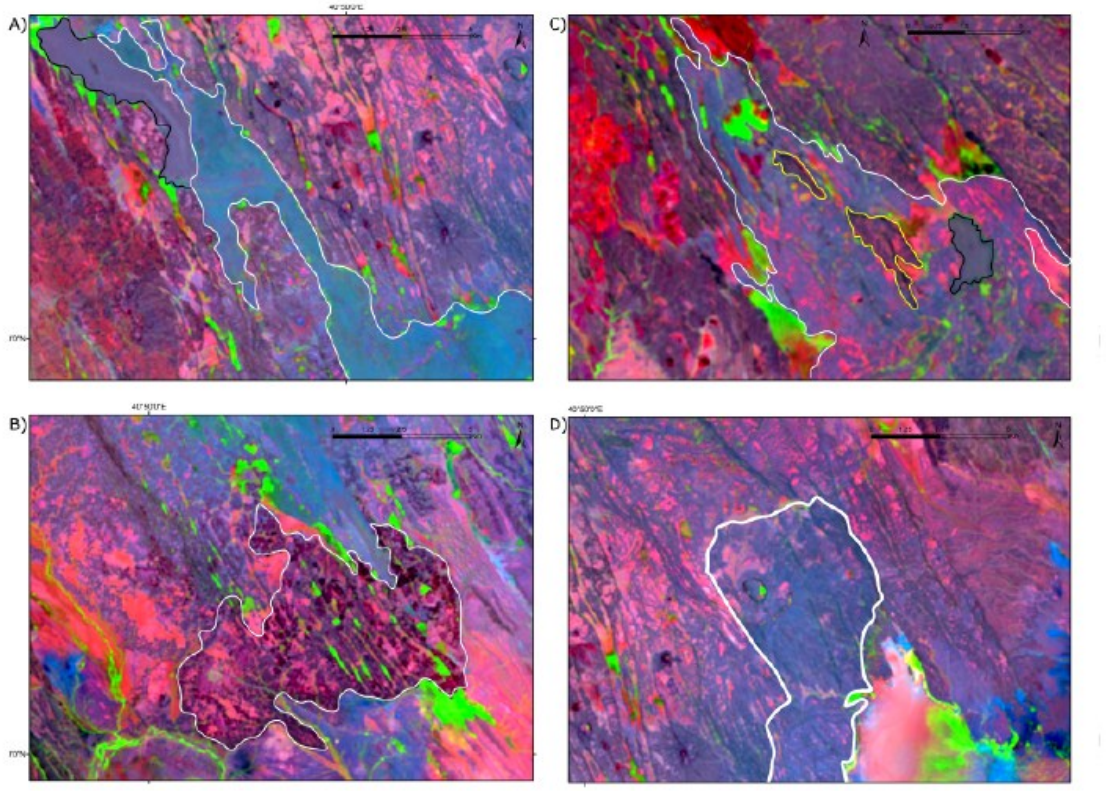

Figure 2.3: *A zoomed view of selected areas in the PCA image used for mapping the diversity of lava flow fields in central Afar. (A) structurally controlled recent lava flow associated with a caldera system hosting a frozen lava lake. (B) distinct lava flows in the southern part of the study area. (C) extent of recent lava flows in the northernmost part of the study area, showing blocks of older basalts (yellow polygons) and the most recent lava flows (black polygon). (D) young lava flows bounded by two tilted basaltic blocks associated with a caldera system in the western part of the study area.*

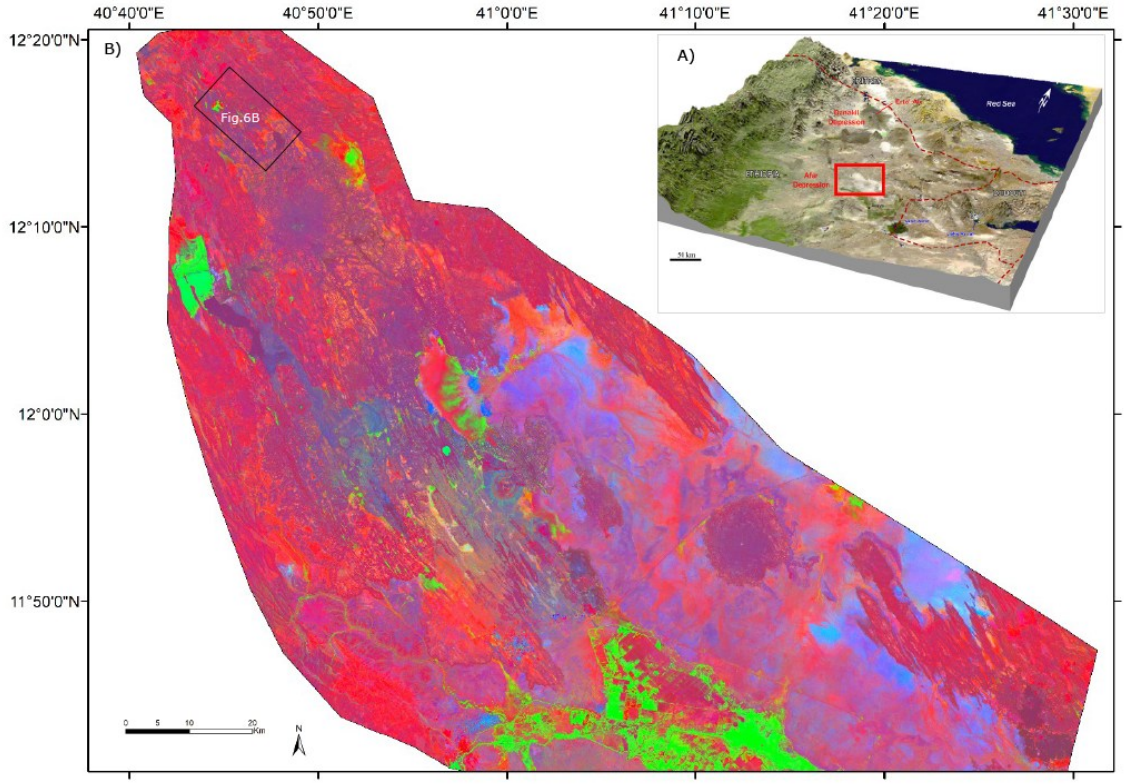

Figure 2.4: *(A) Inset map showing the location of the study area: a perspective view of central Afar generated by draping a Landsat image over a digital elevation model (source: Wikipedia). (B) Decorrelation stretch (DCS) image after enhancement using low-pass filtering computed from Sentinel-2.*

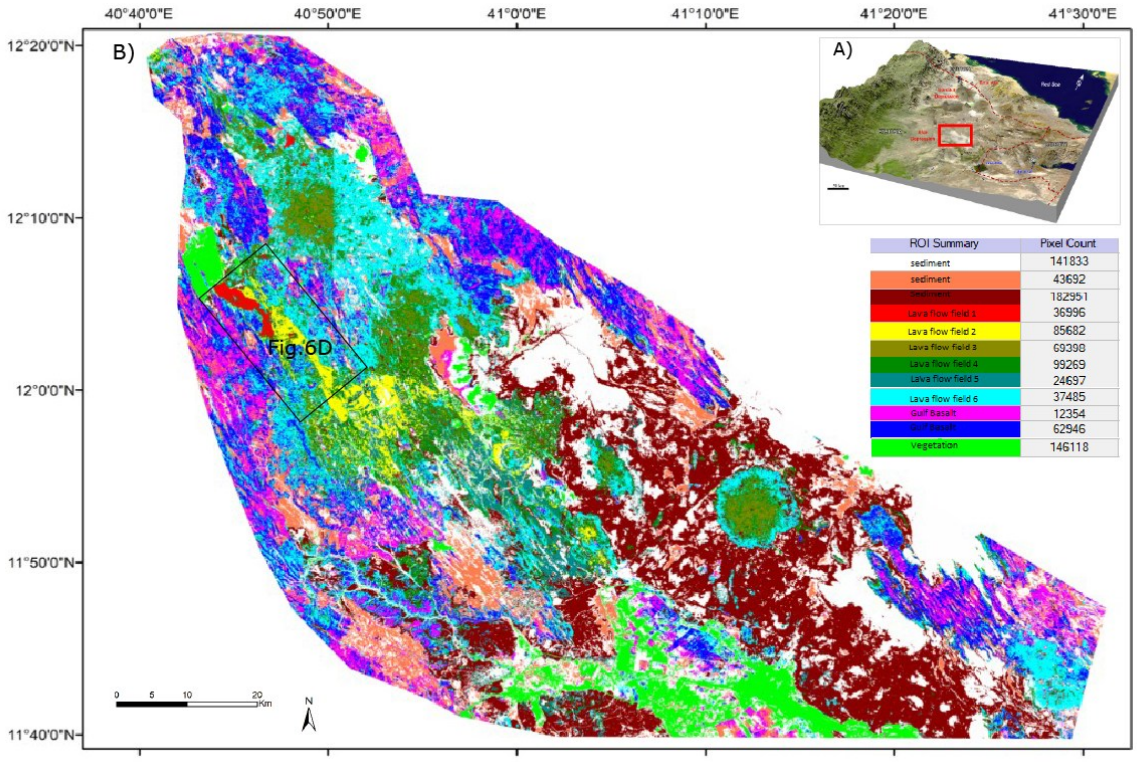

Figure 2.5: *Minimum Distance Classification (MDC) applied to the Sentinel-2 DCS image. (A) Inset map showing the location of the study area: a perspective view of central Afar generated by draping a Landsat image over a digital elevation model (source: Wikipedia). (B) MDC image result after low-pass filtering, capturing multiple sub-layers within a single lava field.*

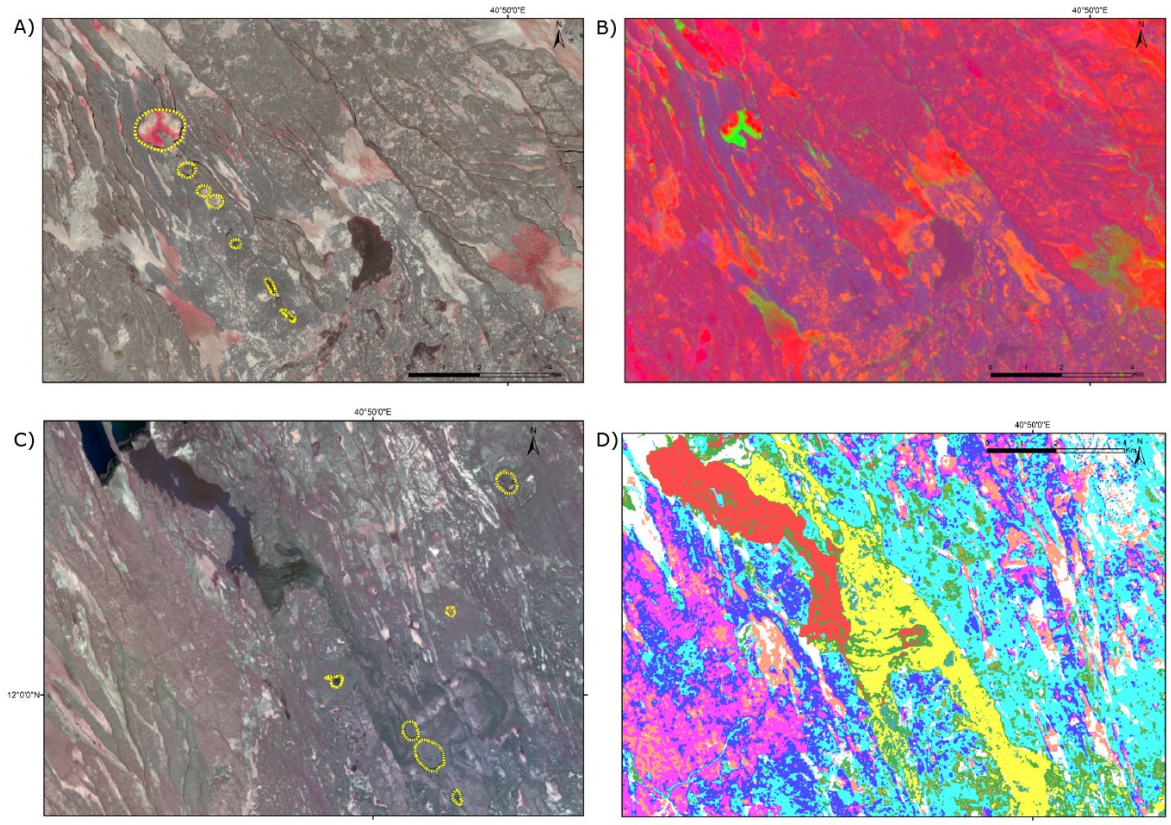

Figure 2.6: *Zoomed views of selected areas highlighting lava flow fields and volcanic structures. (A) Sentinel-2 RGB 4-3-2 composite captured recent lava flows, volcanic, and tectonic structures. (B) DCS image used to distinguish the extent and boundary of lava flow fields. (C) Land Landsat 8 RGB 7-4-1 composite identified lava flows and volcanic centers. (D) MDC image captured sub-layers within lava flow fields. ROI summery and legend are the same as in Figure 2.5.*

2.1.3 Digital Elevation Model Generation

A high-resolution Digital Elevation Model (DEM) of central Afar was generated from 19 Pleaides pairs of images using the Ames Stereo Pipeline software (ASP; Beyer et al., 2018). The ASP software provides various algorithms that can be applied to derive a high-resolution DEM with minimal noise and suitable texture for mapping lava surface (ASP documentation: https://stereopipeline.readthedocs.io/en/latest/stereodefault.html). In flat and low rugosity areas such as central Afar, the More Global Matching algorithm, combined with a census transform cost function (Zabih & Woodfill, 1994) and a Bayes sub-correlation method: (1) Allows the derivation of high-resolution and high-quality results using small correlation windows of 9x9 pixels in comparison to classical block matching algorithms, (2) Offers faster computation compared to classical normalized cross-correlation functions, and (3) Preserves

low-frequency contents in comparison to other refinement methods to achieve sub-pixel accuracy. Before grid generation, outliers were removed, and the triangulation results were smoothed using sliding windows filters and adaptative texture smoothing. A classical processing scheme was applied to the panchromatic pairs (Lacroix et al., 2022): (1) Orthorectification of the images using the publicly available Copernicus 30m DEM and refined sensor models using Rational Polynomial Coefficients (RPC), which describe the relationship between the satellite image and its corresponding ground coordinates. (2) Image correlation between all pairs of images. (3) Generation of 3D cloud points from triangulation. (4) Interpolation of the point cloud to generate a 2 m spatial resolution DEM. Two multispectral Pleiades pairs of images were processed through the freely accessible Form@ter service (https://dinamis.data-terra.org/en/online-processing/) to generate high-resolution Digital Elevation Model (DEM) of Asal rift.

2.2 Cosmogenic Geochronology

Cosmogenic nuclides are produced in rocks when they are exposed to cosmic rays at the Earth's surface. Cosmogenic geochronology is based on the following principles (Gosse & Philips, 2001): (i) cosmic-ray interactions generate rare isotopes such as the radionuclides (^{10}Be, ^{14}C, ^{26}Al, and ^{36}Cl), and the stable noble gases (^{21}Ne and ^{3}He); (ii) production occurs only within the upper few meters of the Earth's surface, as the cosmic-ray flux is effectively shielded at greater depths; and (iii) the production rate of cosmogenic nuclides varies spatially, but is generally assumed to have remained constant through time at a particular location. Geological processes such as volcanism that bring unexposed material to the surface, initiate the accumulation of cosmogenic nuclides, thereby providing a measurable record of surface exposure duration. Landforms ranging in age from a few hundred years to tens of millions of years can be dated (depending on rock or landform weathering rates) by measuring nuclide concentrations (Ivy-Ochs & Kober, 2008).

The Afar Depression, with its arid climate and low erosion rates, provides favorable conditions for terrestrial cosmogenic nuclide (TCN) exposure dating (Medynski et al., 2015). This method requires well-preserved lava surfaces or fault scarps (Gosse & Philips, 2001) and can constrain either the emplacement age of lava flows or the timing of eruptive phase cessation. However, in regions with frequent eruptions, such as rift axial depressions, successive lava flows rapidly bury older surfaces, shielding them from cosmic ray exposure. As a result, only the most recent exposed flows can be dated (Medynski et al., 2015).

2.2.1 Sample preparations and Cosmogenic ^{36}Cl analyses

Cosmogenic ^{36}Cl measurements are widely used to determine the emplacement ages of lava flows (Zreda et al., 1993; Schimmelpfennig et al., 2011). Ideally, the analysis is performed on Ca- and K-bearing minerals, such as feldspars, because their chemistry is well suited for ^{36}Cl production (Licciardi & Pierce, 2008). However, the lack of sufficient phenocrysts in many aphyric lava flows, often necessitates the use of whole-rock samples instead (Medynski et al., 2015).

In this PhD study, a total of 56 lava surface samples were collected to establish ^{36}Cl cosmogenic exposure ages of lava flows: 44 samples from central Afar and 12 samples from the Asal rift, obtained during extensive field campaigns in 2013, 2018, 2022, and 2023. The central Afar lava surfaces generally lack phenocrysts, so ^{36}Cl measurements were performed on whole-rock (matrix) material, whereas the Asal rift lavas are phenocryst-rich, allowing analyses to be carried out on plagioclase separates (Figure A2.2 in Appendix).

Lava samples were crushed and sieved to retrieve100-500 µm grain size fractions. Sieving was conducted under a water bath to remove dust particles, followed by rinsing and oven-drying. For the Asal rift samples, the dried fractions were further processed through a Frantz magnetic separator several times to extract plagioclase separates. The target was to obtain 100-120 g of pure plagioclase separates per sample; However, due to variable plagioclase content, the extracted amounts ranged from 46 g to 210 g. For samples with insufficient pure plagioclase, fractions enriched in plagioclase were used. This approach helped minimize the contribution of the fine-grained groundmass, which is often chlorine-rich and complicates data interpretation. The selected grain-size fractions were then retained for subsequent chemical preparation.

2.2.2 Chemical preparation and extraction of cosmogenic ^{36}Cl

The extraction of cosmogenic ^{36}Cl requires carful chemical preparation of samples, and several protocols have been developed for this purpose (Stone et al., 1996; Schimmelpfennig et al., 2009; Medynski et al., 2015). The chemical preparations were conducted out at the European Centre for Research and Teaching in Environmental Geosciences (CEREGE), France. Throughout the preparation, high-density polyethylene (HDPE) bottles were used.

Sample purification was the first step in the extraction of cosmogenic ^{36}Cl. This process aimed to remove material unrelated to basalt, such as lichens and carbonate residues, as well as atmospheric chlorine trapped in fractures or vesicles. 100-120 gram of sample grains were

rinsed with ultrapure water (Milli-Q, ultra-low in organics) to eliminate fine particles. The samples were then soaked in a nitric acid bath (HNO_3 + Milli-Q water) and loaded on a shaking table for 24 hours.

After purification, two sequential dissolution steps were carried out: (1) dissolving 20% of the initial sample mass, followed by (2) total dissolution of the remaining material. The 20% dissolution step was applied to reduce total chlorine concentrations which is responsible for the formation of ^{36}Cl by low-energy neutron capture on ^{35}Cl and to concentrate ^{36}Cl in the remaining fraction.

Dissolution was performed through immersing the sample mass into a solution of hydrofluoric acid (HF, 60%) and with nitric acid (HNO_3) with Milli-Q water. 0.72 ml of HNO_3 per gram of each sample was added first, followed by 0.36 ml of HF. HNO_3 dissolve carbonates while HF dissolves silicates. To ensure controlled dissolution reaction, the sample bottles were placed in an ice bath, and HF was added slowly, as it can react violently with the samples. The bottles were then sealed and agitated on a shaking table for 12 hours.

Production of cosmogenic ^{36}Cl in rocks occurs through several mechanisms (Schimmelpfennig et al., 2009): (1) spallation of target elements such as K, Ca, Ti, and Fe. (2) capture of slow negative muons, particularly by K and Ca, and (3) low-energy neutron capture by ^{35}Cl. While spallation production rates are relatively well constrained, estimating the contribution from ^{35}Cl neutron capture remains more challenging (Schimmelpfennig et al., 2011). To account for this, before proceeding to total dissolution, 1 g aliquots were taken from the rinsed, etched, and dried samples for determination of these target elements.

For the isotope dilution, a ~99% ^{35}Cl-enriched solution (spike) was added to each sample as well as to blank bottles which were used as chemistry controls (Ivy-Ochs et al., 2004). The spike serves two purposes: (1) it enables simultaneous determination of ^{36}Cl and ^{35}Cl concentrations through isotope dilution, and (2) it ensures that the final chlorine precipitate contains sufficient chlorine to be measurable and above the AMS detection limit (Desilets et al., 2006). The isotopic composition and chlorine concentration of the spike are already known, with a $^{35}Cl/^{37}Cl$ ratio that differs from the natural ratio. Thus, the final measured isotopic ratios reflect the mixture of chlorine derived from both the spike and the sample. The higher the chlorine content of the sample, the closer the measured ratios will approach the natural values.

After spike addition, total dissolution was carried to extract chlorine for isotopic analysis. In this step, the entire sample mass was immersed into a mixture of acid solution (HNO_3 + HF) and loaded on a shaking table for 48 hours.

Following total dissolution, chlorine was recovered as AgCl precipitate. During dissolution, the rock residue formed a hydrofluoric gel, while chlorine remained into the solution. The solution was separated from the gel by centrifugation in pre-cleaned 50 mL tubes (rinsed with Milli-Q water to prevent contamination), allowing the dissolved chlorine to be isolated for further processing. To precipitate AgCl, a 10% $AgNO_3$ solution was then added in large excess to both the samples and blanks to ensure complete chlorine precipitation. The bottles were kept in the dark for 24-48 hours, as AgCl is light-sensitive and prolonged exposure can lead to dissociation of Ag and Cl. The expected precipitate is pure white, and the AgCl was finally recovered by decanting the supernatant.

After the initial recovery, the AgCl precipitate must be further purified to remove sulfur, which has the same molar mass as ^{36}Cl and would otherwise interfere with AMS measurements. To achieve this, the AgCl was redissolved and treated with 1 mL of saturated barium nitrate solution ($Ba(NO_3)_2$), which selectively precipitates $BaSO_4$ and $BaCO_3$ upon exposure to air. The resulting supernatant was then recovered, and AgCl was reprecipitated by adding HNO_3.

2.2.3 Cosmogenic ^{36}Cl analyses

Cosmogenic ^{36}Cl analyses were performed using Accelerator Mass Spectrometry (AMS) of the ASTER instrument at CEREGE, Aix-en-Provence, France (Figure 2.7). Unlike stable cosmogenic nuclides such as ^{3}He, ^{36}Cl is radioactive; thus, the measured concentrations reflect both the accumulation of cosmogenic ^{36}Cl over time and its radioactive decay. Initially, concentrations increase linearly (Figure 2.8) until reaching an equilibrium between production and decay after about 10^4 ka.

The AMS measures the $^{36}Cl/^{35}Cl$ and $^{35}Cl/^{37}Cl$ ratios (Figure A2.3 in appendix), after ionization of the sample particles, with separation based on differences in their mass and charge. AMS accelerates the particles before directing them into the mass spectrometer, allowing the detection of extremely small isotope concentrations with high sensitivity (Elmore & Phillips, 1987).

Measurements were normalized against the in-house CEREGE standard NIMB 2011 (Merchel et al., 2011), assuming a natural ratio of 3.127 for the stable ratio $^{35}Cl/^{37}Cl$. These ratios were then used to calculate ^{36}Cl and Cl concentrations by applying the principles of isotope dilution and the equations outlined in Schimmelpfennig et al. (2009). The measured ratios, along with the derived ^{36}Cl and Cl concentrations, are presented in chapter 3, 4, and 5 of this thesis.



Figure 2.7: *Photo shows the AMS ASTER instrument at CEREGE.*

2.2.4 Calculation of ^{36}Cl cosmogenic exposure ages

Cosmogenic ^{36}Cl exposure ages were calculated using both the Excel® spreadsheet of Schimmelpfennig et al. (2009) and the online Cosmic Ray Exposure Program (CREp; Martin et al., 2017). The age calculators incorporate all relevant production mechanisms of ^{36}Cl, including spallation of Ca, K, Ti, and Fe, slow muon capture by Ca and K, low-energy neutron capture by ^{35}Cl, and nucleogenic production. Input parameters included sample chemical composition, thickness, and topographic shielding, with scaling based on the Lal/Stone time-dependent scheme (Stone, 2000). Sea-level high-latitude (SLHL) production rates applied in the calculations were 42.2 ± 4.8 atoms ^{36}Cl (g Ca)$^{-1}$ yr^{-1} for Ca spallation (Schimmelpfennig et al., 2011), 148.1 ± 7.8 atoms ^{36}Cl (g K)$^{-1}$ yr^{-1} for K spallation (Schimmelpfennig et al., 2014), 13 ± 3 atoms ^{36}Cl (g Ti)$^{-1}$ yr^{-1} for Ti spallation (Fink et al., 2000), 1.9 ± 0.2 atoms ^{36}Cl (g Fe)$^{-1}$ yr^{-1} for Fe spallation (Stone, 2000), and 696 ± 185 neutrons (g air)$^{-1}$ yr^{-1} for epithermal neutron production at the land–atmosphere interface (Marrero et al., 2016). A high-energy neutron attenuation length of 160 g cm^{-2} and a bulk rock density of 2.5 g cm^{-3} were used in all calculations.

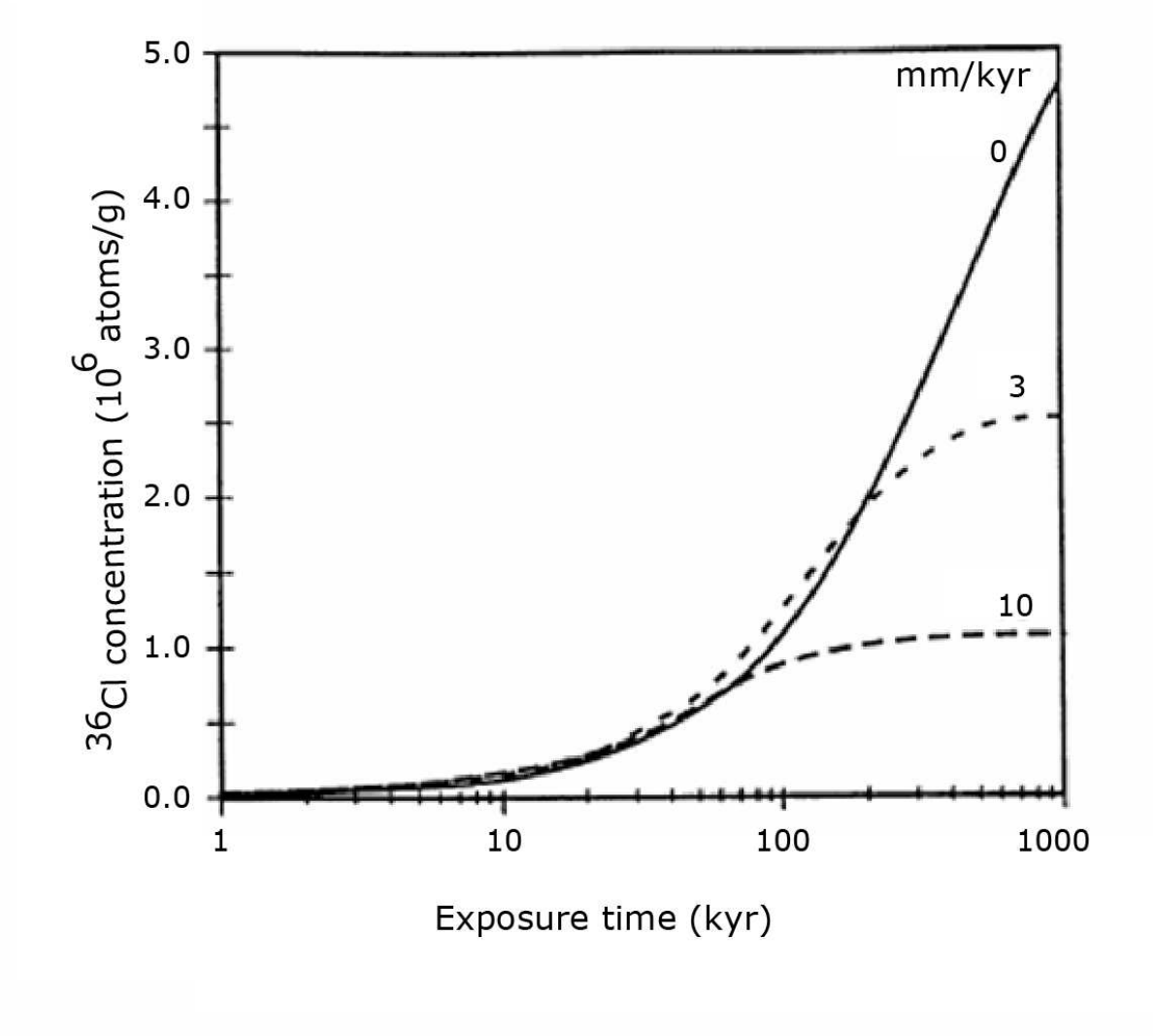

Figure 2.8: *Evolution of cosmogenic 36Cl concentration through time (Gosse and Phillips, 2001). The steady-state situation (no erosion) is shown by the black curve.*

2.3 Geochemical analysis

172 lava samples were collected for major and trace element analysis during field campaigns in 2013, 2018, 2022, and 2023:139 samples from central Afar and 33 samples from the Asal rift. The majority of the central Afar lavas are aphyric, though there are some samples which display a porphyritic texture characterized by plagioclase phenocrysts. In contrast, most lavas from the Asal rift are porphyritic and dominated by plagioclase phenocrysts, with only a few samples exhibiting an aphyric texture.

2.3.1 Quantitative petrographic analysis

To quantify the plagioclase phenocryst content in selected porphyritic lavas from central Afar, a supervised image classification was performed using ENVI 5.6 software. This approach aimed to compare image-based quantitative estimates with qualitative observations made on hand specimens.

High-resolution photographs were taken from cut and polished lava samples to expose the internal textures. These photos displayed the distribution and size of mineral phases, dominated by plagioclase phenocrysts (Figure 2.9). The images were then converted into GeoTIFF format to ensure compatibility with the ENVI software. The supervised Minimum Distance Classification (MDC) algorithm, based on spectral distance metrics was applied. This classification separated the surface mineralogy of each sample into four categories: plagioclase phenocrysts, groundmass/matrix, vesicles, and other accessory components. To train the classifier, Regions of Interest (ROIs) were manually digitized for each mineral phase on all selected images, with multiple representative polygons drawn per class to capture spectral variability.

After MDC, several post-processing steps were applied to improve the results: sieve (to remove isolated pixel groups below a size threshold), clump (to group adjacent pixels of the same class), and majority filter (to smooth small-scale variations and reduce noise). This pixel-based classification was used for quantitative estimation of plagioclase, groundmass, vesicles, and other accessory components for each sample (Table 2.3, in appendix).

Following classification, the output thematic maps were color-coded by class (plagioclase, groundmass, vesicles, and others) and visually inspected using ENVI's layer manager and flicker view tools, allowing side-by-side comparison with the original images. Each map was then exported for integration (Figure 2.9).

To assess the mineralogical composition of the vesicle-free groundmass more accurately, plagioclase percentages were normalized to exclude the vesicular volume. This correction was necessary because vesicles represent void space and do not contribute to the actual mineral content. The normalized plagioclase content was calculated using the following formula:

$$\text{Plagioclase (\%)}_{\text{normalized}} = \frac{\text{Plagioclase (\%)}_{\text{ENVI}}}{\text{100-Vesicles (\%)}_{\text{ENVI}}} \times 100$$

This approach assumes that the distribution of minerals within the solid portion of the rock is uniform, and therefore that the relative proportions of the solid phases remain unchanged when vesicles are excluded.

The percentage of plagioclase phenocrysts obtained from image classification and normalized to exclude vesicular volume was compared with initial estimates from hand specimen. The results show a strong consistency between the two approaches (Table 2.3, in appendix).

2.3.2 Major and Trace element analysis

Sample preparation for major and trace analysis was performed out at the at Centre de Recherches Pétrographiques et Géochimiques (CRPG), Nancy, France. Samples were cut with a saw to remove any weathered portions, and the cut surfaces were ground down to reduce any potential contamination by metals from the saw blade. The lava samples were then crushed using a jaw crusher. The crushed material was cleaned with water and dried overnight in an oven at 85 °C. Finally, the cleaned rock chips were ground to a fine powder using an agate mortar and pestle.

Major and trace element compositions were analysed at the SARM national facility. Major element compositions were measured by Inductively Coupled Plasma Atomic Emission Spectrometer (ICP-OES) and the trace elements were determined using Inductively Coupled Plasma Mass Spectrometry (ICP-MS). Lithium (Li) was measured using atomic absorption, Boron(B) by colorimetry, and Chlorine (Cl) by spectrophotometry. The analytical results are presented in chapter 2, 3, and 4 of this thesis.

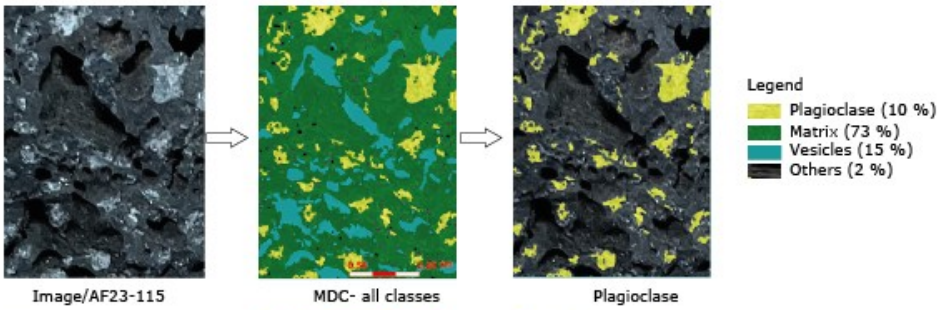
Image/AF23-115
MDC- all classes
Plagioclase
Legend
Plagioclase (10 %)
Matrix (73 %)
Vesicles (15 %)
Others (2 %)

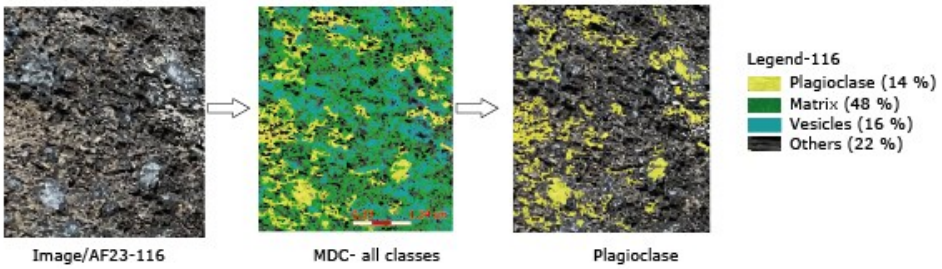
Image/AF23-116
MDC- all classes
Plagioclase
Legend-116
Plagioclase (14 %)
Matrix (48 %)
Vesicles (16 %)
Others (22 %)

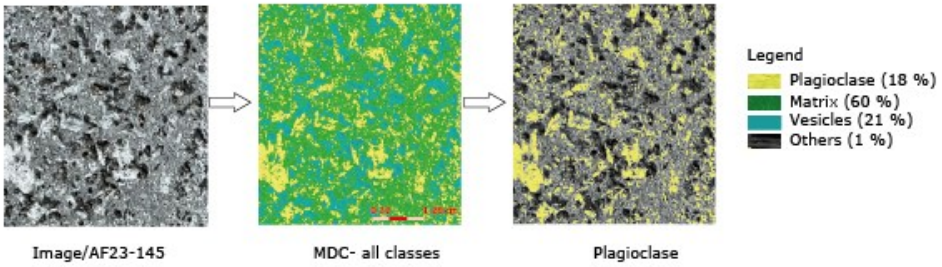
Image/AF23-145
MDC- all classes
Plagioclase
Legend
Plagioclase (18 %)
Matrix (60 %)
Vesicles (21 %)
Others (1 %)

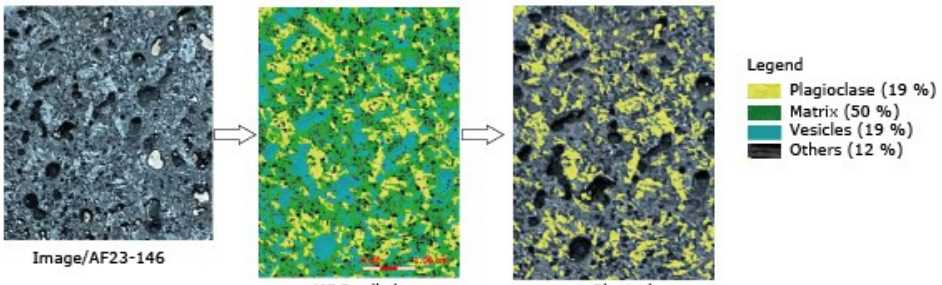
Image/AF23-146
MDC- all classes
Plagioclase
Legend
Plagioclase (19 %)
Matrix (50 %)
Vesicles (19 %)
Others (12 %)

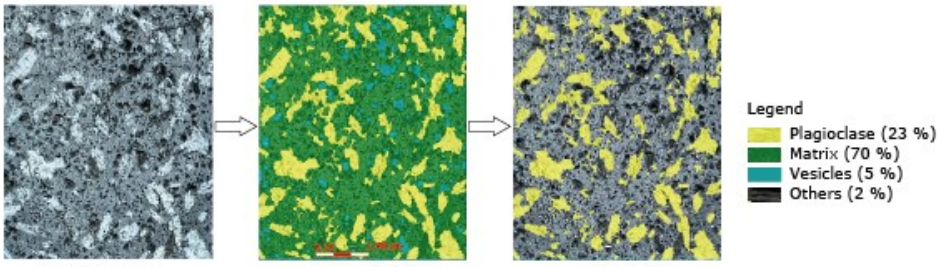
Image/AF23-162
MDC- all classes
Plagioclase
Legend
Plagioclase (23 %)
Matrix (70 %)
Vesicles (5 %)
Others (2 %)

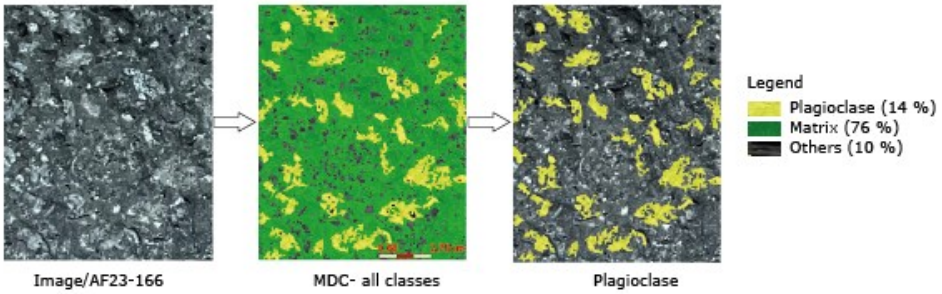
Image/AF23-166
MDC- all classes
Plagioclase
Legend
Plagioclase (14 %)
Matrix (76 %)
Others (10 %)

Figure 2.9: *Quantitative petrographic analysis of lava samples from Central Afar using Minimum Distance Classification.*

2.3.3 Isotope measurement

The Sr, Nd and Pb isotopic compositions were measured on 22 of the lava samples from central Afar. Chemical preparation was performed in the IRISS clean-room facility (STEHLo) at CRPG, following established ion-exchange protocols (Cloquet et al., 2006; Manhes et al., 1980) for Pb, and (Pin et al., 1994; Pin and Santos Zalduegui, 1997) for Sr and Nd. Below is described the sample preparation and analysis procedures.

1) Sample decomposition

Depending on the concentration of Pb, Sr and Nd (determined from trace element analyses), 150-165 mg of finely powdered sample were weighed and placed into 15 mL Savillex® beakers. Digestion was carried out in a mixture of 4 ml concentrated sub-boiled HNO_3 and 1 mL ultrapure HF, followed by heating at 110 °C for 24-48 h until complete dissolution. The HNO_3/HF was evaporated off, and the residues were refluxed in 6 M HCl for 24 h at 70 ° till complete digestion of the powder samples. The sample is then split into two parts and dried in order of further purification of the elements.

2) Chromatographic isolation

Pb was purified using anion-exchange chromatography with AG1X8 resin (Bio-Rad, 200-400 mesh) in mini-columns, following the procedures of (Manhes et al., 1980). Prior to use, the resin bed (0.2 mL) was pre-cleaned by sequentially passing 6 M HCl and 0.8 M HBr to remove potential blanks. The column was then equilibrated in 0.8 M HBr to establish the ionic environment for Pb sorption. Each sample aliquot was redissolved in 1 mL of 0.8 M HBr and quantitatively loaded onto the conditioned column. Under these conditions Pb is retained by the resin, while most major elements are eluted.

The column was then rinsed stepwise with a total of 3 mL 0.8 M HBr (added in several increments to optimize washing) to remove the bulk silicate matrix and trace cations. Pb was quantitatively recovered by stepwise elution with a total of 3.0 mL of 6 M HCl, which strips Pb from the resin while maintaining clean separation from other trace elements. The Pb

fractions were then evaporated to dryness in pre-cleaned Savillex® beakers and re-dissolved in 1 ml of HNO_3 (0.3M) for mass spectrometry.

For Sr and Nd isolation, the remaining residual solutions obtained after Pb separation were used. These residues were dried down and re-dissolved in 2 mL of 2 M HNO_3. Separation of Sr and Nd followed the ion-exchange protocols of (Pin and Santos Zalduegui, 1997), with an additional Ln Spec step for complete isolation of Nd from Sm.

Sr was purified using Sr-Spec resin (Eichrom, 50-100 µm). Columns with 1.5 mL resin bed were first cleaned with 1ml of 6 M HCl and 0.5 ml of 0.05 M HNO_3, and then conditioned in 1 ml of 2 M HNO_3. Then the sample solutions (in 2 M HNO_3) were quantitatively loaded onto the columns, where Sr is strongly retained by the resin while most of the matrix passes through. For reference materials, a calibrated $^{84}Sr/^{87}Sr$ tracer solution was added prior to loading, corresponding to 30 µg of spike, in order to allow isotope dilution calculations. Matrix cations were eluted in several successive steps: three additions of 0.5 mL 2 M HNO_3, followed by two additions of 0.5 mL 7 M HNO_3, then four additions of 1.0 mL 7 M HNO_3, and finally two additions of 0.5 mL 3 M HNO_3. After these washes, a further 0.5 mL of 0.05 M HNO_3 was passed through the column. Strontium was then quantitatively recovered in a new collection vial by eluting the resin with two additions of 0.5 mL 0.05 M HNO_3, followed by two additions of 1.0 mL 0.05 M HNO_3. The combined Sr fractions were evaporated to dryness in pre-cleaned Savillex beakers and re-dissolved in 2.25 M HNO_3 for isotopic analysis.

Nd was separated from the REE fraction using a two-step column chemistry procedure. In the first step, columns were packed with 1.6 mL of resin, cleaned with ultrapure water, and conditioned with a mixture of 1 M HCl + 0.5 M HF (to ⅓ of the column volume), followed by rinsing with water. The resin was then equilibrated with 5 mL of 2 M HNO_3. Samples were loaded stepwise in 2 M HNO_3, beginning with 1 mL aliquots until the full solution (6 mL) was passed through the column. After sample loading, an additional 0.5 mL of water was added before changing the collection beaker. Nd was recovered by elution with 4.5 mL ultrapure water. The collected Nd fraction was dried at 70 °C overnight in open Savillex beakers, then redissolved in 2 mL of 6 M HCl in preparation for the second separation stage.

In the second step, Nd was separated from Sm using Ln-Spec resin (Pin and Santos Zalduegui, 1997). After drying in 6 M HCl, the samples were treated with 1 mL of 0.27 M HCl, ultrasonicated for 30 minutes, and heated in closed beakers at 70 °C for 1 hour. The columns were loaded with Ln-Spec resin and washed with water before being conditioned with three successive additions of 0.1 mL 0.27 M HCl. Samples were loaded stepwise in three additions

of 0.1 mL solution, with 0.1 mL of 0.27 M HCl added between each step to maintain flow. The column was then rinsed with two further additions of 0.1 mL 0.27 M HCl, followed by 3 mL of 0.27 M HCl. Neodymium was finally collected in a clean beaker by elution with 3.5 mL of 0.27 M HCl. The Nd fractions were dried at 80 °C, then dissolved in 0.1 mL of 2% HNO_3. After 30 minutes, 0.9 mL ultrapure water was added, and the solutions were heated at 80 °C overnight to ensure complete dissolution prior to isotopic analysis.

3) Isotopic analysis

Pb isotope ratios were measured using a Thermo Fisher Neptune+ MC-ICP-MS (Figure 2.10a). Thallium was added to each solution from the NIST 997 standard to monitor and correct for instrumental mass bias (W. M. White et al., 2000). Measured Pb isotope ratios were normalized to NIST SRM 981, using values obtained by (Thirlwall, 2002). Long-term reproducibility of the standard runs during this study was within ±100 ppm (2σ) on $^{206}Pb/^{204}Pb$, $^{207}Pb/^{204}Pb$, and $^{208}Pb/^{204}Pb$. Analytical details of the setup and corrections follow the protocols by (Cloquet et al., 2006).

Sr isotope ratios were measured on a Thermo Scientific Triton Plus TIMS operated in multi-collection mode (Figure 2.10b). Five Faraday cups were used to collect the ion beams, allowing simultaneous monitoring of ^{87}Rb to correct for possible isobaric interference. Strontium was loaded onto single Re filaments with a Ta activator. Instrumental mass bias was corrected by internal normalization to a $^{86}Sr/^{88}Sr$ ratio of 0.1194 using the exponential law. The international standard NBS 987 was measured throughout the analytical sessions to monitor accuracy and reproducibility. Procedural blanks averaged around 300 pg Sr, negligible compared to the amounts obtained from the samples.

Nd isotope ratios were determined using a Thermo Scientific Neptune+ MC-ICP-MS (Figure 2.10b). Instrumental mass bias was corrected by internal normalization to a $^{146}Nd/^{144}Nd$ ratio of 0.7219, following the exponential law (Luais et al., 1997). The international standard JNdi-1 was measured throughout analytical sessions to monitor accuracy and reproducibility. The average blank is about 100 pg for Nd and always negligible in front of the Nd from the sample.

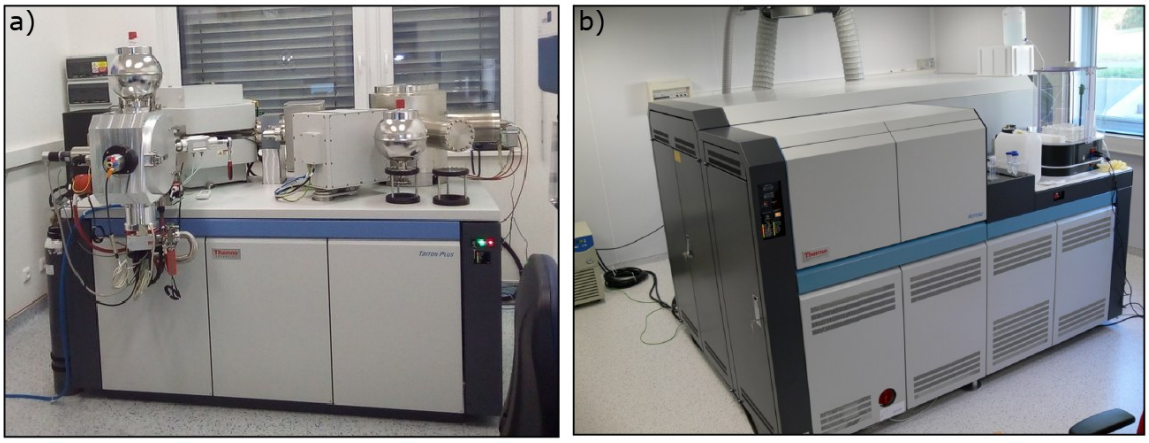

Figure 2.10: *Instruments used for Isotope measurment. a) Thermo Scientific Triton Plus Negative/positive – TIMS. b) Thermo Scientific Neptune Plus – Multicollector.*

Chapter 3

Volcanic activity, magma types and organisation of the Gumat Mali magmatic sub-segment, Central Afar rift (Ethiopia)

Yafet Gebrewold Birhane[1,6], Raphael Pik[1], Nicolas Bellahsen[2], Sarah Gommery[2], Irene Schimmelpfennig[3], Lydéric France[1,4], Simon Daout[1], Jessica Flahaut[1], Dereje Ayalew[5], and Gezahegn Yirgu[5]

[1]CRPG, CNRS, Universite´ de Lorraine, UMR 7358, Vandoeuvre-les-Nancy, France, [2]Sorbonne Universités, UPMC Université Paris 06, CNRS, Institut des Sciences de la Terre de Paris (iSTeP), Paris, France, [3]Aix-Marseille Université, CNRS, Coll France, IRD, INRAE, CEREGE, Aix en Provence, France, [4]Institut Universitaire de France (IUF), [5]School of Earth Sciences, Addis Ababa University, Addis Ababa, Ethiopia, [6]Department of Geology, College of Natural and Computational Sciences, Hawassa University, Ethiopia

In preparation for Journal of Volcanology and Geothermal Research (JVGR)

3. Introduction

The Afar Depression represents a unique natural laboratory where the Ocean Continent Transition (OCT) is actively occurring and can be observed. This region accommodates extension through segmented rifting associated with both magmatism and faulting (Hayward & Ebinger, 1996). Rifting initiated at ~26 Ma (Wolfenden et al., 2005) following the impingement of the Afar mantle plume, which triggered widespread volcanism and lithospheric thinning in the Afar region until now (Hofmann et al., 1997; Ebinger & Casey, 2001; Pik et al., 1999, 2006; Rooney et al., 2012, Stab et al., 2016; Rime et al., 2023). Today, the Afar magmatic rift segments share some structural and volcanic similarities with second-order slow-spreading mid-ocean ridge segments (Carbotte et al., 2016; Ferguson et al., 2013), with an axial volcanic ridge at the centre that transitions to a fault-bounded axial graben towards the tips (e.g., Keir et al., 2009; Watts et al., 2020). They are marked by intense volcanic activity including the emplacement of dike swarms and associated localized faulting (Grandin et al., 2010a; Dumont et al.,2017). Despite such shallow organisational similarities with mid-ocean ridges, mantle is still melting in this OCT context at important depth (~ 70-80 km), being limited by the local Lithosphere – Asthenosphere Boundary (LAB) (Ferguson et al., 2013; Wong et al., 2022). However, the Afar rift segments are not uniform and are organised differently in terms of topographic expression and magma supply (Rime et al., 2023). They also exhibit different crustal thickness, from ~25 km in Central Afar to 15-18 km under the Erta Ale range (Dugda

et al., 2005; Hammond et al., 2011; Reed et al., 2014; Ahmed et al., 2022), which questions potential control by stage or style of rifting (Keir et al., 2011; Stab et al., 2016; Rime et al., 2023). This variability raises key questions about the functioning and organisation of this key OCT context, including how magmas are generated, transferred to the crust, and how do they control/interact with rift segmentation during magmatic accretion.

Documentation of the most recent magmatic and rifting events along the Erta Ale and Dabbahu-Manda Hararo segments provided striking information on the architecture and operation of plumbing systems variation (Field et al., 2012a; Medynski et. al., 2016; Moore et al., 2019; Hutchison et al., 2018; Watts t al., 2023; Pin et al., 2024). However, those data must be supplemented by documentation of the magmato-tectonic activity over timescales ranging from 10^3 to 10^5yr in order to project information obtained on individual events in a long-term evolution and functioning of the segments.

Recent high-resolution studies in Central Afar have provided new insights into the organization of the Dabbahu segment following the 2005-2010 dyking events and eruptions. Medynski et al. (2013, 2015, 2016) used cosmogenic ^{36}Cl and ^{3}He exposure dating combined with geochemistry to identify crustal magmatic reservoirs that controlled the transient development of the axial graben and neovolcanic zone over the last 100 kyr, in agreement with fault development, stress regime and central reservoir – Dabbahu volcano interactions (Dumont et al., 2017, 2019). A combination of geochemical and petrological models associated with geochronological data was also used (Ferguson et al. 2013; Medynski et al., 2013; Field et al., 2013) to identify and discuss rift focussing and thermal regimes between axial and off-axis contexts. Despite its critical importance, the southern part of the Central Afar segment system, known as the Manda Hararo segment, is surprisingly under documented. Barrat et al. (2003) recognized there two geochemically distinct basaltic groups (LREE-enriched and depleted), whose coexistence points to contributions from compositionally heterogeneous mantle sources and questions discrete magmatic pathways within the segment. The internal structure of the segment remains poorly constrained, and is based on sparse K-Ar ages distributed over this wide system from ~ 250 to ~ 30 ka (Lahitte, Gillot, Kidane, et al., 2003).

In this study, we focus on and define a sub-segment of the Manda Hararo system, i.e. the Gumat Mali subsegment, that runs directly southward of the Dabbahu segment on the same tectonic corridor. We combine detailed mapping, volcanological observations, major and trace element analyses, and cosmogenic ^{36}Cl exposure dating of lavas to describe the Gumat Mali sub-segment. We investigate the two geochemically distinct magma types emplaced over the past

few hundred thousand years, describe their occurrence and organisation to reconstruct source occurrence, associated processes and better understand the magma transfer dynamics. We also map precisely, date, and document the style of the most recent historical effusive episodes in order to support the volcanic hazard assessments for the segment.

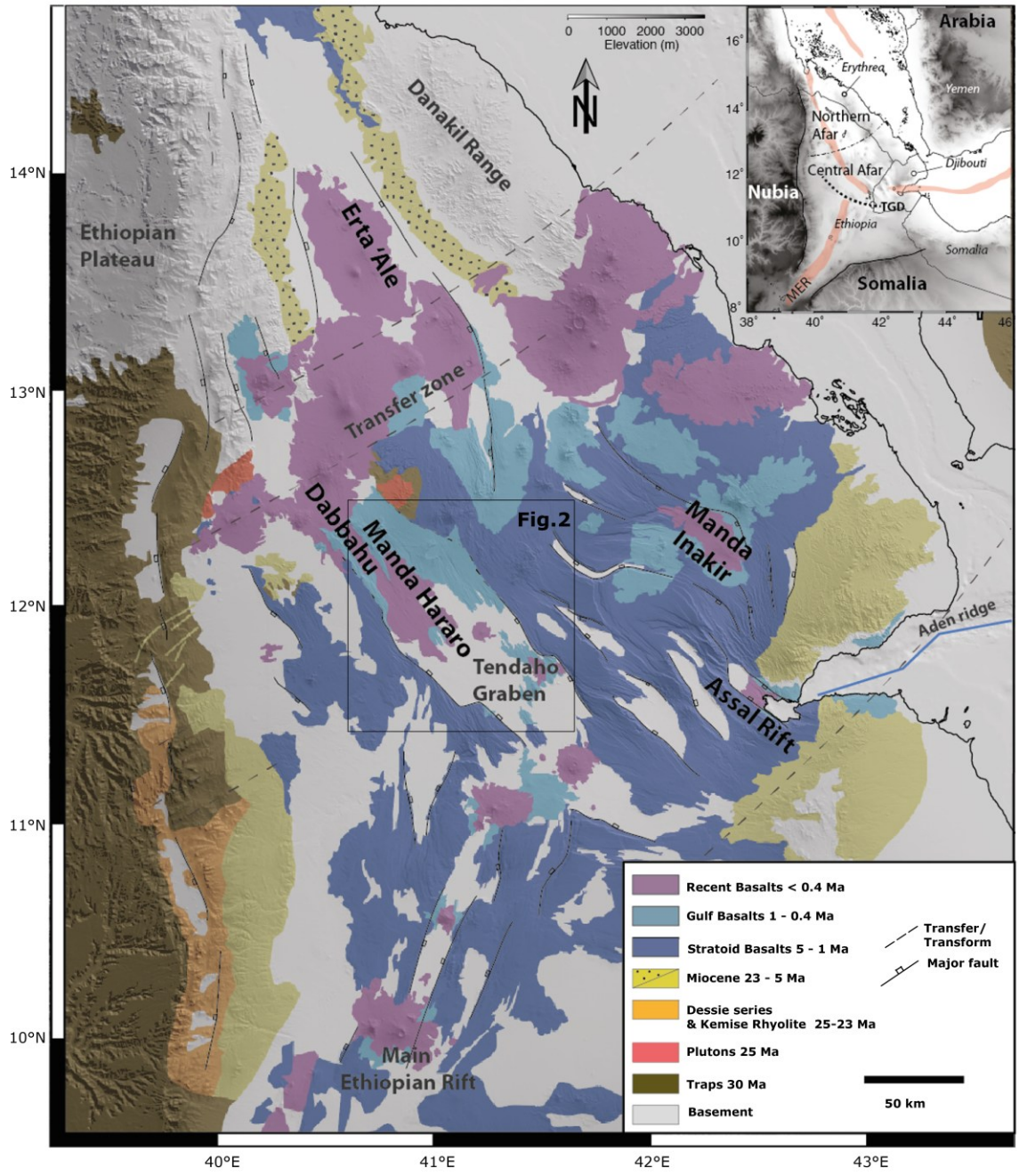

Figure 3.1: *Geological map of Afar modified after Stab et al. (2016)*

3.1 Geological setting

The Afar region marks the junction of three divergent plate boundaries: the Gulf of Aden Ridge, the Red Sea Ridge, and the East African Rift. The separation of the African and Arabian plates has resulted in the formation of the Afar Depression (Figure 3.1). Magmatism in Afar began in the early Oligocene (30 Ma) with the emplacement of voluminous continental flood basalts (CFB), linked to mantle plume activity (Marty et al., 1996; Hofmann et al., 1997; Pik et al., 2006; Bastow et al., 2008). This phase was followed by the Dessie formation, predominantly basaltic and dated at 25 Ma which mark the first localisation of volcanism and tectonics in the magmatic province (Ukstins et al., 2002; Zwaan et al., 2020; Stab et al., 2016). Volcanic activity declined during the Miocene and started again at 8-6 Ma with emplacement of the Dahla formation before significant necking and thinning of the lithosphere (Stab et al., 2016). It then intensified during the Pliocene with the widespread emplacement of the Stratoid basalts (5-1 Ma) which cover ~70% of the Central Afar rift floor (Varet, 1975; Kidane et al., 2003). This was followed by the eruption of Gulf basalts (1-0.4 Ma), associated with increased tectonic segmentation during the southward propagation of the Gulf of Aden rift (Manighetti et al., 1998). Since ~0.4 Ma, magmatic and tectonic activity has localized along discrete en-echelon magmatic segments, typically 60-100 km long and 20-40 km wide (McClusky et al., 2010).

Divergence in Afar proceeds at ~15 mm/yr (McClusky et al., 2010; Lewi et al., 2016), comparable to Iceland and other slow spreading ridges (Carbotte et al., 2006; Doubre et al., 2017). However, the rift remains in a transitional phase, with highly stretched and intruded continental crust that more closely resembles OCT than a fully developed oceanic spreading center (Bastow & Keir, 2011; Hammond et al., 2011). Rifting initiated in the southern Red Sea around 26 Ma (Baker et al., 1996;Ukstins et al., 2002) and propagated into Afar at ~ 25 Ma (Wolfenden et al., 2005). This extension led to significant lithosphere thinning between 6-5 Ma ago. Crustal thickness decreases from ~25 km in Central Afar to 15-18 km in the Erta Ale (Dugda et al., 2005; Hammond et al., 2011; Reed et al., 2014; Ahmed et al., 2022). Initial wide rifting in Central Afar included marginal grabens, but by the late Miocene, deformation localized at depth along mid-crustal detachments, controlling Stratoid volcanism (Stab et al., 2016). Further localisation of volcanism and deformation occurred with the emplacement of the Gulf Basalts ~1 Ma ago in the Tendaho Graben (Figure 3.2; Kidane et al., 2003; Tortelli et al., 2022, 2025). Presently, extension is focused along narrow magmatic segments (Ebinger & Casey, 2001; McClusky et al., 2010; Hammond et al., 2011).

Magmatic segments in Afar (e.g., Erta Ale, Manda Hararo-Dabbahu, and Asal-Ghoubbet), exhibit morphological and structural similarities to slow-spreading mid-ocean ridges, with narrow zones of extension, high magmatic output, and deformation through both faulting and dyke intrusion (Bridges et al., 2012; Buck et al., 2005; Geoffroy, 2005). Strain in these segments is accommodated primarily by dyke intrusion (Wright et al., 2006; Grandin et al., 2010a). These segments are fed by complex magmatic plumbing system with off-axis and on-axis magmatic reservoirs (Field et al., 2012a; Medynski et al., 2013; Moore et al., 2019). Most dykes propagate laterally from these reservoirs. Between 2005 and 2010, 14 such intrusions affected the Dabbahu segment, triggering faulting and eruptions. The 2005 event alone injected 1-2 km³ of mafic magma down to 10 km depth (Grandin et al., 2009, 2010; Ferguson et al., 2010, 2013).

The Manda Hararo axial rift zone (Figure 3.2) has been volcanically active from ~250 ka to recent times, with the most recent lavas dated ~ 30 ka (Lahitte et al., 2003b). It is composed of various volcanoes and emission centres distributed over a wide zone of ~ 30 km. In this system two main parallel sub-segments can be identified. The Manda Hararo sub-segment to the NE, which includes on the same axial direction southward the volcanic centres of Loma and Gabblaytu. The Gumat Mali sub-segment, to the SW, which runs directly in the prolongation of the Dabbahu segment, and is separated from the Manda Hararo sub-segment by a horst of Gulf basalts, defining an en-echelon relay with two distinct corridors of deformation.

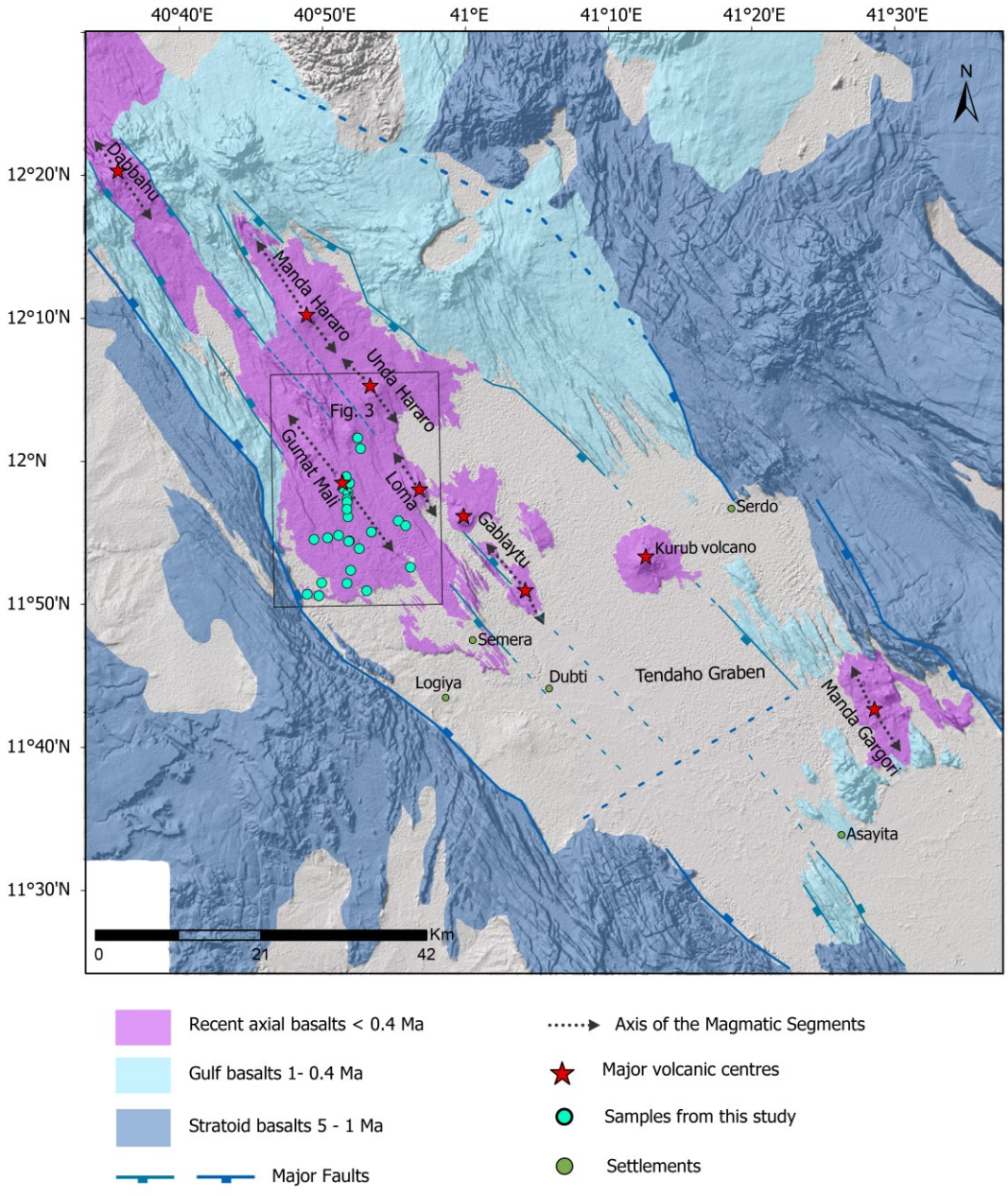

Figure 3.2: *Geological map of magmatic rift segments in Central Afar after Stab et al., (2016). Major volcanic centres (calderas, craters) host potential magmatic reservoirs beneath and are related to segmentation of the rift.*

3.2 Materials and methods

3.2.1 Remote sensing data sets and processing

Before collecting lava surface samples, we conducted detailed mapping of the Gumat Mali sub-segment to distinguish and identify distinct eruptive units. The extents and diversity of lava

fields were mapped using a combination of remote sensing data, including medium-resolution images from Landsat-8 and Sentinel-2, and high-resolution stereo images from the AIRBUS DS Pleiades mission.

The multi-spectral Landsat-8 and Sentinel-2 images were aquiered at level-2 (corrected from atmospheric effects) from the US Geological Survey (http://earthexplorer.usgs.gov) and the Copernicus (https://browser.dataspace.copernicus.eu/) browsers. The 9 and 13 bands of the Landsat-8 OLI and Sentinel-2 MSI sensors with medium spatial-resolution and spectral resolution, enable an advanced land cover mapping at global scale and at high temporal frequency (Phiri et al., 2020; Trigunasih et al., 2023).

19 Pléiades stereo pair of panchromatique and multi-spectral images, covering a surface area of 4535 km^2, were provided by the Incitation à l'utilisation scientifique des images Spot (ISIS) program from Centre national d'études spatiales (CNES) (https://dinamis.teledetection.fr). The spatial resolution of the images is approximately 0.7 meters for the panchromatic channel (wavelength in the 480-830 nm range) and around 2.8 meters for the multi-spectral blue, green, red, and near-infrared channels (Gleyzes et al., 2012). These images also exhibit a wide radiometric range, providing good contrasts over low rugosity regions in comparison to other data sets (see Figure S3.2 in suplementary materials, Bisson et al., 2021; Palaseanu-Lovejoy et al., 2019).

Using ENVI® software, a variety of products were produced and improved using a sequence of interactive techniques, such as false-colour compositing and histogram stretching. Specifically, Sentinel-2 RGB (bands 4-3-2) and Landsat 8 OLI RGB (bands 7-4-1) false-color composites proved effective for mapping volcanic features, and identification of different eruptive units. Statistical manipulation techniques (principal component analyses, decorrelation stretching and minimum distance classification) were applied to enhance visual identification between eruptive units for better interpretation.

3.2.2 Digital Surface Model (DSM) generation

A DSM is a digital representation of the Earth's surface, where each pixel contains ellipsoidal height information, including surface heights of objects and structures such as buildings and vegetation. Constructing a Digital Surface Model (DSM) using Pléiades images has been applied in various contexts when high-resolution elevation data is needed. We generate the

DSMs from 19 Pleaides pairs of images using the Ames Stereo Pipeline software (ASP, Beyer et al., 2018). We employed a classical processing scheme applied to the panchromatic pairs (e.g., Lacroix et al., 2022): (1) Orthorectification of the images using the publicly available Copernicus 30m DSM (Cop-DEM) and refined sensor models using Rational Polynomial Coefficients (RPC), which describe the relationship between the satellite image and its corresponding ground coordinates. (2) Image correlation between all pairs of images. (3) Generation of 3D cloud points from triangulation. (4) Interpolation of the point cloud to generate a 2 m spatial resolution DSM.

The ASP software provides various algorithms that we compare to derive a high-resolution DSM with minimal noise and suitable texture for mapping lava surface (see ASP documentation: https://stereopipeline.readthedocs.io/en/latest/stereodefault.html). In this flat and low rugosity area, we found that the More Global Matching algorithm combined with a census transform cost function (Zabih & Woodfill, 1994) and a Bayes sub-correlation method: (1) Allows for the derivation of high-resolution and high-quality results using small correlation windows of 9x9 pixels in comparison to classical block matching algorithms, (2) Offers faster computation compared to classical normalized cross-correlation functions, and (3) Preserves low-frequency contents in comparison to other refinement methods to achieve sub-pixel accuracy. Before grid generation, we also removed outliers and smoothed the triangulation results using sliding windows filters and adaptative texture smoothing.

3.2.3 Geomorphological Mapping

Using ArcGIS Pro, we combined all remote sensing techniques and the Pleiades-derived DSM to map detailed volcanological features and the extents of lava flow units. This high-resolution mapping allowed us to precisely target sampling locations for dating eruptive sequences. The mapping results were validated through field observations.

3.3 Geochemical analysis

In this study, we present 39 major and trace element analysis of basaltic lava flows sampled across the Gumat Mali sub-segment during field trips organized in 2013, 2018 and 2023. Samples were crushed, powdered, and measured for the major and trace element compositions at Centre de Recherches Pétrographiques et Géochimiques (CRPG-CNRS Nancy-France) using the SARM national facility. The major element compositions were measured by

Inductively Coupled Plasma Atomic Emission Spectrometer (ICP-OES) and the trace elements were determined by Inductively Coupled Plasma Mass Spectrometry (ICP-MS). Li was measured using atomic absorption, B by colorimetry, and Cl by spectrophotometry from the sieved targeted grain size fraction (see section 3.5.1). The sample locations are reported in Figure 3.2 and analysis results are presented in Table S3.1.

3.3.1 In situ-produced ^{36}Cl CRE dating

3.3.1.1 Sampling strategy and analytical method

To establish the ^{36}Cl CRE ages of the lava flows, sampling was conducted during field campaigns in 2013, 2018 and 2023. 10 lava flow samples were collected from the uppermost 2-10 cm of solid rock surfaces using a hammer and chisels. 1 sample (AF13-348) was collected from the top of a large block (from a dense blocks field), while the remaining 9 were taken from lava flows associated with episodes of effusive activities along the fissural system (Figure 3.3). Detailed field data and sample information are provided in Table 3.1. Special attention was given to sample original, flat and non-eroded or dismantled surfaces. This was straightforward for the most recent surfaces of the fissural system investigated here. However, two relatively distal surfaces of underlying older thick pahoehoe lava flows have also been sampled, yet they were explicitly exhibiting evidence of moderate surface reworking (AF13-351 and AF23-97). On top of the wider tumuli (10-15 m in diameter), it was possible to estimate that only the shallowest level of cooling related prismatic blocks was missing for those two flows. The missing thickness has been estimated in the field as 15 ± 5 cm by lateral correlations and has been considered for age calculation. Due to the relatively flat configuration of the Gumat Mali segment, no specific topographic-shielding corrections was necessary for all sampling sites.

Whole rock samples were crushed using a grinder, subsequently sieved with water to remove dust and fine-grained powders, and then dried in an oven. The targeted grain size fraction (250-500 µm) was then retained for further chemical preparations. The low-energy neutron flux in the samples was calculated from whole-rock analyses, primarily using elements (such as Cl, Li, B, Fe, Ti and Al) that affect neutron moderation and absorption (Gosse & Philips, 2001; Schimmelpfennig et al., 2009, 2011). The computed neutron was then used to determine the ^{36}Cl production from capture of the low-energy neutrons on ^{35}Cl (Schimmelpfennig et al., 2009).

The chemical preparation was carried out at the Centre Européen de Recherche et d'Enseignement des Géosciences de l'Environnement (CEREGE, France). 100-120 grams of the sample grains were washed with milli-Q water to remove fine-grained powder and then leached in a dilute HF/HNO3 mixture to dissolve 20% of the initial sample mass to remove atmospheric ^{36}Cl and reduce the potentially Cl-rich mineral phases (Schimmelpfennig et al., 2009). 1 g aliquot of the rinsed and dried grains were taken from these etched samples for the analysis of the major elements (Table S3.2) which provides the concentrations of the target elements. Ca, K, Ti and Fe are the desired targets for ^{36}Cl production through spallation, while Ca and K are the targets for ^{36}Cl production through muon capture. Spike enriched in ^{35}Cl (~99%) was added to each samples and to three chemistry blanks for the isotope dilution (Ivy-Ochs et al., 2004). Then, the final sample grain dissolution of the remaining sample materials (70-100 g) was conducted in a diluted HF/HNO_3 (Ultrapur) acid mixture. The remaining steps applied for precipitations of AgCl and removal of sulfur (whose molar mass is 36) were performed according to the protocol presented in (Schimmelpfennig et al., 2011). ^{36}Cl/^{35}Cl and ^{35}Cl/^{37}Cl ratios were measured by Accelerator Mass Spectrometry (AMS) at the French AMS national facility (ASTER-CEREGE, France). The ratios were normalized to the in-house CEREGE standard NIMB 2011 provided by (Merchel et al., 2011) and assuming a natural ratio of 3.127 for the stable ratio ^{35}Cl/^{37}Cl. We used these measurements to determine the ^{36}Cl and Cl concentrations using the principles of isotope dilution and following the equations in Schimmelpfennig (2009). Measured ratios, and the resulting ^{36}Cl and Cl concentrations are presented in Table 3.2.

Table 3.1: *Locations and description of lava flow samples used for ^{36}Cl dating. For all analysed samples, 250-500µm grain size fraction was used. Scaling factor is according to (Stone, 2000). Two samples marked with an asterisk are affected by erosion and surface deflation.*

Sample Name	Latitude (°N)	Longitude (°E)	Altitude (m)	Sample Thickness (cm)	Mineral used for CRE dating	Stone scaling factor (Neutrons)	Stone scaling factor (Muons)
AF13-341	11.935996	40.862964	440	5	whole rock for ^{36}Cl	0.86	0.76

AF13-345	11.969094	40.857494	464	2	whole rock for ^{36}Cl	0.87	0.77
AF13-348	11.975305	40.864895	478	2	whole rock for ^{36}Cl	0.88	0.78
AF13-349	11.918371	40.890281	439	3.5	whole rock for ^{36}Cl	0.86	0.76
AF13-351*	11.90796	40.8649	436	10	whole rock for 36Cl	0.86	0.76
AF18-01	11.982789	40.860882	476	4	whole rock for ^{36}Cl	0.88	0.78
AF18-02	11.963929	40.863074	462	5.5	whole rock for ^{36}Cl	0.87	0.77
AF18-03	11.956141	40.861775	477	4	whole rock for 36Cl	0.88	0.78
AF23_29	12.015507	40.877684	440	5.5	whole rock for 36Cl	0.86	0.76
AF23_97*	11.931341	40.921657	439	6	whole rock for 36Cl	0.86	0.76

3.3.1.2 ^{36}Cl CRE age calculations

Calculations of ^{36}Cl CRE ages were performed using the Excel® spreadsheet published by (Schimmelpfennig et al., 2009) and the online Cosmic Ray Exposure program (CREp) (https://crep-dev.otelo.univ-lorraine.fr/; Martin et al., 2017). Highly consistent results were obtained from both methods (Table 3.2). All ^{36}Cl production reactions (spallation of the target elements Ca, K, Ti and Fe, slow muon capture by Ca and K, capture of cosmogenic low-energy neutrons by ^{35}Cl and nucleogenic production) were considered in the calculation based on the chemical compositions of the bulk-rock. The time-invariant "St" scaling method by (Stone, 2000) was applied for the calculation of all samples. The following ^{36}Cl sea level and high latitude (SLHL) production rates were used for the calculations: 42.2 ± 4.8 atoms of ^{36}Cl (g Ca)$^{-1}$ yr^{-1} for Ca spallation (Schimmelpfennig et al., 2011), 148.1 ± 7.8 atoms of ^{36}Cl (g K)$^{-1}$ yr^{-1} for K spallation (Schimmelpfennig et al., 2014), 13 ± 3 atoms of ^{36}Cl (g Ti)$^{-1}$ yr^{-1} for spallation of Ti (Fink et al., 2000), 1.9 ± 0.2 atoms of ^{36}Cl (g Fe)$^{-1}$ yr^{-1} for Fe spallation (Stone et al., 2005), and 696 ± 185 neutrons (g air)$^{-1}$ yr^{-1} for the rate of epithermal neutron production from fast neutrons in the atmosphere at the Earth/atmosphere interface (Marrero et al., 2016). We applied a value of 160 g cm^{-2} for the high-energy neutron attenuation coefficient (Schimmelpfennig et al., 2009) and 2.5 g/cm^3 for the bulk rock density.

3.4 Results

3.4.1 Chronology of Lava Flows

The newly established and refined chronology of the Gumat Mali magmatic segment provides a more precise understanding of the recent volcanic activity in the region. By positioning all

lava flows within a new timeframe, those data offer an absolute age framework that aligns with and enhances previous observations.

The new ^{36}Cl CRE ages calculated for the volcanic surfaces from this study (Table 3.2, Figure 3.3) can be divided into (i) a recent historical episode which ranges from 610 ± 190 yr (AF13-349) to 1900 ± 290 yr (AF13-348, Figure 3.7D), and (ii) an underlying older episode of thick pahoehoe flows that exhibit rather consistent exposure ages of 72400 ± 6400 yr (AF13-351, Figure 3.7G) and 73500 ± 6400 yr (AF23-97), for the two surfaces we dated. Note that younger lateral and older underlying episodes have not been dated but can reasonably date from a few tens of kyr to few hundreds of kyr respectively (Figure 3.3 and next section).

For the recent historical activity of the axial system (see Figure 3.3), ages can be tentatively divided into various distinct stages that are consistent with relative chronology and mapping (see next section), even if formally their own intrinsic precisions are sometimes overlapping. The sequence starts with (1) the blocks fields associated with the initial collapse of the main crater, which exhibit an age of 1900 ± 290 yr on top of one of the biggest blocks (~ 1.5 m high, AF13-348, Figure 3.7D). Then (2) a series of early fissural lava flows exhibit consistent ages of 1200 ± 330 yr (AF13-341) and 1200 ± 240 yr (AF18-03). A subsequent episode (3) of effusive activity of the fissural system appears with younger ages for the large lava flows which extend on the eastern side of the axis, 910 ± 190 yr (AF23-29) and 730 ± 240 yr (AF18-01), as well as for very thin lava lake overflows, 840 ± 190 yr (AF13-345), and crater-floor surfaces, 700 ± 230 yr (AF18-02), emplaced on the axial depression. The last identified stage corresponds to the youngest flows emplaced specifically at the northern and southern tip of the segment, with distinct very low albedo and absence of vegetation, from which one flow exhibits the youngest age of the sequence, 610 ± 190 yr (AF13-349).

Table 3.2: *^{36}Cl CRE age of the Lava flows. Cl and ^{36}Cl concentrations were determined from the AMS measurements. Age uncertainties (1σ) includes both production and analytical errors. Numbers in parenthesis correspond to analytical errors only.*

Sample Name	Sample Weight (g)	Mass of Cl in spike (mg)	^{35}Cl/^{37}Cl	^{36}Cl/^{35}Cl (10^{-15})	Cl in Sample (ppm)	^{36}Cl (10^3 atoms g^{-1})	^{36}Cl CRE age (yr.)	^{36}Cl CRE age (yr.) from CREP
AF13-341	89.09	2.018	4.24 ± 1.78	5.73 ± 1.30	80.1 ± 5.8	7.6 ± 1.97	1200 ± 350 (330)	1250±360 (340)
AF 13-345	92.32	2.018	4.26 ± 1.64	3.95 ± 0.71	75.9 ± 5.1	4.758 ± 1.05	840 ± 210 (190)	810±210 (190)

AF13-348	87.72	2.021	8.81 ± 1.7	14.83 ± 1.83	12.9 ± 0.5	8.186 ± 1.15	1900 ± 330 (290)	2100±360 (300)
AF13-349	70.78	2.030	4.58 ± 1.64	2.95 ± 0.68	76.5 ± 4.4	3.524 ± 1.1	610 ± 200 (190)	620±220 (210)
AF13-351	98.05	2.019	11.77 ± 2.4	437.12 ± 24.70	6.4 ± 0.4	207.4±11.9	72400 ± 9400 (6400)	53900±6500 (3300)
AF 18-01	90.13	2.052	4.38 ± 2.11	3.87 ± 1.04	70.9 ± 5.6	4.43 ± 1.45	730 ± 250 (240)	710±270 (260)
AF18-02	93.13	1.992	4.25 ± 2.42	3.59 ± 0.93	74.6 ± 7.2	4.161 ± 1.34	700 ± 240 (230)	600±220 (210)
AF18-03	91.34	2.013	4.10 ± 1.67	5.21 ± 0.87	89.4 ± 6.7	7.418 ± 1.46	1200 ± 270 (240)	1200±270 (240)
AF23-29	90.9	1.992	4.70 ± 3.88	4.86 ± 0.79	54.7 ± 6.7	4.993 ± 0.98	910 ± 200 (190)	910±210 (190)
AF23-97	85.9	2.006	10.56± 3.9	477.90 ± 22.00	10.8± 0.8	268.7± 13.2	73500 ± 9400 (6400)	66400±7700 (3500)
B1	_	2.005	27.64 ± 2.3	1.84 ± 0.62	-	-	-	

3.4.2 Field observations, geological Map and associated volcanic history

Using a combination of remote sensing techniques (see section 3.3) and field work, we constructed a very detailed high-resolution map of lava flows from the Gumat Mali magmatic sub-segment, central Afar (Figure 3.3). We conducted highly detailed volcanological investigations on the most recent volcanic events and products along the axis of the segment by combining high-resolution DEM and satellite images with field observations. Various fissural lava flows have been distinguished and classified into 4 distinct episodes according to their apparent relative chronology, in good coherence with our new ^{36}Cl exposure ages (see previous section). Some additional volcanic features (calderas, craters, scoria cones and eruptive fissures) which represent key criteria for identifying emission centres and associated processes along the segment (Figure 3.5) have also been mapped. We identified that fissure-style eruptions are generally typical of the last rifting episode that affected the segment, even though explosive eruptive styles have been associated to its early activity, as well as some periodic outflows from a non-persistent lava lake.

Underlying volcanic episodes have also been mapped, yet precise identification of individual lava flows is less easy for such older volcanic products. Those flows contrast significantly with the historical ones in being generally thicker, and with a wide lateral extension, representing therefore significantly bigger volumes of magma erupted (Figure 3.3 and Figure 3.4). For those older products, we focused our mapping investigation in trying to discriminate the extension and boundaries of the different types of magmas that have been described previously in the literature for this segment, i.e. incompatible trace elements depleted magmas vs enriched ones (Barrat et al., 2003). This was done using geochemical data from selected samples (see section 4.3), along with remote sensing techniques and field work.

Below is described the detailed sequence of events that affected the Gumat Mali sub-segment starting from the oldest outcropping volcanic episodes.

3.4.2.1 Oldest Volcanic Products

The oldest volcanic products along the axis of the studied magmatic sub-segment are represented by very thick and extensive lava flows. The thickness of those flows is observable along west-dipping faults that run parallel to the sub-segment axis and can reach 15-20 meters (Figure 3.4 and 3.7F), as well as on the narrow graben which outcrop on its western part (Figure 3.4). These basalts appear mostly massive with limited elongated vesicular beds accumulated in-between the various horizontal discontinuities and associated to metric to decametric tumuli-like internal architecture, typical of pahoehoe flow type. These lavas appear dark gray to black in colour and aphyric in texture with fine-grained crystals in the matrix. Those flows cover entirely the segment and can be subdivided into two distinct categories according to their geochemical characteristics, i.e., with depleted or enriched incompatible trace elements compositions (see section 4.3).

The oldest basaltic lava flows that can be observed on the Gumat Mali segment are scarcely outcropping on its southern termination (Figure 3.3), where they overlap horizontally the sediment plain. This basaltic formation exhibits enriched compositions and can be as old as few hundred kyr. This formation is covered by more recent lava flows of depleted geochemical composition, which outcrop extensively on the central part of the segment (Figure 3.3). In its northern and eastern occurrence, this depleted volcanic sequence is covered by a partially indurated clay layer that can reach few tens of centimetres, and which suggests a potentially old age and long residence at the surface in a depressional environment. At the axis of the sub-segment, this lava layer outcrops below the most recent historical volcanic products and can be observable on the walls of the main crater and lip cone (Figure 3.5 A, B). Those lava units completely resurfaced the southernmost part of the segment (Figure 3.3) with well-expressed lava flow fronts, without being covered by any subsequent volcanic or sedimentary products in those places. The two samples of this formation taken for cosmogenic dating exhibit ages of 72400 ± 6400 yr (AF13-351, Figure 3.7G) and 73500 ± 6400 yr (AF23-97). Those ages are significantly younger than one published K/Ar age of this same formation, 219 ± 52 kyr (Lahitte, Gillot, Kidane, et al., 2003) and, despite their mutual consistency, could have been affected by underestimated surface dismantlement (15 cm taken into consideration for our age calculations), or any potential unobserved sediment cover during their exposure history (less probable).

Finally, this formation has been covered on its western and northern edge by younger volcanics that continue to exhibit the same type of thick and extended pahoehoe flows, but which exhibit

different geochemical signature, with more enriched or less pronounced depleted character (see section 4.3). The age of those volcanics is not known, but their surface appearance and the field relationships with the previous depleted formation (Figure 3.3) suggest that they could date several tens of kyr or more.

3.4.2.2 Recent Historical Volcanic Products

Some primary volcanic features of the recent historical activity of the Gumat Mali segment include recent lava flows as well as some very well-preserved eruptive fissures, craters, pyroclastic cones/rings, and spatter accumulations, aligned along the main axis (Figure 3.5). The segment is elongated in a NW-SE direction, with a large main crater, named Teleke Loma (Figure 3.5A), situated slightly towards the south-eastern part of the segment axis, according to the total extension of recent flows (Figure 3.3). This crater has an elliptical shape, measuring approximately 1.4 km in length and 1.1 km in width. The crater's walls are steep and well-defined, contributing to its distinct morphology within the rift segment. On its edges stands an approximately 25 m thick pyroclastic tuff deposit (Figure 3.6). It is emplaced on top of a massive thick pahoehoe lava flow belonging to the depleted formation. At the base, the sequence starts by a thick (12-15 m) moderately indurated layer displaying numerous undulating and poorly sorted beds mainly composed of lapilli and blocks, predominantly dense lithics in nature, and corresponding to deposits of dilute pyroclastic density currents typical of a phreatomagmatic phase. Following this, a 2-3 m thick, crudely stratified and poorly sorted non-indurated tuff layer is observed. It is made of alternating beds of lapilli (scoriaceous mafic juveniles and dense lithics) and coarse ash, with clast-supported beds of lapilli and blocks (mainly dense lithics), corresponding to less energetic pyroclastic density currents, potentially still related to the phreatomagmatic phase. This phreatomagmatic sequence is followed by a well-sorted, clast-supported, 50-70 cm thick bed, predominantly composed of scoriaceous blocks, interspersed with dense lithic blocks (10-15%), typically corresponding to strombolian-type fall deposits. Above the pyroclastic sequence, a 2-4 m thick massive matrix-supported unit emerges. It is made of angular dense lithic (30-50%) lapilli and blocks (up to 1-2 m diameter) embedded within a non-sorted yellowish matrix of weathered ash and lapilli. This massive brownish unit is covering extensively the central part of the segment over 2-3 km distance from the main crater and is topped in multiple places by fields of free ballistic blocks, decreasing in size with distance to crater, and often partially draped by more recent thin lava flows close to the crater. This massive unit and the associated blocks fields witness a major and extremely energetic event, most probably linked to the catastrophic formation and collapse of the main

crater, following the phreatomagmatic phase and the potentially associated weakening of the segment axis shallow structure. The age of this singular event, that starts the recent historical volcanic phase, can be assessed by a CRE dating we performed on top of one of the biggest blocks, which gives 1900 ± 290 yr (~ 1.5 m high, AF13-348, Figure 3.7D).

The floor of the main crater is relatively flat, and is made by an undulated frozen lava flow, suggesting the existence of a paleo-lava lake inside the depression. On this line, there exists evidence that some lavas overflowed the crater's edges, draping over the steep walls, and spilling onto the surrounding volcanic succession. These overflows have left behind on the exterior slopes a layered formation composed by 10-12 centimetric to decimetric thin individual flows (Figure 3.6), suggesting that the activity of the paleo-lake persisted for some time after the crater's creation. Some smaller craters are present northward and southward of the main crater. They display identical floor and laterally preserved paleo-lake levels features indicating periodic activities (Figure 3.5 E and F). Associated to a major lip-cone on its southern termination, this string of craters defines a consistent system over a length of 4 - 5 km in the middle of the segment from where a large part of the recent volcanics originated. Thin lavas are limited to the axis of the segment and remain close to the fissural system, with minimal lateral spread, being bounded by the slight axial depressional topography. They draped over existing block fields, pyroclastic explosive deposits, and fault scarps (Figure 3.5, 3.7C and D), highlighting the very fluid nature of the magma and its interaction with the surrounding landscape. Two of those thin axial lava surfaces have been dated by ^{36}Cl exposure ages at 840 ± 190 yr (AF13-345) and 700 ± 230 yr (AF18-02). However, when the volume of erupted material is substantial, some thicker lava flows (2-3 meters, Figure 3.5 F) tend to overflow laterally, spreading outside the rift axis. While the predominant flow direction reflects a general perpendicular orientation, some of these lava units flowed northward and southward, parallel to the segment axis guided by rift related small depressional topographies (Figure 3.3), or by the deeper depression at the northern end of the segment. Those large flows have been dated at 1200 ± 330 yr (AF13-341), 1200 ± 240 yr (AF18-03), 910 ± 190 yr (AF23-29), 730 ± 240 yr (AF18-01) and 610 ± 190 yr (AF13-349), in relatively good agreement with their relative chronologies (Figure 3.3). Field examination of those lava surfaces show that the morphology varies from smooth to ropey texture, associated to pahohoe-type lava flows. The lava samples exhibit a predominantly dark gray to black color. Most of the samples are aphyric with fine-grained micro-crystals in the matrix. Only one sample (AF13-341) is slightly porphyritic with small euhedral phenocrysts of plagioclase and olivine scattered throughout the sample.

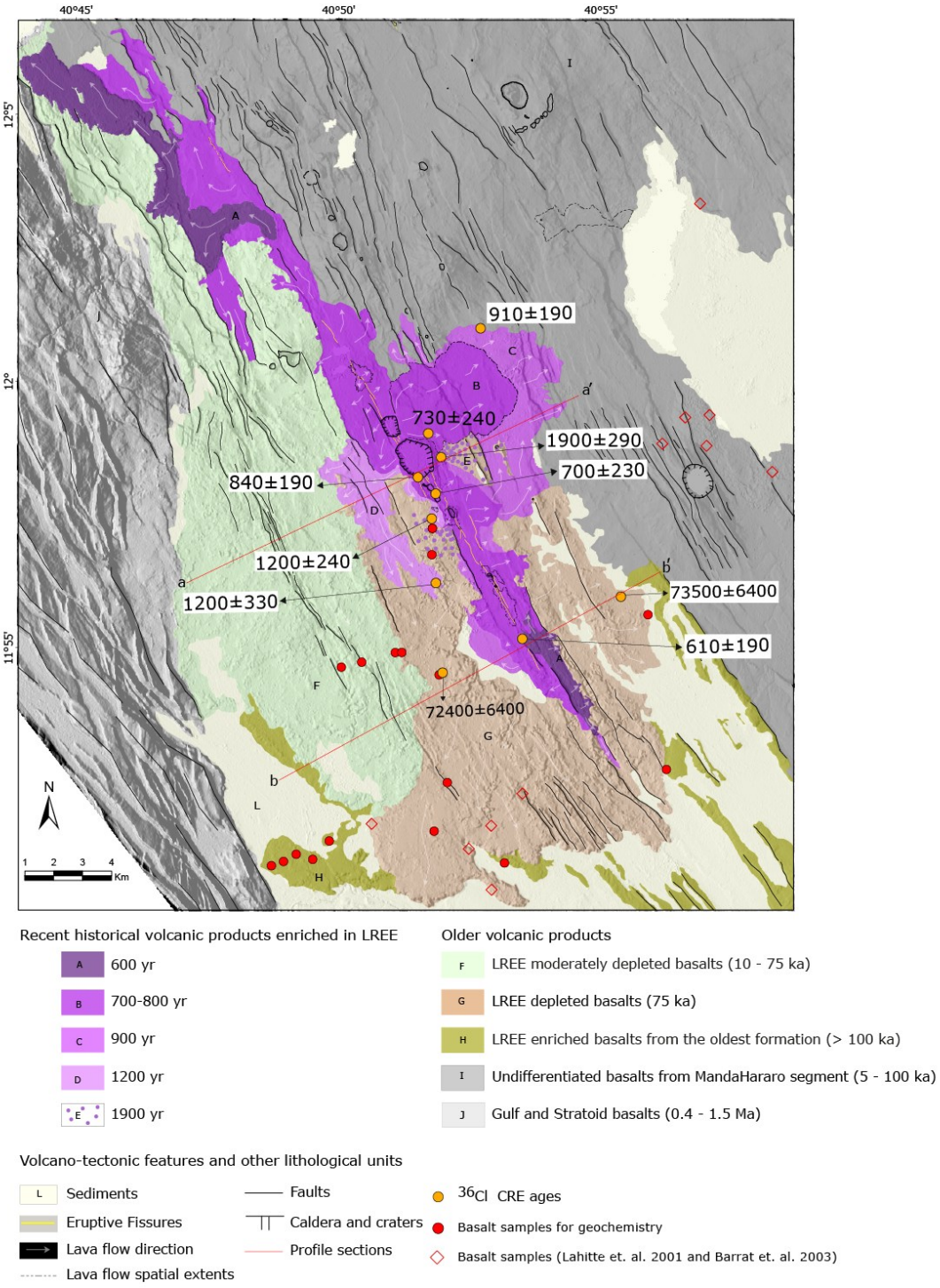

Figure 3.3: *Detailed map of Gumat Mali magmatic sub-segment showing the spatial extent of the various lava series distinguished based on 36Cl CRE ages and lava geochemistry.*

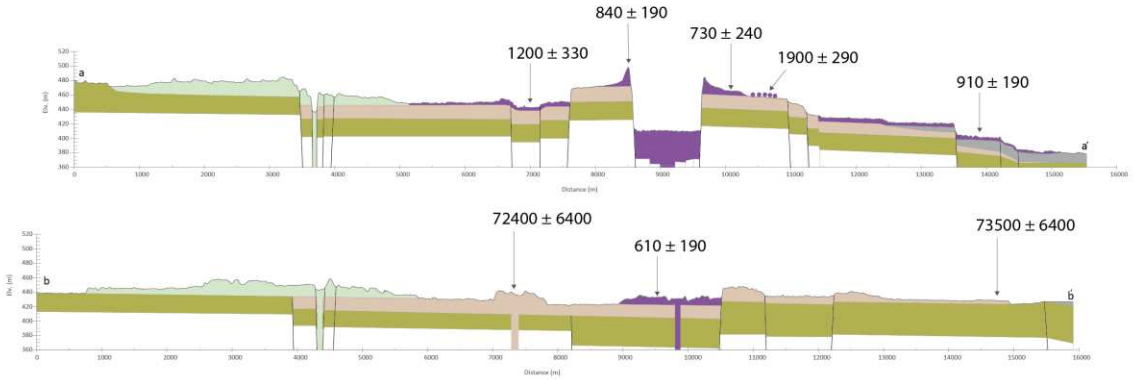

Figure 3.4: *Schematic cross sections illustrating the topographic influence of the fissural eruptions on the rift morphology. Legend is the same as in Figure 3.3.*

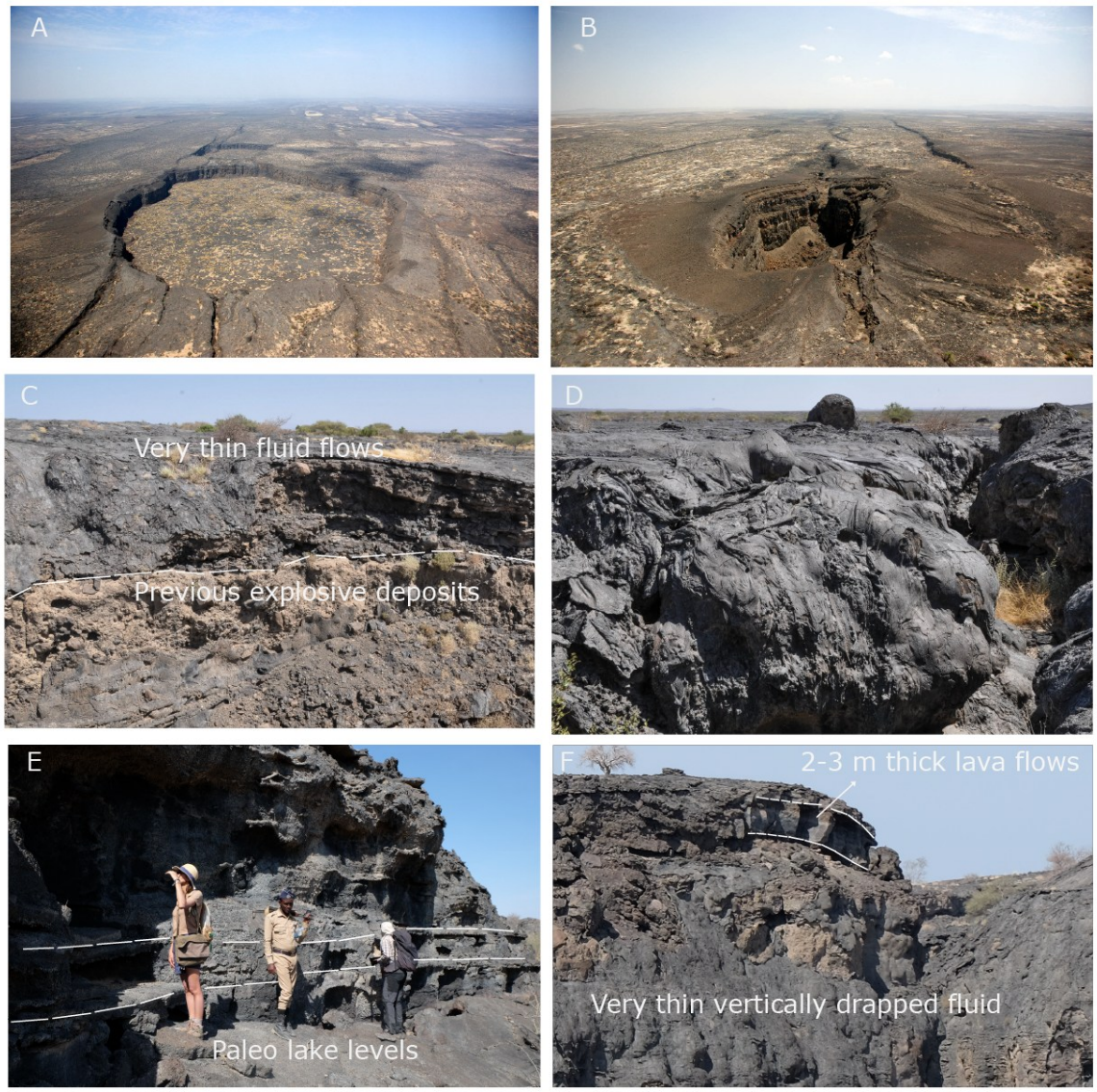

Figure 3.5: *Field photograph of the volcanological features and associated lava flow fields. (A) a frozen lava lake at the main crater, indicative of potential mid-segment magma reservoir. (B) Main cone on the eruptive fissure. (C) Volcanic stratigraphy exposed along the fissure. Succession of thin lava flows due to lava lake overflow draped on the paleo-succession (pyroclastic deposits) of the previous explosive event. (D) Fissure and associated thin and very fluid lava flows. (E) The paleo lava lake levels and cross-beddings accompanied by piles of fluid flows, show prolonged periods of lava retention on the surface. (F) volcanic stratigraphy exposed at the wall of the small crater. Very thin fluid flows draped vertically over the entire secessions and 2-3 m thick young lava flow succeeded by pyroclastic deposits.*

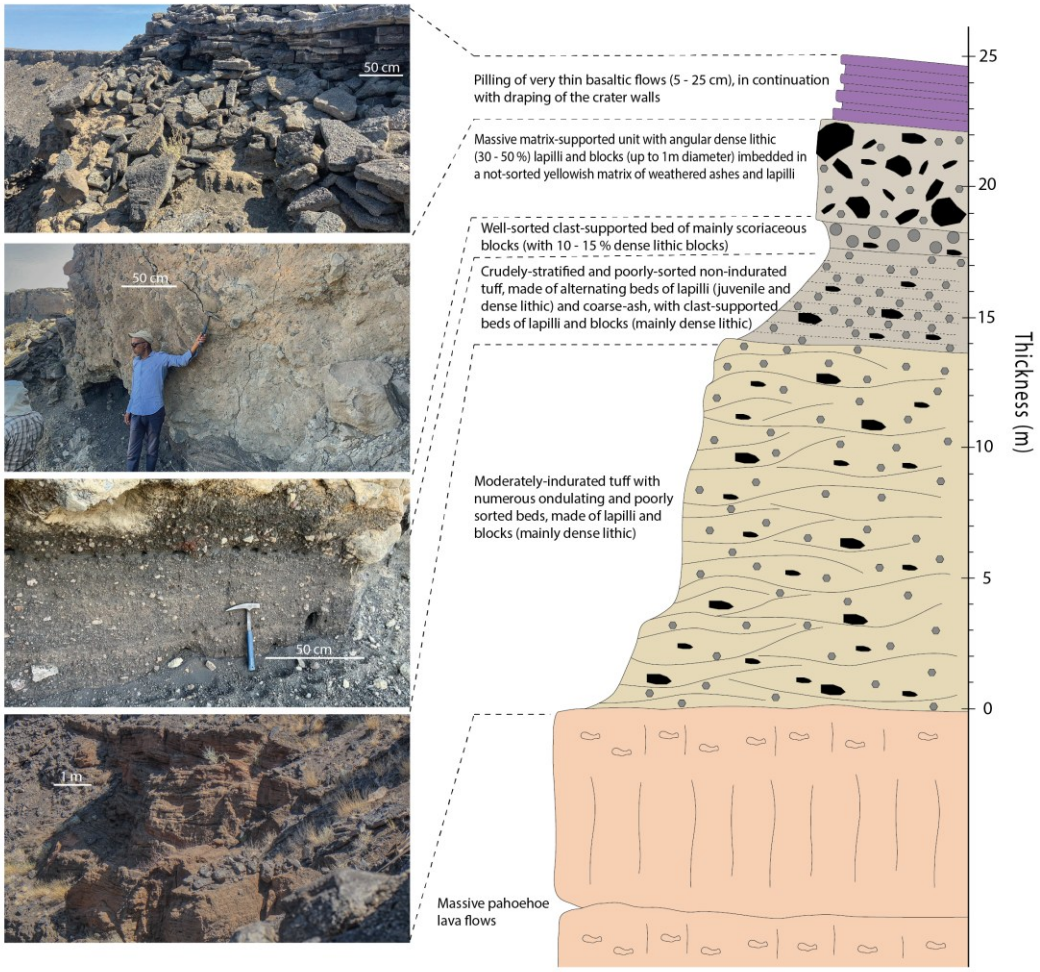

Figure 3.6: *Field photos (right) and carton (left) shows the volcanic stratigraphy constructed at the main crater (Teleke Loma).*



Figure 3.7: *Location, photographs and 36Cl CRE ages of the various lava flow fields. (A, B, C, E) Very thin lava flows sourced from caldera and fissures and linked to the effusive episodes. (D) Basalts from the block field exposed due to the collapse of the main crater during the explosive episode. (F) Field photo showcasing the older volcanics and the most recent historical activity. In the foreground, a series of very recent thin lava flows dominates the landscape indicating more recent volcanic activity. in the background, an old and extensive lava flows are visible, displaying evidence of faulting along its*

surface. (G) Lava flow fronts of the LREE depleted basalts resurfacing the southernmost part of the sub-segment.

3.4.3 Lava geochemistry

All basaltic samples from the Gumat Mali magmatic sub-segment are classified as sub-alkaline basalts in the Total Alkali-Silica (TAS) diagram (Figure 3.8).

The various lava series distinguished on Figure 3.3 have been identified according to their geochemical features, mainly according to their enriched-depleted character relative to Light Rare Earth Elements (LREE) and other incompatible major and trace elements, as has already been proposed by Barrat et al. (2003). This discrimination of distinct lava groups is valid for a given range of differentiation associated with relatively high and primitive MgO content (8-10 wt %), and for which the observed differences must be related to source control rather than to fractional crystallisation processes. Three enriched groups with relatively elevated concentrations (La, Zr, P_2O_5, TiO_2, Figure 3.9 and 3.10) are identified, one at the base of the observed sequence (>100 ka lavas) and the other two at the top, including the most recent fissural episode (0.6-1.2 ka) and a probably older series (10-75 ka). The group with the most depleted character (lowest La, Zr, P_2O_5, TiO_2, concentrations on Figure 3.9 and 3.10) is composed of lavas emplaced in the sequence after the lower-most LREE enriched group, at about 75 ka. It is followed in the western part of the segment by a series of lavas exhibiting intermediate features and moderately depleted characteristics, emplaced after 75 ka. Note that some of the blocks sampled in the periphery of the axial main crater display either intermediate or enriched compositions in agreement with their origin from the shallowest underlying lava pile.

Basalts from the last effusive eruptions exhibit the highest degree of differentiation, with MgO contents ranging from 5.36 to 6.13 wt.%, and consonant associated low Ni (≤53 ppm) and Cr (≤70 ppm) concentrations (Figure 3.10; Figure S3.1; Table S3.1 in supplementary materials). The differentiation stage we observed for this group of basalts is comparable to the one previously described for basalts laterally erupted in the Manda Hararo segment (Lahitte et al., 2001; Barrat et al., 2003), for the off-axis Dabbahu volcano lavas (Medynski et al., 2013), as well as to the Dabbahu axis lavas erupted more recently than 7 ka, including the ones of the 2005-2010 volcano-tectonic crisis (Ferguson et al., 2010; Medynski et al., 2015). In contrast, the older, thick and extensive pahoehoe lava flows emplaced in the Gumat Mali sub-segment display significantly higher MgO content (7.26-10.07 wt.%) indicating a lower degree of

differentiation, comparable to most of the lavas described at the axis of the Dabbahu segment for the 20-40 ka period (axis sensu stricto and Durie volcanism, Medynski et al., 2015).

This relatively restricted and primitive MgO range for the older enriched and depleted groups, between 7.5 and 10 wt. %, does not allow to highlight potential differentiation process other than probable olivine control until that stage. The most recent fissural episode exhibits however more evolved basaltic compositions which contrast in composition with equivalent MgO content of lateral literature data from the Manda Hararo sub-segment (Barrat et al., 2003). Indeed, the Manda Hararo data exhibits typical Fe-Ti and P enrichments associated with classical triangular shaped differentiation trends controlled first by fractionation of clinopyroxene + plagioclase feldspar ± olivine and then by additional fractionation of Fe-Ti oxides (starting at ~ 5.5 wt. % MgO) and apatite (starting at ~ 4 wt.% MgO). For both TiO_2 and P_2O_5, the composition of the recent fissural episode is describing some evolution trends that are cross cutting those typical fractionation trends and are indicative of mixing and hybridisation between basaltic and more evolved liquids in the crustal plumbing system, as it has already been proposed for some of the Dabbahu volcano data (Figure 3.9, Field et al., 2012; Medynski et al., 2013). The behaviour of Al_2O_3 is a bit more complex to interpret and certainly requires additional assimilation of plagioclase associated with the mixing and hybridisation of those magmas (Figure 3.9), as has also been proposed for the Erta Ale range volcanics (J. Pin et al., 2024). Moreover, the range of variation of the La/Sm and Sm/Yb ratios recorded during this last fissural episode is significantly larger than what is expected for a simple clinopyroxene fractional control (Figure 3.10). This observation suggests that mixing between not only two magmas at different stages of differentiation, but also between two different types of magmas, i.e., one more depleted than the other.

The LREE depleted group (and to a lesser extent the intermediate one) exhibits also some distinct and unusual characteristics for magmas with such primitive compositions. They are indeed characterized by very low and off-trend concentrations of the compatible trace element Cr (Figure 3.10), as well as elevated Al_2O_3 (Figure 3.9), compared to the enriched groups. Such features can be hardly related to fractional crystallisation or accumulation processes at that stage of differentiation and have already been related by Barrat et al. (2003) to a specific source composition. The compositional spectrum of this depleted group is also associated to a specific positive Sr anomaly on Figure 3.11, which translates as >> 1 Sr* ratios on Figure 3.10, associated with a slight positive Eu one. This typical pattern, also characterized by prominent positive Ba and negative K anomalies, has been classified by Rooney (2020b) in his synthesis

of EAR magmas as type VI. For comparison, the enriched groups of the Gumat Mali sub-segment typically correspond to the type III of this classification, with more enriched patterns, but similar prominent Ba and K anomalies.

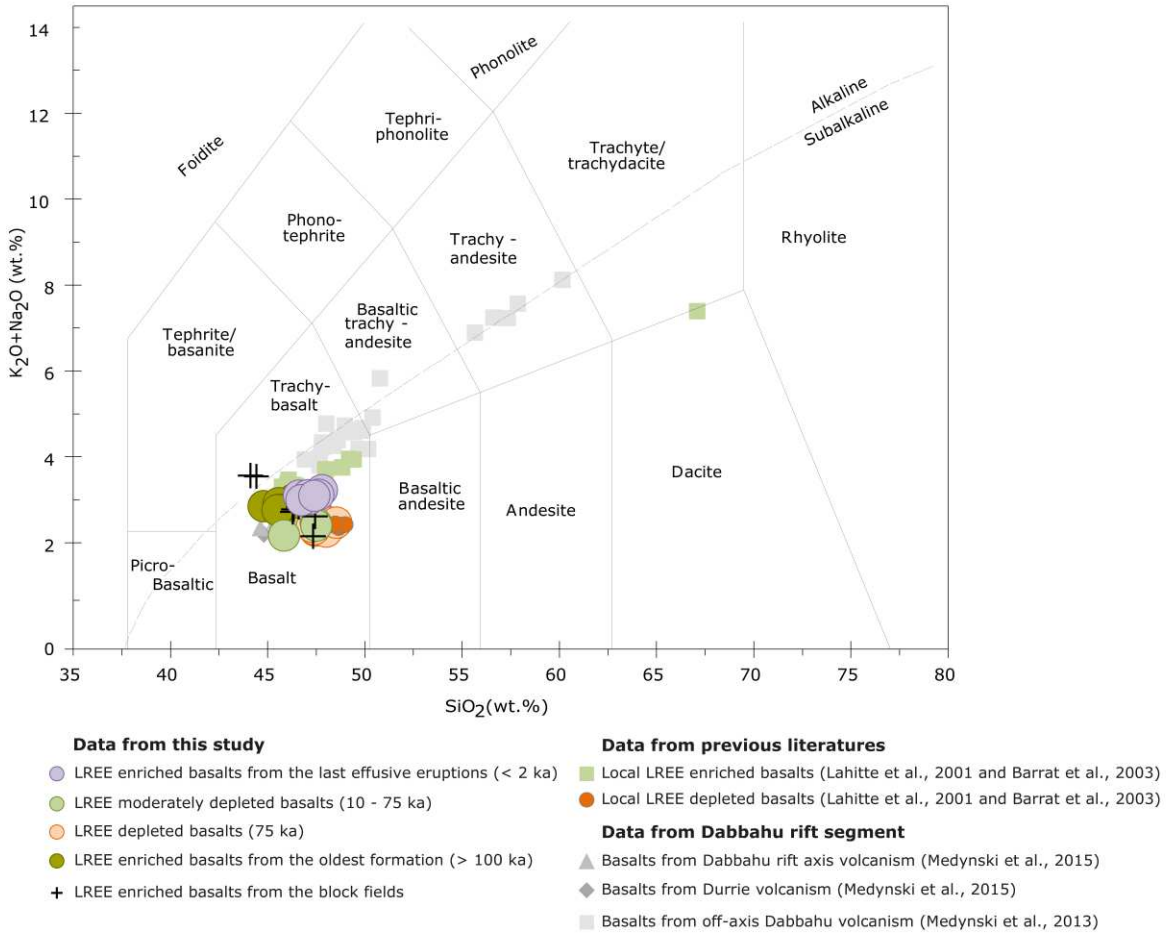

Figure 3.8: *Total Alkali–Silica (TAS) diagrams. Nomenclature of volcanic rocks after Le Bas et al. (1986). Discrimination line between the alkaline and subalkaline group is after Irvine and Barragar (1971).*

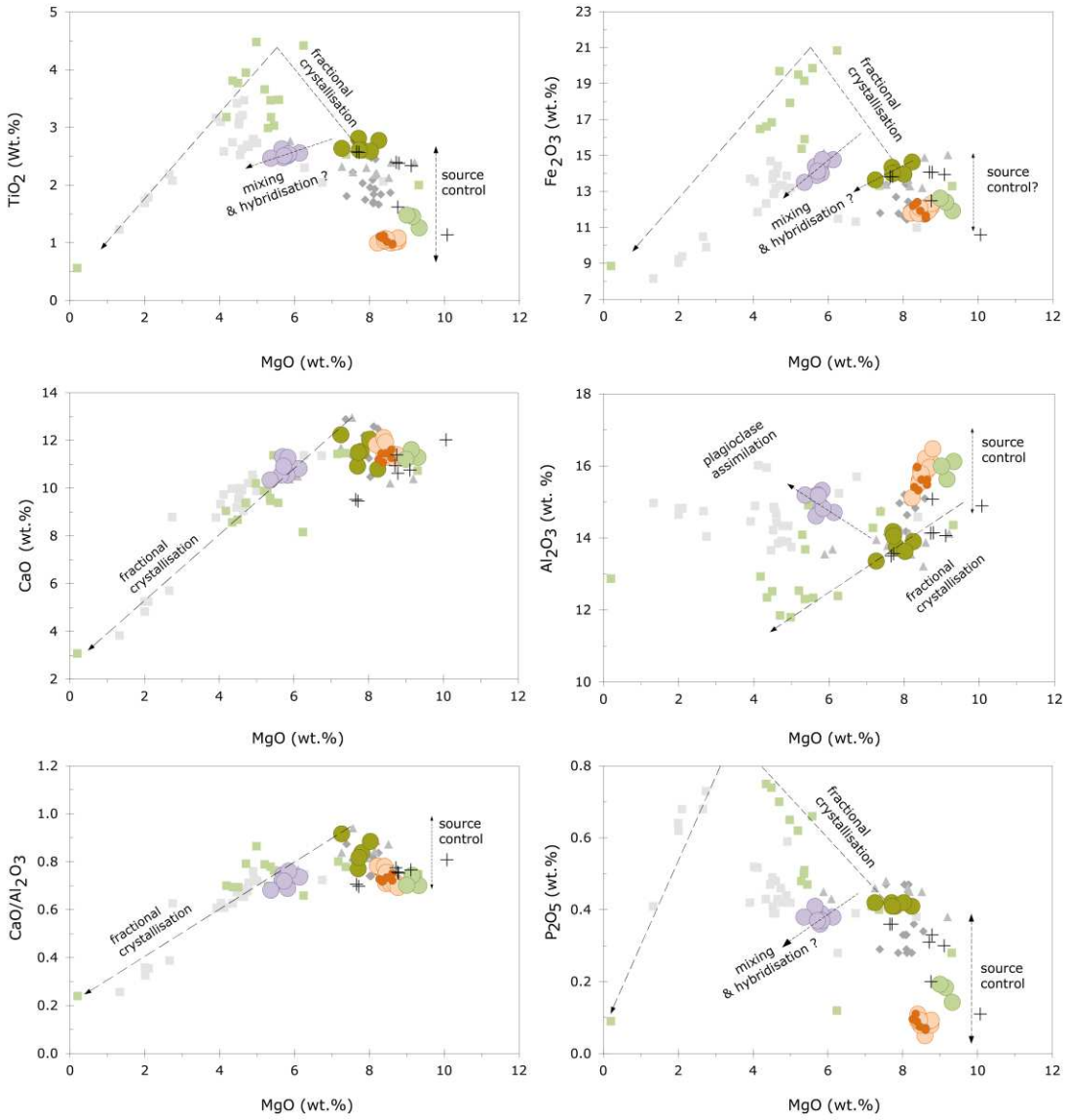

Figure 3.9: *A major element Harker diagrams show variations in major oxides of erupted lavas. The legend is the same as for figure 3.8.*

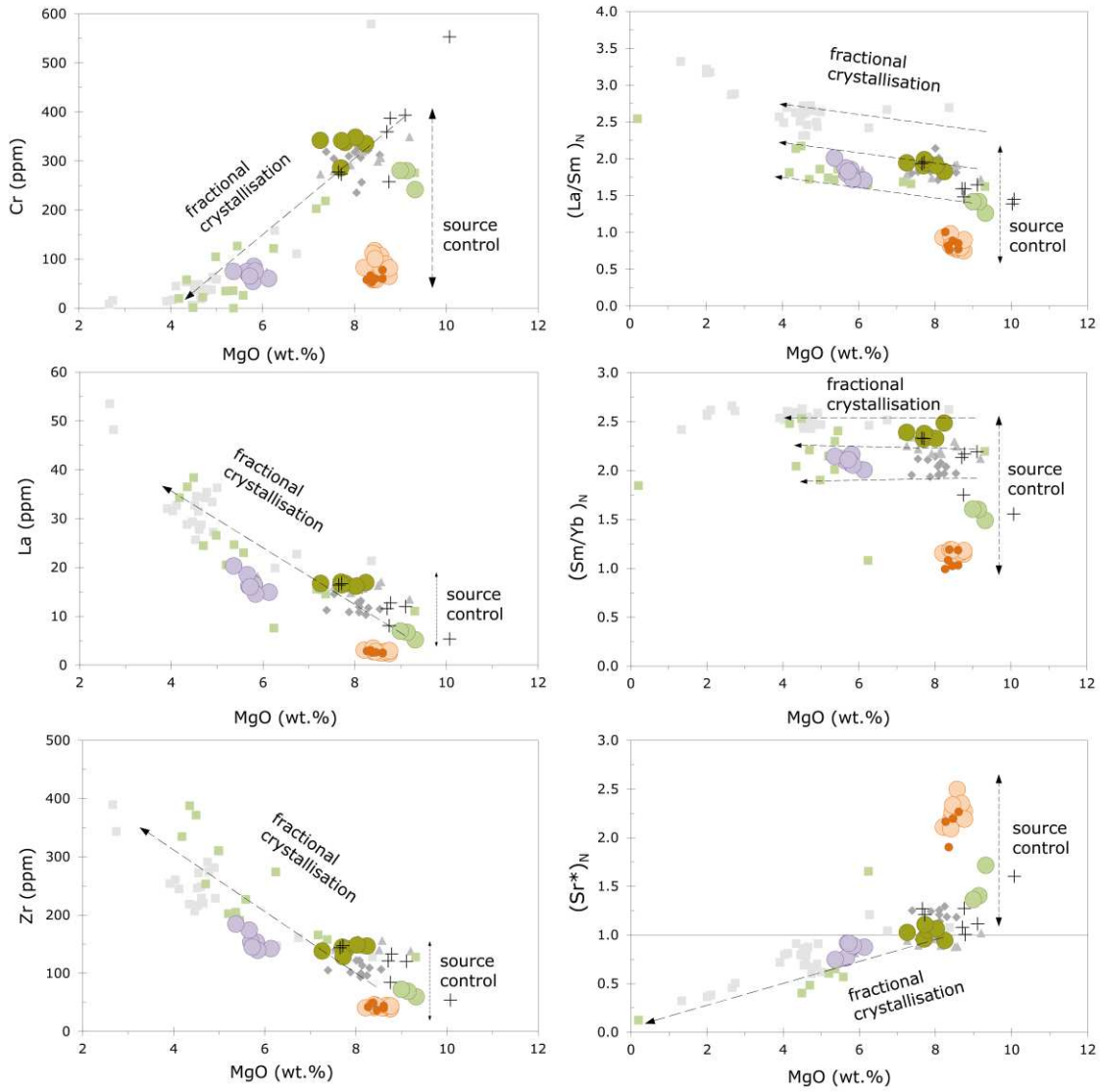

Figure 3.10: *Variations in trace elements between the erupted lavas. The Sr anomaly is calculated as Sr* = Sr/((Pr+Nd)/2) after normalisation to primitive mantle (Sun and McDonough, 1989). The legend is the same as for figure 3.8.*

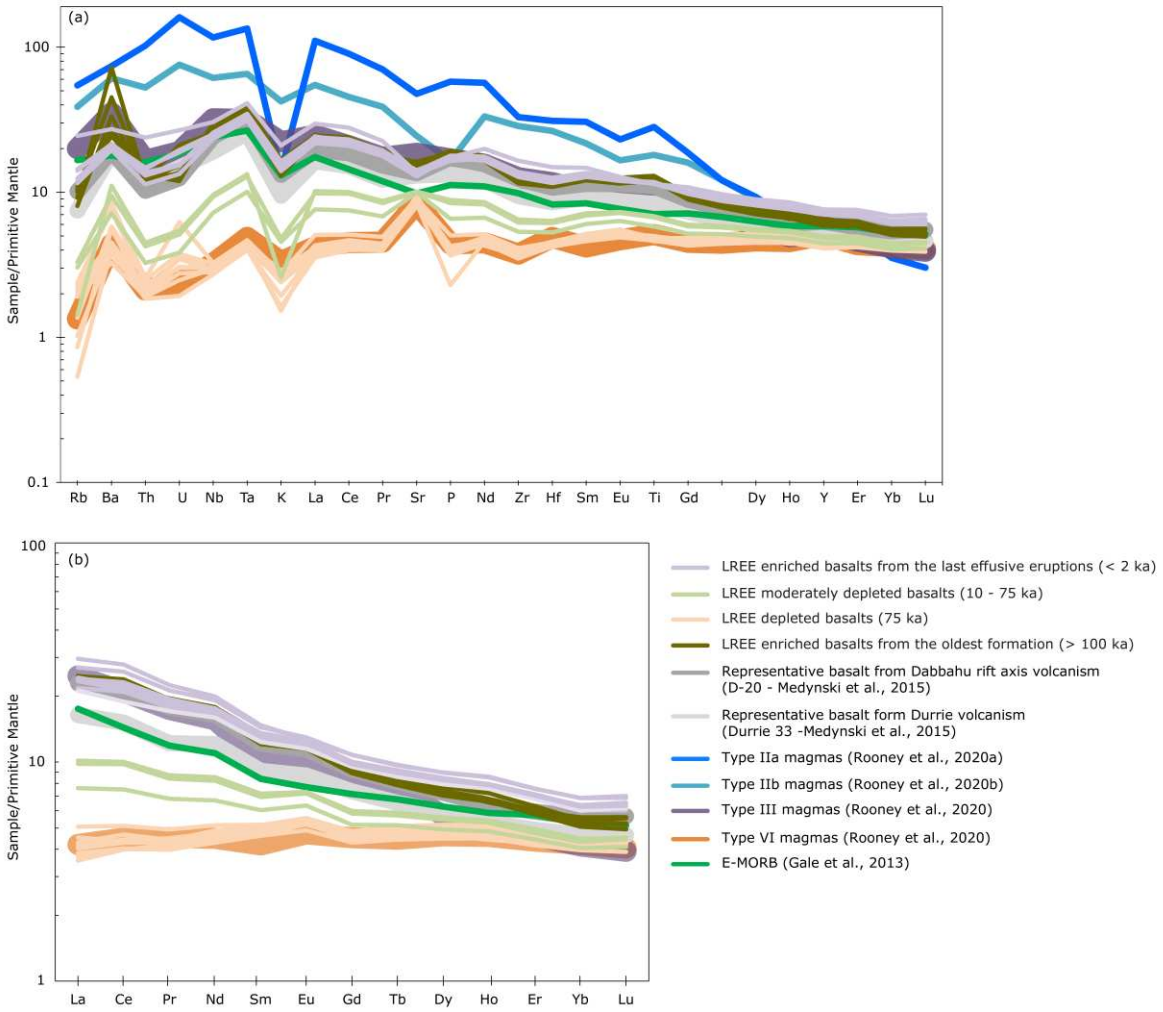

Figure 3.11: *(a) multi-element variation diagram normalized to primitive mantle (Sun and McDonough, 1989). Three lava groups are enriched in incompatible elements: The most recent fissural episode (0.6-1.2 ka, light purple), an older lava series (10-75 ka, bright blue), and the oldest lava series (>100 ka, dark green). In contrast, one lava group dated at about 75 ka is depleted in incompatible trace elements (light orange). This group is followed by a subsequent lava series showing intermediate features with moderate LREE depletion emplaced after 75 ka (light green). (b) Rare Earth Element (REE) patterns of the lava series, normalized to primitive mantle (Sun and McDonough, 1989).*

3.5 Discussion

3.5.1 Nature of the mantle source components

The Gumat Mali sub-segment of Central Afar exhibits two geochemically distinct and contrasted types of magmas emplaced at its axis since a couple of hundred thousand years. Those magma types have already been recognized by Barrat et al.(2003) in this sub-segment. The distinguished lava series are dominantly enriched in LREE. However, some LREE depleted lavas are also found that share similar geochemical characters with some magma types within the Oligocene Ethiopian Plateau basalt (Pik et al., 1999), some basalts within the old stratoid formation from Afar (Alene et al., 2017; Rooney et al., 2023), and some recent Basalts from Djiboutian Afar (Daoud et al., 2010). Despite their strongly contrasted enriched or depleted character, those magma types share similar Ba and Ta peaks on multi-element diagrams (Figure 3.11) compared to the neighbour's elements (Rb, Th, U), which appear as troughs in the pattern, with a notable difference for the depleted type which additionally exhibits positive Sr and Eu anomalies.

Barrat et al. (2003) interpreted independently those characteristics for the two magma types. They attributed the high Ta/Th and Ba/Th (see figure 14B for this study dataset) of the enriched magmas to interactions of mantle-plume originated magmas with hydrothermally altered gabbroic cumulates in the crust, mainly based on correlations with $\delta^{18}O$ isotopic compositions, as previously interpreted for Djiboutian basalts (Barrat et al., 1990, 1993). There is however a point that calls into question the secondary derived character of the Ba peak, which relates to the fact that this hypothesis would be valid for some very common Afar/MER enriched magmas which share the same patterns (Manda Hararo, Djibouti and MER, see compilation of geochemical signature in Rooney, 2017), and not for others which do not exhibit this typical Ba peak (i.e. Erta Ale range) but are also exhibiting $d^{18}O$ evidence of interactions with altered gabbros (Barrat et al., 1998). For the depleted basalts they discarded the potentiality of a MORB source based on Sr and Nd isotopic characteristics, and concluded that the combination of Ba, Sr, and Eu peaks must be related to sources/processes involving the presence of plagioclase. They favoured a genuine origin of those geochemical characteristics, relating it to a mantle-plume source containing gabbroic recycled oceanic lithosphere as it has previously been argued for the Icelandic tholeiites (Chauvel and Hemond, 2000; Skovgaard et al., 2001).

On figure 3.12, we test the alternative possibility that the enriched and depleted characters, some common trace element characteristics (Ba-Ta peak, Rb-Th-U troughs) and some differences (Sr and Eu positive anomalies for the depleted magma) of those Gumat Mali

magmas could result from a single contamination process of LREE-enriched magmas vertically percolating a transcrustal reservoirs system (Annen et al., 2006; Boulanger & France, 2023; Cashman et al., 2017; J. Pin et al., 2024; Tortelli et al., 2024) containing gabbroic cumulates. During porous percolation flow, such a process must be fundamentally based on significant plagioclase assimilation to account for the Sr and Eu anomalies, but also must include important pyroxene assimilation to account for the mid to heavy REE concentrations and patterns. We implemented a mass balance mixing model following Depaolo (1981), in which the melt assimilates a cumulate assemblage composed of clinopyroxene, plagioclase, and olivine (see table Table S3.3 for trace element compositions). We present on Figure 3.12 the most optimised model (30% Pl + 65 % CPX + 5 % Ol) which globally aims to account for the trace element patterns of the LREE depleted group by simulating final interaction between 15% initial melt and 85% of this cumulate assemblage. The approach enabled us to assess that assimilation processes can account for the signatures of several incompatible elements (e.g., Ba, Th, Sr, Pr, Eu, and Nd) observed in the depleted group (Table S3.4, Figure 3.12). However, it fails to reproduce the patterns for most heavy rare earth elements (HREE) and compatible elements such as Cr. Also, whereas one could have anticipated that assimilating enough plagioclase to reproduce the positive Sr and Eu anomalies would raise significantly the Al_2O_3 content of the final magma (i.e. Barrat et al., 2003), the actual result with those proportions is opposite and exhibits a final composition of 12,5 % of Al2O3, significantly lower than the targeted depleted group composition (~ 16 %, Figure 3.9). Furthermore, the required proportion of assimilated mush (85%) is geologically not realistic, particularly for porous flow or reactive melt percolation processes in mush.

All this strongly suggests that mantle source heterogeneities may play a significant role over such potential crustal assimilation processes to account for the geochemical characteristics of the depleted and enriched magma types of central Afar. In this view, Rooney (2020) and Rooney et al. (2023) interpreted the very common enriched magmas exhibiting a pronounced Ba peak (i.e. formally type III magmas) as originating in the sublithospheric mantle from a mixture of mantle-plume material and local ambient mantle. They oppose them with those that do not show such a Ba anomaly (i.e. formally type II magmas, including Erta Ale's ones) and are characterized by other geochemical features suggesting an origin from destabilisation of metasoms recently emplaced in the lithospheric mantle. Recently Wong et al. (2022) compared the geochemical characteristics of some MER and some of those enriched Central Afar type III basalts (i.e. Dabbahu segment) using an inversion model of REE and mantle potential

temperature. They concluded that part of the differences between the two locations could be related to distinct depth of Lithosphere-Asthenosphere Boundary (LAB) and to the presence of more enriched and fusible lithologies in the upwelling mantle beneath Afar, which again questions the nature of the local mantle sources.

Our detailed spatio-temporal investigation of the Gumat Mali segment, in addition to previous ones (Lahitte et al., 2001; Barrat et al., 2003; Ferguson et al., 2013; Medynski et al., 2013, 2015, 2016), confirms the dominance of such enriched type III magmas, the absence of type II magmas, and the scarce occurrence of depleted magmas (i.e. formally type VI of Rooney, 2020d) in the current Central Afar active magmatic segments (Dabbahu, Gumat Mali and Manda Hararo, Figure 3.13B). The new geochemical dataset we provide exhibits a continuous compositional trend for REE and other trace elements ratios, capturing intermediate moderately depleted magmas spread out between enriched and depleted endmembers (Figure 3.13A). Those new data represent an ideal context for identifying and interpreting mantle sources melting, with a succession of basalts emplaced on the same magmatic segment over a rather limited period (< 300 kyrs) and then generated in the framework of stable and common geodynamic conditions. The first order important information delivered by such a continuous compositional trend relates to the interrelated genetic link between the depleted and enriched compositional endmembers, which appear involved in a common melting process sampling them in varying proportions. On figure 3.14A we show a model implicating two distinct enriched (Primitive mantle, Sun and McDonough, 1989) and depleted mantle compositions, melting with identical conditions of mantle mineralogy (28 % of a garnet lherzolite + 72 % of spinel lherzolite, see caption for details), and for which the Gumat Mali compositional trend spread-out along a mixing line joining their 4 % fractional step of melting. Such a model, which is based on a simple standard lherzolitic composition, is only indicative of how those two mantle endmembers could be related in a same coherent melting process. It is beyond the scope of this study to explore in detail the potential mineralogical controls and invert them for precising major external forcing parameters (LAB, mantle potential temperature, …). However, those REE ratios and melting conditions in the field of garnet stability agree with previous investigations and interpretations in Central Afar of deep and hot mantle melting (Ferguson et al., 2013; Medynski et al., 2013, 2015) with a LAB at about 50 – 70 km and a potential mantle temperature of 1500-1560 °C (Wong et al., 2022).

The nature of those mantle components can further be constrained when considering and acknowledging other trace elements characteristics (Figure 3.11), especially the typical Ba

anomaly that characterise both components (see Ba/Th ratio on Figure 3.13B) and could be typically interpreted as related to recycled ocean crustal material in the mantle containing plagioclase, as already recognised in this magmatic segment (Barrat et al., 2003) and on other OIBs (Chauvel and Hemond, 2000). In such a scenario, both components would represent gabbroic ocean-crustal material with various initial mineralogical composition (plagioclase vs. clinopyroxene) modulating the final enriched or depleted characters of those geochemical endmembers embedded in the upwelled mantle. This is also in agreement with the fact that the most depleted magmas exhibit Sr and Eu positive anomalies (Figure 3.11 a,b), as well as very low Cr content (Figure 3.10), potentially linked to a higher initial proportion of plagioclase in the gabbroic assemblage.

Such a compositional trend from enriched and depleted endmembers has already been recognised in older basalts emplaced during the early period of the regional Stratoid formation in Afar (3,8 – 3 Ma, Alene et al., 2017), which share the same geochemical characteristics (i.e. Ba and Sr positive peaks), providing evidence for a long-lived occurrence of those mantle components in the magmatic evolution of the Afar depression. Although the expression of the depleted endmember is rather rare, a small contribution from this component could explain the compositional range seen within the enriched groups in this study (Figure 3.13A), and in Central Afar in general. A similar hypothesis has already been proposed by Medynski et al. (2015) for the two distinct enriched magma types identified at the axis of the Dabbahu segment. This suggests that regional geochemical variability across central Afar rift segments can, in part, be explained by incorporation of small volumes of depleted mantle melts into dominantly enriched melts, which in turn implies to be cautious when interpreting and inverting REE to constrains depth of melting. The fact that this full compositional trend is expressed at the axis of the same active segments, also implies that the involvement of the various depleted and enriched components is not controlled by spatial or temporal geometrical variations of the upwelled mantle. Rather, the expression of the depleted component likely requires specific melting conditions potentially controlled by the lithology and fertility of each mantle components. When the enriched component is present, its stronger trace element concentrations dominate the final magma composition, effectively masking the signature of the depleted component.

This specific type of magmas has been classified recently by Rooney (2020) in his East African Rift review as “type III”. Importantly, the presence of these positive B anomaly and a U-Th trough in our dataset, consistent with Medynski et al. (2015) and Tortelli et al. (2022) contrasts

with the signature of Rooney's type II metasomatized magmas, reflecting the absence of such components at the axial zone of Afar.

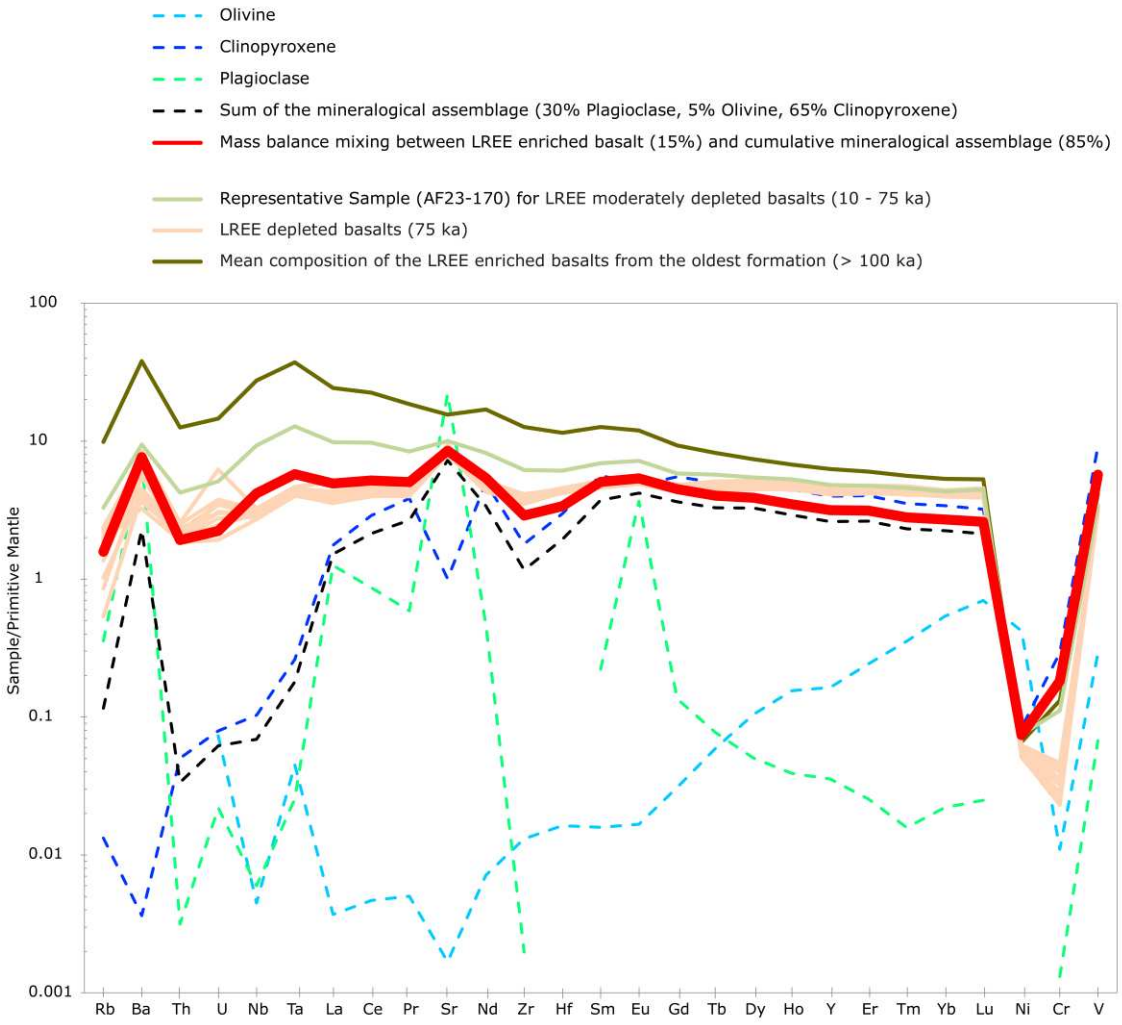

Figure 3.12: *Trace element pattern showing the result of mass balance mixing between LREE enriched basalts and cumulative mineralogical assemblage from the most primitive Afar samples normalized to the primitive mantle (Sun and McDonough, 1989).*

3.5.2 Plumbing system and general organisation of the magmatic sub-segment

Magmatic activity plays a fundamental role in the structural and volcanic evolution of rift segments in Afar (Bastow & Keir, 2011; Medynski et al., 2013). In these rifts, recent magmatism typically manifests as dike injections and fissural eruptions (Ebinger et al., 2008; Grandin et al., 2009; Keir et al., 2009; Ferguson et al., 2010; Medynski et al., 2015; Watts et al., 2020). The Gumat Mali magmatic sub-segment provides an example of such magmatism, with four distinct eruptive episodes since about 300 ka, identified based on volcanological, chronological, and geochemical evidence. It is developed southward of the Dabbahu segment (Medynski et al., 2015) in the same structural corridor, and is distinct from the Manda-Hararo sub-segment developed laterally to the NE along an en echelon relay at the scale of the Tendaho Grabben (Figure 3.2). The sub-segment functions as a ~32 km-long magmatic accretion zone (Figure 3.2), with morpho-tectonic features comparable to slow-spreading mid-ocean ridges, as observed in other Afar segments (Keir et al., 2009; Medynski et al., 2013; Carbotte et al., 2016). The most recent volcanic episode in Gumat Mali (< 2 ka, Figure 3.3) follows a well-defined sequence with an initial phreatomagmatic phase, crater collapse, lava lake formation and subsequent effusive activity from the main central crater or from scattered vents producing various volumes of fissural flows. The alignment of volcanic features along the current axial zone (Figure 3.3 and 3.6 A, B), the presence of main craters, and the occurrence of multiple lava flows along fissural trends all point to episodic magma ascent and eruption controlled by axial structures. These features indicate persistent magma supply from a deeper zone, likely a mid-segment reservoir situated beneath the main crater, which acts as a focal point for magma accumulation, vertical ascent, and lateral magma release and injections. The spatial organization of these recent events shows a correlation with the locations of the oldest volcanics (Figure 3.3) despite significant time gaps marked by intervening sediment layers. Although oldest and recent volcanism occur within the same structural corridor, they exhibit marked contrasts in the style and nature of erupted magmas.

Compared to the recent historical activity, the oldest volcanic episodes produced less differentiated (Figure 3.9), thicker, and laterally extensive flows with significantly larger associated erupted volumes. Geochemically, these include a distinct LREE depleted magma sandwiched between two LREE enriched groups, the most recent historical activity on top and

another one forming the base of the sequence. An intermediate magma series with moderately depleted geochemical signatures was emplaced shortly after the depleted group.

The contrasted magma types (depleted vs. enriched) and the shifts in composition and eruptive volume suggest that different batches of magma at different stages of differentiation were tapped from separate reservoirs. This pattern aligns with the concept of vertically distributed magma storage zones throughout the crust, with both laterally and vertically interconnected magma bodies, and associated with complex interactions and coexistence of compositionally distinct magmas, a model described by (Cashman et al., 2017). Following this view, the early eruptions of voluminous and relatively undifferentiated basalts may witness transfer of deep-seated magmas directly to the surface without intermediate steps of differentiation, whereas the most recent and more evolved basalts could originate from shallower reservoirs. Such a transition in magma characteristics at the axis of the Gumat Mali segment could therefore witness a progressive maturation of the plumbing system over the last 300 ka, with progressive emplacement of shallower and more differentiated reservoirs.

The most recent Gumat Mali volcanic episode (< 2 ka) further illustrates the internal dynamics of this plumbing system. Although age uncertainties limit the resolution of compositional evolution, the erupted lavas exhibit a clear compositional shift, with early lavas being more differentiated, while later ones gradually become less evolved (Figure 3.14). This compositional evolution is also marked by a strong La - Zr correlation and variable La/Sm ratios within a restricted MgO range (Figure 3.14), which reflects mixing and hybridization between two different magma types originating from distinct reservoirs. This compositional evolution probably results from injection into a shallower reservoir of a more primitive magma originating from deeper crustal levels and associated reservoirs. Some compositional characteristics of this lava suite (i.e. Al_2O_3 vs. MgO, Figure 3.9) further evidence interaction with plagioclase-rich mush typical of complex processes associated with magma transfer and percolation in transcrustal plumbing systems. Note that, the hybridization process captured by the last Gumat Mali fissural episode, gradually changed the composition of the magma in the shallower reservoir over a duration of 500-600 years, which is significantly longer than what has been described for the Ardoukoba eruption in the Asal rift (Vigier et al., 1999) or recently in the Reykjaness ridge rifting episode (Halldórsson et al., 2022).

Those data are compatible with the recent petrological model proposed for the Erta Ale segment (Pin et al., 2024) for which a complex architecture has been proposed, with melt storage in mush-dominated zones throughout the crust, where basaltic magmas undergo

protracted differentiation in the deep crust (~15 km) and further evolve through magma mixing and thermal reworking in shallower positions. It is also compatible with what has been previously documented in Central Afar for storage of magmas with shallow (~5-15 km) and deeper Moho-level zones of reservoir location (Grandin et al., 2011; Desissa et al., 2013; Field et al.,2013; Didana et al., 2014; La Rosa et al., 2024), as well as for the Erta Ale segment with shallow (~2-5 km) and deeper (~10-15 km) crustal storage levels (Field et al., 2012; Pagli et al., 2012; Hammond, 2014; Biggs et al., 2021; Chambers et al., 2021). Moreover, comparable plumbing system architecture, composed of crystal-rich, small, interconnected reservoirs with frequent mixing between magmas at different stage of differentiation has also been described in Central Afar for the older Gulf Basalts magmatic episode (0.5-1 Ma, Tortelli et al. (2024).

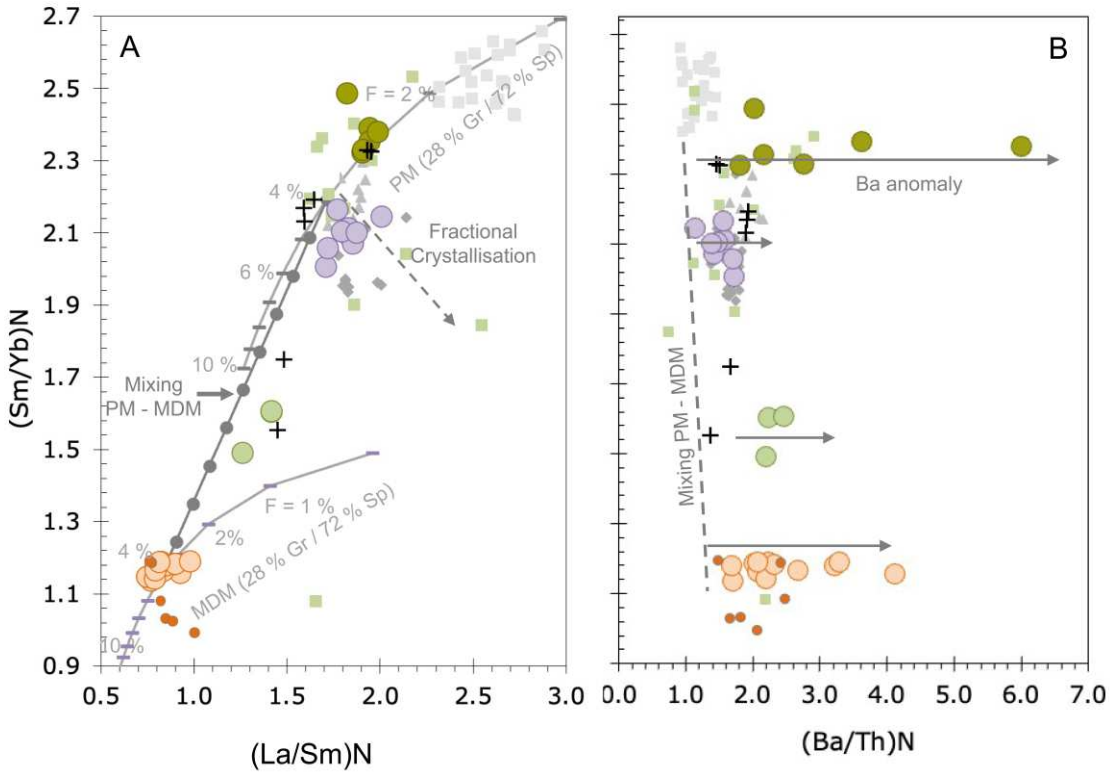

Figure 3.13: *A. (Sm/Yb)N vs. (La/Sm)N of the Gumat Mali samples, normalized to primitive mantle (Sun and McDonough, 1989). The legend is the same as for the Figure 3.8. Curves represent melting model of different types of Lherzolites for melted fractions (F) from 0 to 10 %: one with enriched composition of primitive mantle (PM, Sun and McDonough, 1989), and the other with a depleted composition. The model is based on the non-modal batch melting equations of Shaw (1970). The partition coefficients of the elements used for the model are taken from Mckenzie and O'Nions (1991). Both curves are framed by 28 % from melting of a garnet-rich mantle source (lherzolite) (concentration:*

0.1 Garnet; 0.25 orthopyroxene; 0.15 clinopyroxene; 0.5 olivine) plus 72 % from melting a spinel-rich mantle source (lherzolite) (concentration: 0.25 orthopyroxene; 0.15 clinopyroxene; 0.02 spinel; 0.58 olivine). The mineral modes used for the model are those described by Tortelli et al. (2022): 0.1 Grt; 0.4 Cpx; 0.2 Opx; 0.3 Ol, for the Lherzolite with garnet melting curve; and 0.4 Cpx; 0.2 Opx; 0.1 Sp; 0.3 Ol for the Lherzolite with spinel melting curve. An additional mixing line is joining the two melting curves for F = 4 %. Most of those relatively undifferentiated basalts (MgO > 8 %) spread along this mixing line, with some deviation due to fractional cristalisation modification of the two ratios (indicative). B. (Sm/Yb)N vs. (Ba/Th)N for the Gumat Mali samples, same legend as for figure 3.8.

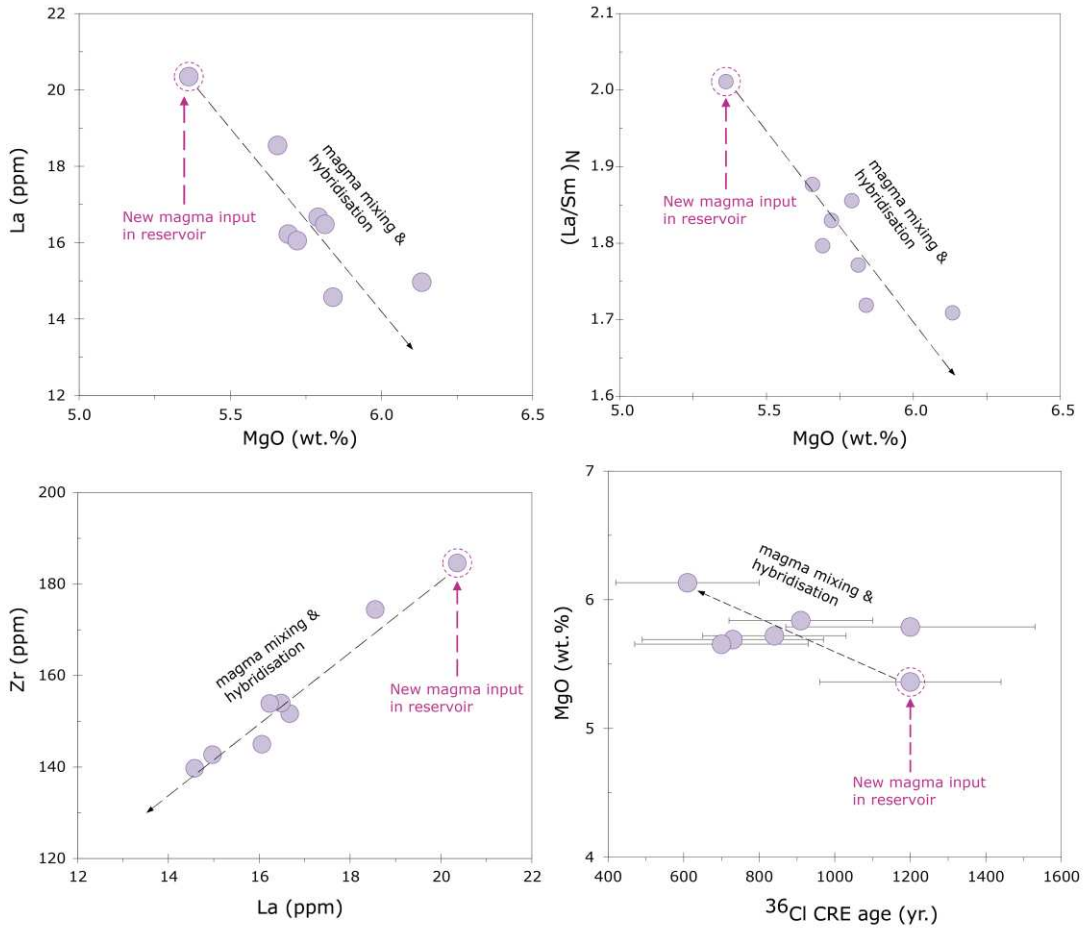

Figure 3.14: *Temporal evolution of magma composition during the most recent magmatic phases at Gumat Mali sub-segment. Legend same as figure 3.8*

3.5.3 Volcanological hazard assessment

The first information of our study regarding volcanological hazard assessment in the Gumat Mali area in Central Afar is represented by the documentation of recent historical activity from ~ 1900 to ~ 600 years ago. Our volcanological, geochemical, and chronological data indicate that the effusive sequence was driven by a reservoir recharge with new and less differentiated magma that hybridised with a more differentiated mush in a shallow reservoir, a process that potentially reinforced the ability of the new magma in this reservoir to be mobilised. The full rifting sequence we document has been emplaced over a couple of hundred years and consequently represents long-lived focussed activity which can be compared to the historical record of the individual rift segments of the Reykjaness peninsula in Iceland that have recently been reactivated (Parks et al., 2025; Riel et al., 2015). Those new data indicates that the axial part of this segment is potentially a zone for future volcanologic hazards.

The documented effusive eruptions (Figure 3.3) reflect typical rifting episodes style that can be compared to the observed Dabbahu crisis northward in Central Afar and the associated lavas emplaced between 2005 and 2010 (Ebinger et al., 2010), or to the ones recently observed in Iceland between 2021 and 2024 with subaerial volcanism dominated by fissural eruptions and associated lava fountaining (Pedersen et al., 2023). Hazards assessments and management during such effusive episodes require monitoring the opened and productive fissures along the axis to further evaluate and forecast spilling of lava according to local topography. Our precise mapping of the last episode documents that lateral maximum propagation of lava flows reached ~ 5 km. Regarding such effusive activity, the main associated hazard for this segment axis concerns the local population that is established in lowlands along the fissural system, which can represent hundreds of persons in the Gumat Mali village and district (kebele).

The other main information of our study for volcanological hazard assessment regards the initiation of the sequence ~ 1900 ± 290 years ago with an extremely energetic phreatomagmatic phase. This phase has been evidenced by a pile of pyroclastic deposits on the edge of the main axial crater which preceded the emplacement of a massive matrix-supported deposit and widespread ballistic block fields extending several kilometers from the main crater. This last phase likely reflects a catastrophic structural failure of the crater before the initiation of the effusive phase. Such energetic phreatomagmatic eruptions occur when rising magma interacts with groundwater at depth. In the periphery of the Gumat Mali segment axis, there exists a water table which appears to be relatively consistent across different locations (lakes in craters) at 360-370 m. This water table level across the segment is consistent with a potential lateral

recharge from the endoreic Saha plain, located east of Gumat Mali and in the continuation of the Manda Hararo sub-segment, which lies at an altitude of approximately 360 meters, and potentially driven northward by the main lowland in-between the Gumat Mali and Dabbahu segments which exhibits a persistent lake lying at an altitude of 346 m. Those data indicates that phreatomagmatic eruptions represent a significant and probable hazard in such a context combining the presence of rising magma along axial rift zones and the presence of widespread shallow water. Such hazards do not only concern the Gumat Mali segment but also the Gabblaitu one (Figure 3.2), which exhibits recent volcanological activity, and therefore represents a regional additional hazard for populations settled nearby those areas including part of the Semera human and economic activity.

Chapter 4

Detailed architecture of the magmatic sub-segments in Central Afar (Ethiopia)

Yafet Gebrewold Birhane[1,6], Raphael Pik[1], Nicolas Bellahsen[2], Sarah Gommery[2], Irene Schimmelpfennig[3], Christophe Cloquet[1], Lyderic France[1,4], Simon Daout[1], Jessica Flahaut[1], Dereje Ayalew[5], and Gezahegn Yirgu[5]

[1]CRPG, CNRS, Universite´ de Lorraine, UMR 7358, Vandoeuvre-les-Nancy, France, [2]Sorbonne Universités, UPMC Université Paris 06, CNRS, Institut des Sciences de la Terre de Paris (iSTeP), Paris, France, [3]Aix-Marseille Université, CNRS, Coll France, IRD, INRAE, CEREGE, Aix en Provence, France, [4]Institut Universitaire de France (IUF), [5]School of Earth Sciences, Addis Ababa University, Addis Ababa, Ethiopia, [6]Department of Geology, College of Natural and Computational Sciences, Hawassa University, Ethiopia

4. Introduction

Extension at continental rifts and oceanic ridges is accommodated by normal faulting and magma injection (Ayele et al., 2007; Carbotte et al., 2006; Ebinger and Casey, 2001; Hayward and Ebinger, 1996; Rowland et al., 2007; Wright et al., 2006). During continental breakup, the faulting, diking, and stretching of initially thick continental lithosphere ultimately gives way to the formation of new oceanic crust at mid-ocean ridge spreading centres. In continental environments, extension is generally dominated by faulting, whereas in magma-rich oceanic ridges, dyke intrusion is the primary mode of extension, controlling crustal growth and rift segmentation (Wright et al., 2012). The transition between these two fundamentally different styles of strain accommodation occurs in the highly attenuated lithosphere of mature continental rifts (Eldholm et al., 2000; Menzies et al., 2002). However, it remains unclear how the transition between these styles of rifting occurs and specifically how faulting and dyke intrusion interact during rift evolution.

The Afar depression, situated within the northern East African Rift (Figure 4.1), is the best location globally in which to study magmatic rift development and processes of the ocean continental transition (OCT). Here, transition is under way between plate extension processes modulated by lithospheric thinning and those controlled by magma intrusion (Bastow and Keir, 2011). Within the rift, deformation is already morphologically organised along magmatic rift segments (Hayward & Ebinger, 1996), as observed in mature oceanic ridges, but within magmatically modified continental crust (Hammond et al., 2011), implying a currently

incomplete transition from continent to ocean (Bastow and Keir, 2011). Afar thus provides a rare opportunity to directly study the evolution and controls of individual rift segments during this transitional stage.

Since ca. 0.4 Ma, deformation in Afar has localized along 60-100 km long and 20-40 km wide en-echelon magmatic rift segments (MRS), closely resembling those of slow-spreading ridges (Hayward & Ebinger, 1996; Ebinger & Casey, 2001; Doubre et al., 2007; McClusky et al., 2010, Dumont et al., 2019). From north to south, the Erta Ale, Dabbahu-Manda Hararo, and Asal-Ghoubbet segments exhibit striking contrasts in morphology and magma supply. The Erta Ale segment is characterized by significantly higher recent melt supply and produced a prominent axial ridge compared to the Dabbahu-Manda Hararo and Asal-Ghoubbet segments, where recent magmatism has been comparatively less voluminous (Figure 4.1). These observations raise key questions concerning why rifting is expressed differently in each of the Afar rift segments. These spatial variations have been interpreted either as differences in rift maturity (Ebinger & Casey, 2001; Manighetti et al., 2001; Bastow & Keir, 2011) or as distinct rifting styles (Stab et al., 2016; Le Gall et al., 2018; Rime et al., 2023). However, these models often result from data that do not document the system at the same time and space scale. Despite extensive geophysical and volcanological studies, the internal architecture of magmatic segments, specifically the organization of magma plumbing systems and their interaction with fault networks, remains poorly constrained in time and space.

In this study, we combine new remote sensing, field investigations, precise geological mapping, geochemical analysis, and cosmogenic ^{36}Cl exposure dating of lavas from the Manda Hararo sub-segment (Figure 4.2 and 4.3) with previously described lateral Gumat Mali sub-segment (Chapter 3 of this thesis, Birhane et al., in prep.) to provide a full highly detailed investigation of the Central Afar magmatic segment system. The aim of this work is to precisely determine the vertical and lateral organisation of magmatic reservoirs, potential interconnections between plumbing systems, and constrain their role in controlling large-scale rift segmentation in this key area of Ocean Continent Transition in Afar.

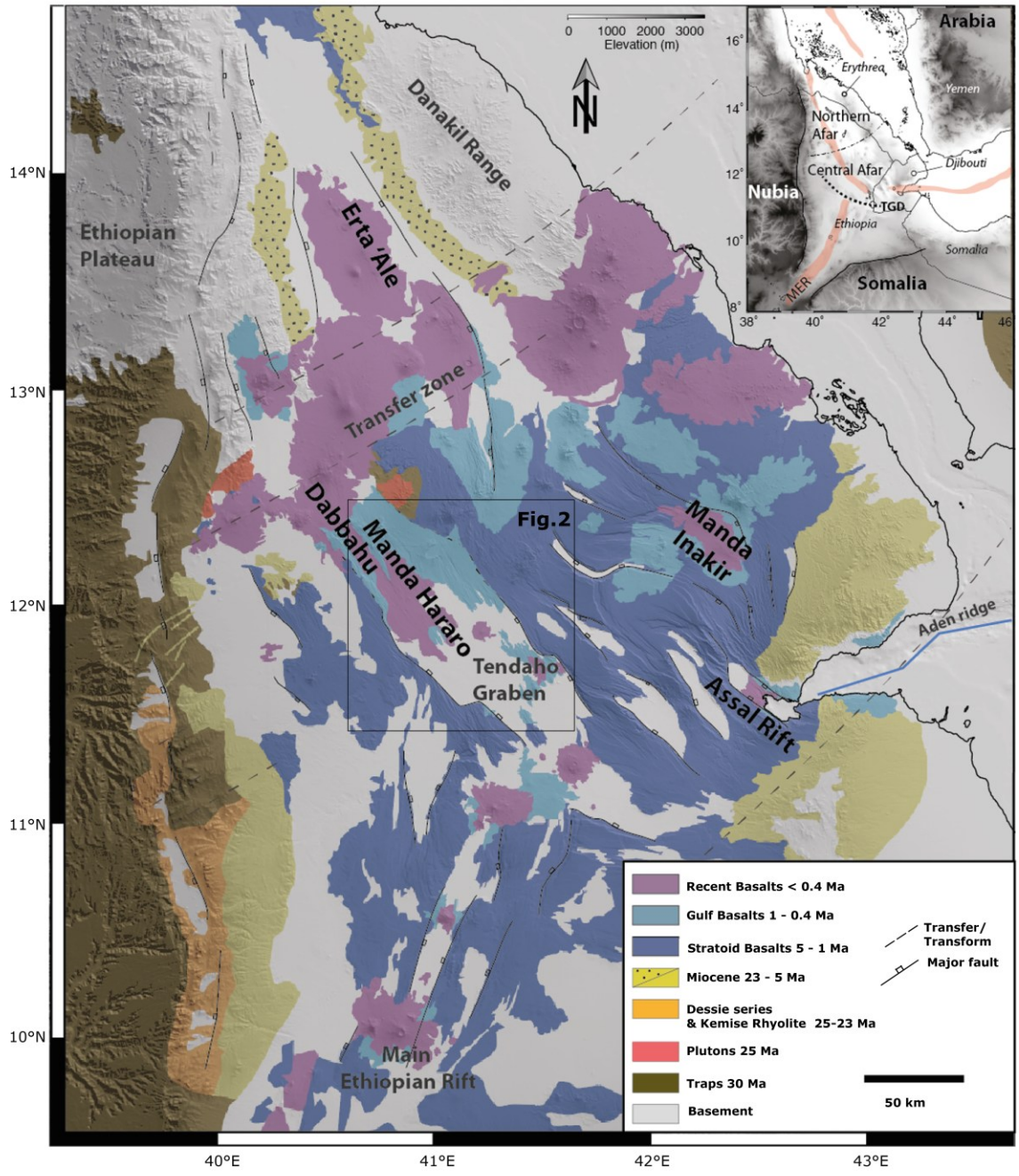

Figure 4.1: *Geological map of Afar modified after Stab et al. (2016)*

4.1 Materials and methods

4.1.1 Geological mapping and sampling

Using a combination of remote sensing techniques and a high-resolution Pleiades-derived Digital Surface Model (DSM), we constructed detailed mapping of the Central Afar sub-segments. This mapping enabled us to distinguish different eruptive units and to determine the extent and diversity of lava fields. The results were validated through field observations. The high-resolution dataset also allowed precise selection of sampling sites for geochemical analyses and surface-exposure dating. Detailed mapping procedures and remote sensing methods are described in Chapter 2 of this thesis and in (Birhane et al., in preparation).

4.1.2 Sampling details

This work presents geochemical and chronological data from 100 new lava flow samples collected in the Central Afar sub-segments during intensive field campaigns in 2013, 2018, and 2023. Sample locations, carefully selected in order to be representative of the flow units identified from the detailed mapping, are reported in Figure 4.2 and in Table S4.1. All 100 lava flow samples were analyzed for major and trace element compositions. Sample preparation and analyses were performed at the Centre for Petrographic and Geochemical Research (CRPG–CNRS, Nancy, France) using the SARM national facility. The fresh rock samples were crushed, powdered, and analyzed for major elements by Inductively Coupled Plasma–Optical Emission Spectrometry (ICP–OES) and for trace elements by Inductively Coupled Plasma–Mass Spectrometry (ICP–MS). Lithium was measured by atomic absorption, boron by colorimetry, and chlorine by spectrophotometry. The results are given in Table S4.1.

The Sr, Nd and Pb isotopic composition was measured on 22 of the lava flow samples. The chemical preparation and analysis procedures are described in Chapter 2 of this thesis. The measurements were performed in clean rooms-STEHLo facility at CRPG, Nancy, and results are given in Table S4.2.

In addition, 30 lava surface samples were dated using cosmogenic ^{36}Cl, following the sampling strategy, chemical preparation, and age calculation procedures described in Birhane et al. (in preparation). Detailed field data and sample information are summarized in Table 4.1. Measurements of $^{36}Cl/^{35}Cl$ and $^{35}Cl/^{37}Cl$ ratios were carried out by Accelerator Mass Spectrometry (AMS) at the French AMS national facility (ASTER-CEREGE, France). Measured ratios, along with calculated ^{36}Cl and Cl concentrations, are presented in Table 4.2.

Table 4.1: *Locations and descriptions of lava surface samples used for ^{36}Cl dating. All analysed samples used the 250-500 µm grain-size fraction. Scaling factors follow Stone (2000).*

Sample Name	Latitude (°N)	Longitude (°E)	Altitude (m)	Sample Thickness (cm)	Mineral used for CRE dating	Stone scaling factor (Neutrons)	Stone scaling factor (Muons)
AF23_24	12.115869	40.876378	450	3.5	whole rock for ^{36}Cl	0.87	0.77
AF23_25	12.106497	40.862404	464	3.5	whole rock for ^{36}Cl	0.88	0.77
AF23_26	12.072275	40.879485	468	3	whole rock for ^{36}Cl	0.88	0.77
AF23_28	12.054942	40.892306	436	3.5	whole rock for ^{36}Cl	0.86	0.76
AF23_35	12.0274	40.899779	404	9	whole rock for ^{36}Cl	0.84	0.75
AF23_36	12.002189	40.909532	387	5	whole rock for ^{36}Cl	0.82	0.74
AF23_37	11.972164	40.921567	428	4	whole rock for ^{36}Cl	0.85	0.76
AF23-48	12.085826	40.961002	426	3	whole rock for ^{36}Cl	0.85	0.76
AF23-74	11.814501	41.076961	372	5	whole rock for ^{36}Cl	0.81	0.74
AF23_87	12.131862	40.860366	455	5	whole rock for ^{36}Cl	0.87	0.77
AF23_90	12.01569	40.906885	395	3.5	whole rock for ^{36}Cl	0.83	0.75
AF23_93	11.96307	40.925562	444	2	whole rock for ^{36}Cl	0.86	0.76
AF23_115	11.859177	41.056649	380	2.5	whole rock for ^{36}Cl	0.82	0.74
AF23_116	11.858816	41.055789	380	3	whole rock for ^{36}Cl	0.82	0.74
AF23_121	11.821658	41.080259	371	2.5	whole rock for ^{36}Cl	0.81	0.74
AF23_122	11.821686	41.080747	371	3	whole rock for ^{36}Cl	0.81	0.74
AF23_123	11.818209	41.069571	373	8.5	whole rock for ^{36}Cl	0.81	0.74
AF23_127	12.072809	40.905063	444	2.5	whole rock for ^{36}Cl	0.86	0.76
AF23_128	12.072198	40.90257	448	3	whole rock for ^{36}Cl	0.86	0.77
AF23_129	12.067883	40.903114	435	4.5	whole rock for ^{36}Cl	0.86	0.76
AF23_131	12.064947	40.901582	427	4.5	whole rock for ^{36}Cl	0.85	0.76
AF23_132	12.058426	40.902768	404	2	whole rock for ^{36}Cl	0.84	0.75
AF23_133	12.050489	40.899144	426	3	whole rock for ^{36}Cl	0.85	0.76
AF23_136	12.143396	40.847947	480	4	whole rock for ^{36}Cl	0.89	0.78
AF23_137	12.138005	40.843692	486	3	whole rock for ^{36}Cl	0.89	0.78
AF23_138	12.138036	40.847858	481	4	whole rock for ^{36}Cl	0.89	0.78
AF23_139	12.121448	40.852569	469	4	whole rock for ^{36}Cl	0.88	0.77
AF23_140	12.068638	40.886028	463	7.5	whole rock for ^{36}Cl	0.87	0.77
AF23_141	12.059326	40.892134	447	5.5	whole rock for 36Cl	0.86	0.77
AF23_142	12.03682	40.897895	420	3.5	whole rock for 36Cl	0.85	0.76

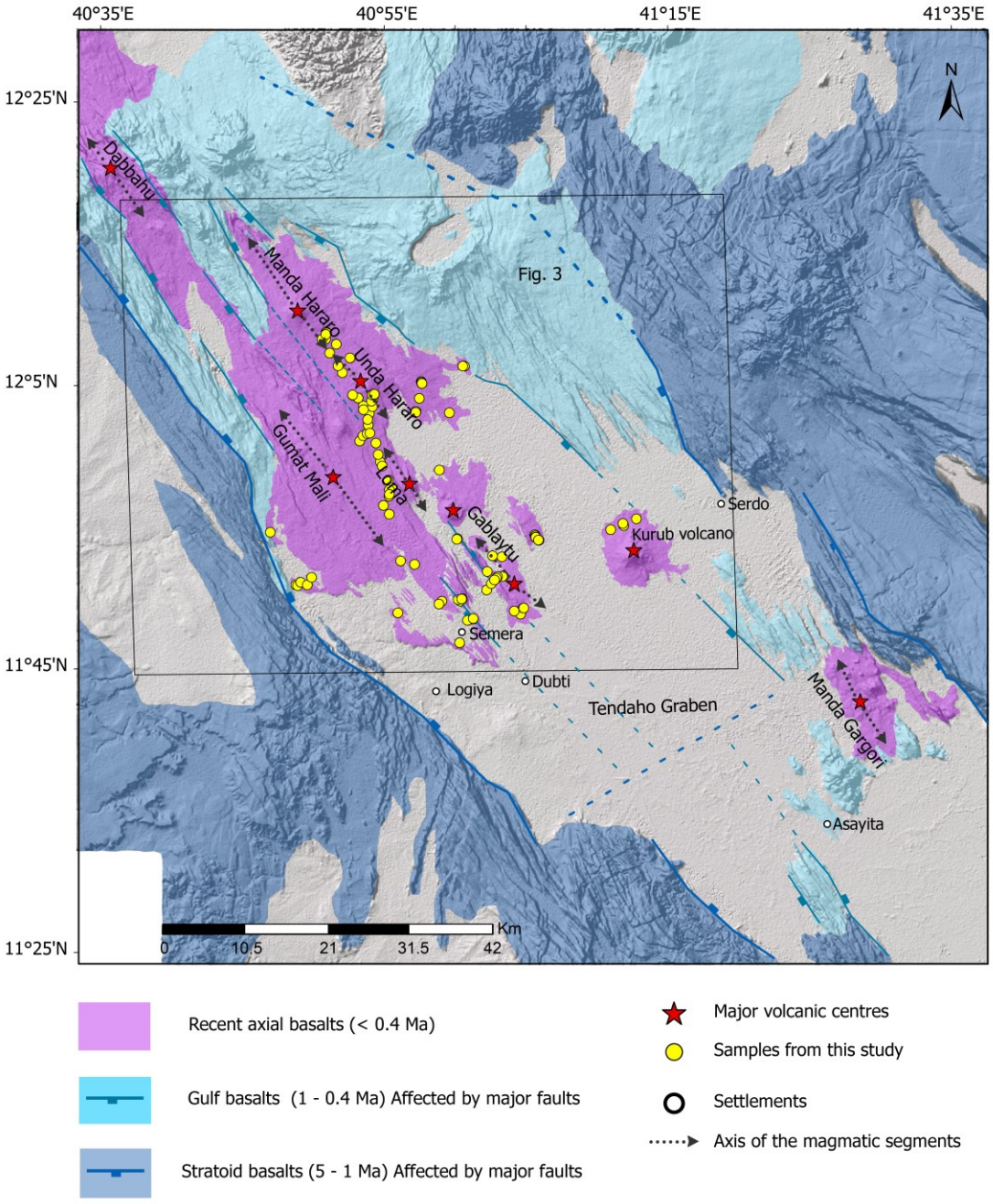

Figure 4.2: *Geological map of central Afar modified after Stab et al., (2016). Major volcanic centres host potential magmatic reservoirs beneath and are related to rift segmentation.*

4.2 Results

4.2.1 Chronology of Lava Flows

We present new chronological data for lava flows outcropping along the various volcanic centres of the Manda Hararo sub-segments of central Afar based on high-resolution ^{36}Cl CRE dating. The results are shown in Figure 4.3 and summarized in Table 4.2.

The Gablaytu volcanic center, exposes the most recent volcanic episodes dated between 1.54 ± 0.20 ka (AF23_115) and 3.15 ± 0.50 ka (AF23_74), based on six lava surfaces from effusive fissural activity. Four samples from large, thin lava flows exhibit individual CRE ages of 3.15 ± 0.50 ka (AF23_74), 2.99 ± 0.40 ka (AF23_121, Figure 4.6 J), 2.85 ± 0.38 ka (AF23_122, Figure 4.6 I), and 2.82 ± 0.42 ka (AF23_123). Two samples, representing the youngest flows in the sequence, exhibit ages of 1.69 ± 0.30 ka (AF23_116, Figure 4.6 H) and 1.54 ± 0.20 ka (AF23_115, Figure 4.6 G).

Northward, along the axial direction of the segment and its Manda Hararo (sensu stricto), Unda Hararo and Loma volcanic centers, the ^{36}Cl CRE ages can be divided into two main volcanic episodes: (1) the most recent episode, ranging from 8.39 ± 0.85 ka (AF23_137, Figure 4.6A) to 18.96 ± 2.60 ka (AF23_48), and (2) the underlying older volcanic episode, ranging from 22.95 ± 2.27 ka (AF23_132, Figure 4.6 E) to 35.05 ± 4.00 ka (AF23_37, Figure 4.6 F).

For the most recent episode, ^{36}Cl CRE ages are represented by 16 dated lava surfaces and can be tentatively divided into three distinct volcanic phases consistent with the relative chronology and mapping. The first volcanic phase, associated with Manda Hararo volcano construction, is constrained by the age of one of the numerous lava flows emplaced on its flanks at 17.26 ± 1.60 ka (AF23_136, Figure 4.6 D) which puts an upper age limit for this phase. Another flow, sourced from a fault-fed magma conduit (Figure 4.3) in the south-eastern part of the volcanic centre, yields an equivalent age of 18.96 ± 2.60 ka (AF23_48), suggesting that during this period volcanism was not strictly concentrated on the Manda volcano itself. The second volcanic phase, associated with a new major fissural episode widely distributed along the segment axis (Figure 4.3), is represented by twelve dated lava surfaces. Four fissural flow surfaces south of the volcano exhibit consistent ages of 10.50 ± 1.14 ka (AF23_87, Figure 4.6 B), 11.67 ± 1.18 ka (AF23_139), 12.32 ± 1.50 ka (AF23_24) and 12.17 ± 1.40 ka (AF23_25). A series of large and thin fissural flows extending further to the southern tip of the sub-segment have individual ages of 14.63 ± 1.64 ka (AF23_133), 13.64 ± 1.70 ka (AF23_35), 13.59 ± 1.40 ka (AF23_36), 13.11 ± 1.45 ka (AF23_90), 11.92 ± 1.27 ka (AF23_140, Figure 4.6 C), 11.68 ± 1.30 ka (AF23_26), 11.29 ± 1.12 ka (AF23_141), and 10.62 ± 1.10 ka (AF23_28). They all

define a coherent system active from ~14 to 10 ka and characterised by MgO decrease from 7.2 to 5.8 wt. % (Figure 4.13). A third magmatic phase is represented by two slightly more recent lava surfaces outcropping on the southern flank of the Manda volcano, that exhibit ages of 9.00 ± 1.05 ka (AF23_138) and 8.39 ± 0.85 ka (AF23_137) and MgO content again in the range 6.2 to 6.4 wt. %, which could tentatively be related to replenishment of the underlying shallow reservoir system with new magma.

The underlying older volcanic episode, ranging from 22.95 ± 2.27 ka (AF23_132, Figure 4.6 E) to 35.05 ± 4.00 ka (AF23_37, Figure 4.6 F), is represented by eight dated lava surfaces from distinct eruptive centers. A lava flow emplaced on the axial depression of the sub-segment, below the recent fissural episode, is dated at 28.12 ± 3.25 ka (AF23_142). Additional activity of this episode corresponds to distinct lava layers from the Unda Hararo volcano flanks, with CRE ages of 28.20 ± 3.50 ka (AF23_128), 27.50 ± 2.70 ka (AF23_131), 26.43 ± 3.35 ka (AF23_129), 25.80 ± 2.65 ka (AF23_127) and 22.95 ± 2.27 ka (AF23_132). The oldest stage of this episode can be documented southward along the Loma crater where two pahoehoe flows exhibit consistent ages of 35.05 ± 4.00 ka (AF23_37) and 33.99 ± 4.00 ka (AF23_93).

4.2.2 Geological Map and Volcanic history

Combining our new data with the ones of Birhane et al. (in preparation, chapter 3 of this thesis) and the ones of S. Gomery's PhD thesis (2025, thesis Ms and in prep.), we produced a high-resolution geological map of the central Afar magmatic sub-segments (Figure 4.3) and associated interpretative cross sections (Figure 4.4). The map is developed by integrating remote sensing data, field observations, ^{36}Cl CRE ages, and geochemical analyses, in order to characterise the distribution, composition, and chronology of magmatic activity. The map also provides some volcanological information, documenting features such as calderas, craters, and eruptive fissures, which are key indicators of emission centres and associated processes along the sub-segments (Figure 4.5).

The volcanic record of the Central Afar segment system globally shows older activity (400-300 ka), now mainly observable at the periphery of the segments and along the central horst, followed by subsequent more recent volcanism emplaced at the axis of the two subsegments (100-0 ka). Early volcanism often exhibits extensive, thick, primitive basaltic flows (see section 4.3.3), later transitioning to more localized and evolved basalts concentrated on various volcanic centres along the Manda Hararo subsegment axis, whereas the Gumat Mali sub-segment continues to experience emplacement of thick and primitive lava flows until the most

recent and historical fissural episode which exhibits more evolved basalts. In the field, lavas appear mostly massive, with vesicular layers concentrated along horizontal discontinuities, and displaying decametric tumuli typical of inflated pahoehoe architecture. Most samples are generally aphyric with fine-grained groundmass crystals, although some samples show porphyritic texture. When present, plagioclase is the most abundant phenocryst, but olivine and pyroxene phenocrysts are also rarely present (see chapter 2 of this thesis).

The oldest recognised volcanics have been dated by Ar/Ar at 397 ± 40 ka on the western side of the Gumat-Mali subsegment, and at 310 ± 161 ka on the eastern side of the Manda Hararo subsegment (Figure 4.4), positioning the emplacement of the Central Afar system at ~ 400 ka, right after the last Gulf basalts dated at 520 ± 80 ka on the western edge, and 495 ± 99 ka at the base of the horst system in the southern part of the segment (Gommery et al., in preparation, Figure 4.4). The volcanic history between 300 ka and 100 ka is difficult to describe precisely. We found no evidence for significant volcanism during this period, except if some lavas have been buried at depth, because of continuous overlapping of flows on top of each other.

The second significant volcanic phase recognised has been dated at ~ 100 ka in various places: in the southern termination of the Gumat Mali sub-segment close to the Semera city (124 ± 24 ka, Lahitte et al., 2003 ; 120 ± 50 ka, Feyissa et al., 2019), north of Gablaytu (110 ± 39, Gommery et al., in prep.), and close to Saha on the Manda Hararo sub-segment (102 ± 35 ka, Lahitte et al., 2003). This episode is largely resurfacing the south-western part of the Gumat Mali sub-segment, overlapping on the flood plain, whereas on the north-eastern side of the rift system our new mapping and dating clearly indicate that it is controled by pre-existing faults developed on the earlier 400-300 ka phase (Figure 4.3 and 4.4). This ~ 100 ka episode also records flexural deformation in between the two sub-segments in their southern part (Figure 4.4). Those volcano-tectonic features globally describe an asymetrical rift system with dominant west verging faults along the Manda Hararo sub-segment, where volcanism has been partly controlled, and surface volume accomodated, by tectonic activity since that time (Figure 4.4).

A subsequent phase of extensive volcanism resurfaced nearly the entire axial graben of the northern Manda Hararo sub-segment, leaving only small remnants of older formations at its margin or exposed at the base of main fault scarps (i.e., sample 70R of Lahitte et al., 2003). This episode exhibits ^{36}Cl CRE ages ranging between 22 and 35 ka, and includes multiple emission centres such as the Unda Hararo partly-collapsed crater (Figure 4.5 A), several smaller craters in the north tip of the sub-segment, and the Loma crater, confirming there some

previous K/Ar ages of Lahitte et al. (2003). The broad spatial distribution of these eruptive vents suggests that this was a major magmatic event at the scale of the entire sub-segment, including differentiated volcanic products in its southern part on the Gablaytu volcanic centre (31 ± 4 ka, Lahitte et al., 2003), as well as activity of the slightly off axis Kurub volcano. The last activity on the northern end of the sub-segment was marked by growth of the Manda Hararo central volcano and associated lava flows erupted on the flanks has been dated at 17 ka and two others at 8 – 9 ka. The Manda Hararo volcanic history has been associated with major dyking and fissural episodes from 14 to 10 ka that produced thin flows along a distance of more than 15 km southward along the segment axis. Most flows advanced perpendicular to the rift axis, although some followed the topography southward, parallel to it.

The most recent volcanic episode of the Manda Hararo sub-segment emplaced at the Gablaytu volcanic centre is dated by our new ^{36}Cl CRE ages between 1.5 and 3.5 ka for flows surfaces outcropping on its southern end, and associated along the fissures with small, strombolian type, pyroclastic cones. Hyaloclastite deposits and associated basaltic flows (Figure 4.5D) continue this very recent volcanic system to the north along the segment axis. Field observations indicate that some of these events started as a hyaloclastite cone and ended as a lava flow (Figure 4.3), which suggests that they most probably were emitted near a paleo-lake shoreline where limited water was available. The age of these deposits is not directly constrained. However, correlation of their stratigraphic position with the latest Holocene highstand of the Tendaho paleo-lake (~ 420 m a.s.l.; 4.6 ka; Mologni et al., 2021) suggests an age of about 4.5 ka.

As already described in Birahne et al. (chapter 3, in prep.), the activity younger than 100 ka along the Gumat Mali subsegment, is composed by two distinct units of widespread and thick pahoehoe flows, exhibiting relatively primary basaltic compositions and variously depleted trace element signatures. The subsequent most recent episode on the axis of the sub-segment, began with an explosive eruption at 1.9 ka, followed by a series of effusive lava flows emplaced between 0.6 and 1.2 ka and associated with an intermittent lava lake in the axial craters.

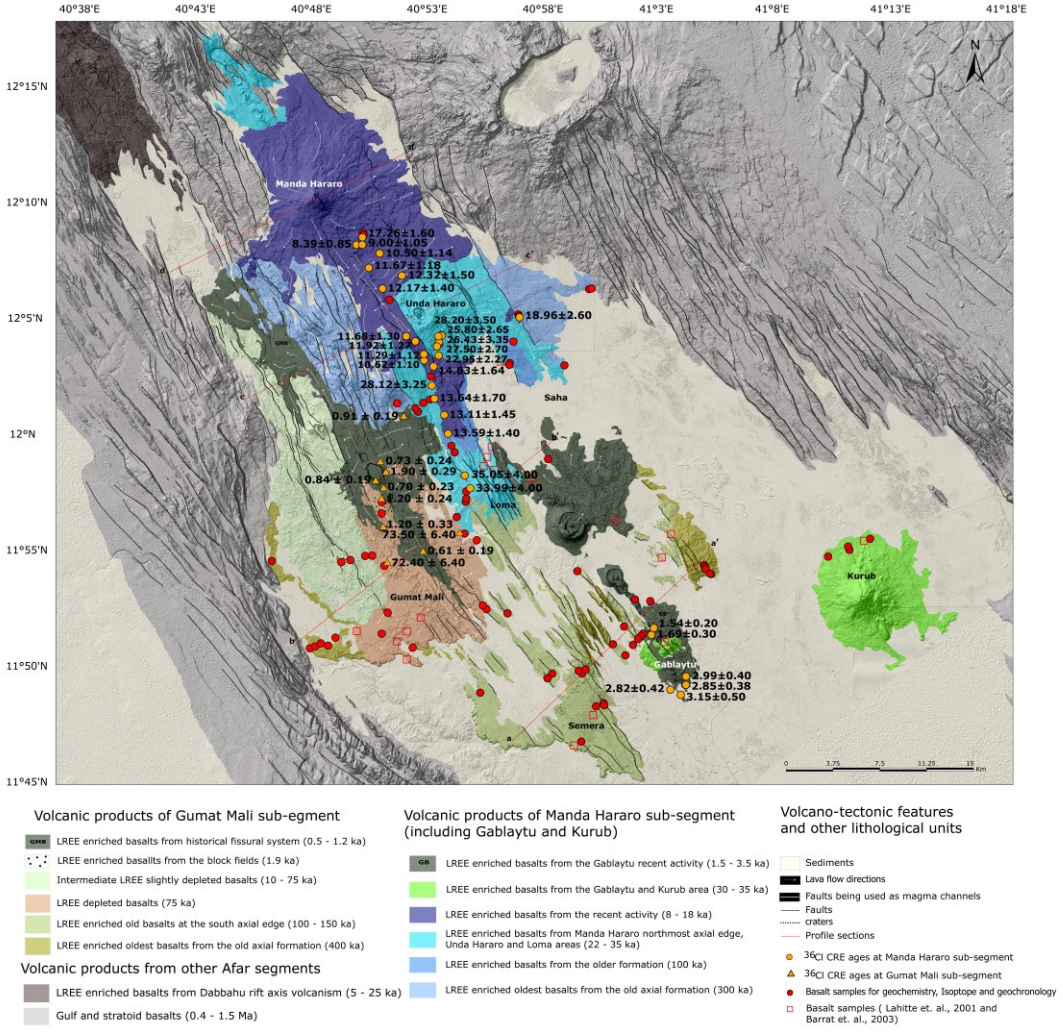

Figure 4.3: *Map of the central Afar sub-segments showing lava flow distribution, ^{36}Cl CRE ages, and key volcanic features.*

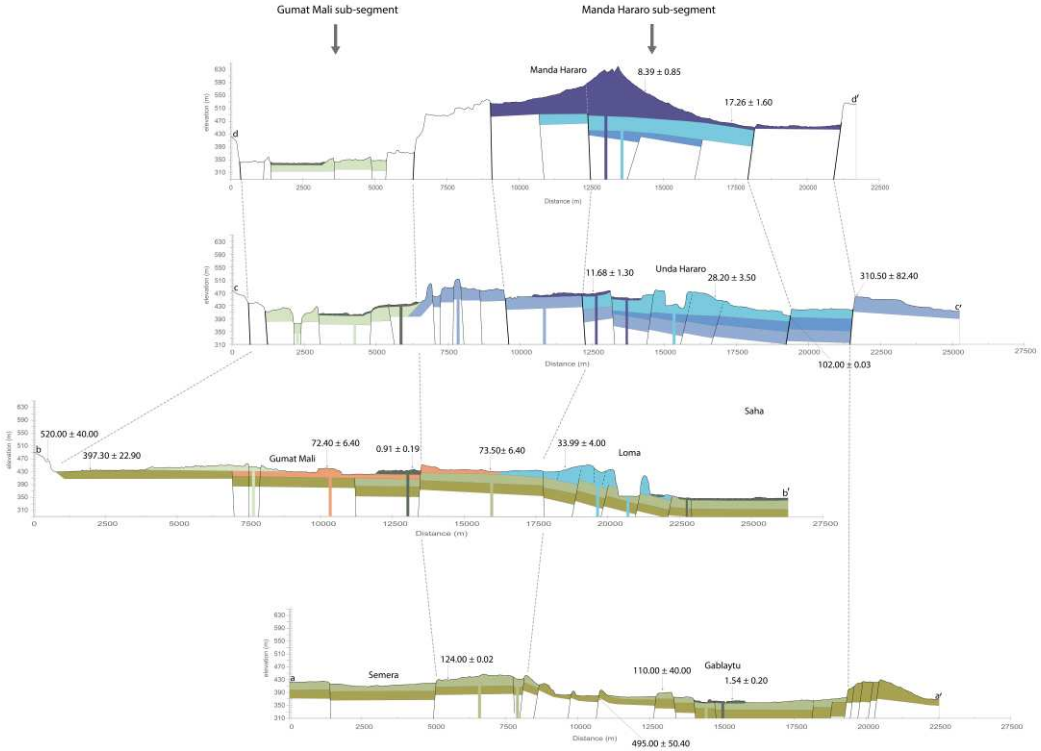

Figure 4.4: *Cross-section map of the central Afar sub-segments, illustrating relationships between magmatic activities with tectonic structures. Legend is the same as in Figure 4.3*

Table 4.2: *^{36}Cl CRE ages of the Lava flows. Chlorine and ^{36}Cl concentrations were determined by the AMS measurement at ASTER-CEREGE, France. Reported age uncertainties (1σ) include both production rate and analytical errors; values in parentheses indicate analytical errors only.*

Sample Name	Sample weight (g)	Mass of Cl in spike (mg)	^{35}Cl/^{37}Cl	^{36}Cl/^{35}Cl	Cl in Sample (ppm)	^{36}Cl (10^3 atoms g^{-1})	^{36}Cl CRE age (ka)
AF23_24	85.04	1.978	4.68±3.60	5.59E-14± 3.86E-15	59.33± 6.71	66.10±6.67	12.32±1.80 (1.50)
AF23_25	81.97	1.991	4.57±3.62	5.24E-14± 3.39E-15	66.84± 7.95	68.00±6.95	12.17±1.80 (1.40)
AF23_26	78.10	1.993	4.73±3.63	5.11E-14± 3.15E-15	63.16v7.07	65.00±6.16	11.68±1.70 (1.30)
AF23_28	79.65	1.993	5.58±3.58	5.20E-14± 3.30E-15	39.57± 3.48	49.90±3.96	10.62±1.40 (1.10)
AF23_35	79.00	1.998	4.64±4.05	5.84E-14± 3.93E-15	65.70± 8.58	76.60±8.27	13.64±2.20 (1.70)
AF23_36	84.70	2.018	4.95±3.67	6.15E-14± 3.66E-15	51.62± 5.38	67.10±5.86	13.59±1.90 (1.40)
AF23_37	92.50	2.009	4.66±3.57	1.48E-13± 6.91E-15	56.51± 6.37	166.00±14.40	35.05±4.90 (4.00)
AF23_48	93.38	1.990	4.29±3.85	7.60E-14± 4.48E-15	72.57± 10.67	101.00±12.00	18.96±3.00 (2.60)
AF23_74	88.90	2.030	4.56±3.61	1.46E-14± 1.92E-15	63.72± 7.56	17.60±2.77	3.15±0.60 (0.50)
AF23_87	67.36	1.994	5.11±3.59	4.48E-14± 2.96E-15	58.60± 5.76	57.50±5.03	10.50±1.44 (1.14)
AF23_90	92.40	2.008	4.85±3.58	6.21E-14± 3.88E-15	50.15± 5.29	64.20±5.85	13.11±1.85 (1.45)
AF23_93	96.10	2.003	4.60±3.61	1.40E-13± 6.66E-15	56.51± 6.59	155.00±14.00	33.99±4.80 (4.00)
AF23_115	100.50	2.003	23.22±3.57	1.70E-14± 2.04E-15	2.24± 0.20	6.28±0.807	1.54±0.27 (0.20)
AF23_116	86.60	2.035	14.21±3.56	1.48E-14± 2.07E-15	6.59± 0.43	7.14±1.07	1.69±0.32 (0.30)
AF23_121	102.50	2.008	4.70±3.71	1.64E-14± 1.56E-15	49.55± 5.70	16.00±1.96	2.99±0.48 (0.40)
AF23_122	81.60	2.007	5.63±3.67	1.52E-14± 1.60E-15	38.31± 3.40	13.80±1.65	2.85±0.45 (0.38)
AF23_123	87.30	2.009	4.59±3.69	1.28E-14± 1.34E-15	62.81±7.52	15.30±2.06	2.82±0.49 (0.42)
AF23_127	83.44	1.991	5.38±3.75	1.19E-13± 6.09E-15	40.48±3.96	115.00±8.46	25.80±3.40 (2.65)
AF23_128	86.28	1.993	4.36±3.58	1.11E-13± 5.61E-15	74.15±9.75	153±1.59	28.20±4.40 (3.50)
AF23_129	89.65	1.989	4.35±3.64	1.09E-13± 5.62E-15	71.55±9.6	145.00±1.54	26.43±4.13 (3.35)
AF23_131	80.02	1.987	5.98±4.06	1.26E-13± 5.98E-15	32.57±3.1	111.00±7.28	27.50±3.50 (2.70)
AF23_132	85.12	1.993	6.06±4.01	1.12E-13± 5.72E-15	29.78±2.77	91.90±6.18	22.95±2.85 (2.27)
AF23_133	87.07	1.990	4.89±3.55	6.86E-14± 4.50E-15	50.41±5.3	73.50±6.73	14.63±2.05 (1.64)
AF23_136	85.50	2.009	5.71±3.81	1.03E-13± 5.17E-15	35.16±3.21	89.00±6.19	17.26±2.24 (1.60)
AF23_137	75.15	2.006	6.09±3.69	4.57E-14± 2.99E-15	34.41±2.87	42.10±3.26	8.39±1.10 (0.85)
AF23_138	80.06	2.002	4.68±3.64	5.14E-14± 3.44E-15	63.69±7.27	65.30±6.52	9.00±1.41 (1.05)
AF23_139	79.23	2.000	5.42±3.60	5.69E-14± 3.42E-15	42.88±3.92	57.30±4.50	11.67±1.52 (1.18)
AF23_140	72.72	2.007	5.09±3.60	5.19E-14± 3.28E-15	55.16±5.46	62.60±5.41	11.92±1.70 (1.27)
AF23_141	66.13	1.999	6.08±3.69	5.04E-14± 3.21E-15	39.1±3.26	52.70±4.00	11.29±1.45 (1.12)
AF23_142	88.48	1.989	4.59±3.66	1.18E-13± 5.93E-15	60.19±7.24	140.00±13.10	28.12±4.00 (3.25)
23_B1	_	1.996	42.72±3.60	9.72E-16± 2.54E-16	_	_	_
23_B2	_	1.991	33.44±3.65	1.03E-15± 2.93E-16	_	_	_
23_B3	_	2.016	47.76±3.83	1.02E-15± 2.82E-16	_	_	_



Figure 4.5: *Field photographs shows volcanological features and associated lava flow fields in the central Afar sub-segments. (A) The Unda Hararo Crater. (B) lip cone at the Guma Mali sub-segment. (C) A Spatter cone associated with lava effusion from the fissural system in the Manda Hararo sub-segment. (D) The hyaloclastite deposits at the Gablaytu area. (E) A dike which transects pre-existing*

lava flows marks the pathway of magma ascent from depth to the surface. (F) Field view of a west-bounding fault scarp of a major rift graben and associated recent lava flows in the Manda Hararo subsegment.

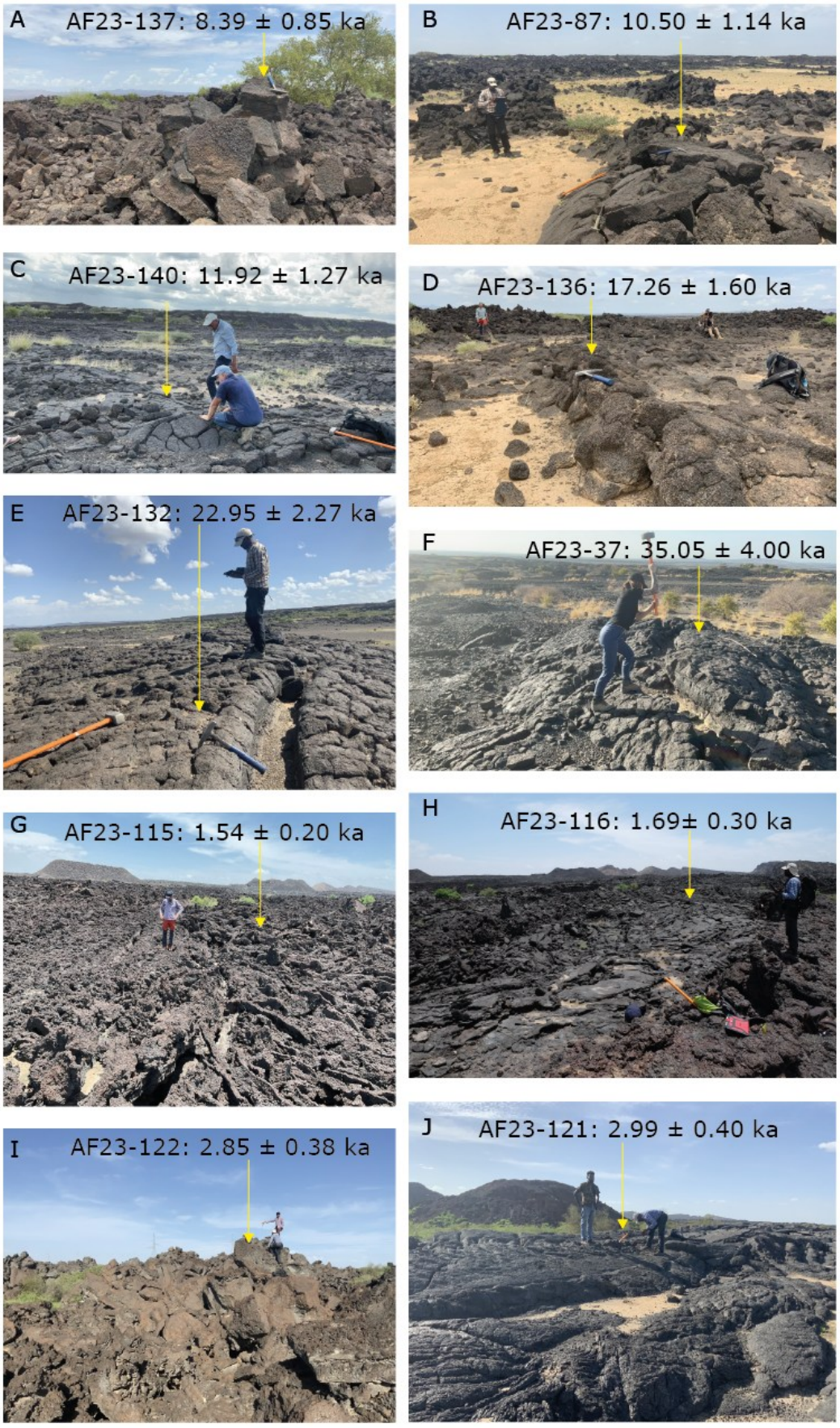
A
AF23-137: 8.39 ± 0.85 ka
B
AF23-87: 10.50 ± 1.14 ka
C
AF23-140: 11.92 ± 1.27 ka
D
AF23-136: 17.26 ± 1.60 ka
E
AF23-132: 22.95 ± 2.27 ka
F
AF23-37: 35.05 ± 4.00 ka
G
AF23-115: 1.54 ± 0.20 ka
H
AF23-116: 1.69± 0.30 ka
I
AF23-122: 2.85 ± 0.38 ka
J
AF23-121: 2.99 ± 0.40 ka

Figure 4.6: *Field photographs and ^{36}Cl CRE ages of representative lava flows. (A) Fragmented lava surface from the most recent volcanic episode of Manda Hararo. (B) Blocky flow from the fissural system of the same episode. (C) Thin lava flow from the major fissural system during the most recent Manda Hararo activity. (D) Dismantled lava surface from the most recent Manda Hararo episode. (E) Lava flow from the Unda Hararo crater. (F) Pahoehoe flow from the Loma crater. (G) A'a flow from the most recent Gablaytu volcanic episode. (H) Volcanic surface from the same episode consists of large angular blocks of lava. The blocky top of this flow is generally graded into a massive unbroken lava interior, with a brecciated layer at the base of the flow. (I) Fragmented A'a flow from the same episode. (J) Very thin, fluid pahoehoe flow from the Gablaytu fissural system during the most recent episode.*

4.2.3 Lava Geochemistry

4.2.3.1 Major and trace element compositions

The lava series from the central Afar rift system are mainly classified as sub-alkaline basalts in the Total Alkali vs. Silica, wt. % (TAS) diagram (Figure 4.7), with minor evolved products observed at Gablaytu area.

Distinct magmatic groups have been recognised in the central Afar rift system based on their geochemical characteristics, mainly their Light Rare Earth Elements (LREE) signatures, and other incompatible major and trace elements. The discrimination of distinct magma types based on LREE-enriched and LREE-depleted geochemical characteristics has been used initially by Barrat et al. (2003) and has been discussed in Birhane et al. (in preparation) with more detailed investigation and mapping of the Gumat Mali subsegment. The various additional magma groups identified and mapped in this study mainly belong to the Manda Hararo sub-segment. They are all characterized by relatively high concentrations of TiO_2, Fe_2O_3, P_2O_5, La, and Zr (Figures 4.8 and 4.9) compared to the depleted Gumat Mali groups (Birhane et al., in preparation), and by prominent positive Ba anomalies and negative K anomalies (Figure 4.10), corresponding to the Type III magmas as classified by (Rooney, 2020b). Another, already recognized (Barrat et al., 2003; Birhane et al., in prep.), difference between the Central Afar magma types concerns the anomalously low Cr content (Figure 4.9) and a significant positive Sr anomaly (Figure 4.11 D) which characterise the depleted magmas. Those new data for the Manda Hararo sub-segment, associated with the highly detailed mapping and field investigation (Figure 4.3), allow us to strictly constrain the occurrence of the depleted magmas in Central Afar to the Gumat Mali subsegment.

Those enriched magma groups display however variable levels of enrichment, reflected by parallel trends on the La/Sm vs MgO and Tb/Yb vs MgO (Figure 4.11), which cannot be accounted for by differentiation process. Projection of those trends to a common 8 wt. % MgO differentiation step (Figure 4.11 A, B) allows us to tentatively define the primitive compositions for those magma groups. When plotted on Figure 4.11 C those primitive compositions restrict the initial compositional range of the enriched endmember of Central Afar magmas to a position compatible with a global mixing between a depleted and an enriched mantle source, as already proposed by Birhane et al. (in prep.). In this model, compositional differences observed for the enriched Central Afar Magmas could result from differential incorporation of a small amount of the local depleted component. At the scale of the Central Afar rift system, we can therefore identify two distinct enriched magma types that are spatially distributed in a coherent manner, with the most enriched one globally corresponding to lavas emplaced in the southern part of the rift system (Gummat Mali, Gablaytu, Kurub, shades of green on figures), whereas lavas emplaced on the northern part (Manda Hararo, Unda Hararo, Loma, shades of blue on figures) display a slightly less enriched character. Note that the geochemical composition of the last effusive episode emplaced from 1200 to 600 yr ago at the axis of the Gumat Mali sub-segment connects it to this last magma type mainly expressed on the northern part of the Manda Hararo sub-segment. Note also that those two magma types display the same compositions than the ones already identified on the northern Dabbahu segment (Medynski et al., 2015), where the axial lavas group exhibits the most enriched composition, whereas the lateral Durrie lavas group exhibits slightly more depleted composition (Figure 4.11).

Regarding the differentiation of those volcanics from the Central Afar Rift system, lavas are mainly basaltic with MgO content ranging from 10 to 4 wt. % (Figure 4.8), and associated to rare, more differentiated dacites-rhyolites outcropping on the oldest part of the Gablaytu volcanic centre (dated ~ 30 ka). There is a general tendency for the oldest lava series (> 40 ka) to exhibit more primitive compositions (MgO > 7.5 wt. %) compared to the most recent ones (Figure 4.8), even if they still exhibit the full differentiation range until low MgO contents close to 4 %. This is except for lavas from the depleted groups that only exhibit primitive compositions at the surface (> 8 wt. % MgO).

On Figure 4.8 and 4.9, differentiation trends are primarily controlled by fractionation of clinopyroxene + plagioclase feldspar ± olivine (starting at ~ 7.5 wt. % MgO) and then followed by additional fractionation of Fe-Ti oxides (starting at ~ 5.5 wt. % MgO) and apatite (starting

at ~ 4 wt.% MgO), which is associated with typical triangular-shape patterns for TiO_2, Fe_2O_3 and P_2O_5. However, the most recent volcanic episodes from Gumat Mali (see discussion in chapter 3; Birahne et al., in prep.) and Gablaytu, as well as some few other lavas from the older groups, deviate from this pattern, showing two distinct evolutionary trends in TiO_2, Fe_2O_3 and P_2O_5 that cross-cut the classical fractionation trends. Moreover, lavas associated with those trends also exhibit compositional deviation in the Al_2O_3 vs MgO graphs, suggesting interaction with plagioclase. The first cross-cutting trend, supported by some of the recent Gablaytu basalts, is essentially linked to plagioclase assimilation and/or accumulation. Although there exists textural evidence for plagioclase accumulation in those porphyritic lavas, quantitative petrographic analysis reveals a percentage of plagioclase phenocrysts insufficient to fully account for the compositional deviation, indicating that it is also necessary to consider plagioclase assimilation at depth, before eruption of the lavas, in order to explain the trends observed (see chapter 2 for details on quantitative estimations). The second cross-cutting trend cannot be exclusively explained by interactions with plagioclase and additionally requires magma mixing and hybridisation processes within the trans-crustal plumbing system. This is consistent with previous observations from the Dabbahu volcano (Figures 4.8; Field et al., 2012a; Medynski et al., 2013) and Erta Ala range (Pin et al., 2024). Cross-comparisons of potential mixing solutions within the various compositional spaces of figure 4.8 and 4.9 suggest that along this trend initial melts could be mixed with a more differentiated mush assemblage containing principally plagioclase, and characterized by residual liquids with MgO content ranging between ~ 2.5 wt. %, if dominated by the liquid, to ~ 5 wt. %, if melt/mineral proportions are ~ 50/50. Those two trends branch in the standard differentiation pattern between 6.5 and 7.5 wt. % MgO, indicating that magmas present within the transcrustal reservoirs system at that key stage of differentiation can either: (i) continue their differentiation process without specific additional interactions for most of them, or (ii) mix and hybridize with plagioclase-rich mush for a limited proportion of them. Magma mixing processes are further supported by trace element ratios (i.e. La/Sm and Tb/Yb on Figures 4.11), for which the various magma groups exhibit complex distribution along the main trends, not fully in agreement with simple fractional crystallization control. This is especially true for La/Sm and very well illustrated by the last fissural episode from the axial Gumat Mali sub-segment which exhibits a very large compositional variation over a very limited MgO range (see detailed discussion on chapter 3, Birhane et al., in prep) crosscutting the full distribution of Central Afar enriched magmas. This highlights the fact that in the complex transcrustal reservoir system such mixing,

and hybridisation processes can also mobilise different types of magmas and not only different stages of differentiation of the same type.

4.2.3.2 Sr, Nd and Pb isotopes

Sr, Nd and Pb isotopes of magma groups from the central Afar rift system are presented in Table S4.2. Those data exhibit $^{87}Sr/^{86}Sr$ in the range 0.7036-0.7043, $^{43}Nd/^{144}Nd$ in the range 0.51284 - 0.51294, and $^{206}Pb/^{204}Pb$ in the range 18.12-18.57. On Figure 4.12 A, they lie within the regional distribution of basalts from the Ethiopian volcanic province generally interpreted (i.e., initially in Rooney et al. (2012), following a model of Schilling et al. (1992) as a mixing between a proposed composition for the Afar mantle plume (of "C" type component composition) and ambient mantle represented by a mixing between the global DM component and a local Pan-African one, delaminated into it. They cluster intimately with those of the local Dabbahu segment (Ferguson et al., 2013; Watts et al., 2025) and Stratoid formation (Alene et al., 2017), as well as with those of the Main Ethiopian Rift (Rooney et al., 2012) and older Continental Flood Basalts (Baker et al., 1996; Chazot and Bertrand, 1993; Pik et al., 1999), and differ significantly from those of other magmatic segments of Afar, including Erta Ale (Watts et al., 2023, 2025) Manda Inakir / Moussa Ali (Deniel et al., 1994), Gabillema and Adda'do (Watts et al., 2025) and Asal (Deniel et al., 1994) that all together cluster at higher $^{206}Pb/^{204}Pb$ and lower $^{87}Sr/^{86}Sr$, closer to the Afar plume composition.

In detail, the distribution of those data for the Central Afar Rift system spans a relatively wide and continuous range defined by three isotopic endmembers, noted C1, C2 and C3 on Figure 4.12 B. Moreover, those endmembers are in relatively good agreement with other apparent clusters from the MER and Central Afar, suggesting that they can share a common and coherent frame of mantle compositions and origin. There exists also a good and continuous correlation between this isotopic spread, especially $^{206}Pb/^{204}Pb$, and the REE ratios that discriminate the depleted and enriched endmembers (Figure 4.12 C and D), with C1-C2 component corresponding to the enriched part and C3 to the depleted part. The discrimination between the two enriched magma types on the base of those isotopic data is less easy and there exist a certain overlap, even if generally the C1 component appears to be documented by lavas from the southern and most enriched one, whereas the C2 component by lavas from the northern and slightly less enriched.

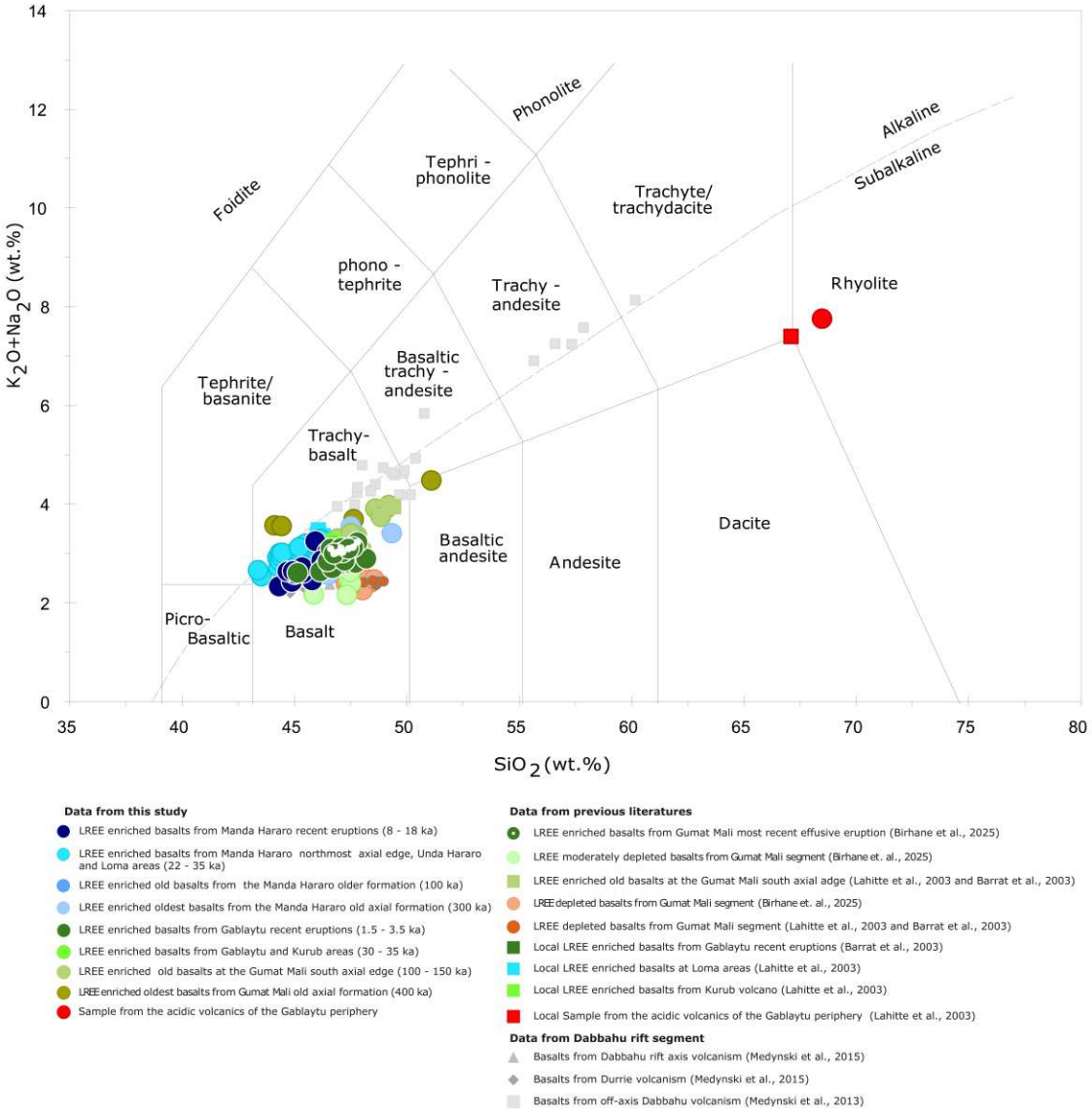

Figure 4.7: *Total Alkali vs. Silica, wt% (TAS) classification diagram for lavas from central Afar sub-segments. Nomenclature of volcanic rocks after Le Bas et al. (1986). Discrimination line between the alkaline and subalkaline group is after Irvine and Barragar (1971).*

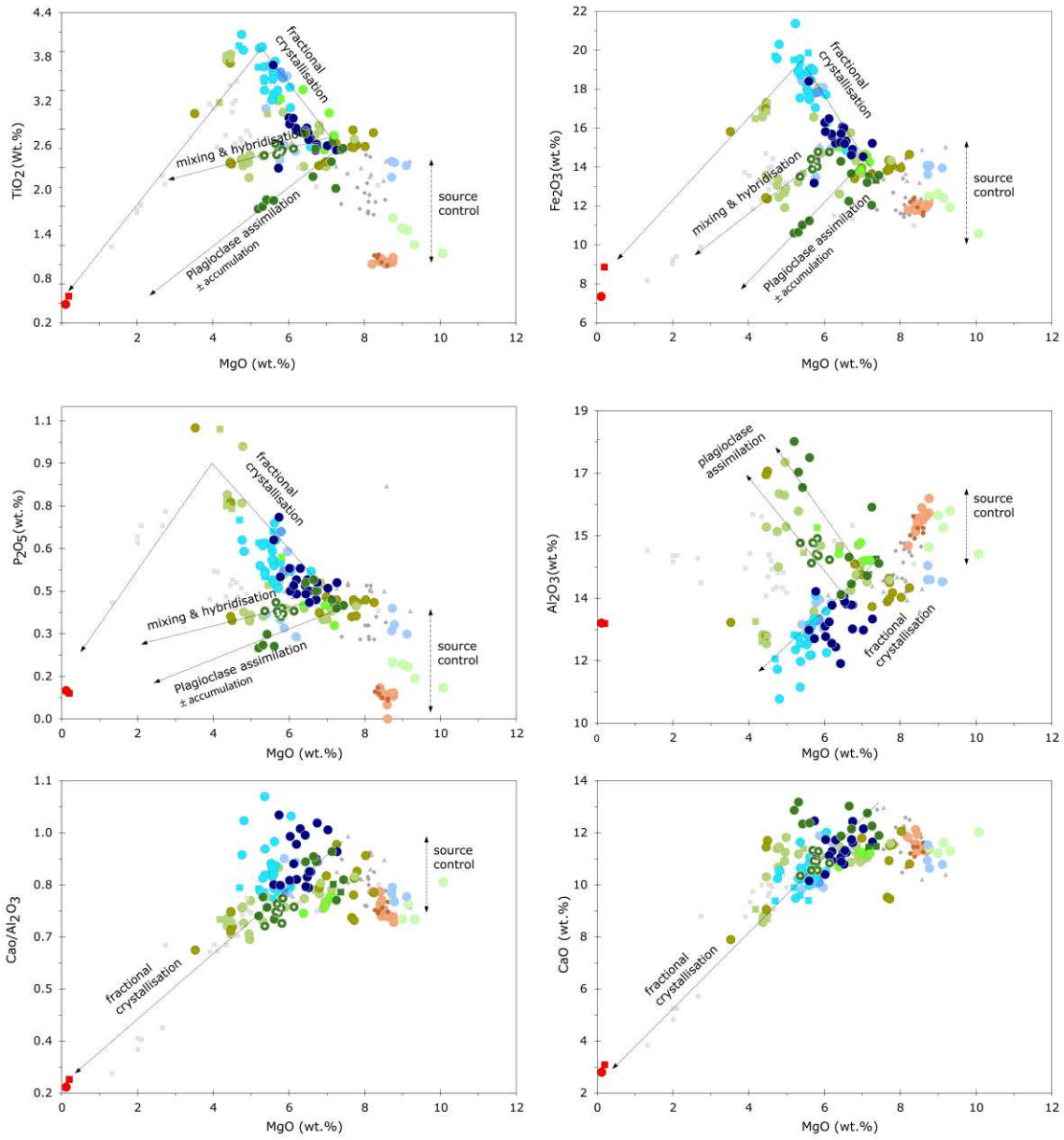

Figure 4.8: *Major element Harker diagrams show variations in major oxides vs MgO among the lavas from central Afar. The legend is the same as for figure 4.7.*

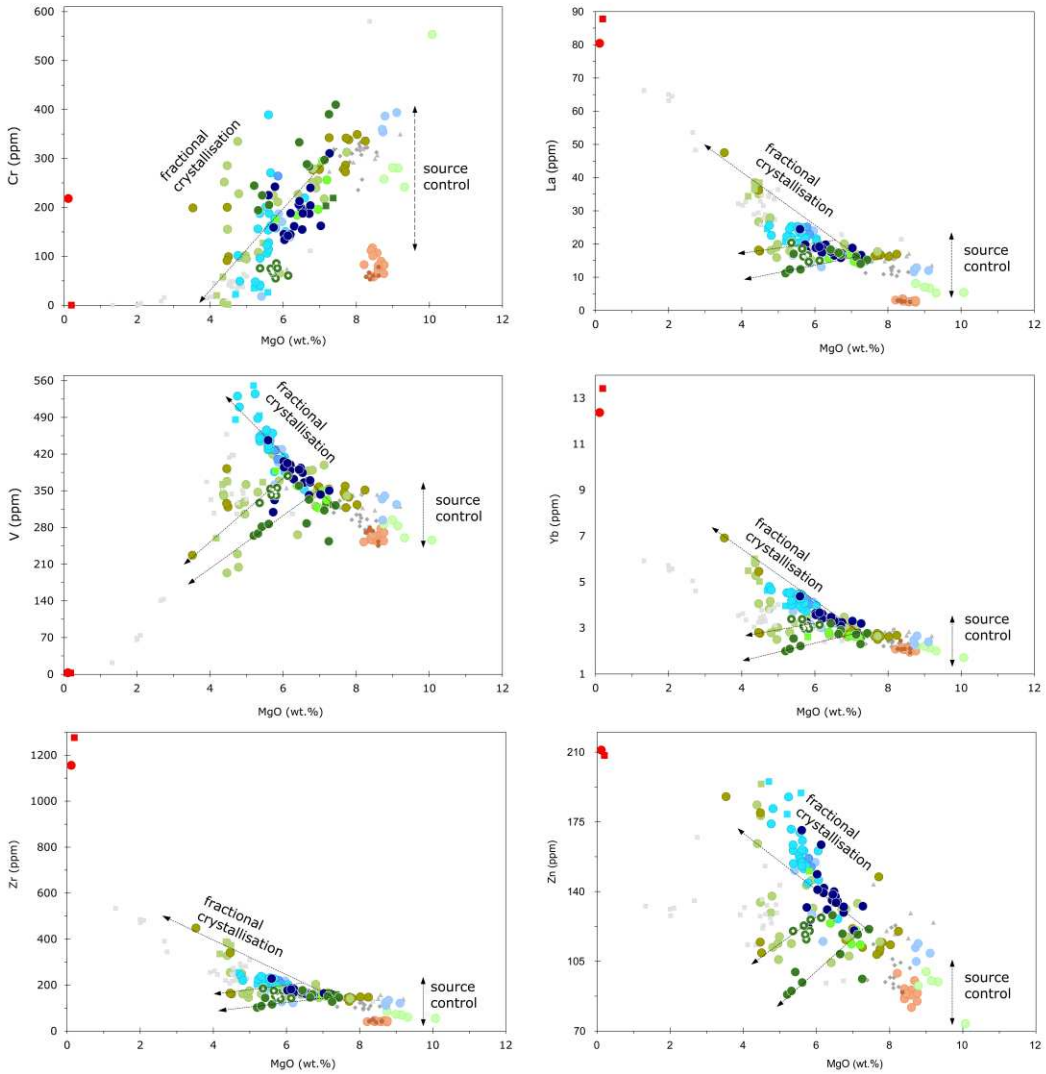

Figure 4.9: *Variations in trace elements vs MgO of lavas from central Afar. The Sr anomaly is calculated as Sr* = Sr/((Pr+Nd)/2) after normalisation to primitive mantle (Sun and McDonough, 1989). The legend is the same as for figure 4.7.*

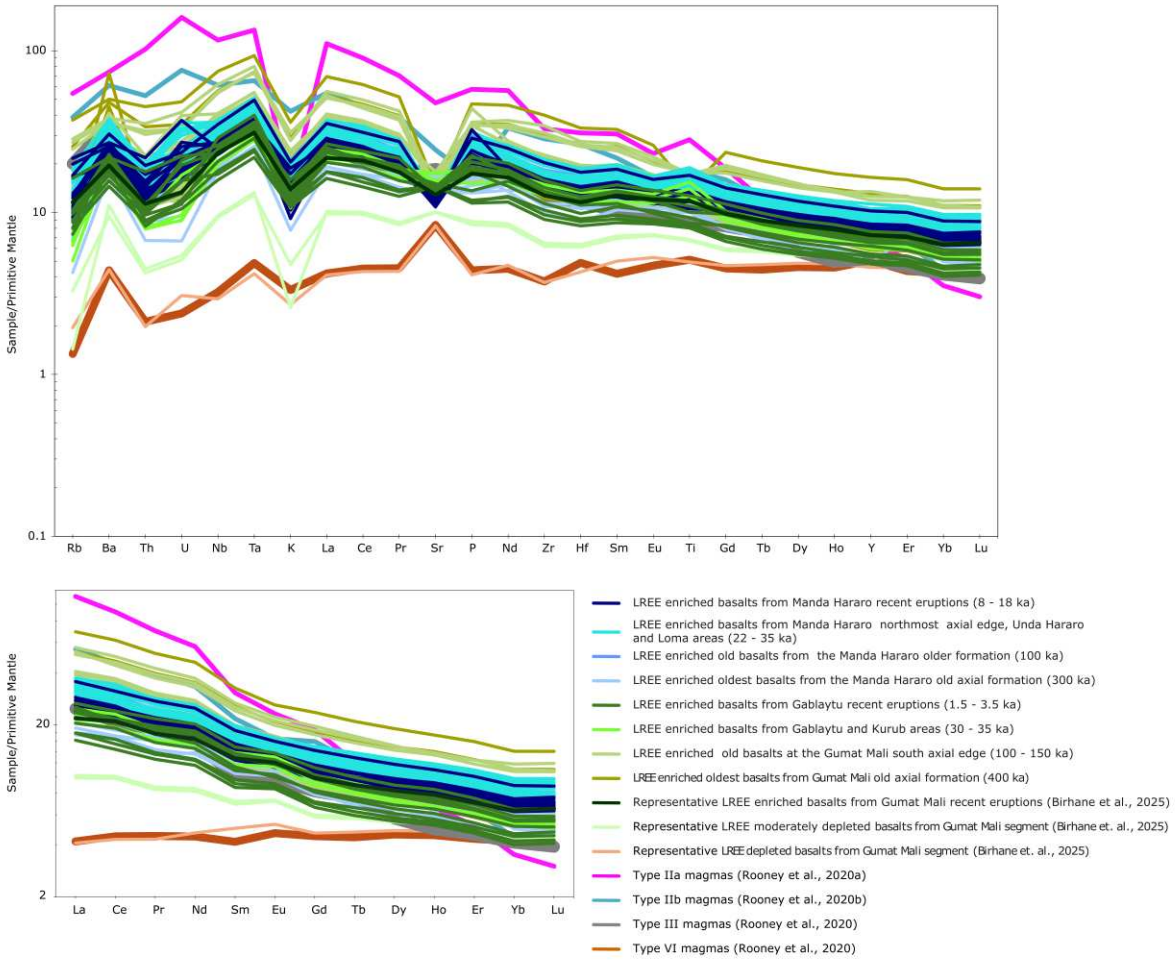

Figure 4.10: *(a) multi-element variation diagram and (b) Rare Earth Element (REE) patterns of the lava series, both normalized to primitive mantle (Sun and McDonough, 1989).*

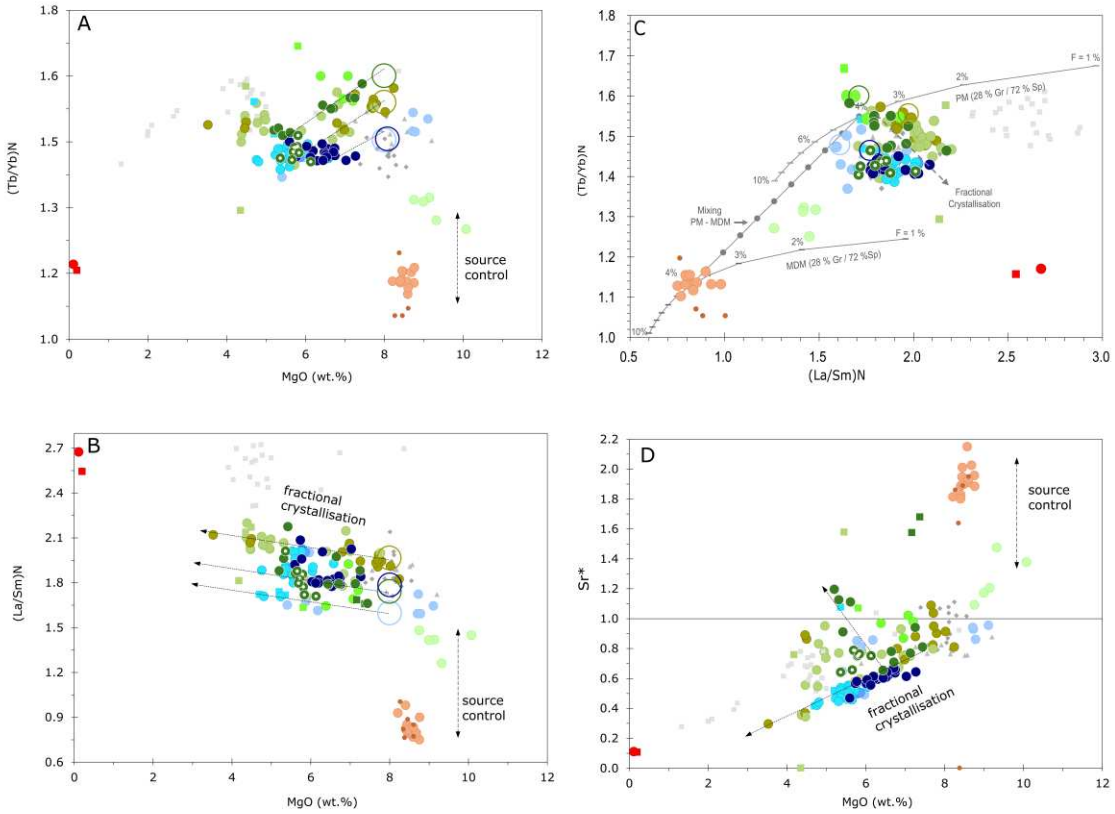

Figure 4.11: *Trace element ratios of lavas from central Afar. Compositions are normalized to primitive mantle (Sun and McDonough, 1989). The melting curve (C) for Tb/Yb versus La/Sm, produced using the same modeling approach and parameters as described in Birhane et al. (in preparation, chapter 3). Legend is the same as for figure 4.7.*

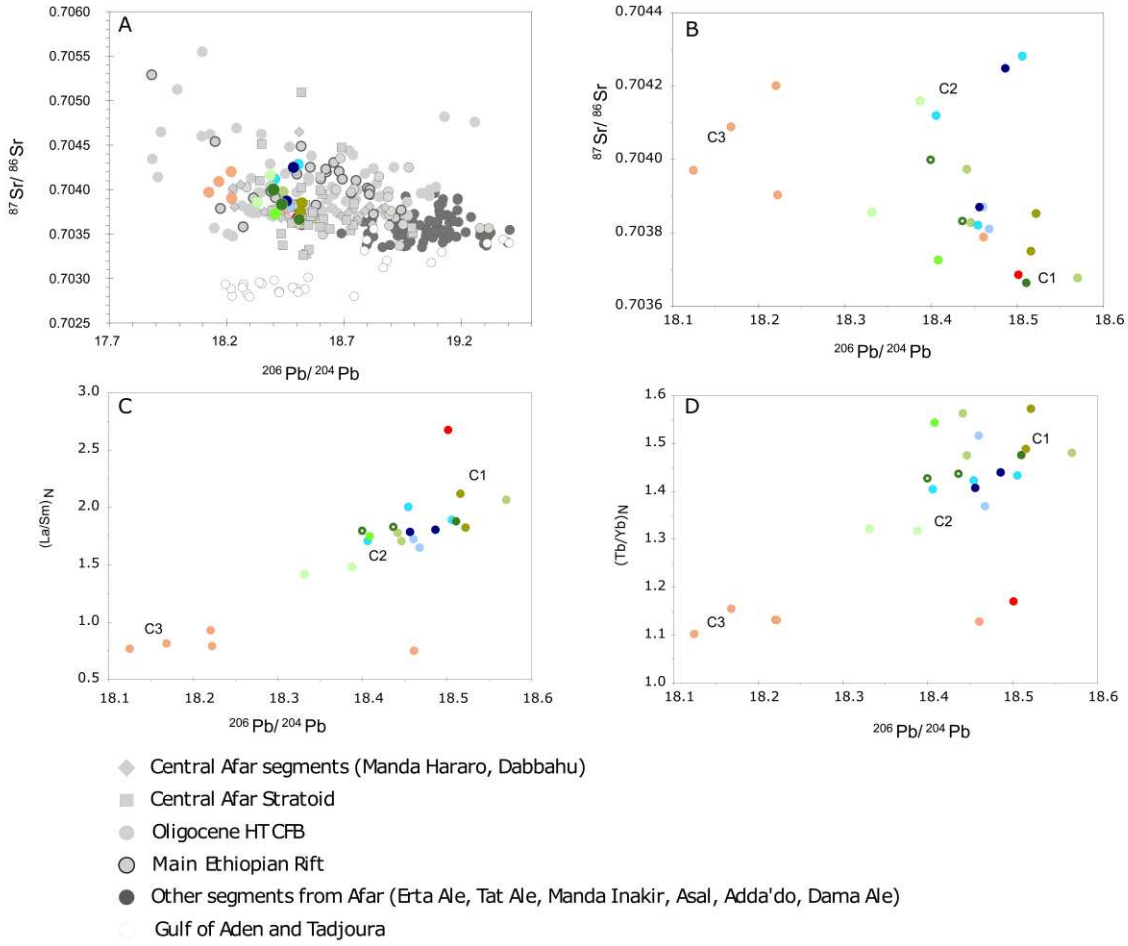

***Figure 4.10**: plots of isotopic composition highlighting the mantle end members and potential mix between various proportions of those components associated with the magma groups from the central Afar sub-segments according to (Rooney et al.,2012) proposition. For samples in this study, legend is the same as for figure 4.7*

4.3 Discussion

4.3.1 Magma types

Geochemical observations integrated with high-resolution lava chronology and mapping across the central Afar sub-segments allow us to distinguish distinct magma types that are spatially separated (Figure 4.3 and 4.4). Trace element ratios and isotopic signatures (Figures 4.11 and 4.12) reveal three principal groups: (i) the most enriched magma series from the southern part of the rift system, (ii) the slightly less enriched magma series from its northern part, and (iii) the depleted and intermediate magma series outcropping along, and strictly restricted to, the GM subsegment. Birhane et al. (in prep., chapter 3) already concluded for the GM subsegment that mantle source heterogeneities may play a significant role rather than potential crustal assimilation processes to account for the geochemical characteristics of the depleted and enriched magma types of central Afar. They proposed that both components would represent gabbroic ocean-crustal material with various initial mineralogical composition (plagioclase vs. clinopyroxene) modulating the final enriched or depleted characters of those geochemical endmembers as well as some of their common (prominent positive Ba anomalies and negative K anomalies) and specific (anomalously low Cr content, significant positive Sr anomaly, for the depleted) characteristics. The highly detailed description we provide in this study at the scale of the full Central Afar rift system confirms this interpretation. Indeed, trace elements ratios and isotope correlations (Figure 4.12) clearly require the occurrence of specific mantle components (C1, C2, and C3) involved in the generation of initial parental magmas and resulting from a common melting process sampling them in varying proportions in the field of garnet stability. These new data enable us to investigate, on a scale not yet documented, mantle heterogeneities at the axis of a magmatic segment in Afar. Those 3 components do not appear to be controlled by large scale spatial geometrical variations of the upwelled mantle (see Watts et al., 2025 for a discussion) but rather reflect some small-scale heterogeneities in part controlled by the lithology and fertility of each mantle component (depleted vs. enriched).

A striking additional feature resides in the fact that the 3 isotopic endmembers we document for the Central Afar magmas also acknowledge for isotopic clustering of other published data from this rift system including the northward Dabbahu segment (Ferguson et al., 2013; Feyissa et al., 2019; Watts et al., 2025), the older Afar Stratoïd formation (Alene et al., 2017; Feyissa et al., 2019), as well as from more distal locations like the MER (Rooney et al., 2012; Ayalew et al., 2016; Castillo et al., 2020) or more older magmatic phases like the Oligocene CFBs (Chazot and Bertrand, 1993; Baker et al., 1996; Pik et al., 1999). On the contrary they contrast

with clustering of other magmatic segments of Afar (Deniel et al., 1994; Watts et al., 2020, 2025) and represent therefore key observations for debates concerning the composition and spatio-temporal heterogeneities of the underlying mantle upwelling (Pik et al., 2006; Rooney et al., 2012; Castillo et al., 2020; Watts et al., 2025).

4.3.2 Differentiation of magmas and crustal processes

The recent enriched magmas (< 40 ka) across the MH and GM sub-segments present a restricted range of differentiation from 7.5 wt.% MgO to slightly more evolved compositions of 5-6 wt.% MgO (Figure 4.13). Overall, the temporal evolution of magmas over the last 40 ka (Figure 4.13) displays compositional oscillations between those two differentiation stages, contrasting with previous periods (> 75 ka) for which more primitive compositions (MgO > 8 wt. %) can be observed. Highly differentiated rhyolitic lavas are extremely rare and can only be observed in the Gablaytu volcanic centre (at ~ 30 ka). Some of these oscillations are particularly well documented by our new ^{36}Cl CRE ages (Figure 4.13) for the most recent volcanic episodes of the MH (8 – 18 ka), Gablaytu (1.5 – 3 ka) and GM (0.6 – 1.2 ka). In this high-resolution record, continuous negative correlations towards low-MgO can be interpreted as differentiation lines, whereas positive one towards high-MgO can represent periodic recharge of the shallow reservoirs by new and less differentiated magma originating from deeper locations in the crust. Some of these magmas additionally show evidence of mixing and hybridisation, involving interaction with more differentiated melts and plagioclase assimilation. Such magmatic processes witness the presence of zones of relatively differentiated mush in the transcrustal plumbing system and their interaction with less differentiated basalts during their migration. Those hybridization/assimilation events appear preferentially documented at the end of the differentiation phases (Figure 4.13). One replenishment process has been precisely captured by the last fissural episode at the axis of the GM sub-segment (Chapter 3, Birhane et al., in prep.), which document and constrain a hybridization event associated with surface eruptions over a period of a few hundred years, contrasting with what has been recently observed in Iceland over a couple of months (Halldórsson et al., 2022) or during the Ardoukoba eruption in 1978 in Djibouti over a week (ref, chapter 5). All those observations suggests that magmas stored at different crustal depths and differentiation stages were repeatedly mobilized, differentiated and interacted over typical timescales of ~0.5 ka for the GM replenishment and 1.5 to 4 ka for the Gablaytu and Manda Hararo differentiation phases respectively. Such a multistage, vertically stratified and time-

dependent transcrustal system organization can acknowledge the observed volcanic and compositional diversity at the surface of the sub-segments of the Central Afar rift system as it has been recently described for the Erta Ale volcano (Pin et al., 2024) and for the previous phase of volcanism in Central Afar (Tortelli et al., 2024).

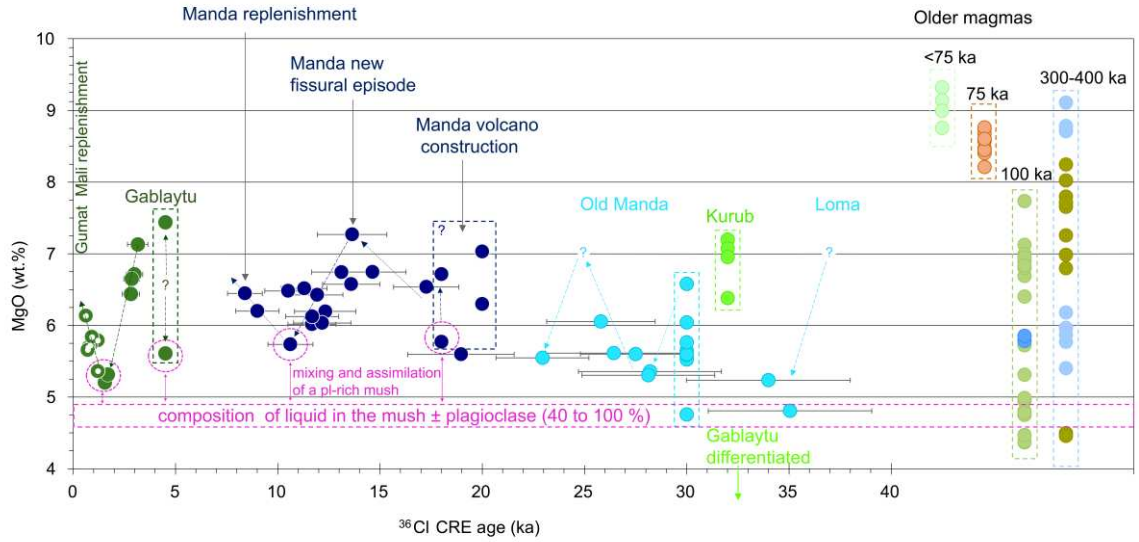

Figure 4.11: *summary compilation of cosmogenic ^{36}Cl age versus degree of differentiation of lavas (represented by MgO concentration) illustrating the evolution of the erupted magmas with time. Legend is the same as for figure 4.7*

4.3.3 Spatial and temporal organisation of the central Afar active sub-segments

The distinct magma types identified in the GM and MH sub-segments reflect differences in both crustal processes and mantle sources. Their spatial distribution indicates that the surface emplacement of each magma type corresponds to specific zones of melt generation in the mantle. Even if strictly localised at GM, the depleted source (Barrat et al., 2003; Birhane et al., 2025 in preparation) likely influenced other magma batches, producing small-scale variations in enrichment (e.g., Tb/Yb, Sr* vs. MgO). Isotopic data further link depleted, intermediate, and enriched melts, indicating a coherent melt generation. Similar geochemical diversity has already been recognized in the Dabbahu segment by Medynski et al. (2015) and mantle melting regime evaluated to be deep and hot below the Lithosphere Asthenosphere Boundary (LAB) at ~ 70 – 90 km (Ferguson et al., 2013; Wong et al., 2022). Different enriched magma types derived from slightly different mantle source mixing suggest that discrete batches of mantle melting were separated in space and time and entered the crust separately below the sub-segments. For the GM and MH sub-segments, the presence and evolution of the two distinct enriched batches of melt indicate a characteristic timescale of magma transfer from the mantle

to the surface of about ~300 ka, with the additional arrival of a depleted batch of melt still preserved within the system (Figure 4.14).

The organization of magmatism in Central Afar is largely controlled by tectonic structures corresponding to the two distinct corridors of the GM and MH sub-segments (Figure 4.3 and 4.4). The position of the en-echellon structuration of the sub-segments is the first-order control on the vertical transfer of melts, influencing their storage in magmatic reservoir and their associated differentiation within the crust.

Early-stage magmatism associated with the enriched batches of melt (400-300 ka) has been marked by the emplacement of voluminous, laterally extensive lava flows at MH and GM, that persisted until recently (> 75 ka) along the GM with the more recent arrival of the depleted batch of melt. Over time (< 100 ka), volcanism became more localized and topographically controlled by axial faults along the sub-segments, especially the MH one. This phase also corresponds to an evolution toward a more mature transcrustal system characterized by magma exchanges between reservoirs with compositions of approximately 7 to 5 wt.% MgO, suggesting continuous connections from the different shallow and deep levels of the transcrustal reservoir system (Figure 4.13 and 4.14). Similar trends in the Dabbahu segment (Medynski et al., 2013, 2015, 2016) were linked to the maturation of the plumbing system and the emergence of rift topography. Our observations and evidence are partly consistent with this model. Indeed, the first order topography at GM and MH rifts appears controlled by on strike large scale tectonic features characterized by asymmetrical deformations combining flexuration and dominant west verging faults (Figure 4.4). The second order topography is however certainly due to magmatically induced fault systems that formed through the mechanical interaction between dike injections and the brittle upper crust in order to accommodate surface deformation above the intrusions when they do not reach the surface. Such a subdued second order rift topography appears rather transient in the GM and MH sub-segments, being periodically erased by subsequent volcanic phases linked to the continuous regime of vertical magma transfer through the transcrustal system (Figure 4.14).

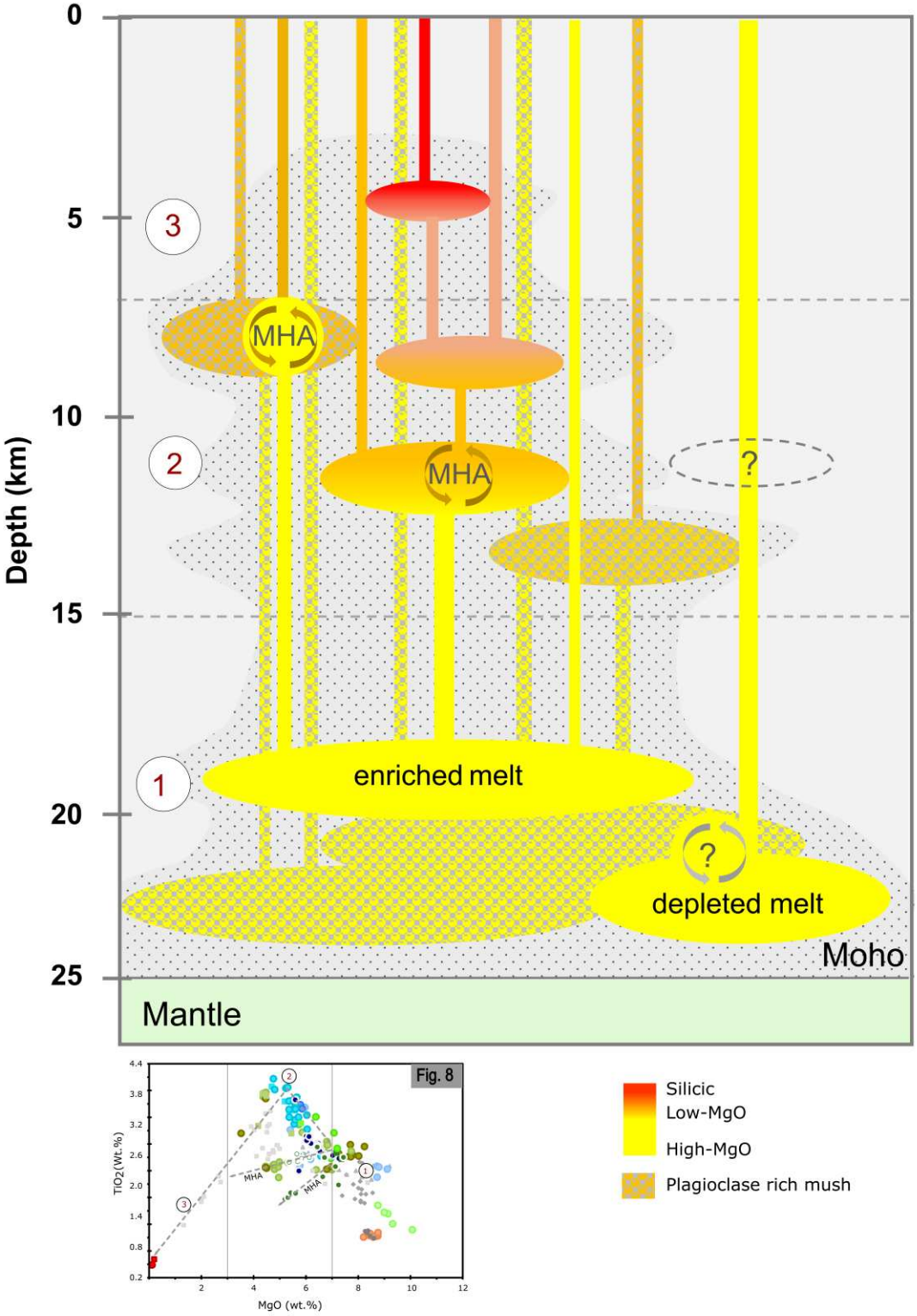

Figure 4.14: *Schematic cartoon depicting magma plumbing system organization in central Afar active sub-segments. Three-stage vertically distributed magma storage zones within the transcrustal system, defined by different stages of magma differentiation, are represented by variation in MgO. Significant amounts of high-MgO lavas of stage (1) erupted at the surface during 300–400 ka. Many of these lavas show evidence of magma hybridization and assimilation (MHA), which is interpreted to result from*

interaction of stage (1) melt with mush of stage (2) during upward magma transfer. This old magmatic phase shows no evidence of eruption from stage (3) at the surface. An additional batch of depleted melt is preserved in the deeper transcrustal system of the Gumat Mali sub-segment during a magmatic phase at 75 ka, with no evidence of stage (2) differentiation. Recent magmatic phases at the Manda Hararo sub-segment (22–35 ka and 8–18 ka) indicate storage in shallower reservoirs and correspond to maturation of the plumbing system. Absence of very-high MgO with rare differentiated lavas at the surface is observed, and eruptions during these phases are mostly from stage (2), dynamically connected with stage (1), evidencing magma replenishment that buffers compositions. Recent volcanic episodes record tapping of deeper reservoirs, with eruptions of stage (1) connected with stage (2) and evidence of MHA. The Gablaytu most recent magmas record plagioclase assimilation during differentiation, while the Gumat Mali record replenishment of a reservoir that experienced MHA with new stage (1) melt.

4.3.4 The ocean continental transition in central Afar

In central Afar, the relationship between tectonic sub-segmentation and mantle melting is key to understand how focalisation develops at the OCT. Here, different magma types identified across the sub-segments correspond to distinct mantle melt batches. The vertical transfer of these melts appears to be controlled by the large-scale tectonic structuration of the sub-segments. However, mantle melting below in the lithosphere may also influence where these tectonic structures form, raising the question of whether the focalisation at the OCT is mainly defined by tectonic structures in the crust, or by zones of mantle melting and transfer below? This has implications for evaluating the focalisation of the extension at the OCT (Ferguson et al., 2013; Medynski et al., 2015). If the focalisation is controlled by the tectonic sub-segmentation, it corresponds to a zone about 15 km wide defined by the width of each sub-segment. If it is controlled by the area of mantle melting, the zone may extend over a significantly broader area and appear less focussed. Overall, the interaction between tectonic segmentation and mantle melting explains the focusing of extension observed at the OCT in central Afar.

Observations of such rift sub-segmentation close to the OCT provide valuable information for models of evolution toward mature oceanic ridge. The various magmatic segments in Afar exhibit contrasted morphology and intensity of volcanic activity since a couple of thousand years with significantly higher volcanism at the surface for the Erta Ale range compared to the Dabahu – Manda Hararo segments of Central Afar. This difference has been related to potential more evolved maturity of the Northern Erta Ale range, closer to final break-up stage, with more

direct trajectory and flux intensity of melts toward the surface, whereas in Central Afar a large majority of melts injected in the crust would be stored at depth participating to accommodation of extension (Keir et al., 2011; Hutchison et al., 2018; others). This view has been recently challenged by (Pin et al., 2024) which described at Erta Ale volcano magmas evolution and differentiation organised with a rather developed transcrustal system and associated important intruded volumes of melts. Our new detailed investigation of the Central Afar rift system also require such type of multilevel reservoir organisation throughout the entire crust and do not appear significantly different according to volcanological, magmatic and petrological processes. In such a context, the apparent discrepancy for the intensity of surface volcanism requires alternative explanations, especially considering the fact that the long-term magmatic flux over the last 4 Ma is much more in favour of Central Afar compared to Northern Afar (Stab et al., 2016; Rime ., 2023). This is particularly true for the Gulf Basalts volcanic phase that has been emplaced on the Tendaho grabben between 1 Ma to 500 ka ago (Figure 4.2) and which witness beginning of localisation of magmatism and tectonic deformation in Central Afar (Stab et al., 2016; Tortelli et al., 2025). This specific volcanic phase emplaced just prior the current active magmatic sub-segments and exhibit structure, morphology and volumes comparable to the present-day volcanic range of Erta Ale, as well as an equivalent transcrustal plumbing system (Tortelli et al., 2024). It thus appears that the current Central Afar rift system we describe in this study does not exhibit significantly contrasted volcanic and petrologic organisation that can support the differential volumes of magma intrusions required to explain the deficit of surface volcanism compared to the Erta Ala range or to the local Gulf Basalts range. In that case, those apparent differences could not be related to any major differences in crustal processes but rather and simply to the current absolute flux of magma coming from the mantle, which could experience some discrete and transient lows in-between major pulses.

Chapter 5

The magmatic cycles of the Asal-Ghoubbet rift segment: volcanic history of the last 10 ka, constrained from high resolution cosmogenic exposure ages

Yafet Gebrewold Birhane[1,5], Juliette Pin[1,3], Lydéric France[1,2], Raphael Pik[1], Gilles Chazot[3], Irene Schimmelpfennig[4]

[1]CRPG, CNRS, Universite´ de Lorraine, UMR 7358, Vandoeuvre-les-Nancy, France ; [2]Institut Universitaire de France (IUF); [3]Laboratoire Géo-Océan (LGO), Institut Universitaire Européen de la Mer (IUEM), Université de Bretagne Occidentale (UBO), Brest, France; [4]Aix-Marseille Université, CNRS, Coll France, IRD, INRAE, CEREGE, Aix en Provence, France; [5]Department of Geology, College of Natural and Computational Sciences, Hawassa University, Ethiopia

5. Introduction

Magmatic and tectonic activities at continental rifts may end-up with the formation of new oceanic basins after a key period of transition between continental and oceanic domains (the Ocean Continent Transition - OCT), as it is currently the case in the Afar depression in the northern part of the east African rift system (Rime et al., 2023). Magmatic cycles in those rifted areas correspond to the periodic episodes of magma generation, ascent, storage, and eruption. These cycles are essential to the development of rifted landscapes and the formation of new crust. They also affect the petrology and structure of the crust, especially during the OCT in magmatic context, which vary based on the volume, timing, and frequency of magmatic events. They can vary in duration and intensity, depending on the rate of magma supply and the tectonic stresses in the rift zone, and are also based on many individual events of magma transfers and injections in the crust, sometimes associated with surface fissural eruptions. Relatively few fissural volcanic events have been recorded in the context of continental rifting. There exists some spectacular examples in Iceland (Greenfield et al., 2022; Hollingsworth et al., 2012; Pedersen et al., 2023; Rooyakkers et al., 2024; Troll et al., 2024). However, they are influenced by the hotspot and mid-oceanic ridge and cannot be considered continental rifts. Similarly, fissural eruptions related to local rifting events occur in Hawaii (Neal et al., 2018), but they are also influenced by the volcanic hotspot, making them quite specific and limited in time and space. In the recent record, the only documented examples of pure continental rifting with ongoing fissural eruptions are the Erta Ale, Dabbahu-Manda Hararo, and Asal-Ghoubbet active magmatic segments in the Afar depression (Figure 5.1).

These active magmatic segments in the Afar present various morphologies, crustal thicknesses, and magma production rates which offer the opportunity to expose extensional structures related to ocean-continent transition (Bastow and Keir, 2011; Stab et al., 2016). These segments are organized differently in terms of topography and magma supply. Such variations have been interpreted either as variations in rifting stages/maturity level (Ebinger and Casey, 2001; Manighetti et al., 2001; Bastow and Keir, 2011) or alternatively potential difference in rifting styles (Stab et al., 2016; Le Gall et al., 2018; Rime et al., 2023). However, the magnitude of volcanism, along with variations in composition, triggering such contrast remains poorly constrained at comparable temporal and spatial scales.

In particular, the recent fissural eruptions in the Asal-Ghoubbet rift segment remain poorly documented. This area also lacks precise age constraints on recent magmatic activity along the axial zone, with only limited dating available for the earliest phreatomagmatic events (Manighetti et al., 1998), or quantification of differentiation duration with isotopic disequilibria (Vigier et al., 1999).

In this study, we present an extensive set of cosmogenic age constraints on the Asal-Ghoubbet segment. We focus our attention on the axial zone lava flows to better understand the dynamics of magma transfer in crust. Combining remote sensing, field investigations, precise geological mapping, major and trace elements analysis and cosmogenic ^{36}Cl exposure dating of lava surfaces, we aim to: (i) describe the geochemical characteristics of the eruption sequence with time, and (ii) identify and quantify the duration of magmatic cycles.

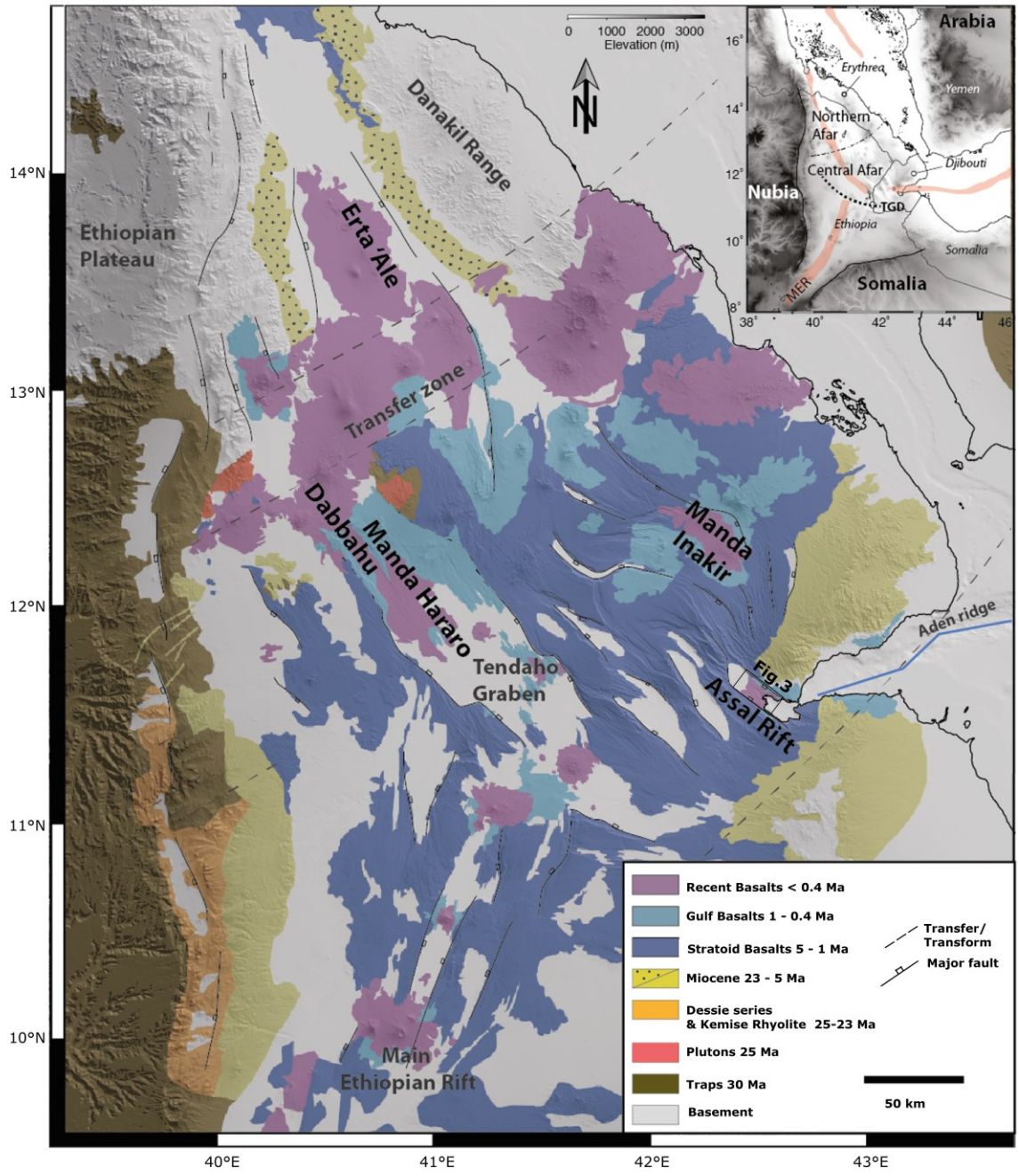

Figure 5.1: *Geological map shows the main active magmatic segments of the Afar depression modified after Stab et al. (2016)*

5.1 Geological setting

The Afar depression represents an archetype of unique geological setting where active continental rifting is currently taking place in a magmatic context at the ocean continent transition (Figure 5.1). This region is part of the broader east African rifting system where the African, Somalian, and Arabian plates are diverging, leading to the thinning of the continental lithosphere and the initiation of oceanic spreading (Hayward & Ebinger, 1996).

In this context, the Asal-Ghoubbet magmatic segment is a NW-SE trending graben, approximately 40 km long and 10 km wide, extending from the northwest shore of Asal lake to the south of Ghoubbet bay (Manighetti et al., 1998). This rift system experiences an extension rate of approximately 15 ± 2 mm/year, oriented perpendicular to the rift axis (Ruegg and Kasser, 1987). This rate is slightly higher than the divergence rate between the Arabian and Somali plates, measured at 13 ± 1 mm/year (Jestin et al., 1994; Vigny et al., 2006). However, the extension rate has varied significantly over time. For instance, it reached a peak of 60 ± 10 mm/year during 1986 –1987 (Doubre et al., 2007) but slowed to around 15 mm/year between 1987 and 2003 (Vigny et al., 2007).

The crust beneath the Asal-Ghoubbet rift thins significantly, from 20–25 km outside the rift to about 5 km near the axis, correlating with intense magmatic and tectonic processes (De Chabalier & Avouac, 1994; Doubre et al., 2007; Hammond et al., 2011). Although not fully oceanic, it resembles slow-spreading mid-ocean ridges in structure, volcanism, and seismic activity (Needham et al., 1976; De Chabalier & Avouac, 1994; Manighetti et al., 1998). The inner floor of the rift is marked by dense arrays of open fissures aligned with normal faults. In contrast, the external margins are seismically and volcanically inactive. The internal margins, however, are collapsed, fractured, and volcanically active. The Asal rift features an axial graben, 300 to 800 m deep, and contains the heavily faulted Fieale volcano, a phreatomagmatic edifice situated in its southeastern inner floor. A potential magmatic reservoir that extends 2 to 3 km laterally, with an unknown thickness, and at a depth of more than 5 km is located beneath the volcano (Pham Vanet al., 1981; Doubre et al., 2007; Smittarello, D. et al., 2016). Active volcanism also occurs to the northwest and southeast of the volcano (Demange et al., 1980; De Chabalier & Avouac, 1994).

Magmatism can occur early and massively during the continental rift evolution, especially when the underlying asthenosphere presents a thermal anomaly like a rising mantle plume, as below Afar-Ethiopia (Marty et al., 1996; Pik et al., 2006; Bastow et al., 2008; Rooney et al., 2012) or later and more sporadically as recorded along the West-Afar margin during the Oligo-

Miocene phase of extension (Wolfenden et al., 2005; Stab et al., 2016). In Central and Southern Afar the Plio-Pleistocene has been marked by the emplacement of an important and again massive phase of volcanism from ~ 4 Ma to ~ 1 Ma, post thining of the lithosphere (Stab et al., 2016), known as the Stratoid formation (Kidane et al., 2003; Lahitte et al., 2003; Tortelli et al., 2025). During the post-stratoid localisation phase, silicic volcanism played a key role in initiating the evolution of the Asal rift (Pinzuti et al., 2013). Around 1 My years ago, rhyolitic domes were emplaced along NW-SE oriented faults, linked to the propagation of the Aden ridge into the region (Lahitte et al., 2003). Gulf basalts series, interpreted as products of eruptions from the fissural system associated with incipient rifting, cover the silicic products (Pinzuti et al., 2013 and references therein). These eruptions began at 853 ± 35 ka with alkaline fissural basaltic flows (picrites) and ended with a shallow marine/lacustrine eruption forming hyaloclastite dated at 326 ± 15 ka ago (Manighetti et al., 1998). The youngest basalts from these series are offset by faults on either side of the Asal rift, defining the boundary of the central series. This magmatic phase sourced from the Fieale central volcano, filling the rift between 300 and 50 ka ago (Manighetti et al., 1998). Basaltic flows older than 150 ± 15 ka spread across the rift zone, whereas flows younger than 87 ± 29 ka were concentrated near the rift axis, abutting fault scarps (De Chabalier & Avouac, 1994). After 90 ka, magmatic activity decreased, and border faults began to develop shaping the modern rift geometry. Normal faults formed on either side of the new inner floor (Manighetti et al., 1998; Pinzuti et al., 2013), which became the site for later axial series eruptions from small volcanic edifices aligned along eruptive fissures. The southwestern part of the internal margins has been dated to 65 ± 24 ka (Manighetti et al., 1998).The most recent volcanic event occurred at Ardoukoba volcano, between November 7 and 14, 1978 (Vigier et al., 1999). This seismo-volcanic event generated fissures, small normal fault scarps, and basaltic fissural eruptions, resulting in ~2 m of horizontal extension and ~70 cm of subsidence (Ruegg and Kasser, 1979; Tarantola et al., 1980; Manighetti et al., 1998). Pinzuti et al. (2013), highlighted a direct correlation between the geochronological ages of basalt samples and their distances to the active rift axis in the Asal rift, as well as a sharp contrast of mantle melting conditions, with shallower melting at the axis of the rift compared to its shoulders. Using K-Ar dating from (Manighetti et al., 1998), and sample distribution, the mean spreading rate of 2.9 ± 0.2 cm/year was calculated over the last 620 ka. Vigier et al., (1999) investigated the last Ardoukoba eruption events on a much more restricted time scale and highlighted the duration of the last differentiation. The crystallization

age of 870 years (from a closed-system model) and 1880 years (from an open-system model) is calculated for the most differentiated magma of the series.

The magmatic processes observed in the Asal-Ghoubbet rift, particularly the occurrence of fissural eruptions, provide critical insights into the early stages of continental break-up. This paper focuses on the very recent magmatic activities which occurred after the past 65 ± 24 ka (Manighetti et al., 1998), to decipher the magmatic cycles at the various volcanic centres of the Asal-Ghoubbet rift system.

5.2 Materials and methods

5.2.1 Remote sensing and Geological Mapping

The spatial extent of recent lava fields within the Asal-Ghoubbet rift segment is mapped using a combination of high-resolution satellite imagery from Google Earth, and high resolution Multispectral (Ms) orthoimages (Figure 5.2) and Digital Surface Models (DSM) derived from Pleiades satellite data.

Two Pleiades stereo pairs in black and front images were freely acquired from French national service platform, Form@ter. Pleiades imagery offers images with high spatial resolution of approximately 0.7 meters for the panchromatic channel (wavelength in the 480–830 nm range) and around 2.8 meters for the multi-spectral blue, green, red, and near-infrared channels (Gleyzes et al., 2012). The multispectral Pleiades images were processed through the freely accessible Form@ter service to generate high-resolution Ms orthoimages and DSM. This approach allowed us for detailed visual interpretation and identify the distinct eruption units that we need to precisely target our lava sampling sites.

The mapping process uses Ms orthoimages and high-resolution DSM combined with ArcGIS data to identify flow patterns, texture differences, and colour variations. The satellite imagery was supplemented by field observations to validate and refine the remote sensing interpretation and enhance the detailed mapping of the various lava fields.

5.2.2 Geochemical data analysis and corrections

5.2.2.1 Bulk-rock measurements

In this study, we analyzed 33 basaltic lava samples collected from various volcanic centres of the Asal-Ghoubbet rift system during a 2022 field expedition. The samples were crushed, powdered, and analyzed for major and trace element compositions at the

Centre de Recherches Pétrographiques et Géochimiques (CRPG-CNRS, Nancy, France). Major element compositions were measured using an Inductively Coupled Plasma Atomic Emission Spectrometer (ICP-OES), while trace element concentrations were determined by Inductively Coupled Plasma Mass Spectrometry (ICP-MS). Sample locations are shown in Figure 5.2, and detailed analytical results after correction for plagioclase accumulation are provided in Table S5.1.

5.2.2.2 Plagioclase Accumulation Correction

Most lava samples studied here are affected by plagioclase mineral accumulation. This is true for most of the inner floor lava samples in the Asal rift (Vigier et al., 1999; Pinzuti et al., 2013). Therefore, the whole-rock composition of the samples is corrected for modal abundances and chemical composition of plagioclase phenocryst. The correction follows the protocol of (Neave & Putirka, 2017; Hartley et al., 2018; Bennett et al., 2019). This was achieved through removing the host plagioclase from the melt until its MgO-Al_2O_3 or TiO_2-Al_2O_3 systematics are consistent with liquid line of descent defined by the bulk composition of aphyric lava flows at the axial zone of the Asal rift and the composition of olivine-hosted melt inclusions (Table S5.4). The primary focus was to distinguish between the contributions of plagioclase and the liquid phase to the geochemical signature of the analysed samples. We choose to use K_2O-MgO systematics as they are both incompatible in plagioclase. All the data presented in the main text are corrected data (Table S5.1). While the corrected values might vary slightly if different liquid lines of descent were considered, the overall trends remain unchanged. The most primitive lava would still be the most primitive, and the most evolved would remain the most evolved. Ni and Cr show wide variations between the dominant less differentiated porphyritic lava samples and the most differentiated aphyric samples (Figure S5.2). This scattering could be due to the plagioclase correction which only affects the less differentiated porphyritic samples. Because of this, we base our interpretations on the plagioclase-corrected whole-rock compositions, as these corrections are necessary to isolate liquid-phase geochemical signatures in the porphyritic samples.

5.2.3 In situ-produced ^{36}Cl Cosmic Ray Exposure (CRE) dating

5.2.3.1 Sampling strategy and Physical preparation

Dating lava flows using cosmogenic isotopes is a robust method for assessing the exposure duration of geological surfaces (Gosse & Philips, 2001; Blard, 2021). When lava flows are exposed at the surface, cosmic rays continuously bombard the uppermost meters of the rocks, producing cosmogenic isotopes that accumulate in the rock's surface layers. By quantifying these isotopes, the exposure age of a sample can be determined. The method used is based on the analysis of ^{36}Cl present in plagioclase, a mineral abundant in the sampled lava flows.

To establish the ^{36}Cl CRE ages for the lava flows, a field campaign has been conducted in 2022. A total of 12 lava flow samples was collected from the uppermost 3-9 cm of solid rock surfaces, over a width of at least 10 cm using a hammer and chisel. Sampling focused on surfaces that have remained exposed to the cosmic rays since their formation. Particular attention was given to assessing whether the targeted flows have been covered by other materials (e.g., sediment layers or water bodies) before last exposure. The samples were taken from flat, non-eroded surfaces, ensuring minimal post emplacement deflation. Recording geographic coordinates using GPS and measuring the angle of incidence (θ) of cosmic rays on the sampled lava surface relative to the volcanic cones and cliffs were also recorded. The lava samples in this study originate from lava flows associated with effusive episodes of the fissural system at the axial volcanic centers of the Asal-Ghoubbet segment (Figure 5.2). Comprehensive field data and sample information are summarized in Table 5.1.

The collected lava samples were crushed and sieved to retrieve100-500 µm grain size fractions. Sieving was conducted under a water bath to remove dust particles. The sieved samples were then rinsed, dried, and passed through a Frantz magnetic separator several times to extract plagioclase. The target was to obtain 100-120 g of pure plagioclase separates for measurement. However, due to variable plagioclase content, the extracted amounts ranged from 46 g to 210 g. For samples with insufficient pure plagioclase, fractions enriched in plagioclase were used. This approach aimed to minimize the fine-grained groundmass, which is often rich in chlorine and complicates data interpretation.

Two samples (22DJ18 and 22DJ47) contained insufficient plagioclase, and measurements were therefore conducted on the matrix (Table 5.1). Additionally, whole-rock samples were powdered for major and trace element analyses (Table S5.1). These analyses were used to compute the low-energy neutron flux in the samples, which induces the ^{36}Cl production from capture of the low-energy neutrons on ^{35}Cl.

***Table 5.1**: Locations and description of lava flow samples used for ^{36}Cl CRE dating. For all analysed samples, 100-500µm grain size fraction was used. Scaling factor is according to (Stone, 2000) and shielding factor is obtained from online topographic shielding calculator, http://stoneage.ice-d.org/math/skyline/skyline_in.html.*

Sample Name	Latitude (°N)	Longitude (°E)	Altitude (m)	Volcanic centres	Thickness (cm)	Mineral used for CRE dating	Shielding factor	Stone scaling factor (Neutrons)	Stone scaling factor (Muons)
22DJ08	11.61211	42.47853	-65	Axial Chain	5	Plagioclase		0.583	0.593
22DJ14	11.58089	42.50178	113	Armae Koma	3	Plagioclase		0.666	0.647
22DJ18	11.56808	42.50608	73	Ghoubbet	9	Matrix		0.646	0.635
22DJ20	11.62725	42.43550	-151	Manda	2.5	Plagioclase	0.959	0.546	0.568
22DJ22	11.62775	42.43931	-139	Manda	3	Plagioclase		0.551	0.572
22DJ24	11.62133	42.44242	-129	Manda	3	Plagioclase		0.555	0.574
22DJ27	11.61408	42.44417	-126	Manda	4	Plagioclase		0.557	0.575
22DJ31	11.55744	42.52589	17	Ghoubbet	3	Plagioclase	0.976	0.619	0.617
22DJ47	11.59500	42.49144	88	Axial Chain	3.5	Matrix		0.654	0.640
22DJ50	11.56814	42.52539	14	Ghoubbet	2	Plagioclase	0.987	0.619	0.617
22DJ62	11.59572	42.47056	9	Manda	2.5	Plagioclase	0.990	0.616	0.615
22DJ65	11.58892	42.47719	2	Secondary chain	2	Plagioclase		0.612	0.613

5.2.3.2 Chemical preparation and ^{36}Cl measurements

The chemical preparation of the samples and cosmogenic ^{36}Cl analyses were conducted at the Centre Européen de Recherche et d'Enseignement des Géosciences de l'Environnement (CEREGE; Aix-en- Provence, France) using accelerator mass spectrometry (AMS). The preparation protocol follows established methods, including those described by (Stone et al., 1996; Schimmelpfennig et al., 2009).

Samples were first cleaned to remove material unrelated to basalt, such as lichens and carbonate residues, and to eliminate atmospheric chlorine trapped in fractures or vesicles. This step involved soaking the samples in a nitric acid (HNO_3) solution with ultrapure water on a shaking table for 24 hours. 100 -120 grams of sample grains were rinsed with Milli-Q water to remove fine particles and leached in a dilute HF/HNO_3 mixture. This process dissolved approximately

20% of the sample mass, reducing atmospheric ^{36}Cl and potential chlorine-rich mineral phases (Schimmelpfennig et al., 2009).

After the purification, two sequential dissolution steps were carried out: (1) dissolving 20% of the sample mass to reduce total chlorine concentrations which is responsible for the formation of ^{36}Cl by low-energy neutron capture on ^{35}Cl and to concentrate ^{36}Cl in the remaining fraction. (2) complete dissolution of the remaining material (70-100 g) in a HF/HNO_3 solution for isotopic analysis. The HNO_3 is first added and then HF. To ensure controlled dissolution, samples were placed in an ice bath while HF was added slowly.

The samples are then sealed and agitated for 12 hours on a shaking table. Some microlith samples dissolved poorly and were left longer in the bath on a hot plate to increase the dissolution kinetics. Aliquots (1 g) were taken from the rinsed and dried etched samples to analyse major elements, trace elements, and target elements (Ca, K, Fe, Ti, and Fe, see Table S5.2 in supplementary materials). Ca, K, Ti and Fe are the desired targets for ^{36}Cl production through spallation, while Ca and K are the targets for ^{36}Cl production through muon capture.

For the isotope dilution, ~99% ^{35}Cl-enriched solution (spike) was added to each samples and to a new bottle that would act as a chemistry blank (Ivy-Ochs et al., 2004). The remaining steps applied for recovery of chlorine as a precipitate of AgCl, removal of sulphates and secondary precipitation of AgCl were performed following the protocol in (Schimmelpfennig et al., 2011). ^{36}Cl and Cl concentrations were determined at the ASTER AMS national facility (CEREGE, France). Three isotopes of chlorine were measured: ^{35}Cl, ^{36}Cl and ^{37}Cl. $^{36}Cl/^{35}Cl$ and $^{36}Cl/^{37}Cl$ ratios were determined by normalizing to a ^{36}Cl in-house CEREGE standard (NIMB 2011) provided by (Merchel et al., 2011). The stable ratio $^{35}Cl/^{37}Cl$ was also normalized to the same standard assuming the natural ratio of 3.127. The measured ratios and the corresponding ^{36}Cl and Cl concentrations are presented in Table 5.2.

5.2.3.3 Topographic-shielding corrections

When calculating surface exposure ages, it is essential to account for potential attenuation effects caused by surrounding topography. If a cliff or volcanic cone partially obstructs cosmic ray exposure, its distance and size must be considered into the correction.

Although most of our lava samples are situated on relatively flat surfaces, some are located near volcanic cones where incident angles exceeding 20° have been measured in the field. To address this, we applied topographic-shielding corrections (Table 5.1) based on the measured incident angle (θ) of cosmic rays relative to the volcanic high. Given that our lava surface

samples were taken from flat areas, θ corresponds to the elevation angle of the surrounding topography at a given azimuth. Several established models (e.g., Dunne et al., 1999; Balco et al., 2008; Balco, 2014) provide equations for determining shielding factors using horizon angles. For our calculations, we utilized the online topographic shielding calculator http://stoneage.ice-d.org/math/skyline/skyline_in.html.

5.2.3.4 ^{36}Cl CRE age calculations

The cosmogenic ^{36}Cl exposure ages were calculated using two methods: the Excel® spreadsheet published by Schimmelpfennig et al. (2009) and the online Cosmic Ray Exposure Program (CREp) (https://crep-dev.otelo.univ-lorraine.fr/; Martin et al., 2017). Relatively similar results were obtained from both methods across most samples (Table 5.2), demonstrating the robustness of the calculations. The age calculators accounts for all ^{36}Cl production reactions, including spallation of the target elements Ca, K, Ti and Fe; slow muon capture by Ca and K; capture of cosmogenic low-energy (i.e., thermal and epithermal) neutrons by ^{35}Cl; and nucleogenic production. Based on the sea level and high latitude (SLHL) production rates, scaling factors, sample chemical composition (Tables S5.1and S5.2), sample thickness, and topographic shielding (Table 5.1), the Lal/Stone time-dependent scaling scheme (Stone, 2000) was applied for the calculation of all samples. The following ^{36}Cl sea level and high latitude (SLHL) production rates were used for the calculations: 42.2 ± 4.8 atoms of ^{36}Cl (g Ca)$^{-1}$ yr^{-1} for Ca spallation (Schimmelpfennig et al., 2011), 148.1 ± 7.8 atoms of ^{36}Cl (g K)$^{-1}$ yr^{-1} for K spallation (Schimmelpfennig et al., 2014), 13 ± 3 atoms of ^{36}Cl (g Ti)$^{-1}$ yr^{-1} for spallation of Ti (Fink et al., 2000), 1.9 ± 0.2 atoms of ^{36}Cl (g Fe)$^{-1}$ yr^{-1} for Fe spallation (Stone et al., 2005), and 696 ± 185 neutrons (g air)$^{-1}$ yr^{-1} for the rate of epithermal neutron production from fast neutrons in the atmosphere at the land/atmosphere interface (Marrero et al., 2016). We used a high-energy neutron attenuation coefficient value of 160 g cm^{-2} and a bulk rock density of 2.5 g cm^{3}.

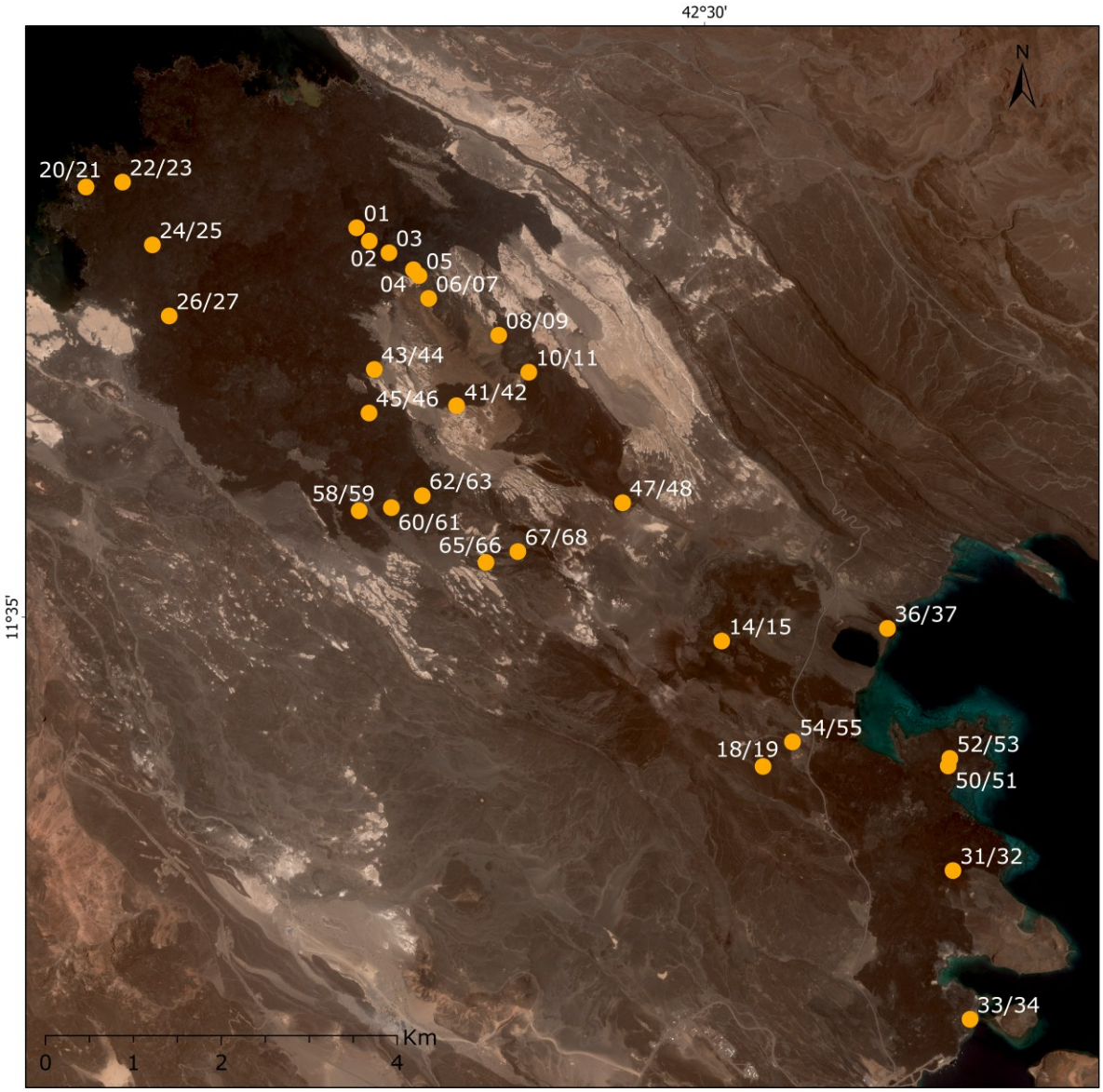

Figure 5.2: *High resolution Ms orthoimage generated from Pleiades satellite data shows the very recent lava flow fields along the axial volcanic centres of Asal-Ghoubbet rift. The yellow dots are the locations of the lava surface samples for geochemistry and cosmogenic ^{36}Cl measurement.*

5.3 Results

5.3.1 Chronology of Lava Flows

We present a new chronology for the axial volcanic centers of the Asal-Ghoubbet segment based on high-resolution cosmogenic ^{36}Cl exposure dating. These precise age constraints provide an absolute timeframe for recent axial volcanism and enable a detailed reconstruction of the segment's volcanic history. The newly determined ^{36}Cl CRE ages for lava surfaces in the various volcanic centres are summarized in Figure 5.3 and 5.4 and Table 5.2. The results

indicate that most lava fields are exceptionally young, with eruption ages ranging from 1 to 3 ka, except for one dated at 8 ka.

The new ^{36}Cl CRE ages for three volcanic surfaces in the Manda volcanic centre reveal a sequence of lava flow emplacement. The most recent episode consists of a'a flows, with ages ranging from 2.20 ± 0.33 ka (22DJ62, Figure 5.5 D) to 2.30 ± 0.43 ka (22DJ27, Figure 5.5 C). These flows overlie an earlier pahoehoe flow dated at 2.70 ± 0.45 ka (22DJ24, Figure 5.5 B). Beneath this, an older pahoehoe flow is dated at 3.10 ± 0.56 ka (22DJ22, Figure 5.5 A). However, a sample from this older episode, collected near the lake (22DJ20, Figure 5.3), exhibited a younger age of 2.10 ± 0.48 ka**,** likely due to surface erosion, water coverage, or alteration.

Two lava surfaces emplaced in the axial chain volcanic centre are dated at 2.90 ± 0.50 ka (22DJ08, Figure 5.5 E) and 1.10 ± 0.28 ka (22DJ47, Figure 5.5 F), with the latter representing the youngest flow in this sequence. The most recent eruptive phase in the volcanic centre occurred at its northwestern end, where basaltic flows (22DJ01-22DJ05, Figure 5.2) were dated at 0.045 ka (Vigier et al., 1999). These flows are the youngest in the Asal rift and are linked to the 1978 Ardoukoba eruption (Demange et al., 1980). The Secondary Chain volcanic centre is represented by a slabby pahoehoe lava flow, dated at 2.40 ± 0.50 ka (22DJ65, Figure 5.5 G), which aligns with the relative chronology and geological mapping (see section 5.3.2). A lava flow sample from the Armae Koma volcanic centre leads to ^{36}Cl CRE age of 2.60 ± 0.50 ka (22DJ14, Figure 5.5 H).

The older lavas in the Ghoubbet volcanic centre were dated at 65 ± 24 ka (Manighetti et al., 1998). However, the recent volcanic sequence begins with a pahoehoe flow from a welded scoria cone, which exhibits a new ^{36}Cl CRE age of 8.20 ± 1.13 ka (22DJ18, Figure 5.5 I). A subsequent effusive episode in this volcanic center includes two lava flows with younger ages of 2.00 ± 0.39 ka (22DJ50) and 1.80 ± 0.35 ka (22DJ31, Figure 5.5 J).

5.3.2 Relative Chronology of Lava Flows

In addition to the new cosmogenic ^{36}Cl exposure ages, we established a relative chronology of lava flows using direct field observations supported by satellite and Pleiades multispectral images. This approach refines the volcanic history of the rift volcanic centers and extends the chronological framework beyond absolute ages. While interpolated ages do not replace absolute dating, they provide useful proxies for assessing eruption timing and distribution of

volcanic activity. The results are illustrated on the geological map (red dots in Figure 5.3) and summarized in Table S5.3.

The relative chronology of lava flows varies across the five volcanic centres. In the Manda one, recent a'a flows show consistent estimated ages between 2.15 ka and 2.25 ka (Figure S5.1 A, B and C). The Axial Chain volcanic centre includes one lava flows with interpolated ages of 3.50 ka (Figure S5.1 D), and two lava flows with consistent estimated ages of 2.80 ka (Figure 5.5 E and S5.1 E). A single A'a-type lava flow in the Secondary Chain volcanic centre has an estimated age of 2.40 ka (Figure S5.1 F). The Armae Koma volcanic centre features two lava flows dated at 2.60 ka (Figure S5.1 G and H). Finally, the Ghoubbet volcanic centre contains two lava surfaces with interpolated ages of 3.50 ka (Figure S5.1 I) and 2.20 ka (Figure S5.1 J).

5.3.3 Field investigations, geological map and associated magmatic history

Combining Pleiades Ms orthoimages and high-resolution DSM with field investigations, very high-resolution geological mapping is provided and aimed at reconstructing the volcanic history and understanding the spatial relationships of the recent eruptive products within the axial zone volcanic centres.

The oldest volcanic activity within the axial zone of the rift is characterized by a phreatomagmatic phase, resulting from the interaction between ascending magma and a water source, either deep or shallow. These episodes produced phreatomagmatic tuff cones, pyroclastic deposits, and reworked hyaloclastites along the internal rift margin, dated at 100 - 300 ka (De Chabalier & Avouac, 1994; Manighetti et al., 1998). One notable feature from this phase is the Fieale cone, a phreatomagmatic tuff cone displaying fault-induced collapse and deformation. Following this phase, aerial Strombolian eruptions partially covered these phreatomagmatic deposits (Figure 5.6 J). More recent volcanic activity in the axial zone is characterized by effusive eruptions from the fissural systems, forming extensive lava fields (Figure 5.3 and 5.4). The most recent historical 1978 eruption in Ardoukoba, is the youngest episode of this ongoing activity at the axial volcanic centres (Demange Jacques Par, Laurent Stieltjes, 1980; Vigier et al., 1999).

This study focuses on the recent magmatic activity over the last 10 ka along the axial magmatic centres, specifically on volcanic events that occurred after 65 ka (Manighetti et al., 1998) and prior to the 1978 Ardoukoba eruptions (Vigier et al., 1999). The detailed sequence of these volcanic events, which continue to shape various axial centres, is described in the following section.

5.3.3.1 Recent aerial volcanic products of various axial centres

The recent volcanic stratigraphy at the axial zone of the Asal Rift is characterized by young lava flows. These volcanic products include basaltic scoria cones, hornitos, and lava flows, distributed across five axial centres: Manda, Axial Chain, Secondary Chain, Armae Koma, and Ghoubbet. The highest lava flow volumes are observed in the southeastern (Ghoubbet) and northwestern (Manda) parts of the axial zone (Figure 5.3).

Field investigations of sampled lava surfaces from each volcanic centre reveal dominant morphologies ranging from smooth to ropey textures, characteristic of pahoehoe lava. Some samples also exhibit a'a-type lava textures. The lava flows are predominantly dark gray to black, with most samples displaying a porphyritic texture, dominated by plagioclase phenocrysts, consistent with previous studies on axial zone lavas (Vigier et al., 1999; Pinzuti et al., 2013). Aphyric samples with fine-grained microcrystals in the matrix were identified in five samples (22DJ18, 22DJ36/37, 22DJ47/48, 22DJ55, and 22DJ68).

5.3.3.1.1 Lava fields of the Manda volcanic centre

The Manda volcanic centre, located in the northwestern part of the axial zone of the Asal rift near Lake Asal (Figure 5.3), is characterized by extensive lava flows whose chronology has been established through cosmogenic ^{36}Cl exposure dating and relative age interpolation (sections 4.1 and 4.2). The most recent effusive activities in this volcanic centre are associated with welded scoria cones and spatter accumulations (Figure 5.6 A), which have produced highly fluid lava flows (e.g., Figure 5.5 D) and various pahoehoe lavas (Figures 5.5 and S5.1). Distinguished lava flows are classified into three eruptive phases based on field relationships, their apparent relative chronology and the new ^{36}Cl CRE ages. The oldest phase consists of a pahoehoe lava with a surface exposure age of 3.10 ± 0.46 ka (Figure 5.5 A). It is overlain by a second pahoehoe flow dated at 2.70 ± 0.46 ka (Figure 5.5 B). The youngest phase is marked by extensive a'a-type lava flows, with ^{36}Cl CRE ages of 2.30 ± 0.43 ka (Figure 5.5 C), 2.20 ± 0.33 ka (Figure 5.5 D); and interpolated ages of 2.25 ka (Figure S5.1 A), 2.20 ka (Figure S5.1 B) and 2.17 ka (Figure S5.1 C).

5.3.3.1.2 Lava fields of the Axial Chain volcanic centre

The Axial Chain volcanic centre consists of various volcanic structures, including welded scoria cones (e.g., Figure 5.6 B), dikes, and associated lava flows. It is one of the most well-

documented parts of the axial zone of the Asal-Ghoubbet rift along with the Fieale (Manighetti et al., 1998; Doubre et al., 2007). The lava flows in this centre appear to be slightly more viscous, as suggested by their surface characteristics, which differ noticeably from those observed in the other axial volcanic centres. We sampled five lava surfaces which were emplaced during four distinct eruptive episodes. The oldest episode produced a pahoehoe lava at the northwestern end of the volcanic centre, with an estimated relative age of 3.50 ka (Figure S5.1 D). This flow is partially covered by the lava flows from recent Ardoukoba activity (Figure 5.3 and S5.1 D). The second episode is a pahoehoe slabby lava flow with a plate-like surface, dated at 2.90 ± 0.50 ka (Figure 5.5 E). This was followed by a third eruptive phase that produced a'a-type lavas with spiny and vesicular textures. Two lava surfaces sampled from this episode have an estimated relative ages of 2.80 ka (Figure 5.5 E and S5.1 E). One of these flows, located in the southwestern part of the volcanic centre is particularly well-defined, as it overlies lacustrine sediments consistent with our mapping (Figure S5.1 E and 5.3). The fourth eruption sequence is represented by a lava surface dated at 1.10 ± 0.28 ka (Figure 5.5 F). The eruption originated from a fissure, where a basaltic dike breached the surface and transitioned into a massive lava flow before cascading downslope as a'a-type lava flows (Figure 5.6 C). The most recent and final episode of effusive activity in this volcanic centre is associated with the historic Ardoukoba eruption. Ardoukoba consists of a group of welded scoria cones (Figure 5.6 B) and associated pahoehoe lava flows located at the northwestern end of the volcanic centre (Figure 5.3). These lavas were emplaced during the November 7 - 14, 1978 eruption, the most recent volcanic event in the Asal rift (Demange et al., 1980).

5.3.3.1.3 Lava fields the Secondary Chain volcanic centre

The Secondary Chain volcanic centre is represented by lava flows of lesser magnitude compared to the other axial volcanic centres of the Asal rift. Two lavas with distinct flow morphologies have been mapped and sampled. The first is a slabby pahoehoe lava surface, which is dated at 2.40 ± 0.43 ka (Figure 5.5 G). This flow overlies lacustrine sediments that are dated to 6 ka (Manighetti et al., 1998), corresponding to the highest paleo-lake level of lake Asal (Figure 5.6 D). Above the pahoehoe lava, a'a-type lava flow was emplaced, with an estimated relative age of 2.40 ka (Figure S5.1 F).

5.3.3.1.4 Lava fields of the Armae Koma volcanic centre

The floor of the Armae Koma crater is characterized by an undulating frozen lava flow, suggesting the presence of a paleo-lava lake within the depression (Figure 5.6 F). This crater is also the source of the lava flows that filled the Fieale crater (Figure 5.6 E). Lavas overflowed the crater's edges, cascading over a paleo-succession of pyroclastic deposits before entering the Fieale crater (Figure 5.6 G). The internal flanks of the crater are lined with basaltic layers, indicating the crater was initially filled with magma, forming a temporary lava lake several meters deep before draining. This filling event is associated with lava fountain activity, with striations visible above the paleo-lake level (Figure 5.6 G). An unwelded scoria cone is located on the eastern external flank of Armae Koma (Figure 5.6 H), likely associated with a distal deposit from this lava fountain episode of Armae Koma. The northeast flank of the crater is partially collapsed and covered with lava flows, suggesting that magma overflowed, causing the collapse and subsequently filling the Fieale crater to form a second temporary lava lake (Figure 5.6 G). A pahoehoe lava surface sampled from the paleo-lake of Fieale is dated at 2.60 ± 0.50 ka (Figure 5.5 H). These lava flows eventually spread towards the Ghoubbet area, covering a crater at the northwest edge of Ghoubbet Bay (Figure 5.3). Two lava surfaces sampled from this area have estimated ages of 2.6 ka (Figure S5.1 G and H).

5.3.3.1.5 Lava fields of the Ghoubbet volcanic centres

The Ghoubbet volcanic centre is characterized by extensive recent lava flows and strombolian scoria cones, which partially cover older phreatomagmatic edifices (Figure 5.6 I and J). We investigated five lava surfaces emplaced during three distinct eruptive phases of the effusive activity. The recent volcanic sequence begins with a pahoehoe flow originating from a welded scoria cone (Figure 5.6 I). This lava flow initially advanced northward, diverting around the cone before covering an axial-directed fault at its base, and ultimately cascading toward the Ghoubbet Bay (Figure 5.3). A lobate, relatively smooth, and ropy surface sample that represents this first-phase event exhibits a new ^{36}Cl CRE age of 8.20 ± 1.13 ka (Figure 5 I). The second eruptive phase produced pahoehoe lava flows around the Ghoubbet-Baddi Koma area, with an estimated relative age of 3.5 ka (Figure S5.1 I). This was followed by a third eruptive phase, which generated another pahoehoe lava flow with an interpolated age of 2.20 ka. A scoria cone (Figure S5.1 J) is perched atop of this lava surface. The final eruption from this edifice produced a'a-type lava flows of limited extent, dated at 2.00 ± 0.39 ka (22DJ50).

Additionally, as part of this third episode, another a'a lava flows has been dated at 1.80 ± 0.35 ka, representing the youngest identified lava in the sequence (Figure 5.5 J).

Table 5.2: *Analytical ^{36}Cl data and ^{36}Cl CRE ages of the lava flows at the Asal-Ghoubbet rift volcanic centres. Age uncertainties (1σ) include production rate errors as well as analytical errors; numbers in parenthesis correspond to analytical errors only.*

Sample Name	Sample weight (g)	Mass of Cl in spike (mg)	$^{35}Cl/^{37}Cl$	$^{36}Cl/^{35}Cl$ (10^{-15})	Cl in Sample (ppm)	^{36}Cl (10^3 atoms g^{-1})	^{36}Cl CRE age (ka)	^{36}Cl CRE age (ka) from CREP
22DJ08	74.12	1.991	50.29 ± 2.15	18.23 ± 3.14	1.78 ± 0.07	8.77 ± 1.53	2.90 ± 0.6 (0.50)	3.10 ± 0.65 (0.55)
22DJ14	48.16	2.032	25.70 ± 2.16	11.66 ± 2.16	6.82 ± 0.23	9.37 ± 1.76	2.60 ± 0.56 (0.50)	2.78 ± 0.61 (0.54)
22DJ18	84.08	2.031	3.90 ± 2.14	23.25 ± 2.31	128.94 ± 14.02	48.19 ± 6.37	8.20 ± 1.56 (1.13)	9.26 ± 1.75 (1.25)
22DJ20	49.36	2.021	50.59 ± 2.21	8.27 ± 1.82	2.69 ± 0.10	5.99 ± 1.35	2.10 ± 0.52 (0.48)	2.20 ± 0.57 (0.51)
22DJ22	46.81	2.022	48.81 ± 2.17	11.45 ± 1.56	2.99 ± 0.11	8.83 ± 1.22	3.10 ± 0.56 (0.46)	3.36 ± 0.61 (0.48)
22DJ24	74.85	2.021	55.20 ± 2.61	15.60 ± 2.43	1.57 ± 0.07	7.49 ± 1.18	2.70 ± 0.53 (0.45)	2.96 ± 0.58 (0.48)
22DJ27	72.65	2.028	23.41 ± 2.23	12.31 ± 2.25	5.09 ± 0.18	6.64 ± 1.23	2.30 ± 0.49 (0.43)	2.39 ± 0.52 (0.46)
22DJ31	57.58	2.024	59.46 ± 2.19	8.81 ± 1.67	1.83 ± 0.07	5.44 ± 1.05	1.80 ± 0.4 (0.35)	1.79 ± 0.41 (0.36)
22DJ47	90.02	2.042	3.62 ± 2.20	5.08 ± 0.99	190.07 ± 30.64	14.35 ± 3.46	1.10 ± 0.36 (0.28)	2.08 ± 0.60 (0.52)
22DJ50	61.98	2.033	4.88 ± 2.30	5.61 ± 1.02	76.39 ± 5.07	8.58 ± 1.63	2.00 ± 0.44 (0.39)	2.2 ± 0.48 (0.43)
22DJ62	60.17	2.011	8.41 ± 2.28	8.91 ± 1.24	25.40 ± 1.05	7.94 ± 1.13	2.20 ± 0.38 (0.33)	2.35 ± 0.42 (0.35)
22DJ65	60.54	2.010	50.80 ± 2.36	12.33 ± 2.12	2.17 ± 0.09	7.29 ± 1.27	2.40 ± 0.50 (0.43)	2.58 ± 0.54 (0.46)
B2	_	2.010	198.60 ± 2.58	0.19 ± 0.06	-	-	-	-

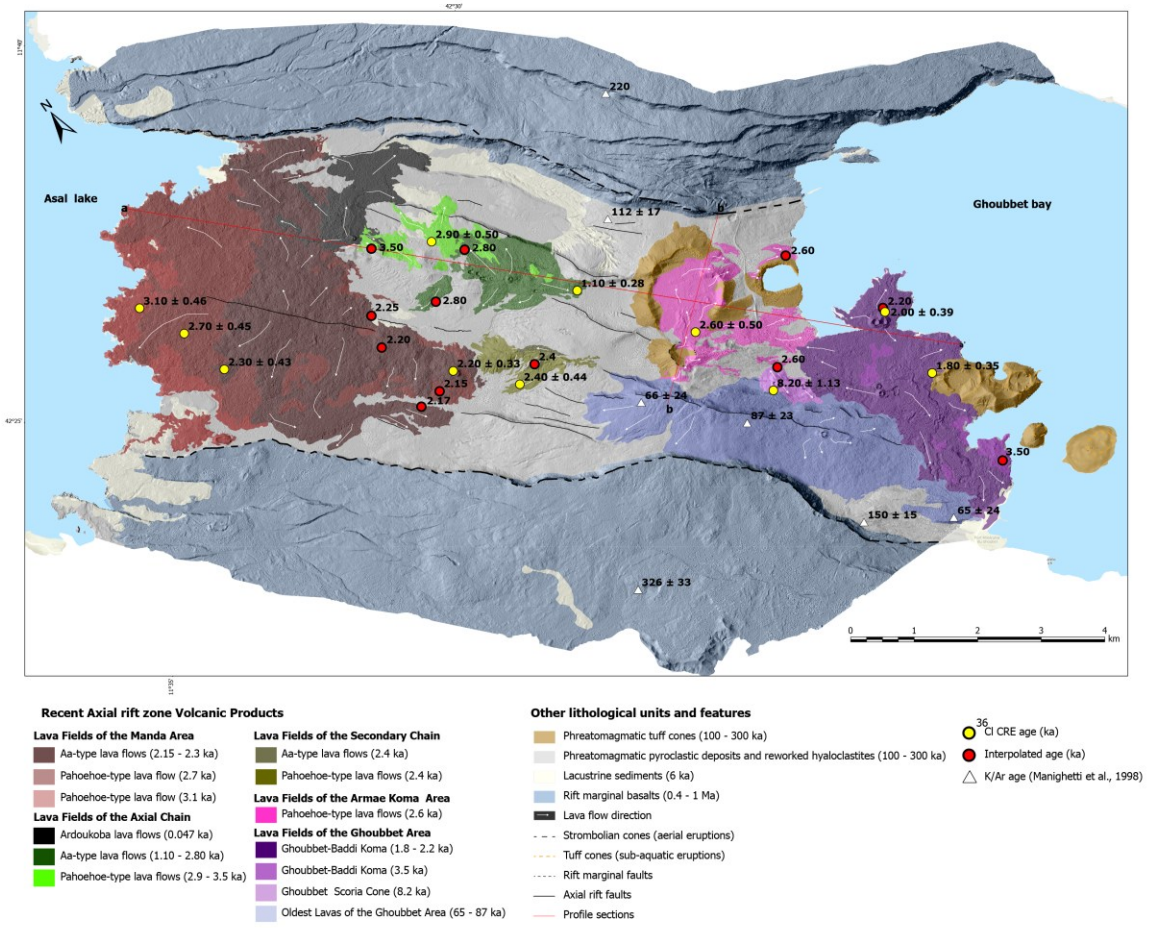

Figure 5.3: *Detailed map of the axial volcanic centres of the Asal-Ghoubbet rift, illustrate the spatial extent of recent basaltic lava flows.*

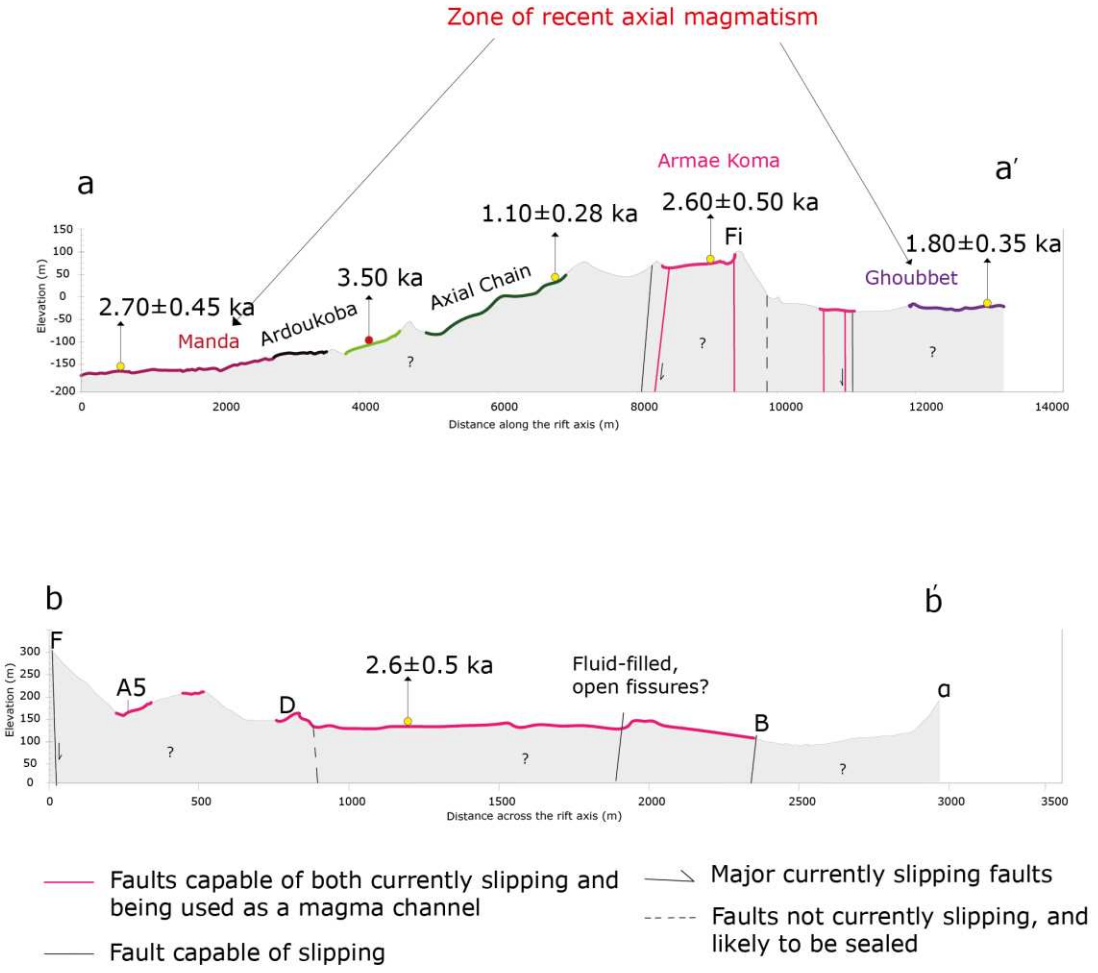

Figure 5.4: *Topographic architecture of the axial volcanic centres of the Asal-Ghoubbet rift. a) Schematic cross-section parallel to the rift axis. b) Cross-section perpendicular to the rift axis. Fi stands for Fieale volcanic edifice. The location of main faults (A5, B, D and F) are from Doubre et al. (2007).*

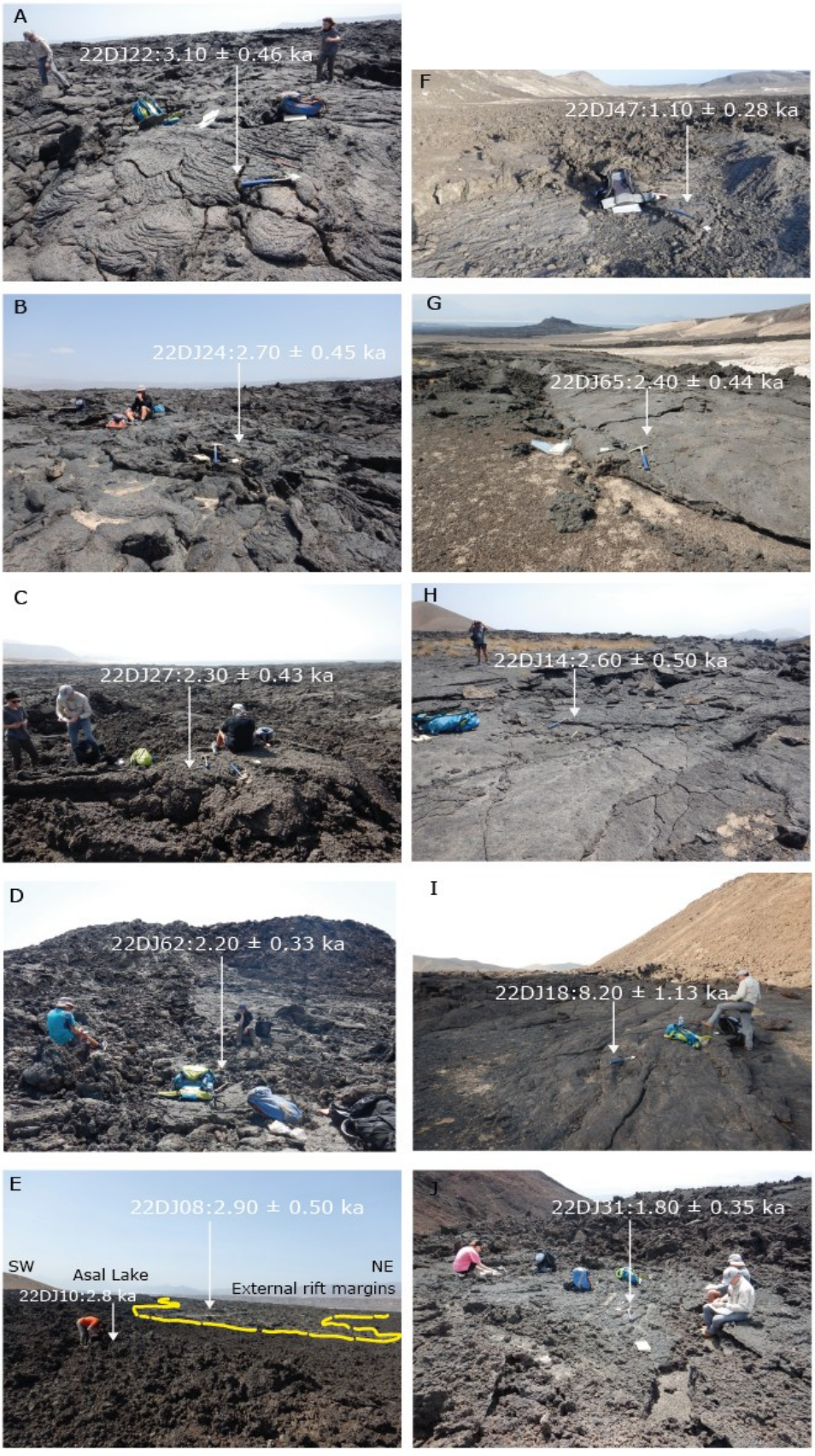
A
22DJ22:3.10 ± 0.46 ka
F
22DJ47:1.10 ± 0.28 ka
B
22DJ24:2.70 ± 0.45 ka
G
22DJ65:2.40 ± 0.44 ka
C
22DJ27:2.30 ± 0.43 ka
H
22DJ14:2.60 ± 0.50 ka
D
22DJ62:2.20 ± 0.33 ka
I
22DJ18:8.20 ± 1.13 ka
E
22DJ08:2.90 ± 0.50 ka
SW
Asal Lake
22DJ10:2.8 ka
NE
External rift margins
J
22DJ31:1.80 ± 0.35 ka

Figure 5.5: *Locations, field photographs, and ^{36}Cl CRE ages of various lava flow fields at the axial rift volcanic centres. (A - D) Lava samples from the Manda volcanic centre: (A) and (B) are Pahoehoe-type lavas while (C) and (D) corresponds to the very fluid aa-type lava flows. (E and F) Lava samples from the axial chain volcanic centre: (E) porphyritic Pahoehoe slabby lava is covered by aphyric aa-type lava flow. (G) Lava sample from the Secondary Chain volcanic centre: (H) pahoehoe Slabby lava flows at the Armae Koma volcanic centre. (I and J) Lava Samples from the Ghoubbet volcanic centre.*

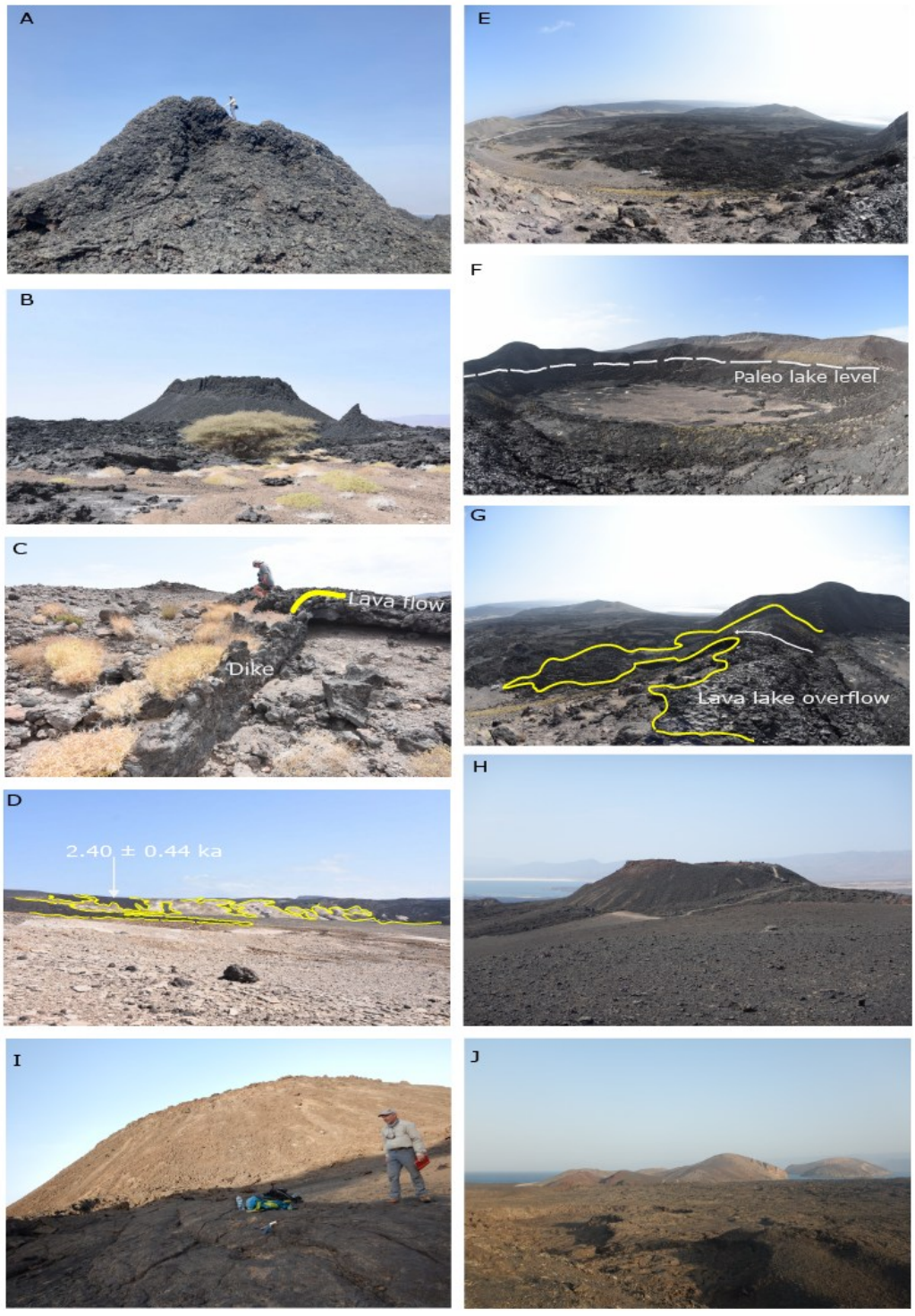

Figure 5.6: *Field photographs showing key volcanological features and associated lava flow fields within the axial volcanic centres. (A) A spatter cone at the Manda volcanic centre. (B) The main Scoria cone of Ardoukoba at the Axial Chain volcanic centre. (C) Dike-fed lava flow at the Axial chain volcanic centre, where a basaltic dike breached the surface, filled fissures and transitioned into a lava flow that*

cascaded downslope towards the southwest. (D) Lava flows at the Secondary Chain volcanic centre covering lacustrine sediments associated with the highest paleo-level of Lake Asal. (E) The Fieale Crater lava lake at the Armae Koma volcanic centre, potentially hosting a mid-segment magma reservoir. This old crater is filled with an additional lava flow mainly sourced from Armae Koma crater (F) Paleo-lake level within the Armae Koma crater lava lake. Striations above this lava lake surface is related to the lava fountain activity. (G) Lava overflows from the Armae Koma crater and draping over paleo-succession of the pyroclastic deposits before flowing into the Fieale crater. (H) Scoria cone at the Armae Koma volcanic centre. (I) welded scoria cone at the Ghoubbet volcanic centre. A layer of welded scoria, covered by a yellow ash layer (related to a pyroclastic surge) about 10 cm thick, which is itself covered by a layer of poorly welded scoria. (J) Phreatomagmatic tuff cones partially covered by strombolian volcanic deposits and the very recent extensive lava flows at the the Ghoubbet volcanic centre.

5.3.4 Major and trace elements

The samples from the Asal rift volcanic centres are classified as sub-alkaline basalts in the Total Alkali-Silica (TAS) diagram (Figure 5.7). These basaltic samples show varying degrees of differentiation, as reflected by their MgO contents and corresponding trace element concentrations (Figure 5.8, 5.9, S5.2 and Table S5.1). Lavas from the Axial Chain volcanic centre (1.10-3.50 ka) exhibit the highest degree of differentiation, with MgO contents ranging from 3.42 to 9.32 wt.%. In contrast, basalts emplaced in the Manda volcanic centre (2.15-3.10 ka) display a relatively restricted and lower degree of differentiation, with MgO contents ranging from 6.89 to 7.97 wt.%. Basalts from the Ardoukoba eruptions (0.047 ka) display MgO contents ranging from 5.98 to 8.75 wt.%. The basalts emplaced in the secondary chain volcanic centre (2.4 ka) are characterized by MgO contents varying between 5.74 and 8.93 wt.%. Basalts emplaced within the Armae Koma volcanic centre (2.6 ka) exhibit MgO contents ranging from 4.89 to 7.06 wt.%.

The variations observed in major elements (Figure 5.8) are compatible with fractional crystallisation from a common parental magma. This process is marked by typical Fe-Ti and P enrichments associated with classical triangular shaped differentiation trends controlled first by fractionation of clinopyroxene + plagioclase feldspar ± olivine and then by additional fractionation of Fe-Ti oxides (starting at ~ 4.5 wt. % Mgo) and apatite (starting at ~ 3.5 wt.% MgO). This evolutionary trend is further supported by trace elements and their ratios (Figure 5.9), which indicate a single differentiation series. However, basalts from the Ardoukoba eruptions (0.047 ka) show slightly lower Tb/Yb ratios compared to other basalts within the volcanic centres (Figure 5.9), which could be interpreted as a change in the melting regime or minor variations in the mantle source.

All lava series identified within the Asal-Ghoubbet segment are enriched in light rare earth elements (LREE) and display prominent positive Ba anomalies and negative K anomalies (Figure 5.10). These geochemical characteristics correspond to Type III magmas, as classified by (Rooney, 2020b) in his synthesis of East African Rift magmas.

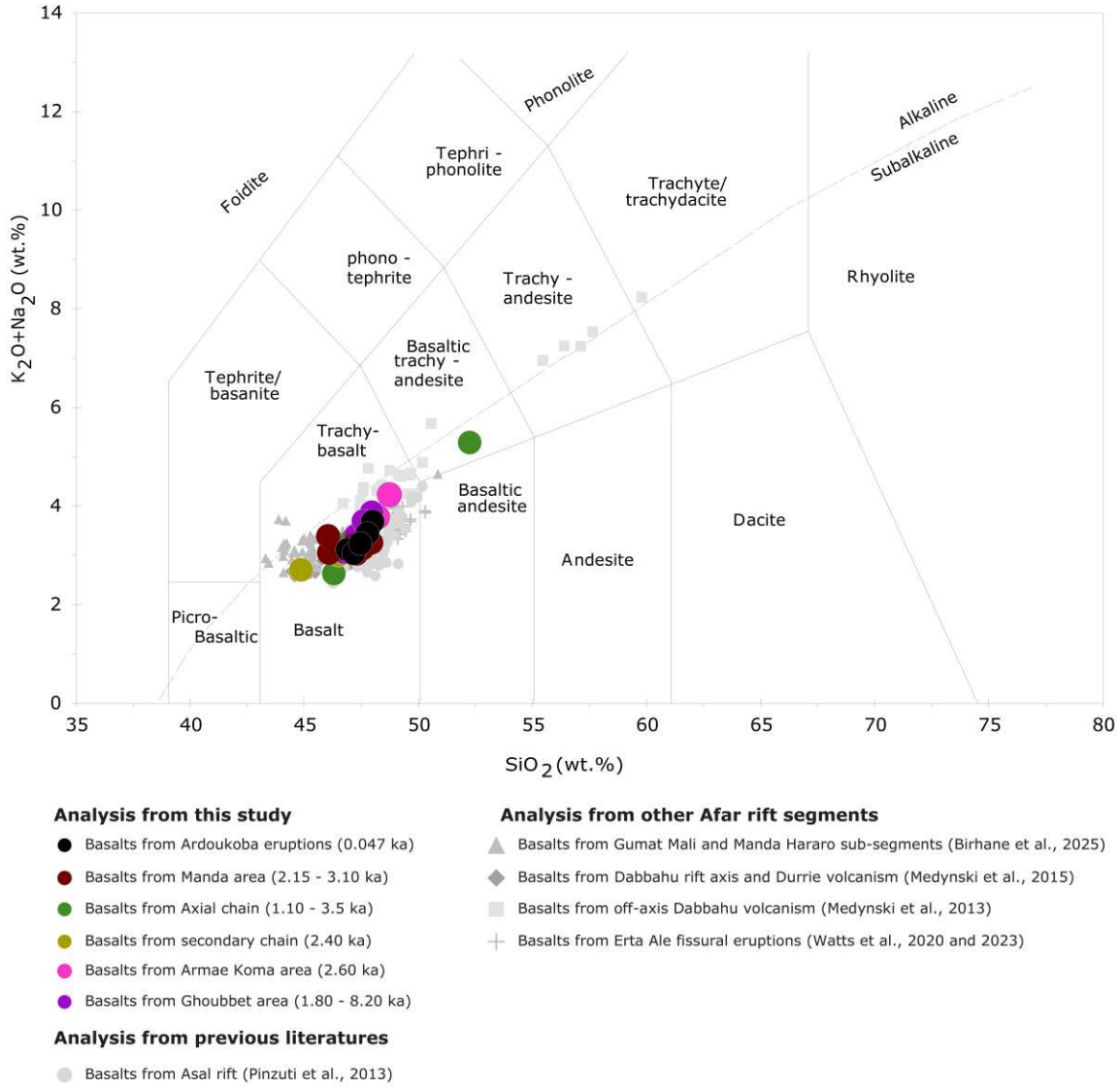

Figure 5.7: *TAS (Total Alkali vs. Silica, wt%) classification diagram for lavas from Asal-Ghoubbet segment. Nomenclature of volcanic rocks after Le Bas et al. (1986). Discrimination line between the alkaline and subalkaline group is after Irvine and Barragar (1971).*

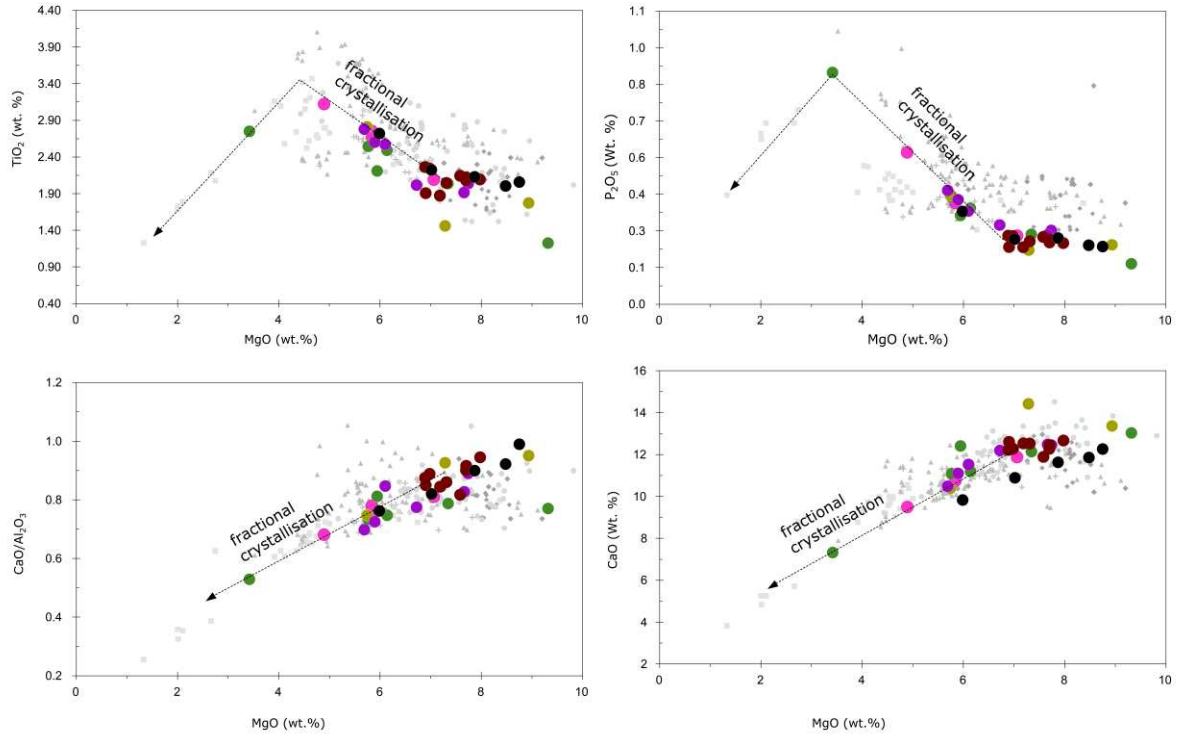

Figure 5.8: *Variations in major elements vs MgO among lava samples. The legend is the same as for Figure 5.7*

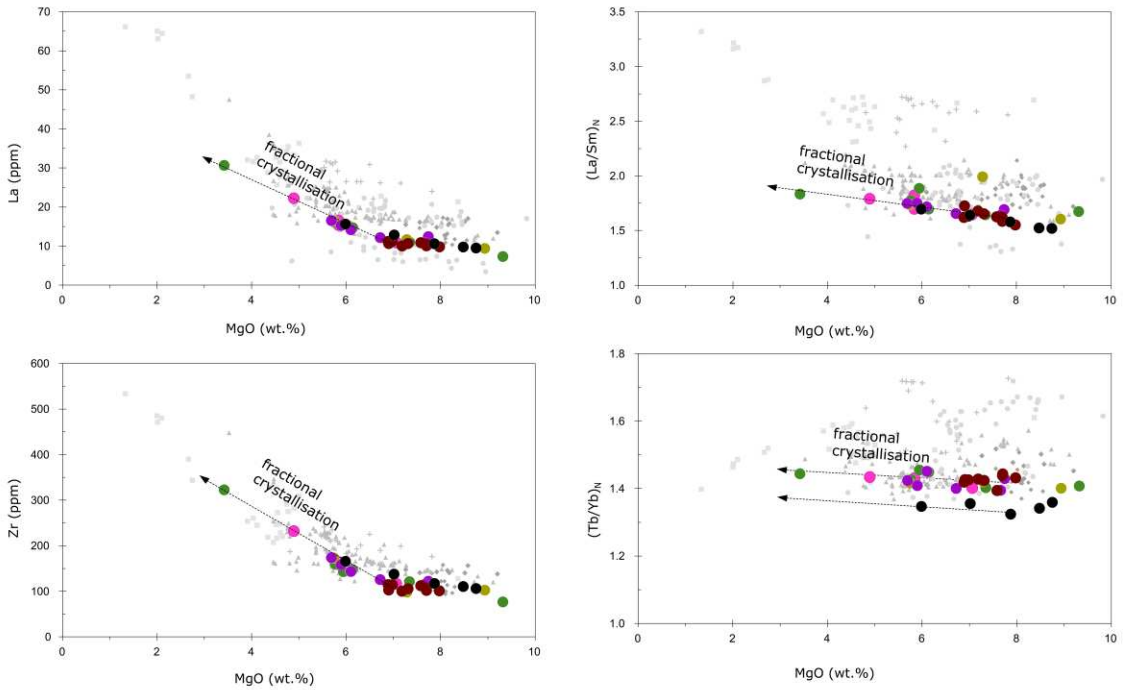

Figure 5.9: *Variations in trace elements between the lava samples. The Sr anomaly is calculated as Sr* = Sr/((Pr+Nd)/2) after normalization to primitive mantle (Sun and McDonough, 1989). The legend is the same as for Figure 5.7*

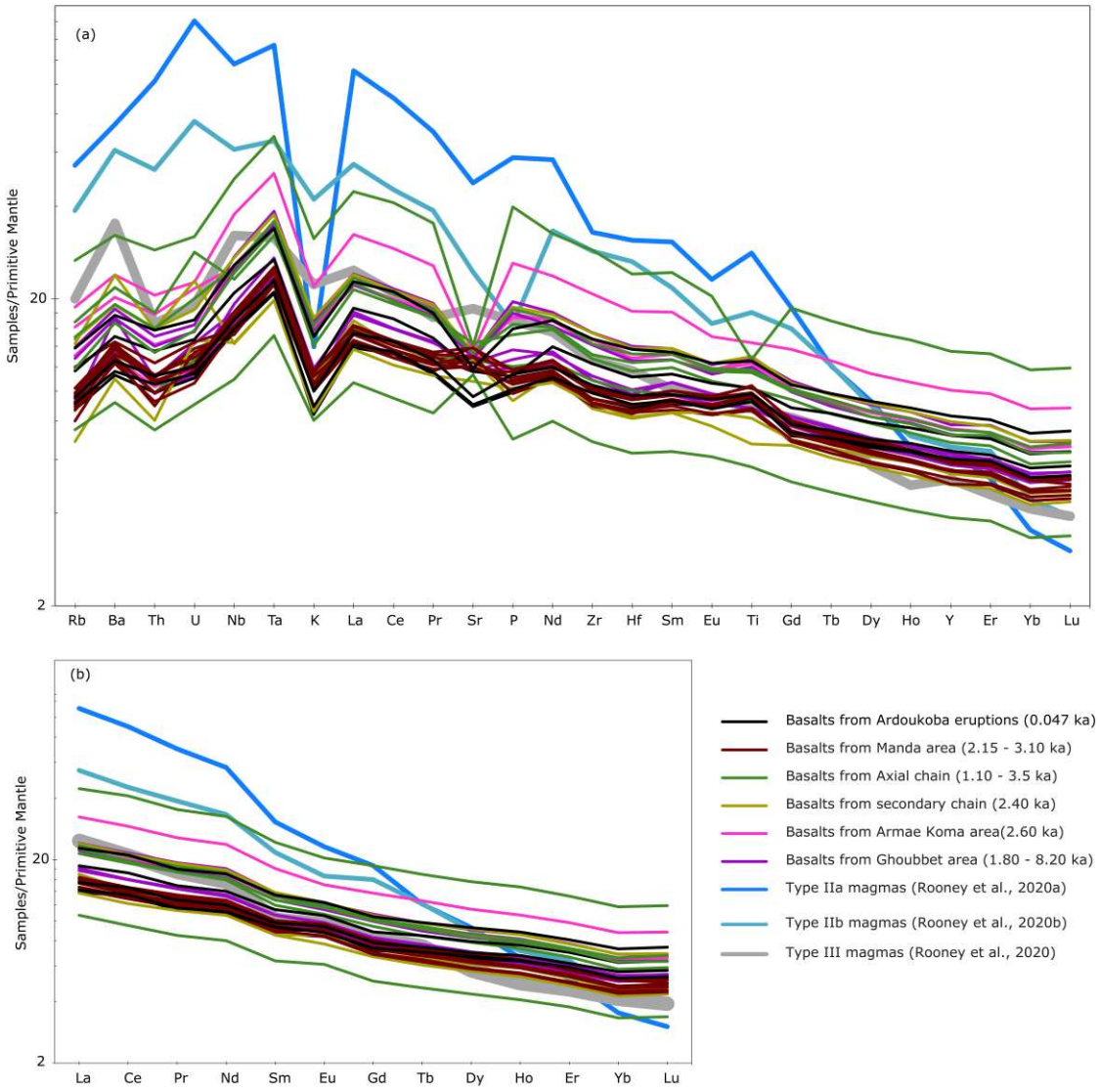

Figure 5.10: *(a) multi-element variation diagram and (b) Rare Earth Element (REE) patterns of the lava series, both normalized to primitive mantle (Sun and McDonough, 1989).*

5.4 Discussion

5.4.1 Magma differentiation and system replenishment

Magmatic cycles correspond to the periodic episodes of magma generation, ascent, storage, and eruption. They can vary in duration and intensity, depending on the rate of magma supply and can also be based on multiple individual events of magma transfer and injection in the crust, sometimes associated with surface fissural eruptions (Medynski et al., 2013). By integrating geochemical observations with high-resolution lava geochronology across the Asal-Ghoubbet segment, we identified and documented two distinct magmatic cycles for the last 3.5 kyr, marked by phases of magma differentiation and system replenishment (Figure 5.11), and distinguished on the base of (i) slightly distinct parental magmas (i.e., Tb/Yb difference figure 9), and (ii) the additional evidence of a closed system phase in between the two cycles. The first cycle occurred around 3.5 ka and lasted up to 1.1 ka. The second and subsequent cycle is associated with the 1978 Ardukoba eruption, which displayed significant magma evolution within only five days.

The first magmatic cycle records alternating phases of differentiation and magma recharge, as indicated by variations in MgO content. Although MgO values range from more evolved compositions (3.42 wt.%) to less evolved ones (9.32 wt.%), most lavas cluster around 7 wt.% MgO. This clustering suggests that while shallow magma reservoirs experienced some differentiation, frequent recharge from a deeper magma source limited the extent of differentiation, maintaining a buffered composition near 7 wt.% MgO. During this first magmatic cycle, all axial volcanic centres of the Asal-Ghoubbet rift were continuously active, operating in an open-system since at least ~3.5 ka (Figure 5.11). However, there was a dramatic change around 1.8 ka, after which frequent basaltic eruptions ceased and only significantly more differentiated lavas erupted. This shift indicates a decline in magma supply and a gradual transition toward a closed magmatic system, culminating around 1.1 ka. The cycle therefore represents a continuous alternative differentiation and replenishments in an open magmatic system between ~3.5 and 1.8 ka, followed by progressive differentiation until 1.1 ka, when evolved magmas were erupted at the Axial Chain volcanic centre. The final recharge event likely triggered the 1.8 ka eruption at the Ghoubbet volcanic centre before magma feeding ceased. The synchronous activity of all volcanic centres during this cycle suggests the presence of a large, interconnected magma reservoir feeding the entire Asal-Ghoubbet system, rather than isolated kilometer-scale magma lenses.

The second magmatic cycle represents the reopening of the magmatic system during the 1978 Ardukoba rifting episode. Following the closure of the crustal magma reservoir around 1.1 ka, this event marks a renewed phase of magmatic activity after a period of quiescence in the Asal-Ghoubbet rift. Magmas erupted during the 1978 eruption exhibit clear compositional shifts at a quite short time scale (Figure 5.12). The first lavas erupted at Ardoukoba already contain higher MgO contents than the evolved magmas erupted at the Axial Chain volcanic center during the first magmatic cycle. The full fissural episode is marked by progressive increase in MgO, a strong La and Zr correlation, and variable La/Sm ratios, suggesting injection of new, more primitive magma into a shallow crustal reservoir. Moreover, the shift in Tb/Yb of all erupted lavas compared to the previous cycle indicates that this less differentiated magma, which has been injected upward, is also a new magma that entered the full transcrustal system. These early Ardukoba lavas likely resulted from the mixing of newly ascending magma from depth with a reactivated shallow crustal reservoir following its reopening. Vigier et al. (1999) proposed that the magmas feeding the 1978 Ardoukoba eruption had differentiated for about 870 years in a closed system and up to 1880 years in an open system before eruption, consistent with our interpretation of periodically replenished magmatic system beneath the Asal-Ghoubbet rift.

A comparable pattern occured in Central Afar sub-segments, where successive eruptions over the past 30 kyr record alternating episodes of differentiation and recharge (Medynski et al., 2015, Birhane et al., in prep. chapter 3). The Gumat Mali and Manda Hararo sub-segments display a comparable magmatic architecture, with magma stored at multiple crustal levels and repeatedly mobilized and mixed, where deeper and less evolved magmas (7-8 wt.% MgO) interact with shallower and more evolved melts (5-6 wt.% MgO). However, in those segments the buffered compositions are below 7 wt.% MgO (Birhane et al., 2025 in preparation), slightly lower than in the Asal system. The timescales of the captured recharge/differentiation processes also vary, operating over ~0.5 ka at Gumat Mali and up to ~4 ka at Manda Hararo, whereas it appears radically shorter in the Asal transcrustal system, as also observed for the recent Icelandic rifting episodes (i.e., Halldórsson et al., 2022). The buffering compositional level observed in the Dabbahu record (Medynski et al., 2015) is significantly higher and appears more constant around 8 wt.% MgO, with a recent shift (< 10 ka) towards more differentiated composition of ~ 5.5 wt. % MgO, suggesting that the recharging magmas there were more primitive than in Gumat Mali-Manda Hararo and Asal–Ghoubbet, or alternatively that the shallow reservoirs were less differentiated. Overall, these observations suggest that variations

in magmatic activity within the Afar magmatic segments is controlled by the balance between magma supply from depth and differentiation within shallow crustal reservoirs, potentially associated with difference of maturity of such transcrustal systems.

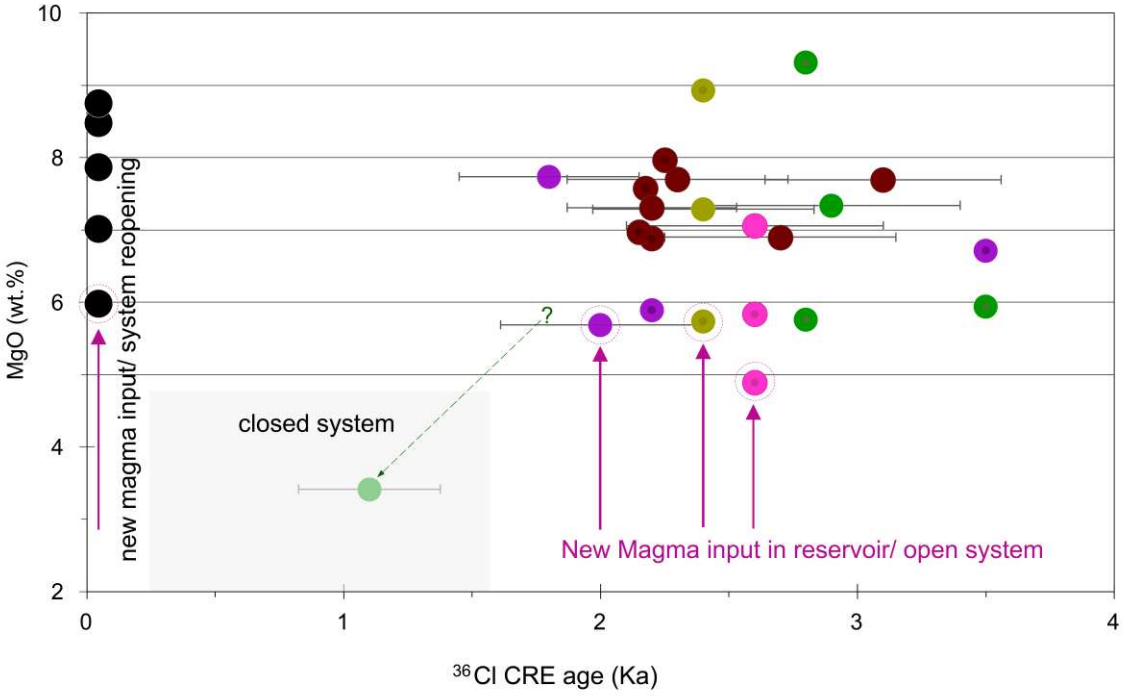

Figure 5.11: *Magma replenishment and differentiation through time at the Asal-Ghoubbet rift segment. Symbols as for Figure 5.7*

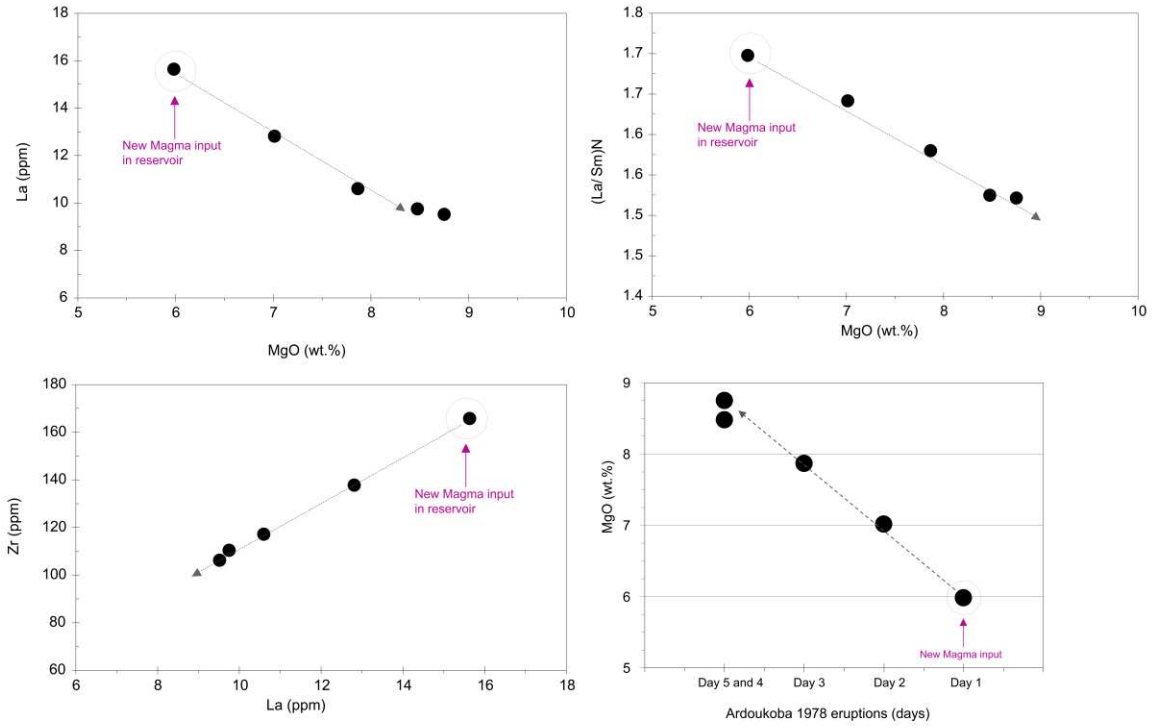

Figure 5.12: *Evolution of magma composition during the 1978 Ardukoba rifting episode. Symbols as for Figure 5.7*

5.4.2 Mantle source of magmas

All lava series emplaced across the Asal-Ghoubbet sub-segments since ~3.5 ka are enriched in light rare earth elements (LREE) and show pronounced Ba and Ta peaks, negative K anomalies, and U-Th troughs on multi-element diagrams (Figure 5.10) consistent with type III magmas classified by (Rooney, 2020b) and lavas described in Central Afar (Tortelli et al., 2024; Birhane et al., in prep.). However,compared to lavas from the first magmatic cycle, those erupted during the 1978 Ardoukoba rifting episode display lower Tb/Yb ratios (Figure 5.9), a trace element ratio sensitive to the presence of garnet in the mantle source but also sensitive to its enriched – depleted character. Compared to Central Afar segments (Figure 5.13), lavas from the first cycle display identical La/Sm and Tb/Yb ratios as the less enriched magma types observed at Dabbahu and Manda Hararo segments, whereas the slightly different composition of the Ardoukoba lavas compares to some of the Gumat Mali lavas with intermediate compositions between the local enriched and depleted mantle components (Birhane et al., in prep. Chapter 3 and 4). Such a compositional trend observed for Central Afar magmas has been interpreted as reflecting gabbroic ocean-crustal material embedded in the upwelled mantle with

various initial mineralogical composition (plagioclase vs. clinopyroxene) modulating the final enriched or depleted character of the melts. This suggests that regional geochemical variability across central and southern Afar rift segments can be explained by incorporation of small volumes of depleted mantle melts into a dominantly enriched melts both originating from the Afar mantle plume. Such a potential scenario in turn implies to be cautious when interpreting and inverting REE to constrains depth of melting, or when interpreting the depleted character of lavas as refleting incorporation of N-MORB mantle source in the generation of melts. Globally it appears that the variously enriched lavas from Central and Southern Afar axial segments are clearly different from other regional or older lava series that require (i) more garnet in the mantle source (off-axis Asal, MER and upper stratoid) and a deeply anchored melting column, or (ii) apparent lower melt fractions (Dabbahu off-axis, Erta Ale), or alternatively more enriched component.

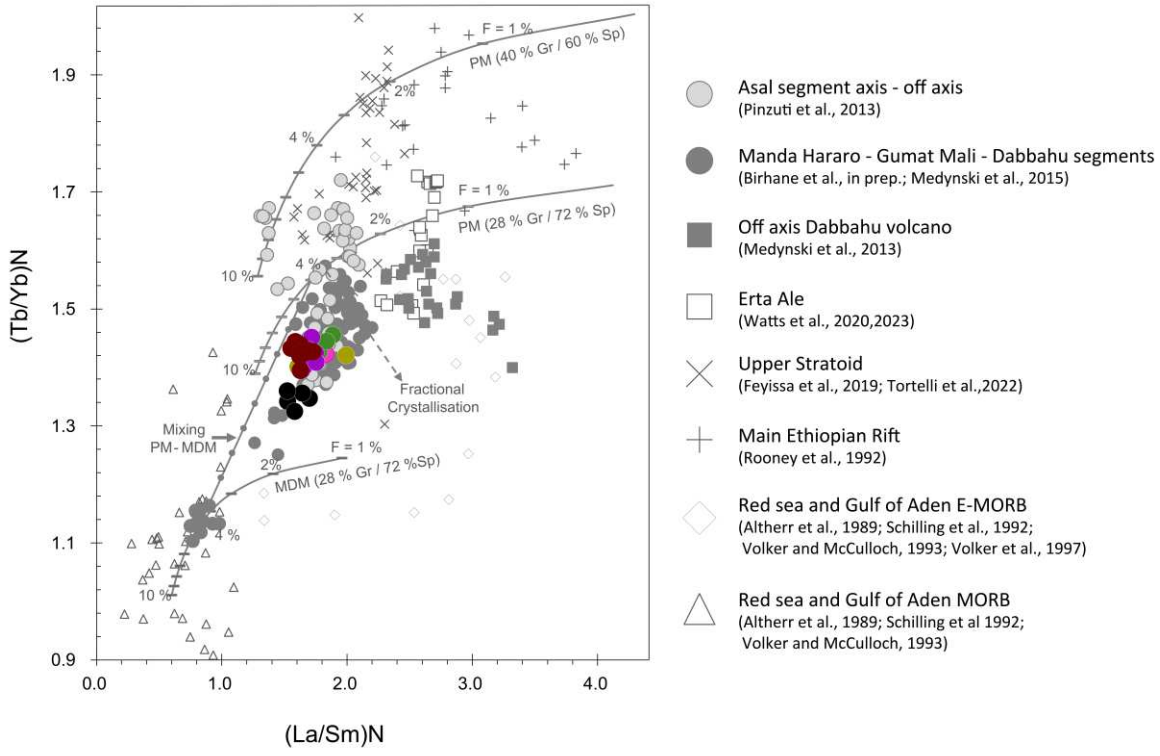

Figure 5.13: *(Tb/Yb)N vs. (La/Sm)N of the Asal-Ghoubbet segment samples, normalized to primitive mantle (Sun and McDonough, 1989). The legend for samples in this study is the same as for Figure 5.7. Curves represent melting model of different types of lherzolites for melted fractions (F) from 0 to 10 %: one with enriched composition of primitive mantle (PM, Sun and McDonough, 1989), and the other with a depleted composition (modified from DM, see Birhane et al., in prep. Chapter 3). The model is based on the non-modal batch melting equations of Shaw (1970). The partition coefficients of the elements used for the model are taken from Mckenzie and O'Nions (1991). Both curves are framed by*

28 % from melting of a garnet-rich mantle source (lherzolite) (concentration: 0.1 Garnet; 0.25 orthopyroxene; 0.15 clinopyroxene; 0.5 olivine) plus 72 % from melting a spinel- rich mantle source (lherzolite) (concentration: 0.25 orthopyroxene; 0.15 clinopyroxene; 0.02 spinel; 0.58 olivine). The mineral modes used for the model are those described by Tortelli et al. (2022): 0.1 Grt; 0.4 Cpx; 0.2 Opx; 0.3 Ol, for the Lherzolite with garnet melting curve; and 0.4 Cpx; 0.2 Opx; 0.1 Sp; 0.3 Ol for the Lherzolite with spinel and amphibole melting curve. An additional mixing line is joining the two melting curves for F = 4 %. Some deviation to the mixing line is due to fractional cristalisation modification of the two ratios (indicative). A second melting curve with higher proportions of garnet (40 % garnet + 60 % spinel) is necessary to account for the off axis Asal basaltic compositions (Pinzuti et al., 2013), as well as for some other regional basaltic compositions (MER, upper Stratoid).

Chapter 6

6. Conclusions and Future Perspectives

Continental rifting is a complex process that spans from the initiation of extension to continental breakup, and in which magmatism plays a fundamental role. The way magmas are transported from the mantle to the surface provides key insights into the dynamics of extension, especially during the Transition between Continental and Oceanic stages, i.e., the OCT. In the Afar region, a triple junction between two oceanic ridges (i.e., Gulf of Adaen and Red Sea) and a continental rift (East African Rift), and a rare ongoing example of OCT, on Earth, extension is currently accommodated through multiple magmatic segments. The magmato-tectonic characteristics of these segments vary in size, extension rate, crustal thickness, magma sources, and in the intensity and frequency of tectonic and volcanic activity. Magmatic and tectonic extension in Afar is concentrated within rift segments that are sometimes considered emerging oceanic ridges due to their maturity. These segments share similarities with slow- to ultra-slow-spreading ridges, given the measured extension rates (15-20 mm/yr; Doubre et al., 2007; McClusky et al., 2010). Structural, magmatic, and crustal variations along rift segments have been proposed to represent different stages of evolution from continental rifting to oceanic spreading (Ebinger & Casey, 2001; Manighetti et al., 2001; Bastow & Keir, 2011). Some studies suggest that the Erta Ale segment represents the final stage of breakup (Bastow & Keir, 2011; Rooney et al., 2014; Hutchison et al., 2018; Moore et al., 2019), characterized by significant ductile deformation and a system dominated by extrusive magmatic activity. In contrast, in the central Afar (Dabbahu-Manda Hararo) segments, extension is still mainly accommodated by magmatic intrusions. However, the Asal-Ghoubbet segment, in direct continuation of the Aden ridge, exhibits morphology and magmatic-tectonic characteristics opposite to those of Erta Ale, despite a similar degree of recent crustal thinning (Doubre et al., 2007; Geoffroy et al., 2014). Thus, rather than interpreting Afar rift segments as successive evolutionary stages (Ebinger & Casey, 2001; Bastow & Keir, 2011) or as a result of ridge propagation (Manighetti et al., 1998), their differences may instead reflect distinct styles of rifting (Stab et al., 2016; Rime et al., 2023), controlled by magma availability and by the long-term interaction between the continental lithosphere and the Afar plume.

The results of this thesis contribute to this debate from the perspective of the organization of magmatic systems in two active rift segments of the Afar depression with contrasting rifting styles: the Gumat Mali - Manda Hararo (Central Afar) and the Asal-Ghoubbet (Southern Afar)

segments. It comprises three major studies, each constraining the timing and evolution of magmatic events through detailed geological mapping, field investigations, cosmogenic ^{36}Cl exposure dating, and lava geochemistry. Together, these studies reveal the diversity of volcanic and magmatic processes during the ocean-continent transition, in terms of magma composition, the organization of melt batches, their residence within the crust, and their interaction with tectonic processes, highlighting that the accommodation of extension through magmatic intrusions is a major process in both rift systems.

6.1 Magmatic functioning of the Gumat Mali sub-segment

In the first study, comprising Chapters 3, we focus on and define a sub-segment of the Dabbahu - Manda Hararo system (DMH), i.e. the Gumat Mali sub-segment (GM), that runs directly southward of the Dabbahu segment on the same tectonic corridor. We combine detailed mapping, volcanological observations, major and trace element analyses, and cosmogenic ^{36}Cl exposure dating of lavas to describe it. The newly established and refined chronology of the Gumat Mali magmatic segment provides a more precise timeframe with 4 distinct episodes including a very detailed chronology of the recent volcanic activity in the region.

Based on this framework, we further investigate the continuous compositional trend for REE and other trace elements ratios, that captures intermediate moderately depleted magmas between enriched and depleted endmembers. We conclude that mantle source heterogeneities may play a significant role rather than potential crustal assimilation processes to account for the geochemical characteristics of the depleted and enriched magma types of central Afar. Moreover, those distinct mantle sources appear involved in a common melting process sampling them in varying proportions, in the field of garnet stability confirming previous investigations and interpretations in Central Afar of deep and hot mantle melting. In such a scenario, both components would represent gabbroic ocean-crustal material with various initial mineralogical composition (plagioclase vs. clinopyroxene) modulating the final enriched or depleted characters of those geochemical endmembers embedded in the upwelled mantle. This suggests that regional geochemical variability across central Afar rift segments can, in part, be explained by incorporation of small volumes of depleted mantle melts into predominantly enriched melts. The fact that this full compositional trend is expressed at the axis of the same active segments, also implies that the involvement of the various depleted and enriched components is not controlled by spatial or temporal geometrical variations of the upwelled mantle. Rather, the expression of the depleted component likely requires specific melting

conditions potentially controlled by the lithology and fertility of each mantle components. When the enriched component is present, its stronger trace element concentrations dominate the final magma composition, effectively masking the signature of the depleted component.

The sub-segment functions as a ~32 km-long magmatic accretion zone, with morpho-tectonic features comparable to slow-spreading mid-ocean ridges, as observed in other Afar segments, with episodic magma ascent and eruption controlled by axial structures. These features indicate persistent magma supply from a deeper zone, likely a mid-segment reservoir situated beneath the main crater with different batches of magma at different stages of differentiation tapped from separate reservoirs, aligned with the concept of vertically distributed magma storage zones in a transcrustal system. Moreover, the transition in magma characteristics at the axis of the Gumat Mali segment could witness a progressive maturation of the plumbing system over the last 300 ka, with progressive emplacement of shallower and more differentiated reservoirs.

The first information of our study regarding volcanic hazard assessment in the Gumat Mali area in Central Afar is represented by the documentation of recent historical activity from ~ 1900 to ~ 600 years ago, driven by a reservoir recharge with new and less differentiated magma that hybridised with a more differentiated mush in a shallow reservoir, a process that potentially reinforced the ability of the new magma in this reservoir to be mobilised. Our detailed volcanological investigation indicates that hazards assessments and management should in part be based on effusive episodes from axial fissures, but should also include potential extremely energetic phreatomagmatic phase, that characterize the initiation of the historical sequence. Such hazards do not only concern the Gumat Mali segment but also the Gablaytu volcanic centre, which exhibits recent volcanological activity, and therefore represents a regional additional risk for populations settled nearby those areas including part of the Semera.

6.2 Organisation of the Central Afar magmatic sub-segments

The second study, discussed in Chapter 4 and focussed on new data for the Manda Hararo sub-segment, document the vertical and lateral organisation of magmatic reservoirs across Central Afar (including Gumat Mali data), potential interconnections between plumbing systems, and constrain their role in controlling large-scale rift segmentation in this key area of Ocean Continent Transition.

Our detailed geological mapping, cosmogenic ^{36}Cl dating, and geochemical data from the Manda Hararo and Gumat Mali sub-segments indicate that magmatic and tectonic processes have been closely linked since at least 400 ka. The evolution of these sub-segments indicates

that a transcrustal magmatic system was established around 300 - 400 ka, characterized by vertically and laterally connected magma reservoirs and repeated replenishment events.

The temporal evolution of magmas over the last 20 ka suggests that melts stored at different crustal depths and differentiation stages were repeatedly mobilized, differentiated and interacted over typical timescales. Plagioclase assimilation is particularly evident at Gumat Mali and Gablaytu, indicating the presence of crustal mush zones and dynamic magma reservoirs. These observations suggest a multistage, vertically stratified, time-dependent transcrustal system organization, where mantle-derived inputs interact with evolving crustal reservoirs to produce the observed magmatic diversity. The distinct magma types identified across the sub-segments reflect differences in both crustal processes and mantle sources. The spatial distribution of magma types and their geochemical evolution indicate that surface emplacement corresponds to specific zones of melt generation in the mantle and that tectonic structures strongly control the location and pathways of magma ascent.

The organization of magmatism in the central Afar sub-segments is largely controlled by tectonic structures, with major faults acting as preferential zones for magma transfer and storage. The en-echelon segmentation of the rift exerts a first-order control on the position of magmatic reservoirs, influencing both vertical melt transport and crustal differentiation. Over time, magmatism became progressively localized along the axial zones, evolving toward a mature transcrustal plumbing system characterized by repeated magma injection, hybridization, and eruption. The interaction between tectonic segmentation and mantle melting explains the focusing of extension observed at the ocean-continent transition in central Afar. The relationship between tectonic sub-segmentation and mantle melting is key to understand how focalization develops at the OCT. Observations of such rift sub-segmentation close to the OCT provide valuable information for models of mature oceanic ridge development and highlight the progressive evolution of central Afar toward an oceanic type spreading system.

6.3 Magmatic functioning of Asal-Ghoubbet rift system

The third study, outlined in Chapter 5, presents an extensive set of cosmogenic age constraints on the Asal-Ghoubbet rift segment, focusing on axial zone lava flows to better understand the dynamics of magma transfer in the crust. The results indicate that most lava fields are exceptionally young, with eruption ages ranging from 1 to 3.5 ka, except for one dated at 8 ka. By integrating geochemical observations with high-resolution lava geochronology across the Asal-Ghoubbet rift system, we identified and documented two distinct magmatic cycles,

marked by phases of magma differentiation and system replenishment. The first cycle occurred around 3.5 ka and lasted up to 1.1 ka, while the second is associated with the 1978 Ardoukoba eruption, which displayed significant magma evolution within just five days. Those synchronous activities of all volcanic centers during the first cycle suggest the presence of a large, interconnected magma reservoir feeding the entire Asal–Ghoubbet system, rather than isolated kilometer-scale magma lenses. Following the closure of the magmatic system after the first cycle, the second cycle likely involved renewed input of magma derived from a distinct batch of mantle melt. Our observations and results suggest that variations in magmatic activity within the Afar magmatic segments are controlled by the balance between magma supply from depth and differentiation within shallow crustal reservoirs.

All lava series emplaced across the Asal-Ghoubbet rift system since ~3.5 ka are enriched in light rare earth elements (LREE) and show pronounced Ba and Ta peaks, negative K anomalies, and U-Th troughs on multi-element diagrams consistent with lavas described in Central Afar. They also display identical La/Sm and Tb/Yb ratios suggesting that regional geochemical variability across central and southern Afar rift segments can be explained by incorporation of small volumes of depleted mantle melts into dominantly enriched melts both originating from the Afar mantle plume. Such a potential scenario in turn implies to be cautious when interpreting and inverting REE to constrains depth of melting, or when interpreting the depleted character of lavas as refleting incorporation of N-MORB mantle source in the generation of melts. Globally it appears that the variously enriched lavas from Central and Southern Afar axial segments are clearly different from other regional or older lava series that require (i) more garnet in the mantle source (off-axis Asal, MER and upper stratoid) and then deeply anchored melting column, or (ii) apparent lower melt fractions (Dabbahu off-axis, Erta Ale), or alternatively more enriched component.

6.4 Future Perspectives

The results presented in this thesis highlight the central role of vertically and laterally organized transcrustal magmatic systems in accommodating extension during the OCT in Afar. There are numerous avenues of research that could continue to expand this work, summarised below:

Petrological studies: Detailed mineral chemistry and melt inclusion studies would allow quantification of thermobarometric constraints on magma storage depths of the different magma batches identified in Central Afar. Such approaches would help to better constrain the

longevity, and temporal evolution of magma reservoirs inferred from geochemical trends, particularly the progressive maturation of shallow storage zones at Gumat Mali and Manda Hararo sub-segments. These data would provide independent constraints on the architecture of transcrustal systems and refine interpretations of magma recharge and hybridization processes.

Tectonic investigations: Although this thesis demonstrates that tectonic segmentation exerts a first-order control on magma ascent pathways and reservoir localization, detailed mapping of fault networks, combined with geodetic, seismic, or structural analyses, would help to quantify the faults linked with dike injection and extensional processes. Such work would be particularly valuable for assessing how strain is partitioned between tectonic and magmatic processes in segments exhibiting contrasting rifting styles, and for improving volcanic hazard assessments in actively extending Central Afar.

Extending the study to other Afar segments: The Plumbing system organization in time developed for central Afar would benefit from comparative, integrated studies of other Afar rift segments, such as the Erta Ale segment. Applying a similar combination of detailed geological mapping, high-precision lava geochronology, and geochemical characterization would allow to determine whether the results of this thesis can be fully extrapolated to the whole Afar rift segments.

References

Abdallah, A., Courtillot, V., Kasser, M., Le Dain, A.-Y., Lépine, J.-C., Robineau, B., Ruegg, J.-C., Tapponnier, P. & Tarantola, A. (1979). Relevance of Afar seismicity and volcanism to the mechanics of accreting plate boundaries. Nature, 282(5734), 17–23. https://doi.org/10.1038/282017a0

Alene, M., Hart, W. K., Saylor, B. Z., Deino, A., Mertzman, S., Haile-Selassie, Y., & Gibert, L. B. (2017). Geochemistry of Woranso–Mille Pliocene basalts from west-central Afar, Ethiopia: Implications for mantle source characteristics and rift evolution. Lithos, 282–283, 187–200. https://doi.org/10.1016/j.lithos.2017.03.005

Allard, P., Tazieff, H., & Dajlevic, D. (1979). Observations of seafloor spreading in Afar during the November 1978 fissure eruption. Nature, 279(5707), 30–33. https://doi.org/10.1038/279030a0

Altherr, R., Henjes-Kunst, F., Puchelt, H., & Baumann, A. (1988). Volcanic activity in the Red Sea axial trough — evidence for a large mantle diapir? Tectonophysics, 150(1–2), 121–133. https://doi.org/10.1016/0040-1951(88)90298-3

Annen, C., Blundy, J. D., & Sparks, R. S. J. (2006). The genesis of intermediate and silicic magmas in deep crustal hot zones. Journal of Petrology, 47(3), 505–539. https://doi.org/10.1093/petrology/egi084

Aufaristama, M., Hoskuldsson, A., Jonsdottir, I., Ulfarsson, M. O., & Thordarson, T. (2018). New insights for detecting and deriving thermal properties of lava flow using infrared satellite during 2014-2015 effusive eruption at Holuhraun, Iceland. Remote Sensing, 10(1), 1–24. https://doi.org/10.3390/rs10010151

Ayalew, D., Jung, S., Romer, R. L., Kersten, F., Pfänder, J. A., & Garbe-schönberg, D. (2016). Petrogenesis and origin of modern Ethiopian rift basalts: Constraints from isotope and trace element geochemistry. LITHOS, 258–259, 1–14. https://doi.org/10.1016/j.lithos.2016.04.001

Ayalew, D., Pik, R., Bellahsen, N., France, L., & Yirgu, G. (2019). Differential Fractionation of Rhyolites During the Course of Crustal Extension, Western Afar (Ethiopian Rift). Geochemistry, Geophysics, Geosystems, 20(2), 571–593. https://doi.org/10.1029/2018GC007446

Ayele, A., Stuart, G., Bastow, I., & Keir, D. (2007). The August 2002 earthquake sequence in north Afar: Insights into the neotectonics of the Danakil microplate. 48(August 2002), 70–79. https://doi.org/10.1016/j.jafrearsci.2006.06.011

Baker, J., Snee, L., & Menzies, M. (1996). A brief Oligocene period of flood volcanism in Yemen: Implications for the duration and rate of continental flood volcanism at the Afro-Arabian triple junction. Earth and Planetary Science Letters, 138(1–4), 39–55. https://doi.org/10.1016/0012-821x(95)00229-6

Balco, G., Stone, J. O., Lifton, N. A., & Dunai, T. J. (2008). A complete and easily accessible means of calculating surface exposure ages or erosion rates from 10Be and 26Al measurements. Quaternary Geochronology, 3(3), 174–195. https://doi.org/10.1016/j.quageo.2007.12.001

Balco, G. (2014). Simple computer code for estimating cosmic ray shielding by oddly shaped objects. Quaternary Geochronology, 22, 175–182. https://doi.org/10.1016/j.quageo.2013.12.002

Barberi, F., & Varet, J. (1970). The Erta Ale volcanic range (Danakil Depression, northern Afar, Ethiopia). Bulletin of Volcanology, 34(4), 848–917. https://doi.org/10.1007/BF02596805

Barberi, F., Borsi, S., Ferrara, G., Marinelli, G., Santacroce, R., Tazieff, H., & Varet, J. (1972). Evolution of the Danakil Depression (Afar, Ethiopia) in light of radiometric age determinations. Journal of Geology, 80(6), 720–729. https://doi.org/10.1086/627797

Barrat, J. A., Jahn, B. M., Joron, J. L., Auvray, B., & Hamdi, H. (1990). Mantle heterogeneity in northeastern Africa: evidence from Nd isotopic compositions and hygromagmaphile element geochemistry of basaltic rocks from the Gulf of Tadjoura and southern Red Sea regions. Earth and Planetary Science Letters, 101(2–4), 233–247. https://doi.org/10.1016/0012-821X(90)90156-R

Barrat, J. A., Jahn, B. M., Fourcade, S., & Joron, J. L. (1993). Magma genesis in an ongoing rifting zone: The Tadjoura Gulf (Afar area). Geochimica et Cosmochimica Acta, 57(10), 2291–2302. https://doi.org/10.1016/0016-7037(93)90570-M

Barrat, J. A., Fourcade, S., Jahn, B. M., Cheminée, J. L., & Capdevila, R. (1998). Isotope (Sr, Nd, Pb, O) and trace-element geochemistry of volcanics from the Erta'Ale range (Ethiopia). Journal of Volcanology and Geothermal Research, 80(1–2), 85–100. https://doi.org/10.1016/S0377-0273(97)00016-4

Barrat, J. A., Joron, J. L., Taylor, R. N., Fourcade, S., Nesbitt, R. W., & Jahn, B. M. (2003). Geochemistry of basalts from Manda Hararo, Ethiopia: LREE-depleted basalts in Central Afar. Lithos, 69(1–2), 1–13. https://doi.org/10.1016/S0024-4937(03)00044-6

Bastow, I. D., Stuart, G. W., Kendall, J., & Ebinger, C. J. (2005). Upper-mantle seismic structure in a region of incipient continental breakup: northern Ethiopian rift. 479–493. https://doi.org/10.1111/j.1365-246X.2005.02666.x

Bastow, I. D., Nyblade, A. A., Stuart, G. W., Rooney, T. O., & Benoit, M. H. (2008). Upper mantle seismic structure beneath the Ethiopian hot spot: Rifting at the edge of the African low-velocity anomaly. Geochemistry, Geophysics, Geosystems, 9(12). https://doi.org/10.1029/2008GC002107

Bastow, I. D., Pilidou, S., Kendall, J.-M., & Stuart, G. W. (2010). Melt-induced seismic anisotropy and magma-assisted rifting in Ethiopia: Evidence from surface waves. Geochemistry, Geophysics, Geosystems, 11(6), Q0AB05. https://doi.org/10.1029/2010GC003036

Bastow, I. D., & Keir, D. (2011). The protracted development of the continent-ocean transition in Afar. Nature Geoscience, 4(4), 248–250. https://doi.org/10.1038/ngeo1095

Belachew, M., Ebinger, C. J., Coté, D., Keir, D., Rowland, J. V., Hammond, J. O. S., & Ayele, A. (2011). Comparison of dike intrusions in an incipient seafloor-spreading segment in Afar, Ethiopia: Seismicity perspectives. Journal of Geophysical Research: Solid Earth, 116(B6), B06405. https://doi.org/10.1029/2010JB007908

Bennett, E. N., Jenner, F. E., Millet, M. A., Cashman, K. V., & Lissenberg, C. J. (2019). Deep roots for mid-ocean-ridge volcanoes revealed by plagioclase-hosted melt inclusions. Nature, 572(7768), 235–

239. https://doi.org/10.1038/s41586-019-1448-0

Beyer, R. A., Alexandrov, O., & McMichael, S. (2018). The Ames Stereo Pipeline: NASA's Open-Source Software for Deriving and Processing Terrain Data. Earth and Space Science, 5(9), 537–548. https://doi.org/10.1029/2018EA000409

Biggs, J., Ayele, A., Fischer, T. P., Fontijn, K., Hutchison, W., Kazimoto, E., Whaler, K., & Wright, T. J. (2021). Volcanic activity and hazard in the East African Rift Zone. Nature Communications, 12(1), 1–12. https://doi.org/10.1038/s41467-021-27166-y

Birhanu, Y., R. Bendick, S. Fisseha,E. Lewi, M. Floyd, R. King, andR. Reilinger (2016). GPS constraints on broad scale extension in the Ethiopian Highlands and Main Ethiopian Rift. Geophys. Res. Lett., 43, 6844–685. https://doi.org/10.1002/2016GL069890

Bisson, M., Spinetti, C., Andronico, D., Palaseanu-Lovejoy, M., Fabrizia Buongiorno, M., Alexandrov, O., & Cecere, T. (2021). Ten years of volcanic activity at Mt Etna: High-resolution mapping and accurate quantification of the morphological changes by Pleiades and Lidar data. International Journal of Applied Earth Observation and Geoinformation, 102(May), 102369. https://doi.org/10.1016/j.jag.2021.102369

Blard, P.-H. (2021). Cosmogenic ^{3}He in terrestrial rocks: A review. Chemical Geology, 586, 120543. https://doi.org/10.1016/j.chemgeo.2021.120543

Boulanger, M., & France, L. (2023). Cumulate Formation and Melt Extraction from Mush-Dominated Magma Reservoirs: The Melt Flush Process Exemplified at Mid-Ocean Ridges. Journal of Petrology, 64(2), 1–20. https://doi.org/10.1093/petrology/egad005

Bridges, D. L., Mickus, K., Gao, S. S., Abdelsalam, M. G., & Alemu, A. (2012). Magnetic stripes of a transitional continental rift in Afar. Geology, 40(3), 203–206. https://doi.org/10.1130/G32697.1

Buck, W. R. (1991). Modes of continental lithospheric extension. Journal of Geophysical Research, 96(B12), 161–178. https://doi.org/10.1029/91jb01485

Buck, W. R. (1993). Effect of lithospheric thickness on the formation of high- and low-angle normal faults. Geology, 21(10), 933-936.
https://doi.org/10.1130/00917613(1993)021<0933:EOLTOT>2.3.CO;2

Buck, W. R. (2004). Consequences of asthenospheric variability on continental rifting. In G. D. Karner, B. Taylor, N. W. Driscoll, & D. L. Kohlstedt (Eds.), Rheology and deformation of the lithosphere at continental margins (pp. 1–30). Columbia University Press, New York.
https://doi.org/10.7312/karn12738-001

Buck, W. R., Lavier, L. L., & Poliakov, A. N. B. (2005). Modes of faulting at mid-ocean ridges. Nature, 434(7034), 719–723. https://doi.org/10.1038/nature03358

Buck, W. R. (2006). The role of magma in the development of the Afro-Arabian Rift System, Geological Society, London, Special Publications, 259(1), 43–54.
https://doi.org/10.1144/GSL.SP.2006.259.01.05

Buck, W. R., Einarsson, P., & Brandsdóttir, B. (2006). Tectonic stress and magma chamber size as controls on dike propagation: Constraints from the 1975-1984 Krafla rifting episode. Journal of Geophysical Research: Solid Earth, 111(12), 1–15. https://doi.org/10.1029/2005JB003879

Burke, K. (2011). Plate tectonics, the wilson cycle, and mantle plumes: Geodynamics from the top. Annual Review of Earth and Planetary Sciences, 39, 1–29. https://doi.org/10.1146/annurev-earth-040809-152521

Calais, E., Ebinger, C., Hartnady, C., & Nocquet, J. M. (2006). Kinematics of the East African Rift from GPS and earthquake slip vector data service Permission Subscribe Kinematics of the East African Rift from GPS and earthquake slip vector data. Geological Society Special Publication, 259. https://doi.org/10.1144/GSL.SP.2006.259.01.03

Cannat, M., Sauter, D., Lavier, L., Bickert, M., Momoh, E., & Leroy, S. (2019). On spreading modes and magma supply at slow and ultraslow mid-ocean ridges. Earth and Planetary Science Letters, 519, 223–233. https://doi.org/10.1016/j.epsl.2019.05.012

Carbotte, S. M., Detrick, R. S., Harding, A., Canales, J. P., Babcock, J., Kent, G., Van Ark, E., Nedimovic, M., & Diebold, J. (2006). Rift topography linked to magmatism at the intermediate spreading Juan de Fuca Ridge. Geology, 34(3), 209–212. https://doi.org/10.1130/G21969.1

Carbotte, S. M., Smith, D. K., Cannat, M., & Klein, E. M. (2016). Tectonic and magmatic segmentation of the Global Ocean Ridge System: A synthesis of observations. Geological Society Special Publication, 420(1), 249–295. https://doi.org/10.1144/SP420.5

Cashman, K. V., Sparks, R. S. J., & Blundy, J. D. (2017). Vertically extensive and unstable magmatic systems: A unified view of igneous processes. Science, 355(6331). https://doi.org/10.1126/science.aag3055

Chambers, E. L., Harmon, N., Rychert, C. A., & Keir, D. (2021). Variations in melt emplacement beneath the northern East African Rift from radial anisotropy. Earth and Planetary Science Letters, 573, 117150. https://doi.org/10.1016/j.epsl.2021.117150

Chauvel, C., & He, C. (2000). Melting of a complete section of recycled oceanic crust: Trace element and Pb isotopic evidence from Iceland. February 1–22. https://doi.org/10.1029/1999GC000002

Cloquet, C., Carignan, J., & Libourel, G. (2006). Atmospheric pollutant dispersion around an urban area using trace metal concentrations and Pb isotopic compositions in epiphytic lichens. Atmospheric Environment, 40(3), 574–587. https://doi.org/10.1016/j.atmosenv.2005.09.073

Colman, A., Sinton, J. M., White, S. M., McClinton, J. T., Bowles, J. A., Rubin, K. H., Behn, M. D., Cushman, B., Eason, D. E., Gregg, T. K. P., Grönvold, K., Hidalgo, S., Howell, J., Neill, O., & Russo, C. (2012). Effects of variable magma supply on mid-ocean ridge eruptions: Constraints from mapped lava flow fields along the Galápagos Spreading Center. Geochemistry, Geophysics, Geosystems, 13(8), Article Q08014. https://doi.org/10.1029/2012GC004163

Corradino, C., Ganci, G., Cappello, A., Bilotta, G., Hérault, A., & Del Negro, C. (2019). Mapping recent

lava flows at Mount Etna using multispectral Sentinel-2 images and machine learning techniques. Remote Sensing, 11(16). https://doi.org/10.3390/rs11161916

Corti, G., van Wijk, J., Cloetingh, S., & Morley, C. K. (2007). Tectonic inheritance and continental rift architecture: Numerical and analogue models of the East African Rift system. Tectonics, 26(6), 1–13. https://doi.org/10.1029/2006TC002086

Daoud, M. A., Maury, R. C., Barrat, J.-A., Taylor, R. N., Le Gall, B., Guillou, H., Cotten, J., & Rolet, J. (2010). A LREE-depleted component in the Afar plume: further evidence from Quaternary Djibouti basalts. Lithos, 114(3–4), 327–336. https://doi.org/10.1016/j.lithos.2009.09.008

De Chabalier, J.-B., & Avouac, J.-P. (1994). Kinematics of the Asal Rift (Djibouti) Determined from the Deformation of Fieale Volcano. Science, 265(5179), 1677–1681. https://doi.org/10.1126/science.265.5179.1677

Demange Jacques Par, Laurent Stieltjes, and J. V. (1980). The Asal erutiopn of November 1978. Bulletin de La Société Géologique de France, 837–843. https://doi.org/10.2113/gssgfbull.S7-XXII.6.837

Deniel, C., Vidal, P., Coulon, C., Vellutini, P. J., & Piguet, P. (1994). Temporal evolution of mantle sources during continental rifting: the volcanism of Djibouti (Afar). Journal of Geophysical Research, 99(B2), 2853–2869. https://doi.org/10.1029/93JB02576

DePaolo, D. J. (1981). Trace element and isotopic effects of combined wall-rock assimilation and fractional crystallization. Earth and Planetary Science Letters, 53(2), 189–202. https://doi.org/10.1016/0012-821X(81)90153-9

Deprez, A., Doubre, C., Masson, F., & Ulrich, P. (2013). Seismic and aseismic deformation along the East African Rift System from a reanalysis of the GPS velocity field of Africa. Geophysical Journal International, 193(3), 1353–1369. https://doi.org/10.1093/gji/ggt085

Desilets, D., Zreda, M., Almasi, P. F., & Elmore, D. (2006). Determination of cosmogenic 36Cl in rocks by isotope dilution: innovations, validation, and error propagation. Chemical Geology, 233(3–4), 185–195. https://doi.org/10.1016/j.chemgeo.2006.03.001

Desissa, M., Johnson, N. E., Whaler, K. A., Hautot, S., Fisseha, S., & Dawes, G. J. K. (2013). A mantle magma reservoir beneath an incipient mid-ocean ridge in Afar, Ethiopia. Nature Geoscience, 6(10), 861–865. https://doi.org/10.1038/ngeo1925

Didana, Y. L., Thiel, S., & Heinson, G. (2014). Magnetotelluric imaging of upper crustal partial melt at Tendaho graben in Afar, Ethiopia. Geophysical Research Letters, 41(9), 3089–3095. https://doi.org/10.1002/2014GL060000

Doubre, C., Manighetti, I., Dorbath, L., Dorbath, C., Bertil, D., & Delmond, J. C. (2007). Crustal structure and magmato-tectonic processes in an active rift (Asal-Ghoubbet, Afar, East Africa): 2. Insights from the 23-year recording of seismicity since the last rifting event. Journal of Geophysical Research: Solid Earth, 112(B5). https://doi.org/10.1029/2006jb004333

Doubre, C., Déprez, A., Masson, F., Socquet, A., Lewi, E., Grandin, R., Nercessian, A., Ulrich, P., De Chabalier, J. B., Saad, I., Abayazid, A., Peltzer, G., Delorme, A., Calais, E., & Wright, T. (2017). Current deformation in Central Afar and triple junction kinematics deduced from GPS and InSAR measurements. Geophysical Journal International, 208(2), 936–953. https://doi.org/10.1093/gji/ggw434

Dugda, M. T., Nyblade, A. A., Julia, J., Langston, C. A., Ammon, C. J., & Simiyu, S. (2005). Crustal structure in Ethiopia and Kenya from receiver function analysis: Implications for rift development in eastern Africa. Journal of Geophysical Research: Solid Earth, 110(1), 1–15. https://doi.org/10.1029/2004JB003065

Dugda, M. T., & Nyblade, A. A. (2006). New constraints on crustal structure in eastern Afar from the analysis of receiver functions and surface wave dispersion in Djibouti. 259, 239–251. https://doi.org/10.1144/GSL.SP.2006.259.01.19

Dumont, S., Klinger, Y., Socquet, A., Doubre, C., & Jacques, E. (2017). Magma influence on propagation of normal faults: Evidence from cumulative slip profiles along Dabbahu-Manda-Hararo rift segment (Afar, Ethiopia). Journal of Structural Geology, 95, 48–59. https://doi.org/10.1016/j.jsg.2016.12.008

Dumont, S., Klinger, Y., Socquet, A., Escartín, J., Grandin, R., Jacques, E., Medynski, S., & Doubre, C. (2019). Rifting Processes at a Continent-Ocean Transition Rift Revealed by Fault Analysis: Example of Dabbahu-Manda-Hararo Rift (Ethiopia). Tectonics, 38(1), 190–214. https://doi.org/10.1029/2018TC005141

Dunbar, J. A., & Sawyer, D. S. (1989). How pre-existing weaknesses control the style of continental breakup. Journal of Geophysical Research: Solid Earth, 94(B6), 7278–7292. https://doi.org/10.1029/JB094iB06p07278

Dunne, J., Elmore, D., & Muzikar, P. (1999). Scaling factors for the rates of production of cosmogenic nuclides for geometric shielding and attenuation at depth on sloped surfaces. Geomorphology, 27(1–2), 3–11. https://doi.org/10.1016/S0169-555X(98)00086-5

Dziak, R. P., Fox, C. G., & Schreiner, A. E. (1995). The June-July 1993 seismo-acoustic event at CoAxial segment, Juan de Fuca Ridge: Evidence for a lateral dike injection. Geophysical Research Letters, 22(2), 135–138. https://doi.org/10.1029/94GL01857

Ebinger, C. J., & Sleep, N. H. (1998). Cenozoic magmatism throughout East Africa resulting from impact of a single plume. Nature, 395(6704), 788–791. https://doi.org/10.1038/27417

Ebinger, C. J., & Casey, M. (2001). Continental breakup in magmatic provinces: An Ethiopian example. Geology, 29(6), 527–530. https://doi.org/10.1130/0091-7613(2001)029<0527:CBIMPA>2.0.CO;2

Ebinger, C. (2005). Continental break-up: The East African perspective. Astronomy and Geophysics, 46(2), 2.16-2.21. https://doi.org/10.1111/j.1468-4004.2005.46216.x

Ebinger, C. J., Keir, D., Ayele, A., Calais, E., Wright, T. J., Belachew, M., Hammond, J. O. S.,

Campbell, E., & Buck, W. R. (2008). Capturing magma intrusion and faulting processes during continental rupture: Seismicity of the Dabbahu (Afar) rift. Geophysical Journal International, 174(3), 1138–1152. https://doi.org/10.1111/j.1365-246X.2008.03877.x

Ebinger, C., Ayele, A., Keir, D., Rowland, J., Yirgu, G., Wright, T., Belachew, M., & Hamling, I. (2010). Length and timescales of rift faulting and magma intrusion: The afar rifting cycle from 2005 to present. Annual Review of Earth and Planetary Sciences, 38(February), 439–466. https://doi.org/10.1146/annurev-earth-040809-152333

Eldholm, O., Gladczenko, T. P., Skogseid, J., & Planke, S. (2000). Atlantic volcanic margins: A comparative study. Geological Society Special Publication, 167, 411–428. https://doi.org/10.1144/GSL.SP.2000.167.01.16

Elmore, D., & Phillips, F. M. (1987). Accelerator mass spectrometry for measurement of long-lived radioisotopes. Science, 236(4801), 543–550. https://doi.org/10.1126/science.236.4801.543

\Erbello, A., Colleps, C., Melnick, D., Sobel, E. R., Bookhagen, B., Pingel, H., & Al., E. (2024). Magma-Assisted Continental Rifting: The Broadly Rifted Zone in SW Ethiopia, East Africa. Tectonics, 43. https://doi.org/10.1029/2022TC007651

F. Zwaan, G. Corti, F.Sani, D. Keir, A.A. Muluneh, F. Illaley-Kemp, and M. P. (2020). Structural Analysis of the Western Afar Margin, East Africa: Evidence for Multiphase Rotational Rifting. AGU, 1–25. https://doi.org/10.1029/2019TC006043

Ferguson, D. J., Barnie, T. D., Pyle, D. M., Oppenheimer, C., Yirgu, G., Lewi, E., Kidane, T., Carn, S., & Hamling, I. (2010). Recent rift-related volcanism in Afar, Ethiopia. Earth and Planetary Science Letters, 292(3–4), 409–418. https://doi.org/10.1016/j.epsl.2010.02.010

Ferguson, D. J., MacLennan, J., Bastow, I. D., Pyle, D. M., Jones, S. M., Keir, D., Blundy, J. D., Plank, T., & Yirgu, G. (2013). Melting during late-stage rifting in Afar is hot and deep. Nature, 499(7456), 70–73. https://doi.org/10.1038/nature12292

Fernandes, R. M. S., Ambrosius, B. A. C., Noomen, R., Bastos, L., Combrinck, L., Miranda, J. M., & Spakman, W. (2004). Angular velocities of Nubia and Somalia from continuous GPS data: implications on present-day relative kinematics. 222, 197–208. https://doi.org/10.1016/j.epsl.2004.02.008

Feyissa, D. H., Kitagawa, H., Bizuneh, T. D., Tanaka, R., Kabeto, K., & Nakamura, E. (2019). Transition from Plume-driven to Plate-driven Magmatism in the Evolution of the Main Ethiopian Rift. Journal of Petrology, 60(8), 1681–1715. https://doi.org/10.1093/petrology/egz043

Field, L., Blundy, J., Brooker, R. A., Wright, T., & Yirgu, G. (2012a). Magma storage conditions beneath Dabbahu Volcano (Ethiopia) constrained by petrology, seismicity, and satellite geodesy. Bulletin of Volcanology, 74(5), 981–1004. https://doi.org/10.1007/s00445-012-0580-6

Field, L., Barnie, T., Blundy, J., Brooker, R. A., Keir, D., Lewi, E., & Saunders, K. (2012b). Integrated field, satellite, and petrological observations of the November 2010 eruption of Erta Ale. Bulletin of Volcanology, 74(10), 2251–2271. https://doi.org/10.1007/s00445-012-0660-7

Field, L. P., Blundy, J. D., Calvert, A. T., & Yirgu, G. (2013). Magmatic history of Dabbahu, a composite volcano in the Afar Rift, Ethiopia. Geological Society of America Bulletin, 125(1–2), 128–147. https://doi.org/10.1130/B30560.1

Fitton, J. G., Saunders, A. D., Larsen, L. M., Hardarson, B. S., & Norry, M. J. (1998). Volcanic rocks from the southeast Greenland Margin at 63°N: composition, petrogenesis, and mantle sources. Proceedings of the Ocean Drilling Program: Scientific Results, 152, 331–350. https://doi.org/10.2973/odp.proc.sr.152.233.1998

Forsyth, D., & Uyedaf, S. (1975). On the Relative Importance of the Driving Forces of Plate Motion. Geophysical Journal of the Royal Astronomical Society, 43(1), 163–200. https://doi.org/10.1111/j.1365-246X.1975.tb00631.x

Fox, C. G., Radford, W. E., Dziak, R. P., Lau, T. -K, Matsumoto, H., & Schreiner, A. E. (1995). Acoustic detection of a seafloor spreading episode on the Juan de Fuca Ridge using military hydrophone arrays. Geophysical Research Letters, 22(2), 131–134. https://doi.org/10.1029/94GL02059

Franco Barberi, and J. V. (1977). Volcanism of Afar: Small-scale plate tectonics implications. 70904.

Franke, D. (2013). Rifting, lithosphere breakup and volcanism: Comparison of magma-poor and volcanic rifted margins. Marine and Petroleum Geology, 43, 63–87. https://doi.org/10.1016/j.marpetgeo.2012.11.003

French, S. W., & Romanowicz, B. (2015). Broad plumes rooted at the base of the Earth's mantle beneath major hotspots. Nature, 525(7567), 95–99. https://doi.org/10.1038/nature14876

Furman, T., & Graham, D. (1999). Erosion of lithospheric mantle beneath the East African Rift system: Geochemical evidence from the Kivu volcanic province. Lithos, 48(1–4), 237–262. https://doi.org/10.1016/S0419-0254(99)80014-7

Furman, T., Bryce, J., Rooney, T. O., Hanan, B. B., Yirgu, G., & Ayalew, D. (2006). Heads and tails: 30 million years of the Afar plume. In G. Yirgu, C. J. Ebinger, & P. K. H. Maguire (Eds.), The Afar Volcanic Province within the East African Rift System (Geological Society, London, Special Publications 259, pp. 95–119). https://doi.org/10.1144/GSL.SP.2006.259.01.01

Furman, T., Nelson, W. R., & Elkins-tanton, L. T. (2016). Evolution of the East African rift: Drip magmatism, lithospheric thinning, and mafic volcanism. Geochimica et Cosmochimica Acta, 185, 418–434. https://doi.org/10.1016/j.gca.2016.03.024

Gale, A., Dalton, C. A., Langmuir, C. H., Su, Y., & Schilling, J. G. (2013). The mean composition of ocean ridge basalts. Geochemistry, Geophysics, Geosystems, 14(3), 489–518. https://doi.org/10.1029/2012GC004334

Gani, N. D. S., Gani, M. R., & Abdelsalam, M. G. (2007). Blue Nile incision on the Ethiopian Plateau: Pulsed plateau growth, Pliocene uplift, and hominin evolution. GSA Today, 17(9), 4–11. https://doi.org/10.1130/GSAT01709A.1

Geoffroy, L. (2005). Volcanic passive margins. Comptes Rendus - Geoscience, 337(16), 1395–1408.

https://doi.org/10.1016/j.crte.2005.10.006

Geoffroy, L., Le Gall, B., Daoud, M. A., & Jalludin, M. (2014). Flip-flop detachment tectonics at nascent passive margins in SE Afar. Journal of the Geological Society, 171(5), 689–694. https://doi.org/10.1144/jgs2013-135

Gilles Chazot and Herve Bertrand. (1993). Mantle Sources and Magma-Continental Crust Interactions During Early Red Sea-Gulf of Aden Rifting in Southem Yemen: Elemental and Sr, Nd, Pb Isotope Evidence.JournalofGeophysicalResearch,98,1819–1835. https://doi.org/https://doi.org/10.1029/92JB02314

Gillespie, A. R., Kahle, A. B., & Walker, R. E. (1986). Color enhancement of highly correlated images. I. Decorrelation and HSI contrast stretches. Remote Sensing of Environment, 20(3), 209–235. https://doi.org/10.1016/0034-4257(86)90044-1

Gleyzes, M. A., Perret, L., & Kubik, P. (2012). Pleiades System Architecture and Main Performances. The International Archives of the Photogrammetry, Remote Sensing and Spatial Information Sciences, 537–542. https://doi.org/10.5194/isprsarchives-xxxix-b1-537-2012

Gosse, J. C., & Phillips, F. M. (2001). Terrestrial in situ cosmogenic nuclides: theory and application. Quaternary Science Reviews, 20(14), 1475–1560. https://doi.org/10.1016/S0277-3791(00)00171-2

Grandin, R., Socquet, A., Binet, R., Klinger, Y., Jacques, E., De Chabalier, J. B., King, G. C. P., Lasserre, C., Tait, S., Tapponnier, P., Delorme, A., & Pinzuti, P. (2009). September 2005 Manda hararo-dabbahu rifting event, Afar (Ethiopia): Constraints provided by geodetic data. Journal of Geophysical Research: Solid Earth, 114(8). https://doi.org/10.1029/2008JB005843

Grandin, R., Socquet, A., Jacques, E., Mazzoni, N., De Chabalier, J. B., & King, G. C. P. (2010a). Sequence of rifting in Afar, Manda-Hararo rift, Ethiopia, 2005-2009: Time-space evolution and interactions between dikes from interferometric synthetic aperture radar and static stress change modeling. Journal of Geophysical Research: Solid Earth, 115(10), 2005–2009. https://doi.org/10.1029/2009JB000815

Grandin, R., Socquet, A., Doin, M. P., Jacques, E., De Chabalier, J. B., & King, G. C. P. (2010b). Transient rift opening in response to multiple dike injections in the Manda Hararo rift (Afar, Ethiopia) imaged by time-dependent elastic inversion of interferometric synthetic aperture radar data. Journal of Geophysical Research: Solid Earth, 115(9). https://doi.org/10.1029/2009JB006883

Grandin, R., Jacques, E., Nercessian, A., Ayele, A., Doubre, C., Socquet, A., Keir, D., Kassim, M., Lemarchand, A., & King, G. C. P. (2011). Seismicity during lateral dike propagation: Insights from new data in the recent Manda Hararo–Dabbahu rifting episode (Afar, Ethiopia). Geochemistry, Geophysics, Geosystems, 12(4), Q0AB08. https://doi.org/10.1029/2010GC003434

Grandin, R., Socquet, A., Doubre, C., Jacques, E., & C.P. King, G. (2012). Elastic thickness control of lateral dyke intrusion at mid-ocean ridges. Earth and Planetary Science Letters, 319–320, 83–95. https://doi.org/10.1016/j.epsl.2011.12.011

Greenfield, T., Winder, T., Rawlinson, N., Maclennan, J., White, R. S., Ágústsdóttir, T., Bacon, C. A., Brandsdóttir, B., Eibl, E. P. S., Glastonbury-Southern, E., Gudnason, E. Á., Hersir, G. P., & Horálek, J. (2022). Deep long period seismicity preceding and during the 2021 Fagradalsfjall eruption, Iceland. Bulletin of Volcanology, 84(12). https://doi.org/10.1007/s00445-022-01603-2

Halldórsson, S. A., Marshall, E. W., Caracciolo, A., Matthews, S., Bali, E., Rasmussen, M. B., Ranta, E., Robin, J. G., Guðfinnsson, G. H., Sigmarsson, O., Maclennan, J., Jackson, M. G., Whitehouse, M. J., Jeon, H., van der Meer, Q. H. A., Mibei, G. K., Kalliokoski, M. H., Repczyńska, M. M., Rúnarsdóttir, R. H., … Stefánsson, A. (2022). Rapid shifting of a deep magmatic source at Fagradalsfjall volcano, Iceland. Nature, 609(7927), 529–534. https://doi.org/10.1038/s41586-022-04981-x

Hamling, I. J., Ayele, A., Bennati, L., Calais, E., Ebinger, C. J., Keir, D., Lewi, E., Wright, T. J., & Yirgu, G. (2009). Geodetic observations of the ongoing Dabbahu rifting episode: new dyke intrusions in 2006 and 2007. 989–1003. https://doi.org/10.1111/j.1365-246X.2009.04163.x

Hammond, J. O. S., Kendall, J. M., Stuart, G. W., Keir, D., Ebinger, C., Ayele, A., & Belachew, M. (2011). The nature of the crust beneath the Afar triple junction: Evidence from receiver functions. Geochemistry, Geophysics, Geosystems, 12(12). https://doi.org/10.1029/2011GC003738

Hammond, J. O. S., Kendall, J. M., Stuart, G. W., Keir, D., Ebinger, C., Ayele, A., & Belachew, M. (2012). The nature of the crust beneath the Afar triple junction: Evidence from receiver functions. Geochemistry, Geophysics, Geosystems, 12(12). https://doi.org/10.1029/2011GC003738

Hammond, J. O. S., Kendall, J.-M., Wookey, J., Stuart, G. W., Keir, D., & Ayele, A. (2014). Differentiating flow, melt, or fossil seismic anisotropy beneath Ethiopia. Geochemistry, Geophysics, Geosystems, 15(5), 1878–1894. https://doi.org/10.1002/2013GC005185

Hammond, J. O. S. (2014). Constraining melt geometries beneath the Afar Depression, Ethiopia from teleseismic receiver functions: The anisotropic H-κ stacking technique. Geochemistry, Geophysics, Geosystems, 15(4), 1316–1332. https://doi.org/10.1002/2013GC005186

Hanan, B. B., & Graham, D. W. (1996). Lead and helium isotope evidence from oceanic basalts for a common deep source of mantle plumes. Science, 272(5264), 991–995. https://doi.org/10.1126/science.272.5264.991

Hansen, S. E., Nyblade, A. A., & Benoit, M. H. (2012). Mantle structure beneath Africa and Arabia from adaptively parameterized P-wave tomography: Implications for the origin of Cenozoic Afro-Arabian tectonism. Earth and Planetary Science Letters, 319–320, 23–34. https://doi.org/10.1016/j.epsl.2011.12.023

Hartley, M. E., Bali, E., Maclennan, J., Neave, D. A., & Halldórsson, S. A. (2018). Melt inclusion constraints on petrogenesis of the 2014–2015 Holuhraun eruption, Iceland. Contributions to Mineralogy and Petrology, 173(2), 1–23. https://doi.org/10.1007/s00410-017-1435-0

Hayward, N. J., & Ebinger, C. J. (1996). Variations in the along-axis segmentation of the Afar Rift system. Tectonics, 15(2), 244–257. https://doi.org/10.1029/95TC02292

Head, E. M., Maclean, A. L., & Carn, S. A. (2013). Mapping lava flows from Nyamuragira volcano (1967-2011) with satellite data and automated classification methods. Geomatics, Natural Hazards and Risk, 4(2), 119–144. https://doi.org/10.1080/19475705.2012.680503

Hofmann, C., Courtillot, V., Féraud, G., Rochette, P., Yirgu, G., Ketefo, E., & Pik, R. (1997). Timing of the ethiopian flood basalt event and implications for plume birth and global change. Nature, 389(6653), 838–841. https://doi.org/10.1038/39853

Hollingsworth, J., Leprince, S., Ayoub, F., & Avouac, J. P. (2012). Deformation during the 1975-1984 Krafla rifting crisis, NE Iceland, measured from historical optical imagery. Journal of Geophysical Research: Solid Earth, 117(11), 1–24. https://doi.org/10.1029/2012JB009140

Hopper, J. R., & Buck, W. R. (1993). The initiation of rifting at constant tectonic force: Role of diffusion creep. Journal of Geophysical Research: Solid Earth, 98(B9), 16,213–16,221. https://doi.org/10.1029/93JB01725

Huismans, R., & Beaumont, C. (2011). Depth-dependent extension, two-stage breakup and cratonic underplating at rifted margins. Nature, 473(7345), 74–78. https://doi.org/10.1038/nature09988

Huismans, R. S., & Beaumont, C. (2014). Rifted continental margins: The case for depth-dependent extension. Earth and Planetary Science Letters, 407, 148–162. https://doi.org/10.1016/j.epsl.2014.09.032

Hutchison, W., Mather, T. A., Pyle, D. M., Boyce, A. J., Gleeson, M. L. M., Yirgu, G., Blundy, J. D., Ferguson, D. J., Vye-Brown, C., Millar, I. L., Sims, K. W. W., & Finch, A. A. (2018). The evolution of magma during continental rifting: New constraints from the isotopic and trace element signatures of silicic magmas from Ethiopian volcanoes. Earth and Planetary Science Letters, 489, 203–218. https://doi.org/10.1016/j.epsl.2018.02.027

Illsley-Kemp, F., Savage, M. K., Keir, D., Hirschberg, H. P., Bull, J. M., Gernon, T. M., Hammond, J. O. S., Kendall, J. M., Ayele, A., & Goitom, B. (2017). Extension and stress during continental breakup: Seismic anisotropy of the crust in Northern Afar. Earth and Planetary Science Letters, 477, 41–51. https://doi.org/10.1016/j.epsl.2017.08.014

Illsley-Kemp, F., Greenfield, T., & Keir, D. (2018). Seismic anisotropy reveals a dynamic link between adjacent magmatic segments prior to dyke intrusion. Journal of Geophysical Research: Solid Earth, 123(11), 9800–9816. https://doi.org/10.1029/2018JB016420

Ivy-Ochs, S., Synal, H. A., Roth, C., & Schaller, M. (2004). Initial results from isotope dilution for Cl and 36Cl measurements at the PSI/ETH Zurich AMS facility. Nuclear Instruments and Methods in Physics Research, Section B: Beam Interactions with Materials and Atoms, 223–224(SPEC. ISS.), 623–627. https://doi.org/10.1016/j.nimb.2004.04.115

Ivy-Ochs, S., & Kober, F. (2008). Surface exposure dating with cosmogenic nuclides. E and G Quaternary Science Journal, 57(1–2), 179–209. https://doi.org/10.3285/eg.57.1-2.7

Jestin, F., Huchon, P., & Gaulier, J. M. (1994). The Somalia plate and the East African Rift System:

Present-day kinematics. Geophysical Journal International, 116(3), 637–654. https://doi.org/10.1111/j.1365-246X.1994.tb03286.x

Keir, D., Hamling, I. J., Ayele, A., Calais, E., Ebinger, C., Wright, T. J., Jacques, E., Mohamed, K., Hammond, J. O. S., Belachew, M., Baker, E., Rowland, J. V., Lewi, E., & Bennati, L. (2009). Evidence for focused magmatic accretion at segment centers from lateral dike injections captured beneath the Red Sea rift in Afar. Geology, 37(1), 59–62. https://doi.org/10.1130/G25147A.1

Keir, D., Belachew, M., Ebinger, C. J., Kendall, J.-M., Hammond, J. O. S., Stuart, G. W., Ayele, A., & Rowland, J. V. (2011). Mapping the evolving strain field during continental breakup from crustal anisotropy in the Afar Depression. Nature Communications, 2, 285. https://doi.org/10.1038/ncomms1287

Keir, D., Bastow, I. D., Pagli, C., & Chambers, E. L. (2013). The development of extension and magmatism in the Red Sea rift of Afar. Tectonophysics, 607, 98–114. https://doi.org/10.1016/j.tecto.2012.10.015

Kendall, J. M., Pilidou, S., Keir, D., Bastow, I. D., Stuart, G. W., & Ayele, A. (2006). Mantle upwellings, melt migration and the rifting of Africa: Insights from seismic anisotropy. Geological Society Special Publication, 259, 55–72. https://doi.org/10.1144/GSL.SP.2006.259.01.06

Kidane, T., V. Courtillot, I. Manighetti, L. Audin, P. Lahitte, X. Quidelleur, P.-Y. Gillot, Y. Gallet, J. Carlut, and T. Haile (2003). New paleomagnetic and geochronologic results from Ethiopian Afar: Block rotations linked to rift overlap and propagation and determination of a ~2 Ma reference pole for stable Africa. J. Geophys. Res., 108(B2). https://doi.org/10.1029/2001jb000645

Kusznir, N., & Karner, G. (1985). Dependence of the flexural rigidity of the continental lithosphere on rheology and temperature. Nature, 316, 138–142. https://doi.org/10.1038/316138a0

Kusznir, N. J., & Park, R. G. (1987). The extensional strength of the continental lithosphere: Its dependence on geothermal gradient, and crustal composition and thickness. Geological Society Special Publication, 28(28), 35–52. https://doi.org/10.1144/GSL.SP.1987.028.01.04

La Rosa, A., Pagli, C., Wang, H., Sigmundsson, F., Pinel, V., & Keir, D. (2024). Simultaneous rift-scale inflation of a deep crustal sill network in Afar, East Africa. Nature Communications, 15(1), 1–8. https://doi.org/10.1038/s41467-024-47136-4

Lacroix, P., Gavillon, T., Bouchant, C., Lavé, J., Mugnier, J. L., Dhungel, S., & Vernier, F. (2022). SAR and optical images correlation illuminates post-seismic landslide motion after the Mw 7.8 Gorkha earthquake (Nepal). Scientific Reports, 12(1), 1–13. https://doi.org/10.1038/s41598-022-10016-2

Lahitte, P., Gillot, P. Y., & Courtillot, V. (2003a). Silicic central volcanoes as precursors to rift propagation: The Afar case. Earth and Planetary Science Letters, 207(1–4), 103–116. https://doi.org/10.1016/S0012-821X(02)01130-5

Lahitte, P., Gillot, P.-Y., Kidane, T., Courtillot, V., & Bekele, A. (2003b). New age constraints on the timing of volcanism in central Afar, in the presence of propagating rifts. Journal of Geophysical

Research: Solid Earth, 108(B2). https://doi.org/10.1029/2001jb001689

Lahitte, P., Coulié, E., Mercier, N., Kidane, T., & Gillot, P.-Y. (2001). Chronology of K-Ar and TL volcanism at the southern ends of the Red Sea spreading center in Afar since 300 ka. Earth and Planetary Science (Série IIA), 332(1), 13–20. https://doi.org/10.1016/S1251-8050(00)01491-9

Le Gall, B., Leleu, S., Pik, R., Jourdan, F., Chazot, G., Ayalew, D., Yirgu, G., Cloquet, C., & Chauvet, F. (2018). The Red Beds series in the Erta Ale segment, North Afar. Evidence for a 6 Ma-old post-rift basin prior to continental rupturing. Tectonophysics, 747–748(September), 373–389. https://doi.org/10.1016/j.tecto.2018.10.002

Leroy, S., d'Acremont, E., Tiberi, C., Basuyau, C., Autin, J., Lucazeau, F., & Sloan, H. (2010). Recent off-axis volcanism in the eastern Gulf of Aden: Implications for plume-ridge interaction. Earth and Planetary Science Letters, 293(1–2), 140–153. https://doi.org/10.1016/j.epsl.2010.02.036

Leroy, S., Razin, P., Autin, J., Bache, F., d'Acremont, E., Watremez, L., Robinet, J., Baurion, C., Denèle, Y., Bellahsen, N., Lucazeau, F., Rolandone, F., Rouzo, S., Kiel, J. S., Robin, C., Guillocheau, F., Tiberi, C., Basuyau, C., Beslier, M. O., … Al Lazki, A. (2012). From rifting to oceanic spreading in the Gulf of Aden: A synthesis. Arabian Journal of Geosciences, 5(5), 859–901. https://doi.org/10.1007/s12517-011-0475-4

Lewi, E., Keir, D., Birhanu, Y., Blundy, J., Stuart, G., Wright, T., & Calais, E. (2016). Use of a high-precision gravity survey to understand the formation of oceanic crust and the role of melt at the southern Red Sea rift in Afar, Ethiopia. Geological Society Special Publication, 420(1), 165–180. https://doi.org/10.1144/SP420.13

Licciardi, J. M., & Pierce, K. L. (2008). Cosmogenic exposure-age chronologies of Pinedale and Bull Lake glaciations in greater Yellowstone and the Teton Range, USA. Quaternary Science Reviews, 27(7–8), 814–831. https://doi.org/10.1016/j.quascirev.2007.12.005

Lister, G. S., & Davis, G. A. (1989). The origin of metamorphic core complexes and detachment faults formed during Tertiary continental extension in the northern Colorado River region, U.S.A. Journal of Structural Geology, 11(1–2), 65–94. https://doi.org/10.1016/0191-8141(89)90036-9

Lu, G., & Huismans, R. S. (2021). Melt volume at Atlantic volcanic rifted margins controlled by depth-dependent extension and mantle temperature. Nature Communications, 12, 3894. https://doi.org/10.1038/s41467-021-23981-5

Luais, B., Telouk, P., & Albarède, F. (1997). Precise and accurate neodymium isotopic measurements by plasma-source mass spectrometry. Geochimica et Cosmochimica Acta, 61(22), 4847–4854. https://doi.org/10.1016/S0016-7037(97)00293-7

Macdonald, K. C. (1982). Mid-ocean ridges: fine-scale tectonic, volcanic, and hydrothermal processes within the plate boundary zone. Annual Review of Earth and Planetary Sciences, 10, 155–190. https://doi.org/10.1146/annurev.ea.10.050182.001103

MacLeod, C. J., & Yaouancq, G. (2000). A fossil melt lens in the Oman ophiolite: implications for

magma chamber processes at fast spreading ridges. Earth and Planetary Science Letters, 176(3–4), 357–373. https://doi.org/10.1016/S0012-821X(00)00020-0

Makris, J., & Ginzburg, A. (1987). The Afar Depression: transition between continental rifting and sea-floor spreading. Tectonophysics, 141(1–3), 199–214. https://doi.org/10.1016/0040-1951(87)90186-7

Manhès, G., Allègre, C. J., Dupré, B., & Hamelin, B. (1980). Lead isotope study of basic-ultrabasic layered complexes: Speculations about the age of the Earth and primitive mantle characteristics. Earth and Planetary Science Letters, 47(3), 370–382. https://doi.org/10.1016/0012-821X(80)90024-2

Manighetti, I., Tapponnier, P., Gillot, P. Y., Jacques, E., Courtillot, V., Armijo, R., Ruegg, J. C., & King, G. (1998). Propagation of rifting along the Arabia-Somalia plate boundary: Into Afar. Journal of Geophysical Research: Solid Earth, 103(3), 4947–4974. https://doi.org/10.1029/97jb02758

Manighetti, I., Tapponnier, P., Courtillot, V., Gallet, Y., Jacques, E., & Gillot, P. Y. (2001). Strain transfer between disconnected, propagating rifts in Afar. Journal of Geophysical Research: Solid Earth, 106(B7), 13613–13665. https://doi.org/10.1029/2000jb900454

Marrero, S. M., Phillips, F. M., Caffee, M. W., & Gosse, J. C. (2016). CRONUS-Earth cosmogenic ^{36}Cl calibration. Quaternary Geochronology, 31, 199–219. https://doi.org/10.1016/j.quageo.2015.10.002

Martin, L. C. P., Blard, P. H., Balco, G., Lavé, J., Delunel, R., Lifton, N., & Laurent, V. (2017). The CREp program and the ICE-D production rate calibration database: A fully parameterizable and updated online tool to compute cosmic-ray exposure ages. Quaternary Geochronology, 38, 25–49. https://doi.org/10.1016/j.quageo.2016.11.006

Marty, B., Pik, R., & Gezaheg, Y. (1996). Helium isotopic variations in Ethiopian plume lavas: Nature of magmatic sources and limit on lower mantle contribution. Earth and Planetary Science Letters, 144(1–2), 223–237. https://doi.org/10.1016/0012-821x(96)00158-6

McClusky, S., Reilinger, R., Ogubazghi, G., Amleson, A., Healeb, B., Vernant, P., Sholan, J., Fisseha, S., Asfaw, L., Bendick, R., & Kogan, L. (2010). Kinematics of the southern Red Sea-Afar Triple Junction and implications for plate dynamics. Geophysical Research Letters, 37(5), 1–5. https://doi.org/10.1029/2009GL041127

McKenzie, D. (1978). Some remarks on the development of sedimentary basins. Earth and Planetary Science Letters, 40(1), 25–32. https://doi.org/10.1016/0012-821X(78)90071-7

McKenzie, D. P., & Jackson, J. A. (1983). The relationship between strain rates, crustal thickening, paleomagnetism, finite strain and fault movements within a deforming zone. Earth and Planetary Science Letters, 65(1), 182–202. https://doi.org/10.1016/0012-821X(83)90198-X

Medynski, S., Pik, R., Burnard, P., Williams, A., Vye-Brown, C., Ferguson, D., Blard, P. H., France, L., Yirgu, G., Seid, J. I., Ayalew, D., & Calvert, A. (2013). Controls on magmatic cycles and development of rift topography of the Manda Hararo segment (Afar, Ethiopia): Insights from cosmogenic 3He investigation of landscape evolution. Earth and Planetary Science Letters, 367, 133–145. https://doi.org/10.1016/j.epsl.2013.02.006

Medynski, S., Pik, R., Burnard, P., Vye-Brown, C., France, L., Schimmelpfennig, I., Whaler, K., Johnson, N., Benedetti, L., Ayelew, D., & Yirgu, G. (2015). Stability of rift axis magma reservoirs: Spatial and temporal evolution of magma supply in the Dabbahu rift segment (Afar, Ethiopia) over the past 30 kyr. Earth and Planetary Science Letters, 409, 278–289. https://doi.org/10.1016/j.epsl.2014.11.002

Medynski, S., Pik, R., Burnard, P., Dumont, S., Grandin, R., Williams, A., Blard, P. H., Schimmelpfennig, I., Vye-Brown, C., France, L., Ayalew, D., Benedetti, L., Yirgu, G., Arnold, M., Aumaître, G., Bourlès, D., & Ked-Dadouche, K. (2016). Magmatic cycles pace tectonic and morphological expression of rifting (Afar depression, Ethiopia). Earth and Planetary Science Letters, 446, 77–88. https://doi.org/10.1016/j.epsl.2016.04.014

Menzies, M. A., Klemperer, S. L., Ebinger, C. J., & Baker, J. (2002). Characteristics of volcanic rifted margins. Special Paper of the Geological Society of America, 362, 1–14. https://doi.org/10.1130/0-8137-2362-0.1

Merchel, S., Bremser, W., Alfimov, V., Arnold, M., Aumaître, G., Benedetti, L., Bourlès, D. L., Caffee, M., Fifield, L. K., Finkel, R. C., Freeman, S. P. H. T., Martschini, M., Matsushi, Y., Rood, D. H., Sasa, K., Steier, P., Takahashi, T., Tamari, M., Tims, S. G., Tosaki, Y., Wilcken, K. M., & Xu, S. (2011). Ultra-trace analysis of ^{36}Cl by accelerator mass spectrometry: An interlaboratory study. Analytical and Bioanalytical Chemistry, 400(9), 3125–3132. https://doi.org/10.1007/s00216-011-4979-2

Mologni, C., Bruxelles, L., Schuster, M., Davtian, G., Ménard, C., Orange, F., Doubre, C., Cauliez, J., Taezaz, H. B., Revel, M., & Khalidi, L. (2021). Holocene East African monsoonal variations recorded in wave-dominated clastic paleo-shorelines of Lake Abhe, Central Afar region (Ethiopia & Djibouti). Geomorphology, 391, 107896. https://doi.org/10.1016/j.geomorph.2021.107896

Moore, C., Wright, T., Hooper, A., & Biggs, J. (2019). The 2017 Eruption of Erta 'Ale Volcano, Ethiopia: Insights into the Shallow Axial Plumbing System of an Incipient Mid-Ocean Ridge. Geochemistry, Geophysics, Geosystems, 20(12), 5727–5743. https://doi.org/10.1029/2019GC008692

Morgan, W. J. (1972). Plate motions and deep mantle convection. Memoir of the Geological Society of America, 132(2), 7–22. https://doi.org/10.1130/MEM132-p7

Natali, C., Beccaluva, L., Bianchini, G., Ellam, R. M., Savo, A., Siena, F., & Stuart, F. M. (2016). High-MgO lavas associated to CFB as indicators of plume-related thermochemical effects: The case of ultra-titaniferous picrite – basalt from the Northern Ethiopian – Yemeni Plateau. Gondwana Research, 34, 29–48. https://doi.org/10.1016/j.gr.2016.02.009

Neal, C. A., Brantley, S. R., Antolik, L., Babb, J. L., Burgess, M., Calles, K., Cappos, M., Chang, J. C., Conway, S., Desmither, L. G., Dotray, P., Elias, T., Fukunaga, P., Fuke, S., Johanson, I. A., Kamibayashi, K., Kauahikaua, J. P., Lee, R. L., Pekalib, S., Miklius, A., Million, W., Moniz, C. J., Nadeau, P. A., Okubo, P., Parcheta, C., Patrick, M. R., Shiro, B., Swanson, D. A., Tollett, W., Trusdell, F., Younger, E. F., Zoeller, M. H., Montgomery-Brown, E. K., Anderson, K. R., Poland, M. P., Ball,

J. L., Bard, J., Coombs, M. L., Dietterich, H. R., Kern, C., Thelen, W. A., Cervelli, P. F., Orr, T. R., Houghton, B. F., Gansecki, C., Hazlett, R., Lundgren, P., Diefenbach, A. K., Lerner, A. H., Waite, G., Kelly, P. J., Clor, L., Werner, C., Mulliken, K., Fisher, G., & Damby, D. (2019). The 2018 rift eruption and summit collapse of Kīlauea Volcano. Science, 363(6425), 367–374. https://doi.org/10.1126/science.aav7046

Neave, D. A., & Putirka, K. D. (2017). A new clinopyroxene-liquid barometer, and implications for magma storage pressures under Icelandic rift zones. American Mineralogist, 102(4), 777–794. https://doi.org/10.2138/am-2017-5968

Needham, H. D., Choukroune, P., Cheminee, J. L., Le Pichon, X., Francheteau, J., & Tapponnier, P. (1976). The accreting plate boundary Ardoukôba Rift (northeast Africa) and the oceanic Rift Valley. Earth and Planetary Science Letters, 28(3), 439–453. https://doi.org/10.1016/0012-821X(76)90205-3

Nyblade, A. A., & Robinson, S. W. (1994). The African Superswell. Geophysical Research Letters, 21(9), 765–768. https://doi.org/10.1029/94GL00631

Oppenheimer, C., & Francis, P. (1997). Remote sensing of heat, lava and fumarole emissions from Erta Ale volcano, Ethiopia. 18.8(April), 1661–1692. https://doi.org/10.1080/014311697218043

Pagli, C., Wright, T. J., Ebinger, C. J., Yun, S. H., Cann, J. R., Barnie, T., & Ayele, A. (2012). Shallow axial magma chamber at the slow-spreading Erta Ale Ridge. Nature Geoscience, 5(4), 284–288. https://doi.org/10.1038/ngeo1414

Pagli, C., Wang, H., Wright, T. J., Calais, E., & Lewi, E. (2014). Current plate boundary deformation of the Afar rift from a 3-D velocity field inversion of InSAR and GPS. Journal of Geophysical Research: Solid Earth, 119, 8562–8575. https://doi.org/10.1002/2014JB011391

Pagli, C., Yun, S.-H., Ebinger, C., Keir, D., & Hammond, W. C. (2019). Strike-slip tectonics during rift linkage. Geology, 47(1), 31–34. https://doi.org/10.1130/G45345.1

Palaseanu-Lovejoy, M., Bisson, M., Spinetti, C., Buongiorno, M. F., Alexandrov, O., & Cecere, T. (2019). High-resolution and accurate topography reconstruction of Mount Etna from Pleiades satellite data. Remote Sensing, 11(24), 2983. https://doi.org/10.3390/rs11242983

Parks, M., Drouin, V., Sigmundsson, F., Hjartardóttir, Á. R., Geirsson, H., Pedersen, G. B. M., Belart, J. M. C., Barsotti, S., Lanzi, C., Vogfjörd, K., Hooper, A., Ófeigsson, B., Hreinsdóttir, S., Gestsson, E. B., Þrastarson, R. H., Einarsson, P., Tolpekin, V., Rotheram-Clarke, D., Gunnarsson, S. R., … Pinel, V. (2025). 2023–2024 inflation-deflation cycles at Svartsengi and repeated dike injections and eruptions at the Sundhnúkur crater row, Reykjanes Peninsula, Iceland. Earth and Planetary Science Letters, 658. https://doi.org/10.1016/j.epsl.2025.119324

Paterno R. Castillo, Xijun Liu, P. S. (2020). The geochemistry and Sr-Nd-Pb isotopic ratios of high 3 He / 4 He Afar and MER basalts indicate a significant role of the African Superplume in EARS magmatism. 377. https://doi.org/10.1016/j.lithos.2020.105791

Pedersen, G. B. M., Pfeffer, M. A., Barsotti, S., Tarquini, S., De'michieli Vitturi, M., Óladóttir, B. A.,

& Prastarson, R. H. (2023). Lava flow hazard modeling during the 2021 Fagradalsfjall eruption, Iceland: applications of MrLavaLoba. Natural Hazards and Earth System Sciences, 23(9), 3147–3168. https://doi.org/10.5194/nhess-23-3147-2023

Pham Van, N., Boyer, D., Le Mouel, J.-L., & Courtillot, V. (1981). Identification of a magma chamber in the Ghoubbet-Asal rift (Djibouti) from a magnetotelluric experiment. Earth and Planetary Science Letters, 52(2), 372–380. https://doi.org/10.1016/0012-821X(81)90190-4

Phiri, D., Simwanda, M., Salekin, S., Nyirenda, V. R., Murayama, Y., & Ranagalage, M. (2020). Sentinel-2 data for land cover/use mapping: A review. Remote Sensing, 12(14), 2291. https://doi.org/10.3390/rs12142291

Picazo, S., Müntener, O., Manatschal, G., Bauville, A., Karner, G., & Johnson, C. (2016). Mapping the nature of mantle domains in Western and Central Europe based on clinopyroxene and spinel chemistry: Evidence for mantle modification during an extensional cycle. Lithos, 266–267, 233–263. https://doi.org/10.1016/j.lithos.2016.08.029

Pik, R., Deniel, C., Coulon, C., Yirgu, G., & Marty, B. (1999). Isotopic and trace element signatures of Ethiopian flood basalts: Evidence for plume-lithosphere interactions. Geochimica et Cosmochimica Acta, 63(15), 2263–2279. https://doi.org/10.1016/S0016-7037(99)00141-6

Pik, R., Marty, B., Carignan, J., & Lavé, J. (2003). Stability of the Upper Nile drainage network (Ethiopia) deduced from (U-Th)/He thermochronometry: Implications for uplift and erosion of the Afar plume dome. Earth and Planetary Science Letters, 215(1–2), 73–88. https://doi.org/10.1016/S0012-821X(03)00457-6

Pik, R., Marty, B., & Hilton, D. R. (2006). How many mantle plumes in Africa? The geochemical point of view. Chemical Geology, 226(3–4), 100–114. https://doi.org/10.1016/j.chemgeo.2005.09.016

Pik, R., Marty, B., Carignan, J., Yirgu, G., & Ayalew, T. (2008). Timing of East African Rift development in southern Ethiopia: Implication for mantle plume activity and evolution of topography. Geology, 36(2), 167–170. https://doi.org/10.1130/G24233A.1

Pik, R., Bellahsen, N., Leroy, S., Denèle, Y., Razin, P., Ahmed, A., & Khanbari, K. (2013). Structural control of basement denudation during rifting revealed by low-temperature (U-Th-Sm)/He thermochronology of the Socotra Island basement-Southern Gulf of Aden margin. Tectonophysics, 607, 17–31. https://doi.org/10.1016/j.tecto.2013.07.038

Pin, C., Briot, D., Bassin, C., & Poitrasson, F. (1994). Concomitant separation of strontium and samarium-neodymium for isotopic analysis in silicate samples, based on specific extraction chromatography. Analytica Chimica Acta, 298(2), 209–217. https://doi.org/10.1016/0003-2670(94)00274-6

Pin, C., & Santos Zalduegui, J. F. (1997). Sequential separation of light rare-earth elements, thorium and uranium by miniaturized extraction chromatography: Application to isotopic analyses of silicate rocks. Analytica Chimica Acta, 339(1–2), 79–89. https://doi.org/10.1016/S0003-2670(96)00499-0

Pin, J., Chazot, G., France, L., Abily, B., Gurenko, A., Bertrand, H., & Loppin, A. (2024). Protracted Magma Evolution and Transcrustal Magmatic Plumbing System Architecture at Erta Ale Volcano (Afar, Ethiopia). Journal of Petrology, 65(12). https://doi.org/10.1093/petrology/egae118

Pinzuti, P., Humler, E., Manighetti, I., & Gaudemer, Y. (2013). Petrological constraints on melt generation beneath the Asal Rift (Djibouti) using quaternary basalts. Geochemistry, Geophysics, Geosystems, 14(8), 2932–2953. https://doi.org/10.1002/ggge.20187

Péron-Pinvidic, G., Manatschal, G., Alves, T. M., Andersen, T. B., Andrés-Martinez, M., Autin, J., Ball, P., Brune, S., Buiter, S. J. H., Cadenas, P., Cresswell, G., Epin, M. E., Gómez-Romeu, A., Gouiza, M., Harkin, C., Heine, C., Hopper, J., Jackson, C. A.-L., Jolivet, L., … Zwaan, F. (2019). Rifted margins: State of the art and future challenges. Frontiers in Earth Science, 7, 218. https://doi.org/10.3389/feart.2019.00218

Reed, C. A., Almadani, S., Gao, S. S., Elsheikh, A. A., Cherie, S., Abdelsalam, M. G., Thurmond, A. K., & Liu, K. H. (2014). Receiver function constraints on crustal seismic velocities and partial melting beneath the Red Sea rift and adjacent regions, Afar Depression. Journal of Geophysical Research: Solid Earth, 119(3), 2138–2152. https://doi.org/10.1002/2013JB010719

Riel, B., Milillo, P., Simons, M., Lundgren, P., Kanamori, H., & Samsonov, S. (2015). The collapse of BárÐarbunga caldera, Iceland. Geophysical Journal International, 202(1), 446–453. https://doi.org/10.1093/gji/ggv157

Rime, V., Foubert, A., Ruch, J., & Kidane, T. (2023). Tectonostratigraphic evolution and significance of the Afar Depression. Earth-Science Reviews, 244, 104519. https://doi.org/10.1016/j.earscirev.2023.104519

Rogers, N. W. (2006). Basaltic magmatism and the geodynamics of the East African Rift System. Geological Society Special Publication, 259, 77–93. https://doi.org/10.1144/GSL.SP.2006.259.01.08

Rooney, T. O., Hanan, B. B., Graham, D. W., Furman, T., Blichert-toft, J., & Schilling, J. (2012). Upper Mantle Pollution during Afar Plume-Continental Rift Interaction. 53(2). https://doi.org/10.1093/petrology/egr065

Rooney, T. O., Bastow, I. D., Keir, D., Mazzarini, F., Movsesian, E., Grosfils, E. B., Zimbelman, J. R., Ramsey, M. S., Ayalew, D., & Yirgu, G. (2014). The protracted development of focused magmatic intrusion during continental rifting. Tectonics, 33(6), 875–897. https://doi.org/10.1002/2013TC003514

Rooney, T. O., Nelson, W. R., Dosso, L., Furman, T., Hanan, B., Rooney, T. O., Nelson, W. R., Dosso, L., Furman, T., & Hanan, B. (2014). The role of continental lithosphere metasomes in the production of HIMU-like magmatism on the northeast African and Arabian plates. https://doi.org/10.1130/G35216.1

Rooney, T. O. (2017). The Cenozoic magmatism of East-Africa: Part I — Flood basalts and pulsed magmatism. LITHOS, 286–287, 264–301. https://doi.org/10.1016/j.lithos.2017.05.014

Rooney, T. O. (2020a). The Cenozoic magmatism of East Africa : Part II – Rifting of the mobile belt.

LITHOS, 360–361, 105291. https://doi.org/10.1016/j.lithos.2019.105291

Rooney, T. O. (2020b). The Cenozoic magmatism of East Africa: Part III – Rifting of the craton. LITHOS, 360–361, 105390. https://doi.org/10.1016/j.lithos.2020.105390

Rooney, T. O. (2020c). The Cenozoic magmatism of East Africa: Part IV – The terminal stages of rifting preserved in the Northern East African Rift System. Lithos, 360–361, 105381. https://doi.org/10.1016/j.lithos.2020.105381

Rooney, T. O. (2020d). The Cenozoic magmatism of East Africa: Part V – Magma sources and processes in the East African Rift. Lithos, 360–361. https://doi.org/10.1016/j.lithos.2019.105296

Rooney, T. O., Brown, E. L., Bastow, I. D., Arrowsmith, J. R., & Campisano, C. J. (2023). Magmatism during the continent – ocean transition. Earth and Planetary Science Letters, 614. https://doi.org/10.1016/j.epsl.2023.118189

Rooyakkers, S. M., Carroll, K. J., Gutai, A. F., Winpenny, B., Bali, E., Guðfinnsson, G. H., Maclennan, J., Sigmundsson, F., Jónasson, K., Mutch, E. J. F., Neave, D. A., Robin, J. G., Grönvold, K., & Halldórsson, S. A. (2024). Hydraulically linked reservoirs simultaneously fed the 1975–1984 Krafla Fires eruptions: Insights from petrochemistry. Earth and Planetary Science Letters, 646(September). https://doi.org/10.1016/j.epsl.2024.118960

Rosenbaum, G., Weinberg, R. F., & Regenauer-Lieb, K. (2008). The geodynamics of lithospheric extension. Tectonophysics, 458(1–4), 1–8. https://doi.org/10.1016/j.tecto.2008.07.016

Rowland, J. V., Baker, E., Ebinger, C. J., Keir, D., Kidane, T., Biggs, J., Hayward, N., & Wright, T. J. (2007). Fault growth at a nascent slow-spreading ridge: 2005 Dabbahu rifting episode, Afar. Geophysical Journal International, 171(3), 1226–1246. https://doi.org/10.1111/j.1365-246X.2007.03584.x

Ruegg, J. C., & Kasser, M. (1987). Deformation across the Asal-Ghoubbet Rift, Djibouti: uplift and crustal extension 1979–1986. Geophysical Research Letters, 14(7), 745–748. https://doi.org/10.1029/GL014i007p00745

Ruegg J.C., M. Kasser, J. C. L. and A. T. (1979). Geodetic measurements of rifting associated with a seismo-volcanic crisis in Afar. https://doi.org/10.1029/GL006i011p00817

Sandvol, E., Seber, D., Calvert, A., & Barazangi, M. (1998). Grid search modeling of receiver functions: Implications for crustal structure in the Middle East and North Africa. Journal of Geophysical Research: Solid Earth, 103(B11), 26 899–26 917. https://doi.org/10.1029/98JB02238

Saria, E., E. Calais, D. S. Stamps, D. Delvaux, and C. J. H. Hartnady (2014), Present-day kinematics of the East African Rift. J. Geophys. Res. Solid Earth, 119, 3584–3600. https://doi.org/10.1002/2013JB010901

Schilling, J.-G. (1973). Afar mantle plume: Rare earth evidence. Nature Physical Science, 242, 2–5. https://doi.org/10.1038/physci242002a0

Schilling, J.-G., Kingsley, R. H., Hanan, B. B., & McCully, B. L. (1992). Nd-Sr-Pb isotopic variations

along the Gulf of Aden: Evidence for Afar mantle plume–continental lithosphere interaction. Journal of Geophysical Research: Solid Earth, 97(B7), 10 927–10 966. https://doi.org/10.1029/92JB00415

Schimmelpfennig, I., Benedetti, L., Finkel, R., Pik, R., Blard, P. H., Bourlès, D., Burnard, P., & Williams, A. (2009). Sources of in-situ 36Cl in basaltic rocks. Implications for calibration of production rates. Quaternary Geochronology, 4(6), 441–461. https://doi.org/10.1016/j.quageo.2009.06.003

Schimmelpfennig, I., Benedetti, L., Garreta, V., Pik, R., Blard, P. H., Burnard, P., Bourlès, D., Finkel, R., Ammon, K., & Dunai, T. (2011). Calibration of cosmogenic 36Cl production rates from Ca and K spallation in lava flows from Mt. Etna (38°N, Italy) and Payun Matru (36°S, Argentina). Geochimica et Cosmochimica Acta, 75(10), 2611–2632. https://doi.org/10.1016/j.gca.2011.02.013

Schimmelpfennig, I., Schaefer, J. M., Putnam, A. E., Koffman, T., Benedetti, L., Ivy-Ochs, S., Schlüchter, C., Arnold, M., Aumaître, G., Bourlès, D., & Keddadouche, K. (2014). 36Cl production rate from K-spallation in the European Alps (Chironico landslide, Switzerland). Journal of Quaternary Science, 29(5), 407–413. https://doi.org/10.1002/jqs.2720

Schmidt, G., Franchi, F., Salvini, F., Selepeng, A. T., Luzzi, E., Schmidt, C., & Atekwana, E. A. (2023). Tectonophysics Fault controlled geometries by inherited tectonic texture at the southern end of the East African Rift System in the Makgadikgadi Basin, northeastern Botswana. Tectonophysics, 846(December 2022), 229678. https://doi.org/10.1016/j.tecto.2022.229678

Sembroni, A., Faccenna, C., Becker, T. W., Molin, P., & Abebe, B. (2016). Long-term, deep-mantle support of the Ethiopia-Yemen Plateau. Tectonics, 35(2), 469–488. https://doi.org/10.1002/2015TC004000

Skovgaard, A. C., Storey, M., Baker, J., Blusztajn, J., & Hart, S. R. (2001). Osmium–oxygen isotopic evidence for a recycled and strongly depleted component in the Iceland mantle plume. Earth and Planetary Science Letters, 194(1–2), 259–275. https://doi.org/10.1016/S0012-821X(01)00549-0

Smittarello, D., R. G., J.-B. De Chabalier, C. D., A. Deprez, F. Masson, A. Socquet, A., & Saad, I. A. (2016). Transient deformation in the Asal-Ghoubbet Rift (Djibouti) since the 1978 diking event: Is deformation controlled by magma supply rates? Journal of Geophysical Research, 121(8), 6030–6052. https://doi.org/10.1002/2016JB013069

Solomon, S. C., Richardson, R. M., & Bergman, E. A. (1980). Tectonic stress: models and magnitudes. Journal of Geophysical Research, 85(B11), 6086–6092. https://doi.org/10.1029/JB085iB11p06086

Stab, M., Bellahsen, N., Pik, R., Quidelleur, X., Ayalew, D., & Leroy, S. (2016). Modes of rifting in magma-rich settings: Tectono-magmatic evolution of Central Afar. Tectonics, 35(1), 2–38. https://doi.org/10.1002/2015TC003893

Stone, J. O., Allan, G. L., Fifield, L. K., & Cresswell, R. G. (1996). Cosmogenic chlorine-36 from calcium spallation. Geochimica et Cosmochimica Acta, 60(4), 679–692. https://doi.org/10.1016/0016-7037(95)00429-7

Stone, J. O. (2000). Air pressure and cosmogenic isotope production. Journal of Geophysical Research:

Solid Earth, 105(B10), 23,753–23,759. https://doi.org/10.1029/2000JB900181

Sun, S. S., & McDonough, W. F. (1989). Chemical and isotopic systematics of oceanic basalts: Implications for mantle composition and processes. Geological Society Special Publication, 42(1), 313–345. https://doi.org/10.1144/GSL.SP.1989.042.01.19

Szymanski, E., Stockli, D. F., Johnson, P. R., & Hager, C. (2016). Thermochronometric evidence for diffuse extension and two-phase rifting within the Central Arabian margin of the Red Sea Rift. Tectonics, 35(12), 2863–2895. https://doi.org/10.1002/2016TC004336

Tarantola, A., Ruegg, J.-C., & Lépine, J.-C. (1980). Geodetic evidence for rifting in Afar, 2: Vertical displacements. Earth and Planetary Science Letters, 48(2), 363–370. https://doi.org/10.1016/0012-821X(80)90200-9

Tazieff, H., Varet, J., Barberi, F., & Giglia, G. (1972). Tectonic significance of the Afar (or Danakil) Depression. Nature, 235(5334), 144–147. https://doi.org/10.1038/235144a0

Thirlwall, M. F. (2002). Multicollector ICP-MS analysis of Pb isotopes using a 207pb-204pb double spike demonstrates up to 400 ppm/amu systematic errors in TI-normalization. Chemical Geology, 184(3–4), 255–279. https://doi.org/10.1016/S0009-2541(01)00365-5

Tortelli, G., Gioncada, A., Pagli, C., Braschi, E., Gebru, E. F., & Keir, D. (2022). Constraints on the Magma Source and Rift Evolution from Geochemistry of the Stratoid Flood Basalts (Afar, Ethiopia). Geochemistry, Geophysics, Geosystems, 23(8), 1–21. https://doi.org/10.1029/2022GC010434

Tortelli, G., Gioncada, A., Pagli, C., Braschi, E., Gebru, E. F., & Keir, D. (2024). From melt- to crystal-rich magmatic systems during rift localization: Insights from mineral chemistry in Central Afar (Ethiopia). Contributions to Mineralogy and Petrology, 179, 87. https://doi.org/10.1007/s00410-024-02164-7

Tortelli, G., Gioncada, A., Pagli, C., Barfod, D. N., Corti, G., Sani, F., Mark, D. F., Dymock, R. C., Gebru, E. F., & Keir, D. (2025). Volcanism records plate thinning driven rift localization in Afar (Ethiopia) since 2-2.5 million years ago. Communications Earth and Environment, 6(1). https://doi.org/10.1038/s43247-025-02356-4

Trigunasih, N. M., Narka, I. W., & Saifulloh, M. (2023). Mapping eruption affected area using Sentinel-2A imagery and machine learning techniques. Journal of Degraded and Mining Lands Management, 11(1), 5073–5083. https://doi.org/10.15243/jdmlm.2023.111.5073

Troll, V. R., Deegan, F. M., Thordarson, T., Tryggvason, A., Krmíček, L., Moreland, W. M., Lund, B., Bindeman, I. N., Höskuldsson, Á., & Day, J. M. D. (2024). The Fagradalsfjall and Sundhnúkur Fires of 2021–2024: A single magma reservoir under the Reykjanes Peninsula, Iceland? Terra Nova, May 1–10. https://doi.org/10.1111/ter.12733

Ukstins, I. A., Renne, P. R., Wolfenden, E., Baker, J., Ayalew, D., & Menzies, M. (2002). Matching conjugate volcanic rifted margins: 40Ar/39Ar chrono-stratigraphy of pre- and syn-rift bimodal flood volcanism in Ethiopia and Yemen. Earth and Planetary Science Letters, 198(3–4), 289–306.

https://doi.org/10.1016/S0012-821X(02)00525-3

Unglert, K., Radić, V., & Jellinek, A. M. (2016). Principal component analysis vs. self-organizing maps combined with hierarchical clustering for pattern recognition in volcano seismic spectra. Journal of Volcanology and Geothermal Research, 320, 58–74. https://doi.org/10.1016/j.jvolgeores.2016.04.014

Vigier, N., Bourdon, B., Joron, J. L., & Allègre, C. J. (1999). U-decay series and trace element systematics in the 1978 eruption of Ardoukoba, Asal rift : Timescale of magma crystallization. Earth and Planetary Science Letters, 174(1–2), 81–98. https://doi.org/10.1016/s0012-821x(99)00256-3

Vigny, C., Huchon, P., Ruegg, J., Khanbari, K., & Asfaw, L. M. (2006). Confirmation of Arabia plate slow motion by new GPS data in Yemen. 111(April 2005), 1–14. https://doi.org/10.1029/2004JB003229

Vigny, C., Chabalier, J. De, Ruegg, J., Huchon, P., Feigl, K. L., Cattin, R., Asfaw, L., & Kanbari, K. (2007). Twenty-five years of geodetic measurements along the Tadjoura- Asal rift system, Djibouti, East Africa. 112, 1–12. https://doi.org/10.1029/2004JB003230

Volker, F., McCulloch, M. T., & Altherr, R. (1993). Submarine basalts from the Red Sea: New Pb, Sr, and Nd isotopic data. Geophysical Research Letters, 20(10), 927–930. https://doi.org/10.1029/93GL00050

Vye-Brown, C., Smith, K., & Wright, T. (2013). Active rifting, magmatism and volcanism in the Afar Depression, Ethiopia. Large Igneous Provinces Commission. January 1–10. https://nora.nerc.ac.uk/id/eprint/500327

Watts, E. J., Gernon, T. M., Taylor, R. N., Keir, D., Siegburg, M., Jarman, J., Pagli, C., & Gioncada, A. (2020). Evolution of the Alu-Dalafilla and Borale volcanoes, Afar, Ethiopia. Journal of Volcanology and Geothermal Research, 408, 107094. https://doi.org/10.1016/j.jvolgeores.2020.107094

Watts, E. J., Gernon, T. M., Taylor, R. N., Keir, D., & Pagli, C. (2023). Magmatic evolution during proto-oceanic rifting at Alu, Dalafilla and Borale Volcanoes (Afar) determined by trace element and Sr-Nd-Pb isotope geochemistry. Lithos, 456–457(August), 107311. https://doi.org/10.1016/j.lithos.2023.107311

Watts, E. J., Rees, R., Jonathan, P., Keir, D., Taylor, R. N., Siegburg, M., Chambers, E. L., Pagli, C., Cooper, M. J., Michalik, A., Milton, J. A., Hincks, T. K., Gebru, E. F., Ayele, A., Abebe, B., & Gernon, T. M. (2025). Mantle upwelling at Afar triple junction shaped by overriding plate dynamics. Nature Geoscience, 18(7), 661–669. https://doi.org/10.1038/s41561-025-01717-0

Wenbin Xu, Lei Xie, Yosuke Aoki, Eleonora Rivalta, and S. J. (2020). Volcano-Wide Deformation After the 2017 Erta Ale Dike Intrusion, Ethiopia, Observed with Radar Interferometry. https://doi.org/10.1029/2020JB019562

White, R., & McKenzie, D. (1989). Magmatism at rift zones: the generation of volcanic continental margins and flood basalts. Journal of Geophysical Research, 94(B6), 7685–7729. https://doi.org/10.1029/JB094iB06p07685

White, W. M., Albarède, F., & Télouk, P. (2000). High-precision analysis of Pb isotope ratios by multi-collector ICP-MS. Chemical Geology, 167(3–4), 257–270. https://doi.org/10.1016/S0009-2541(99)00182-5

Wichura, H., Bousquet, R., Oberhänsli, R. O., Strecker, M. R., & Trauth, M. H. (2011). The Mid-Miocene East African Plateau: A pre-rift topographic model inferred from the emplacement of the phonolitic Yatta lava flow, Kenya. Geological Society Special Publication, 357(1), 285–300. https://doi.org/10.1144/SP357.15

Wilson, J.T. (1966). Did the Atlantic close and then re-open? Nature, 211, 676–681. https://doi.org/10.1038/211676a0

Wilson, R. W., Houseman, G. A., Mccaffrey, K. J. W., Doré, A. G. & Buiter, S. J. H. (2019). Fifty Years of the Wilson Cycle Concept in Plate Tectonics. Geological Society, London, Special Publications, 470, 1–17. https://doi.org/10.1144/SP470-2019-58

Wolfenden, E., Ebinger, C., Yirgu, G., Deino, A., & Ayalew, D. (2004). Evolution of the northern Main Ethiopian rift: Birth of a triple junction. Earth and Planetary Science Letters, 224(1–2), 213–228. https://doi.org/10.1016/j.epsl.2004.04.022

Wolfenden, E., Ebinger, C., Yirgu, G., Renne, P. R., & Kelley, S. P. (2005). Evolution of a volcanic rifted margin: Southern Red Sea, Ethiopia. Bulletin of the Geological Society of America, 117(7–8), 846–864. https://doi.org/10.1130/B25516.1

Wong, K., Ferguson, D., Matthews, S., Morgan, D., Tadesse, A. Z., Sinetebeb, Y., & Yirgu, G. (2022). Exploring rift geodynamics in Ethiopia through olivine-spinel Al-exchange thermometry and rare-earth element distributions. Earth and Planetary Science Letters, 597, 117820. https://doi.org/10.1016/j.epsl.2022.117820

Wright, T. J., Ebinger, C., Biggs, J., Ayele, A., Yirgu, G., Keir, D., & Stork, A. (2006). Magma-maintained rift segmentation at continental rupture in the 2005 Afar dyking episode. Nature, 442(7100), 291–294. https://doi.org/10.1038/nature04978

Wright, T. J., Sigmundsson, F., Pagli, C., Belachew, M., Hamling, I. J., Brandsdóttir, B., Keir, D., Pedersen, R., Ayele, A., Ebinger, C., Einarsson, P., Lewi, E., & Calais, E. (2012). Geophysical constraints on the dynamics of spreading centres from rifting episodes on land. Nature Geoscience, 5(4), 242–250. https://doi.org/10.1038/ngeo1428

Xu, W., Rivalta, E., & Li, X. (2017). Magmatic architecture within a rift segment: Articulate axial magma storage at Erta Ale volcano, Ethiopia. Earth and Planetary Science Letters, 476, 79–86. https://doi.org/10.1016/j.epsl.2017.07.051

Yirgu, G., & Ayele, A. (2006). Recent seismovolcanic crisis in northern Afar, Ethiopia. EOS, Transactions American Geophysical Union, 87(33), 325–336. https://doi.org/10.1029/2006EO330001

Zabih, R., & Woodfill, J. (1994). Non-parametric local transforms. https://doi.org/10.1007/BFb0028345

Zreda, M. G., Phillips, F. M., Kubik, P. W., Sharma, P., & Elmore, D. (1993). Cosmogenic ^{36}Cl dating of a young basaltic eruption complex, Lathrop Wells, Nevada. Geology, 21(1), 57–60. https://doi.org/10.1130/0091-7613(1993)021<0057:CCDOAY>2.3.CO;2

Appendices

Appendix I (Chapter 2)

Table 2.1: *Summary of remote sensing datasets*

Instrument	Data type	Entity ID
Landsat 8 OLI	Level 2 Reflectance	LC08_L2SP_167052_20211029_20211108_02_T1
Sentinel-2	Level 2A Reflectance	S2A_MSIL2A_20220113T074301_N0301_R092_T37PGP_20220113T104646.SAFE
		S2A_MSIL2A_20220113T074301_N0301_R092_T37PFP_20220113T104646.SAFE

Table 2.2: *Characteristic of spectral band of Landsat 8 (USGS) and Sentinel-2 (ESA)*

Landsat 8 band	Name	central wavelength (µm)	Wavelength (Lower-upper, µm)	Bandwidth (µm)	Resolution (m)
1	Coastal / Aerosol	0.443	0.435-0.451	0.016	30
2	Blue	0.482	0.452-0.512	0.060	30
3	Green	0.561	0.533-0.590	0.057	30
4	Red	0.655	0.636-0.673	0.037	30
5	Near Infrared	0.865	0.851-0.879	0.028	30
6	Shortwave Infrared 1	1.609	1.567-1.651	0.085	30
7	Shortwave Infrared 2	2.201	2.107-2.294	0.187	30
8	Panchromatic	0.590	0.503-0.676	0.172	15
9	Cirrus	1.373	1.363-1.384	0.020	30
10	Thermal Infrared Sensor 1	10.895	10.60-11.19	0.590	100
11	Thermal Infrared Sensor 2	12.005	11.50-12.51	1.010	100
Sentinel-2 band	**Name**	**Central wavelength (µm)**	**Wavelength (Lower-upper, µm)**	**Bandwidth (µm)**	**Resolution (m)**
1	Coastal / Aerosol	0.443	0.421-0.457	0.036	60
2	Blue	0.494	0.439-0.535	0.096	10
3	Green	0.560	0.537-0.582	0.045	10
4	Red	0.665	0.646-0.685	0.039	10
5	Vegetation Red Edge 1	0.704	0.694-0.714	0.020	20
6	Vegetation Red Edge 2	0.740	0.731-0.749	0.018	20
7	Vegetation Red Edge 3	0.781	0.768-0.796	0.028	20
8	Near Infrared	0.834	0.767-0.908	0.141	10

Table 2.2 continued

8a	Narrow Near Infrared	0.864	0.848-0.881	0.033	20

9	Water Vapour / Red Edge	0.944	0.931-0.958	0.027	60
10	Cirrus	1.375	1.338-1.414	0.076	60
11	Shortwave Infrared 1	1.612	1.539-1.681	0.142	20
12	Shortwave Infrared 2	2.194	2.072-2.312	0.240	20

Table 2.3: *Comparison of visual estimates from hand specimen and Minimum Distance classification (MDC) for plagioclase abundance in central Afar porphyritic lava samples. Plagioclase percentages from MDC, are normalized to exclude vesicular volume.*

Samples	Plagioclase (%) Hand Specimen	Plagioclase (%) ENVI	Plagioclase (%) Normalized	Matrix (%)	Vesicles (%)	Others (%)
AF23-71B	< 25%	25%	25%	72%	–	3%
AF23-115	< 15%	10%	12%	73%	15%	2%
AF23-116	< 10%	14%	17%	48%	16%	22%
AF23-145	< 15%	18%	23%	60%	21%	1%
AF23-146	< 10%	19%	23%	50%	19%	12%
AF23-162	< 25%	23%	24%	70%	5%	2%
AF23-166	< 10%	14%	14%	76%	–	10%

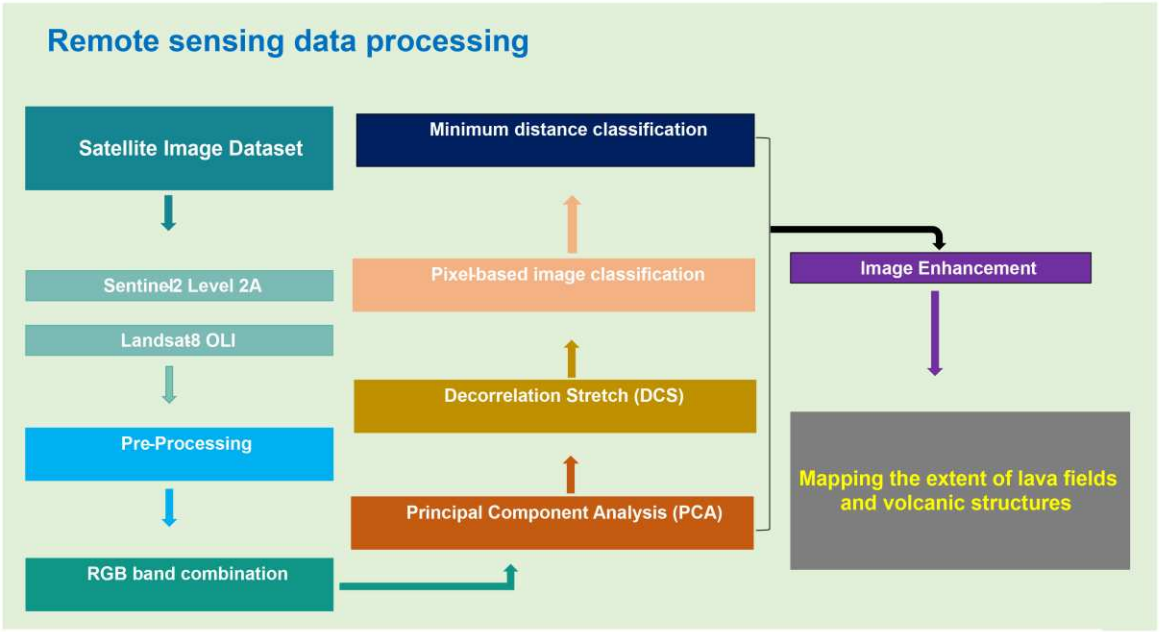

Figure A2.1: *The Workflow adopted to map lava flows and volcanic structures using Landsat 8 OLI and Sentinel-2 MSI datasets.*

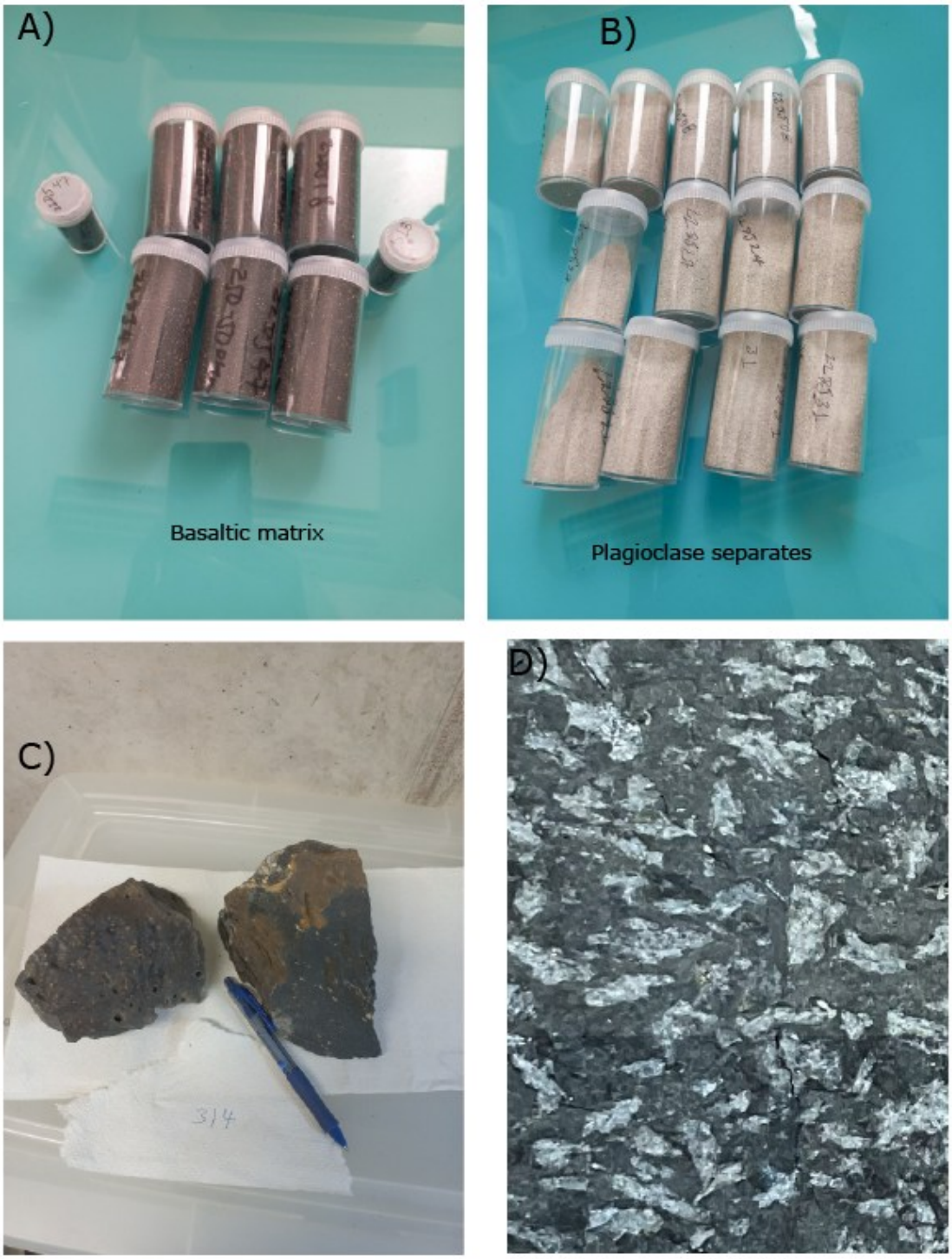

Figure A2.2: *Lava samples that undergone physical preparation for cosmogenic ^{36}Cl measurements. (A) Whole-rock samples from central Afar with 250-500 µm grain-size fraction. (B) Plagioclase separates of 100-120 µm grain-size fraction from Asal rift. (C) Aphyric lava sample from central Afar. (D) Plagioclase-rich lava sample from the Asal rift.*

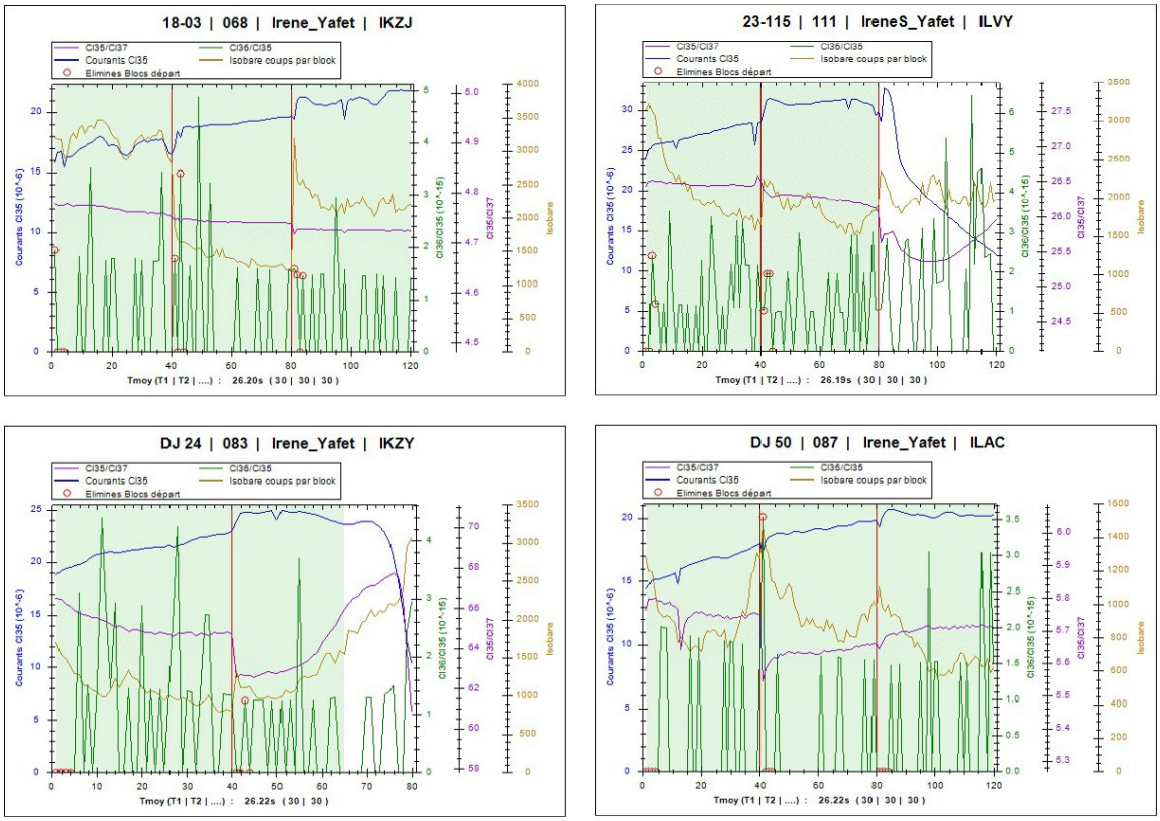

Figure A2.3: *Graphical illustration of AMS measurements of the $^{36}Cl/^{35}Cl$ and $^{35}Cl/^{37}Cl$ ratios for lava samples from the central Afar and Asal rift.*

Appendix II (Chapter 3)

Table S3.1*: Major (in wt.%) and trace element (in ppm) concentrations in bulk rock samples before chemical treatment. Analysis performed at the at the Service d'Analyse des Roches et des Minéraux (SARM-CRPG, Nancy, France).*

Sample ID	AF13 - 52	AF13 - 53	AF13-341	AF13-342a	AF13-342b	AF13-342c	AF13-343a	AF13-343b	AF13-343c	AF13-345
Latitude (°N)	11.850	11.858	11.936	11.953	11.953	11.953	11.953	11.953	11.953	11.969
Longitude (°E)	40.823	40.862	40.863	40.862	40.862	40.862	40.862	40.862	40.862	40.857
SiO_2	46.37	48.31	46.87	47.91	47.97	48.17	44.41	44.11	47.33	46.62
Al_2O_3	14.18	15.86	14.87	15.53	15.72	15.60	13.57	13.50	14.89	15.18
Fe_2O_3			14.29	12.03	12.00	12.03	13.83	13.82	10.59	14.13
MnO	0.22	0.18	0.22	0.19	0.18	0.19	0.20	0.20	0.16	0.21
MgO	7.70	8.59	5.79	8.41	8.47	8.41	7.72	7.66	10.07	5.72
CaO	10.93	11.34	10.90	11.58	11.48	11.45	9.46	9.53	12.03	10.92
Na_2O	2.54	2.38	2.56	2.37	2.39	2.37	2.64	2.66	1.99	2.67
K_2O	0.47	0.07	0.46	0.08	0.08	0.08	0.91	0.91	0.17	0.43
TiO_2	2.81	1.02	2.51	1.05	1.05	1.07	2.57	2.58	1.14	2.51
P_2O_5	0.42	0.05	0.36	0.09	0.08	0.09	0.36	0.36	0.11	0.37
Rb	6.73	1.23	9.14	1.47	1.33	1.23	16.70	16.30	1.48	7.89
Ba	170.00	22.71	148.07	31.51	25.19	31.03	150.90	141.94	49.69	144.86
Th	1.14	0.16	1.25	0.19	0.18	0.17	1.21	1.19	0.44	1.10
U	0.27	0.05	0.40	0.07	0.07	0.06	0.33	0.33	0.12	0.32
Nb	21.31	2.10	17.50	2.13	2.11	2.09	17.67	17.48	5.30	17.07
Ta	1.63	0.18	1.37	0.18	0.18	0.17	1.41	1.40	0.43	1.31
La	17.01	2.56	16.67	2.89	2.77	2.83	16.69	16.39	5.36	16.06
Ce	39.55	7.08	39.58	7.80	7.62	7.67	39.19	38.62	13.02	38.16
Pb	2.48	0.76	2.45	0.69	0.65	0.74	1.98	1.75	0.71	2.34
Pr	5.38	1.16	5.11	1.21	1.22	1.20	5.07	5.01	1.77	4.96
Sr	324.10	176.30	281.53	184.71	183.52	174.68	384.07	396.31	182.94	287.12
Nd	24.11	6.18	23.14	6.60	6.45	6.39	22.67	22.14	8.36	22.48
Sm	5.77	2.16	5.80	2.27	2.26	2.23	5.52	5.49	2.39	5.67
Zr	145.10	41.66	151.70	43.00	42.51	41.38	147.32	143.88	54.00	145.01
Eu	2.12	0.90	2.04	0.93	0.93	0.89	1.93	1.90	0.91	2.01
Gd	5.76	2.78	5.90	2.85	2.88	2.80	5.48	5.39	2.62	5.79
Dy	5.45	3.43	6.19	3.70	3.70	3.59	5.57	5.51	3.11	5.98
Y	30.00	20.35	33.02	21.02	21.17	20.84	28.82	28.16	16.94	31.85
Ho	1.07	0.73	1.30	0.82	0.82	0.79	1.14	1.13	0.68	1.25
Yb	2.76	2.11	3.12	2.12	2.13	2.08	2.64	2.62	1.71	2.98
Tb	0.92	0.51	0.98	0.53	0.54	0.52	0.89	0.88	0.47	0.94
Er	2.87	2.05	3.42	2.23	2.23	2.19	2.97	2.93	1.84	3.27
Tm	0.42	0.32	0.47	0.32	0.32	0.32	0.41	0.41	0.26	0.46
Lu	0.42	0.33	0.47	0.32	0.33	0.32	0.40	0.40	0.26	0.45
Ni	113.80	107.00	50.82	100.90	102.86	99.70	113.01	111.42	198.29	52.22

Table S3.1: Continued

Cr	286.40	71.75	54.95	58.48	58.05	59.75	273.32	277.80	553.52	65.79
V	359.00	264.20	347.53	259.50	255.74	256.66	341.00	345.95	256.04	351.97
Ga	18.76	17.29	20.66	17.16	17.57	16.82	18.70	18.47	14.91	20.49
Cu	105.90	167.60	157.68	131.57	144.53	133.08	105.08	101.32	115.74	165.70
Zn	147.40	90.61	120.17	86.54	88.01	86.16	111.75	108.94	72.95	115.96
Cs			0.16	0.03	0.03	0.02	0.09	0.08	< L.D.	0.12
Sc	40.13	39.74	37.85	39.39	38.37	39.51	35.99	36.34	37.81	36.73
As			0.67	< L.D.	< L.D.	< L.D.	< L.D.	< L.D.	< L.D.	0.66
Mo	0.99		0.84	< L.D.	< L.D.	< L.D.	0.58	0.58	< L.D.	0.81
Cd	0.24	0.14	0.21	0.16	0.14	0.16	0.09	0.09	0.09	0.13
Sb	< L.D.	< L.D.	< L.D.	< L.D.	< L.D.	< L.D.	< L.D.	< L.D.	< L.D.	< L.D.
W	0.28	< L.D.	< L.D.	< L.D.	< L.D.	< L.D.	< L.D.	< L.D.	< L.D.	0.86
Sn	1.43	0.67	1.85	0.77	1.06	1.14	1.71	1.80	0.95	3.04
Ge	1.70	1.65	1.49	1.29	1.29	1.30	1.44	1.41	1.24	1.43
In	0.11	0.07	0.08	0.05	0.05	0.05	0.07	0.07	0.05	0.07
Be	0.91		0.95	0.31	0.28	0.31	0.86	0.87	0.39	0.94
Co	49.14	54.88	45.06	54.03	54.43	53.00	48.97	48.06	50.24	44.27
Hf	3.59	1.31	3.87	1.38	1.41	1.33	3.64	3.67	1.56	3.63
Cl			75	<2			<2			120
Li			5.96	38			<20			5.98
B			3.3	3.7			4.87			2.3
Sample ID	**AF13-347a**	**AF13-347b**	**AF13-347c**	**AF13-348**	**AF13-349**	**AF13-350**	**AF13-351**	**AF18-01**	**AF18-02**	**AF18-03**
Latitude (°N)	**11.975**	**11.975**	**11.975**	**11.975**	**11.918**	**11.918**	**11.908**	**11.983**	**11.964**	**11.956**
Longitude (°E)	**40.865**	**40.865**	**40.865**	**40.865**	**40.890**	**40.890**	**40.865**	**40.861**	**40.863**	**40.862**
SiO_2	46.28	46.35	46.59	47.45	47.08	47.15	47.59	46.76	47.80	47.61
Al_2O_3	14.07	14.14	14.14	15.08	14.71	15.32	15.51	15.20	14.61	15.19
Fe_2O_3	13.94	14.07	14.07	12.49	14.77	14.01	12.14	13.90	14.40	13.51
MnO	0.21	0.21	0.21	0.19	0.22	0.21	0.19	0.21	0.22	0.21
MgO	9.11	8.71	8.78	8.75	6.13	5.81	8.26	5.69	5.66	5.36
CaO	10.77	10.94	10.63	11.40	10.83	10.56	11.56	11.32	10.56	10.35
Na_2O	2.39	2.44	2.44	2.38	2.69	2.53	2.23	2.54	2.67	2.49
K_2O	0.33	0.34	0.41	0.24	0.42	0.49	0.09	0.45	0.56	0.63
TiO_2	2.34	2.39	2.38	1.62	2.56	2.51	1.05	2.48	2.63	2.47
P_2O_5	0.30	0.31	0.33	0.20	0.38	0.39	0.11	0.38	0.41	0.38
Rb	4.73	4.85	6.27	3.18	7.33	9.15	1.57	8.95	11.19	15.52
Ba	117.33	112.31	128.72	75.82	136.54	149.83	114.82	150.36	169.11	190.19
Th	0.74	0.72	0.82	0.56	0.97	1.16	0.20	1.23	1.48	2.02
U	0.20	0.20	0.23	0.15	0.28	0.33	0.09	0.41	0.42	0.56
Nb	13.11	13.51	14.95	8.78	16.59	18.36	2.09	17.87	20.46	21.71
Ta	1.05	1.07	1.17	0.69	1.28	1.42	0.19	1.39	1.59	1.68
La	12.00	11.57	12.77	8.09	14.97	16.48	3.28	16.23	18.55	20.35
Ce	29.04	29.29	32.41	20.59	37.14	41.04	7.92	40.25	45.88	49.45
Pb	2.47	1.34	1.28	0.99	2.20	1.87	1.28	2.43	3.00	3.49

Table S3.1: Continued

Pr	3.92	3.94	4.30	2.80	4.90	5.35	1.33	5.19	5.87	6.20
Sr	278.33	270.55	275.15	227.05	271.22	294.56	181.40	298.98	279.96	286.73
Nd	18.11	18.18	19.90	12.93	22.28	23.84	7.03	23.25	25.92	26.96
Sm	4.71	4.69	5.19	3.53	5.66	6.01	2.30	5.84	6.39	6.54
Zr	120.44	121.25	133.31	84.34	142.72	154.02	42.84	153.92	174.47	184.62
Eu	1.77	1.77	1.90	1.33	2.02	2.10	0.92	2.05	2.18	2.14
Gd	4.81	4.86	5.25	3.79	5.85	5.98	2.96	5.83	6.43	6.44
Dy	4.98	5.00	5.38	4.18	6.12	6.24	3.77	6.10	6.61	6.59
Y	25.82	26.76	28.41	22.76	33.01	32.81	21.07	32.73	35.12	34.67
Ho	1.03	1.05	1.12	0.90	1.29	1.30	0.84	1.29	1.40	1.40
Yb	2.39	2.44	2.66	2.24	3.13	3.08	2.19	3.08	3.38	3.39
Tb	0.78	0.79	0.86	0.65	0.96	0.99	0.55	0.96	1.04	1.05
Er	2.69	2.70	2.93	2.37	3.39	3.42	2.27	3.37	3.63	3.62
Tm	0.37	0.37	0.40	0.33	0.47	0.48	0.34	0.47	0.52	0.51
Lu	0.36	0.37	0.40	0.34	0.48	0.47	0.33	0.47	0.51	0.52
Ni	177.29	164.67	188.78	127.40	53.29	56.69	103.59	52.03	48.77	52.15
Cr	393.68	359.71	387.68	258.00	60.85	85.43	91.96	69.58	74.81	75.42
V	323.04	333.49	338.72	286.05	378.19	340.68	259.42	341.98	353.31	326.67
Ga	18.17	18.53	19.19	17.64	20.68	20.56	17.25	20.40	20.61	21.25
Cu	118.56	129.03	150.84	124.85	162.36	153.27	127.65	154.40	153.52	145.71
Zn	108.97	111.62	113.87	92.70	126.81	120.23	91.43	118.40	122.82	120.18
Cs	0.05	0.05	0.02	0.03	0.08	0.15	0.03	0.17	0.18	0.34
Sc	36.55	37.30	36.62	38.92	39.94	36.49	40.67	36.28	37.63	34.79
As	< L.D.	< L.D.	< L.D.	< L.D.	< L.D.	0.61	< L.D.	0.98	0.90	1.13
Mo	0.58	0.56	0.58	< L.D.	0.77	0.78	< L.D.	0.81	0.90	0.90
Cd	0.10	0.10	0.11	0.11	0.13	0.13	0.22	0.15	0.25	0.15
Sb	< L.D.	< L.D.	< L.D.	< L.D.	< L.D.	< L.D.	< L.D.	< L.D.	< L.D.	0.08
W	< L.D.	< L.D.	< L.D.	< L.D.	< L.D.	< L.D.	< L.D.	< L.D.	< L.D.	< L.D.
Sn	1.41	1.31	1.64	1.00	1.62	1.56	0.71	1.73	2.27	2.39
Ge	1.43	1.44	1.43	1.35	1.52	1.50	1.30	1.47	1.55	1.52
In	0.06	0.07	0.07	0.06	0.08	0.08	0.07	0.08	0.10	0.08
Be	0.66	0.72	0.72	0.50	0.87	0.93	0.35	0.88	1.00	1.13
Co	54.90	54.41	55.00	52.38	47.44	44.05	53.76	43.66	42.85	41.71
Hf	3.09	3.11	3.40	2.26	3.57	3.89	1.40	3.88	4.42	4.60
Cl				23	64		63	140	190	69
Li				4.14	5.68		7.01	6.52	7.15	8.45
B				2	2		2.1	2.8	2.4	4.3
Sample ID	**AF18-04**	**AF23_29**	**AF23_41**	**AF23_42**	**AF23_43**	**AF23_44**	**AF23-97**	**AF23-99**	**AF23-107**	**AF23_167**
Latitude (°N)	**11.945**	**12.016**	**11.848**	**11.849**	**11.852**	**11.848**	**11.931**	**11.926**	**11.855**	**11.911**
Longitude (°E)	**40.862**	**40.878**	**40.810**	**40.814**	**40.818**	**40.884**	**40.922**	**40.930**	**40.829**	**40.839**
SiO_2	48.37	47.41	46.36	44.80	45.56	45.60	47.47	47.46	45.53	47.84
Al_2O_3	16.05	14.82	13.90	13.36	13.76	13.63	15.12	15.99	14.06	15.91
Fe_2O_3	12.12	14.78	14.65	13.65	14.07	13.96	11.80	12.04	13.99	11.85

Table S3.1: Continued

MnO	0.19	0.22	0.22	0.23	0.22	0.22	0.19	0.18	0.22	0.18
MgO	8.75	5.84	8.24	7.26	7.80	8.02	8.21	8.60	7.72	8.44
CaO	11.38	11.28	10.80	12.24	11.54	12.06	11.82	11.38	11.51	11.28
Na_2O	2.36	2.67	2.43	2.37	2.46	2.38	2.19	2.25	2.34	2.40
K_2O	0.05	0.42	0.50	0.48	0.47	0.39	0.09	0.06	0.43	0.09
TiO_2	1.02	2.54	2.78	2.64	2.61	2.59	1.00	1.01	2.61	1.03
P_2O_5	0.08	0.37	0.41	0.42	0.41	0.42	0.35	< L.D.	0.41	0.09
Rb	0.34	6.84	6.94	6.39	6.61	5.10	1.05	0.65	5.83	1.51
Ba	28.12	134.53	185.14	315.27	189.28	232.46	60.96	28.44	505.87	52.68
Th	0.16	0.95	1.11	1.05	1.06	1.02	0.18	0.17	1.02	0.20
U	0.04	0.29	0.25	0.28	0.27	0.44	0.25	0.07	0.32	0.06
Nb	1.93	15.43	21.11	19.23	19.36	18.23	1.91	1.95	18.38	2.14
Ta	0.17	1.25	1.61	1.49	1.54	1.43	0.16	0.16	1.49	0.17
La	2.44	14.58	16.93	16.75	16.72	16.17	3.11	2.64	16.48	2.87
Ce	7.07	33.50	42.31	39.96	40.09	38.74	7.71	7.18	38.21	7.73
Pb	0.86	1.58	1.51	1.63	1.48	1.50	0.80	0.59	1.76	0.72
Pr	1.13	4.72	5.34	5.07	5.08	4.93	1.24	1.10	4.90	1.21
Sr	176.28	266.44	317.17	325.58	333.63	330.77	176.69	168.80	342.26	187.52
Nd	6.00	21.61	24.01	22.58	22.56	22.28	6.40	5.81	22.23	6.42
Sm	2.10	5.48	5.99	5.57	5.56	5.47	2.16	2.04	5.36	2.18
Zr	39.14	139.74	147.05	138.47	142.66	148.68	40.91	40.94	128.81	43.47
Eu	0.88	1.93	2.09	1.98	2.01	1.93	0.87	0.82	1.93	0.88
Gd	2.68	5.67	5.82	5.48	5.48	5.42	2.79	2.56	5.30	2.73
Dy	3.48	5.84	5.71	5.47	5.47	5.42	3.54	3.30	5.19	3.58
Y	19.89	31.62	29.34	28.75	28.51	28.31	19.57	18.65	26.68	20.39
Ho	0.78	1.24	1.18	1.11	1.11	1.11	0.78	0.74	1.08	0.78
Yb	2.03	2.96	2.68	2.59	2.62	2.61	2.08	1.95	2.50	2.05
Tb	0.50	0.92	0.92	0.88	0.88	0.87	0.51	0.48	0.85	0.51
Er	2.13	3.26	3.02	2.89	2.89	2.88	2.17	2.00	2.78	2.17
Tm	0.30	0.47	0.43	0.41	0.42	0.41	0.31	0.31	0.41	0.32
Lu	0.32	0.46	0.41	0.39	0.39	0.39	0.31	0.29	0.37	0.31
Ni	104.26	58.96	130.66	122.55	133.53	135.05	99.20	104.94	135.76	121.52
Cr	64.94	75.84	335.73	342.45	338.24	348.95	83.10	81.25	341.93	117.44
V	254.19	355.06	351.40	353.36	337.69	323.41	252.27	252.46	317.72	256.18
Ga	16.97	19.77	19.13	17.88	18.11	17.66	16.42	16.14	17.49	17.02
Cu	96.12	151.30	104.33	98.49	112.21	102.78	125.19	106.04	100.88	141.80
Zn	84.95	125.81	120.09	111.96	114.46	113.30	98.95	81.84	109.64	89.11
Cs		0.08	0.10	0.07	0.07	0.05	0.03	< L.D.	0.07	0.04
Sc	40.20	39.04	37.91	39.02	36.87	37.51	39.54	40.05	35.97	38.89
As	< L.D.	< L.D.	0.80	1.20	1.32	0.72	0.51	< L.D.	0.89	0.40
Mo	< L.D.	0.92	0.95	1.40	1.11	1.35	0.51	< L.D.	1.19	0.54
Cd	0.09	0.12	0.11	0.21	0.13	0.13	0.20	0.09	0.18	0.10
Sb	< L.D.	< L.D.	0.17	0.16	0.18	0.14	0.08	0.20	0.22	0.21

Table S3.1: Continued

W	< L.D.	< L.D.	< L.D.	< L.D.	< L.D.	< L.D.	< L.D.	< L.D.	< L.D.	0.24
Sn	0.68	1.21	1.15	1.03	1.29	1.04	0.54	0.65	1.16	0.70
Ge	1.32	1.44	1.51	1.41	1.40	1.34	1.22	1.17	1.40	1.30
In	0.05	0.09	0.09	0.09	0.08	0.08	0.06	0.06	0.08	0.06
Be	0.23	0.87	0.93	0.85	0.91	0.86	0.30	0.30	0.85	0.28
Co	54.11	45.94	51.65	48.48	50.20	49.91	52.35	54.24	49.71	55.64
Hf	1.31	3.50	3.79	3.47	3.55	3.54	1.30	1.30	3.36	1.37
Cl		97		98	77	98	160		145	94
Li		5.74		6.01	6.63	7.24	5.35		6.28	4.69
B		2.9		7.3	4.7	7	4.2		3.7	2.4

Sample ID	**AF23_168**	**AF23_169**	**AF23_170**	**AF23_171**	**AF23_172**	**AF23_173**	**AF23_174**	**AF23_176**
Latitude (°N)	**11.911**	**11.911**	**11.910**	**11.914**	**11.914**	**11.907**	**11.874**	**11.877**
Longitude (°E)	**40.839**	**40.839**	**40.833**	**40.850**	**40.852**	**40.864**	**40.866**	**40.936**
SiO_2	48.27	47.49	47.51	45.86	48.03	47.42	47.29	48.54
Al_2O_3	16.21	16.12	15.64	16.00	15.96	16.48	15.53	15.78
Fe_2O_3	11.74	11.93	12.41	12.63	11.93	12.33	11.78	12.09
MnO	0.18	0.18	0.20	0.20	0.19	0.19	0.19	0.19
MgO	8.57	9.32	9.14	8.99	8.68	8.76	8.40	8.45
CaO	11.50	11.30	11.62	11.22	11.29	11.41	12.12	11.94
Na_2O	2.40	2.33	2.26	2.09	2.21	2.25	2.29	2.38
K_2O	0.08	0.14	0.14	0.08	0.05	0.07	0.08	0.09
TiO_2	1.00	1.26	1.46	1.48	1.01	1.09	1.04	1.07
P_2O_5	0.08	0.14	0.18	0.19	0.09	0.09	0.11	0.09
Rb	1.21	1.92	2.09	0.91	0.54	0.87	1.28	1.41
Ba	29.77	50.06	66.11	77.36	38.86	40.48	58.88	31.50
Th	0.16	0.28	0.36	0.38	0.18	0.21	0.22	0.18
U	0.06	0.08	0.11	0.11	0.08	0.08	0.13	0.06
Nb	2.01	5.15	6.64	6.83	2.11	2.29	2.32	2.17
Ta	0.16	0.41	0.53	0.55	0.18	0.19	0.19	0.18
La	2.52	5.23	6.74	6.98	2.82	2.95	3.48	2.78
Ce	7.11	13.30	17.34	17.79	7.87	8.29	9.07	7.60
Pb	0.54	0.68	1.14	0.89	0.56	1.02	0.83	0.51
Pr	1.10	1.88	2.32	2.40	1.22	1.22	1.36	1.18
Sr	191.49	209.93	211.62	213.08	198.16	180.39	191.60	189.26
Nd	6.02	9.05	11.13	11.54	6.55	6.30	6.97	6.27
Sm	2.06	2.68	3.07	3.19	2.29	2.12	2.30	2.20
Zr	40.98	59.73	69.25	72.65	44.96	44.02	46.16	43.91
Eu	0.88	1.06	1.21	1.23	0.93	0.87	0.91	0.90
Gd	2.64	3.09	3.47	3.56	2.88	2.70	2.89	2.78
Dy	3.44	3.63	4.02	4.12	3.81	3.47	3.68	3.55
Y	19.77	20.24	21.93	22.67	21.58	19.79	21.69	20.58
Ho	0.77	0.79	0.87	0.89	0.84	0.77	0.82	0.79
Yb	2.00	2.00	2.13	2.20	2.18	1.99	2.14	2.06

Table S3.1: Continued

Tb	0.50	0.56	0.62	0.63	0.55	0.51	0.53	0.52
Er	2.10	2.13	2.28	2.38	2.30	2.06	2.26	2.13
Tm	0.32	0.31	0.34	0.35	0.35	0.32	0.34	0.32
Lu	0.31	0.30	0.33	0.33	0.34	0.31	0.33	0.31
Ni	121.59	155.04	145.35	141.65	119.38	111.64	117.91	110.11
Cr	106.99	241.97	280.38	281.14	89.93	82.38	111.88	100.99
V	256.27	260.34	282.80	294.36	277.48	270.15	262.45	265.41
Ga	17.77	17.24	16.94	17.34	18.32	17.25	17.04	16.86
Cu	133.71	137.92	171.42	105.81	128.22	96.38	157.04	125.00
Zn	87.99	94.63	95.26	99.84	95.35	88.98	91.24	88.76
Cs	< L.D.	0.03	0.03	0.03	< L.D.	0.03	0.03	0.02
Sc	38.50	36.27	39.01	40.24	39.53	41.58	39.43	41.01
As	< L.D.	0.26	< L.D.	0.47	0.39	0.47	0.61	0.35
Mo	0.44	0.40	0.41	0.33	0.30	0.28	0.59	0.41
Cd	0.10	0.09	0.22	0.13	0.10	0.13	0.18	0.08
Sb	0.20	0.21	< L.D.	0.20	0.19	0.08	0.22	0.21
W	0.21	0.21	< L.D.	0.24	0.27	< L.D.	0.25	0.24
Sn	0.67	0.79	0.78	0.85	0.66	0.72	1.13	0.67
Ge	1.29	1.28	1.33	1.34	1.39	1.25	1.27	1.22
In	0.06	0.06	0.08	0.07	0.07	0.06	0.07	0.06
Be	0.28	0.37	0.44	0.46	0.32	0.32	0.31	0.31
Co	56.53	57.73	56.33	56.92	60.18	57.05	55.93	54.78
Hf	1.30	1.63	1.89	1.96	1.41	1.36	1.40	1.37
Cl	265	30	35	26	39	54	65	43
Li	4.27	4.53	4.95	6.32	5.23	6.04	5.71	4.67
B	<2	<2	2.3	2.7	<2	3.3	<2	<2

Table S3.2: *Concentrations of the target element oxides, measured in splits taken from the samples after the chemical pre-treatment (acid etching). Analysis performed at the SARM-CRPG, Nancy, France.*

Samples	**SiO_2 (%)**	**Al_2O_3 (%)**	**Fe2O3(%)**	**MnO (%)**	**MgO (%)**	**CaO (%)**	**Na_2O (%)**	**K_2O (%)**	**TiO_2 (%)**	**P_2O_5 (%)**	**LOI**
AF13-341	50.17 ±1.01	14.97±0.30	12.30±0.25	0.19±0.04	3.43±0.34	11.20±0.22	2.66±0.27	0.46±0.11	2.91±0.29	0.33±0.10	0.39
AF13-345	50.50±1.01	14.58±0.29	12.43±0.25	0.19±0.04	4.44±0.44	10.43±0.21	2.62±0.26	0.40±0.10	2.57±0.26	0.35±0.10	0.36
AF13-348	51.01±1.01	14.07±0.28	9.80±0.20	0.16±0.03	7.33±0.15	11.68±0.23	2.27±0.23	0.23±0.06	1.89±0.19		0.52
AF13-349	49.57±0.90	13.11±0.26	14.02±0.28	0.21±0.04	4.88±0.49	10.58±0.21	2.53±0.25	0.43±0.11	3.06±0.31	0.24±0.10	0.36
AF13-351	50.92±1.01	15.02±0.30	10.74±0.21	0.17±0.03	5.76±0.12	11.65±0.23	2.25±0.23	0.08±0.02	1.16±0.12		1.25
AF18-01	49.96±1.01	15.19±0.30	12.28±0.25	0.18±0.04	3.51±0.35	11.26±0.23	2.67±0.27	0.44±0.11	2.93±0.29	0.36±0.10	0.14
AF18-02	50.24±1.01	14.50±0.29	12.81±0.26	0.19±0.04	3.97±0.40	10.64±0.21	2.82±0.28	0.54±0.11	2.93±0.29	0.39±0.10	0.04
AF18-03	49.63±0.90	14.76±0.30	12.63±0.25	0.19±0.04	3.95±0.40	10.65±0.21	2.66±0.27	0.49±0.12	2.76±0.28	0.37±0.10	1.28

AF23-29	50.35 ±1.01	14.96±0.30	12.29±0.25	0.19±0.04	3.73±0.37	11.25 ± 0.23	2.77±0.28	0.45±0.11	2.89±0.29	0.33±0.10	0.18
AF23-97	52.01 ±1.04	14.99±0.30	10.41±0.21	0.17±0.03	5.36±0.11	11.75 ± 0.23	2.28±0.23	0.07±0.02	1.19±0.12		1.21

Table S3.3: *Trace element composition of host minerals in the most primitive Afar samples, measured by Electron Probe X-Ray Microanalysis at CRPG-Nancy. These values represent the cumulative mineralogical assemblage of the crystal mush used in the mass balance mixing model.*

Samples	Minerals	Li	Be	B	Sc	Ti	V	Cr	Mn	Ni	Rb	Sr	Gd
La_9	Plageoclase	2.4270	0.3690	3.5708	0.5819	726.7126	5.3413	1.5616	36.3645		0.2875	481.4314	0.0979
La_10	Plageoclase	2.1901	0.2373	3.3337	0.7520	658.7625	5.7072	4.6067	40.2630		0.2631	480.3191	0.0956
La_25	Plageoclase	1.8814	0.1086	1.6477	0.5748	436.5266	5.5562	3.7552	45.9569		0.1295	433.1034	0.0488
La_7	Olivine	4.5430		3.9487	10.9944	283.9456	23.3556	10.1029	4203.6502	820.3194		0.0365	
La_23	Olivine	5.4427		2.7962	11.7289	287.8761	24.8594	56.5969	4408.5030	862.6350		0.1197	
La_31	Olivine	4.3911		1.7234	11.3642	268.7383	23.7716	26.0497	3851.5064	781.4066		0.0307	0.0132
La_8	Olivine	4.0940		2.5092	10.8821	269.5233	22.6292	7.8512	4121.3161	806.0542		0.0346	0.0206
La_22	Olivine	4.8440	0.0044	2.2655	11.8922	255.5126	24.2062	37.8129	4327.9788	859.3353		0.0051	0.0212
La_36	Olivine	4.6263		1.0613	11.5044	266.9959	23.6347	27.5806	3924.5780	790.7896		0.0226	0.0186
La_1	Clinopyroxene	1.1651	0.1024	5.0476	142.8969	9983.6393	808.1003	417.9234	1753.5883	162.4550		20.9428	4.3351
La_2	Clinopyroxene	0.7685	0.0506	5.6801	134.7832	7993.3375	750.7442	959.6926	1488.9840	172.2961	0.0084	20.7764	3.2805
La_27	Clinopyroxene	1.2612	0.0138	2.2732	139.4354	8925.6734	785.3039	549.1574	1535.8242	155.6179		22.1926	3.6226
La_28	Clinopyroxene	1.0385	0.0137	2.5063	124.2581	6770.0278	673.0456	935.0769	1408.8970	162.0432		20.3149	2.5909
La_32	Clinopyroxene	0.9465	0.0349	1.9353	133.6383	6757.7924	709.2972	5702.2750	1166.8633	169.0757		20.7273	2.5380
La_33	Clinopyroxene	1.1283	0.0664	2.0553	143.6913	8278.3310	777.0621	816.7555	1438.8951	156.5418		22.0265	3.3943
Samples	**Minerals**	**Y**	**Zr**	**Nb**	**Ba**	**La**	**Ce**	**Pr**	**Nd**	**Sm**	**Eu**	**Th**	
La_9	Plageoclase	0.1656	0.0179	0.0031	67.3877	0.9897	1.7377	0.1836	0.6953	0.1039	0.7231		
La_10	Plageoclase	0.1766	0.0248	0.0026	59.0244	0.9170	1.6334	0.1734	0.6754	0.1078	0.6797		
La_25	Plageoclase	0.1432	0.0236	0.0071	32.5198	0.6808	1.2377	0.1314	0.5339	0.0838	0.4458	0.0003	
La_7	Olivine	0.7508	0.0984	0.0018	0.0398					0.0102	0.0032		
La_23	Olivine	0.7742	0.1762	0.0042	0.0660			0.0018	0.0135	0.0042	0.0027		
La_31	Olivine	0.7316	0.1955	0.0049	0.0250	0.0032	0.0057	0.0012	0.0104	0.0052	0.0024		
La_8	Olivine	0.7283	0.1334	0.0034	0.0618	0.0018	0.0112	0.0009	0.0073	0.0083	0.0028		
La_22	Olivine	0.7756	0.1197	0.0020					0.0031	0.0083	0.0026		
La_36	Olivine	0.7096	0.1585	0.0028	0.0135		0.0080	0.0017	0.0139	0.0061	0.0033		
La_1	Clinopyroxene	23.7426	26.0004	0.0888		1.5113	6.4223	1.3507	8.8809	3.2814	1.0216	0.0054	
La_2	Clinopyroxene	17.5263	19.8449	0.0667	0.0130	1.1006	4.7587	1.0206	6.4192	2.3885	0.7948	0.0046	
La_27	Clinopyroxene	19.6598	21.3726	0.0749		1.3951	5.9789	1.2207	7.7020	2.8649	0.8823	0.0036	
La_28	Clinopyroxene	14.4985	14.1919	0.0525	0.0610	1.0036	4.2829	0.8650	5.5097	2.0579	0.6726	0.0035	
La_32	Clinopyroxene	14.2342	18.0941	0.0804	0.0080	0.9422	3.9022	0.7995	4.9809	1.8570	0.6303	0.0041	
La_33	Clinopyroxene	19.1927	20.9470	0.0781	0.0194	1.3058	5.4807	1.0930	7.0481	2.5940	0.8179	0.0045	
Samples	**Minerals**	**Tb**	**Dy**	**Ho**	**Er**	**Tm**	**Yb**	**Lu**	**H**	**Ta**	**Pb**	**U**	
La_9	Plageoclase	0.0086	0.0400	0.0067	0.0144	0.0012	0.0104	0.0010		0.0010	0.2835	0.0004	
La_10	Plageoclase	0.0090	0.0385	0.0067	0.0140	0.0010	0.0111	0.0018			0.2827	0.0004	
La_25	Plageoclase	0.0074	0.0326	0.0058	0.0082	0.0013	0.0111				0.1535	0.0006	
La_7	Olivine	0.0069	0.0734	0.0240	0.1149	0.0273	0.2516	0.0559	0.0044		0.0341	0.0044	
La_23	Olivine	0.0062	0.0780	0.0270	0.1150	0.0263	0.2864	0.0461	0.0027			0.0031	
La_31	Olivine	0.0064	0.0845	0.0255	0.1070	0.0257	0.2820	0.0528	0.0080	0.0018	0.0263	0.0006	
La_8	Olivine	0.0057	0.0761	0.0240	0.1206	0.0275	0.2688	0.0557	0.0069		0.0438	0.0008	
La_22	Olivine	0.0068	0.0788	0.0268	0.1282	0.0263	0.2599	0.0530	0.0039		0.0362	0.0002	
La_36	Olivine	0.0064	0.0721	0.0256	0.1128	0.0242	0.2449	0.0466	0.0044		0.0315	0.0000	
La_1	Clinopyroxene	0.7346	5.0576	1.0155	2.6291	0.3603	2.3030	0.3412	1.2483	0.0124	0.0354	0.0014	
La_2	Clinopyroxene	0.5346	3.6956	0.7452	1.9855	0.2703	1.7435	0.2397	0.9477	0.0125	0.0219	0.0009	
Table S3.3: Continued													
La_27	Clinopyroxene	0.5844	3.9237	0.7816	2.0656	0.2751	1.8113	0.2502	0.9757	0.0100	0.0260	0.0011	
La_28	Clinopyroxene	0.4283	2.8764	0.5605	1.5133	0.2040	1.2849	0.1814	0.6260	0.0081	0.0184	0.0041	
La_32	Clinopyroxene	0.4008	2.8447	0.5436	1.4499	0.1954	1.2743	0.1817	0.8386	0.0110	0.0278	0.0012	
La_33	Clinopyroxene	0.5647	3.7368	0.7318	1.9317	0.2574	1.6380	0.2320	0.8927	0.0105	0.0338	0.0012	

Table S3.4: *The trace element compositions after mass balance mixing between the LREE enriched basalts (15%) with cumulative mineralogical assemblage (85%).*

Mixing	Rb	Ba	Th	U	Nb	Ta	La	Ce	Pr	Sr	Nd	Zr	Hf
% Of Melt Fraction	15%	15%	15%	15%	15%	15%	15%	15%	15%	15%	15%	15%	15%
% Of Plageoclase Fractionating	30%	30%	30%	30%	30%	30%	30%	30%	30%	30%	30%	30%	30%
% Of Olivine fractionating	5%	5%	5%	5%	5%	5%	5%	5%	5%	5%	5%	5%	5%
% Of Clinopyroxene fractionating	65%	65%	65%	65%	65%	65%	65%	65%	65%	65%	65%	65%	65%
AF13 - 52	1.68	5.58	2.04	1.95	4.54	6.10	5.01	5.16	5.20	8.48	5.55	2.93	3.39
AF23 - 41	1.73	5.91	1.99	1.85	4.50	6.06	4.99	5.40	5.17	8.43	5.54	2.96	3.49

AF23_42	1.60	8.70	1.89	2.07	4.10	5.62	4.95	5.20	5.02	8.49	5.38	2.85	3.33
AF23_43	1.65	6.00	1.90	1.99	4.13	5.78	4.94	5.21	5.03	8.55	5.38	2.90	3.37
AF23_44	1.30	6.92	1.84	3.21	3.89	5.39	4.82	5.09	4.95	8.52	5.35	2.98	3.37
AF23-107	1.47	12.79	1.84	2.35	3.92	5.60	4.89	5.05	4.93	8.61	5.34	2.72	3.28
Mean	**1.57**	**7.65**	**1.92**	**2.24**	**4.18**	**5.76**	**4.93**	**5.18**	**5.05**	**8.51**	**5.42**	**2.89**	**3.37**

Mixing	**Sm**	**Eu**	**Gd**	**Tb**	**Dy**	**Ho**	**Y**	**Er**	**Tm**	**Yb**	**Lu**	**Ni**	**Cr**
% Of Melt fraction	15%	15%	15%	15%	15%	15%	15%	15%	15%	15%	15%	15%	15%
% Of Plageoclase fractionating	30%	30%	30%	30%	30%	30%	30%	30%	30%	30%	30%	30%	30%
% Of Olivine fractionating	5%	5%	5%	5%	5%	5%	5%	5%	5%	5%	5%	5%	5%
% Of clinopyroxene fractionating	65%	65%	65%	65%	65%	65%	65%	65%	65%	65%	65%	65%	65%
AF13 - 52	5.13	5.47	4.54	4.07	3.89	3.45	3.21	3.13	2.82	2.75	2.65	0.07	0.18
AF23 - 41	5.20	5.44	4.55	4.07	3.95	3.56	3.19	3.18	2.84	2.72	2.64	0.07	0.18
AF23_42	5.06	5.35	4.47	4.02	3.90	3.49	3.17	3.14	2.79	2.69	2.60	0.07	0.18
AF23_43	5.06	5.37	4.47	4.02	3.90	3.49	3.16	3.14	2.81	2.70	2.59	0.07	0.18
AF23_44	5.03	5.30	4.45	4.00	3.89	3.49	3.15	3.14	2.79	2.70	2.59	0.07	0.18
AF23-107	4.99	5.30	4.42	3.97	3.84	3.46	3.10	3.11	2.79	2.67	2.55	0.07	0.18
Mean	**5.08**	**5.37**	**4.48**	**4.02**	**3.89**	**3.49**	**3.16**	**3.14**	**2.81**	**2.71**	**2.60**	**0.07**	**0.18**

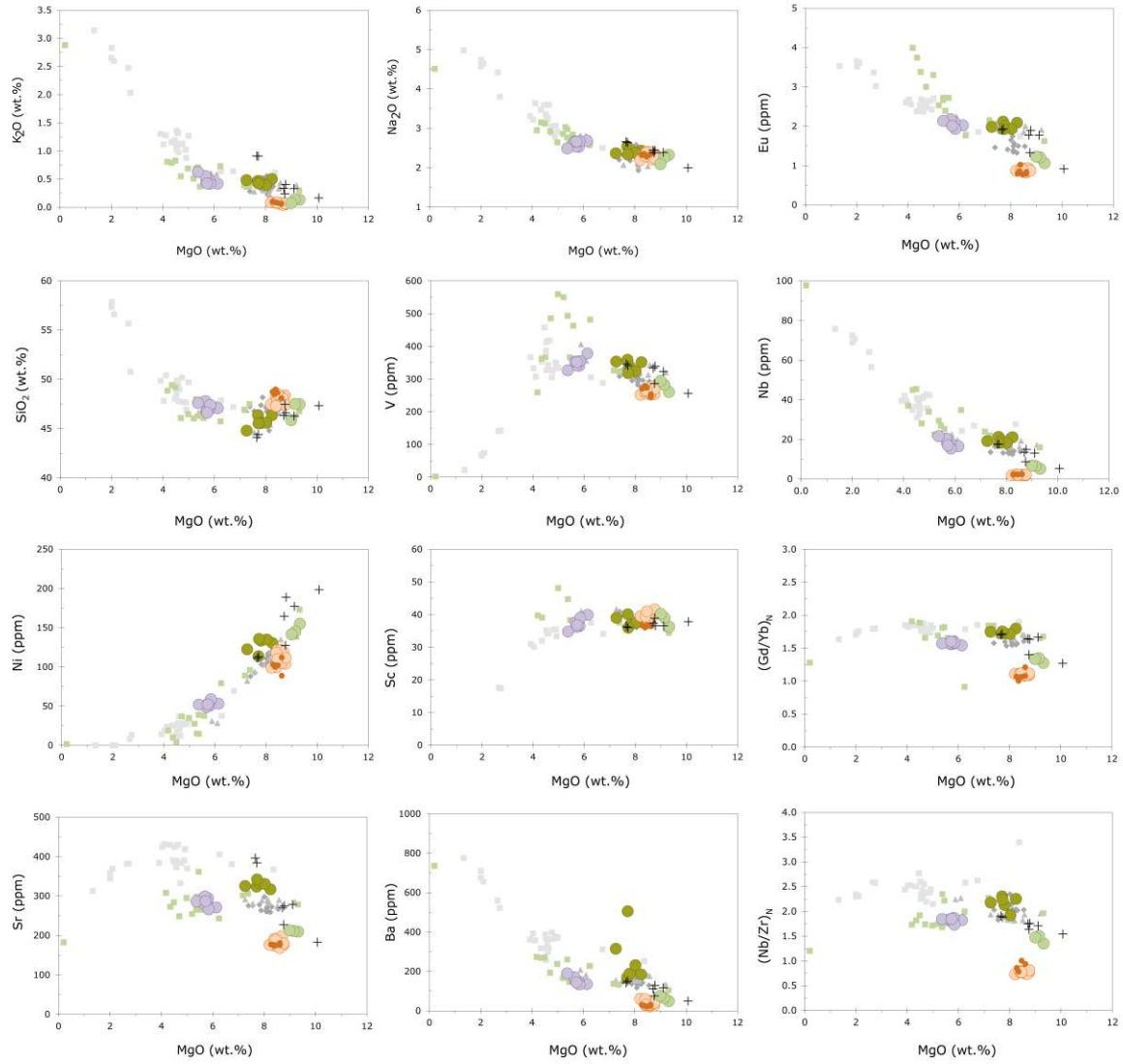

Figure S3.1: *Major and trace elements variations of the lava series in the binary diagrams. The legend is same as for the Figure 3.8.*

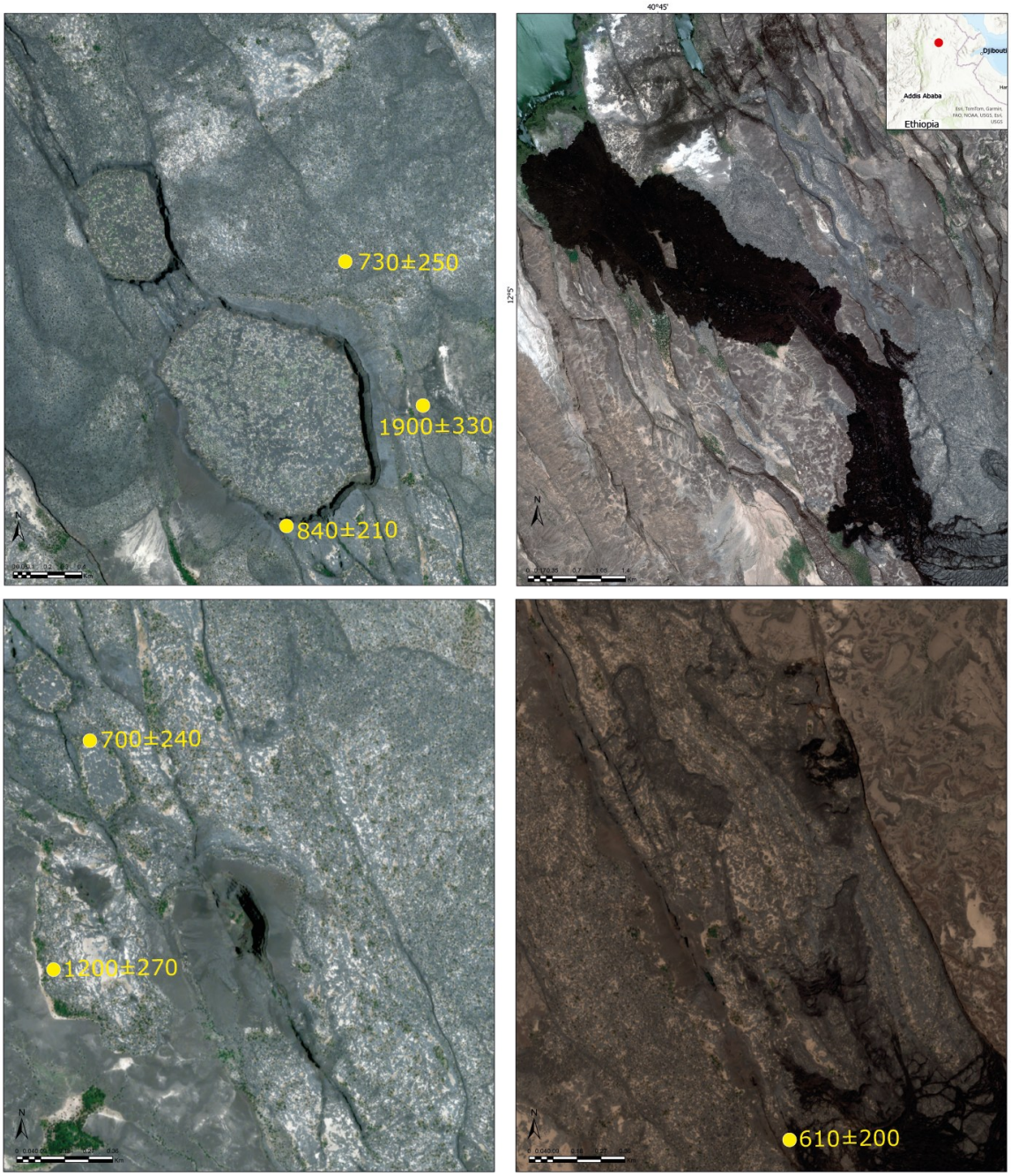

Figure S3.2: *multi-spectral orthoimages shows the main crater with paleo-lava lake inside. A major lip-cone is present on the southern part of the crater. Thin lava units flowed northward, parallel to the segment axis, guided by topographic depressions.*

Appendix III (Chapter 4)

Table S4.1: *Major (in wt.%) and trace element (in ppm) concentrations in bulk rock samples before chemical treatment. Analysis performed at the at the Service d'Analyse des Roches et des Minéraux (SARM-CRPG, Nancy, France).*

Sample ID	AF13 - 54	AF13-317	AF13-319	AF13_320A	AF13-320BC	AF13-321	AF13-322	AF13-323	AF23_24B	AF23_25B	AF23_26B	AF23_27	AF23_28B
Latitude (°N)	11.781	11.911	12.107	12.106	12.106	12.051	11.984	11.903	12.116	12.106	12.072	12.072	12.055
Longitude (°E)	41.005	40.783	41.013	41.011	41.011	40.993	40.982	41.003	40.876	40.862	40.879	40.879	40.892
SiO_2	49.20	47.38	49.32	45.57	45.49	45.52	46.37	46.75	45.37	44.69	45.35	46.12	44.32
Al_2O_3	12.55	15.11	13.47	13.57	13.46	12.53	14.60	14.07	12.30	12.50	12.92	13.69	12.44
Fe_2O_3	16.58	14.76	13.48	14.92	14.94	17.89	13.57	14.58	15.69	15.81	16.48	17.05	13.18
MnO	0.28	0.22	0.21	0.25	0.23	0.29	0.22	0.22	0.23	0.25	0.25	0.25	0.22
MgO	4.37	5.90	5.77	5.87	6.18	5.56	7.44	7.12	6.20	6.03	6.13	5.76	5.74
CaO	8.56	11.11	10.04	11.89	11.65	10.57	11.89	11.05	11.28	11.74	11.12	10.26	12.45
Na_2O	3.15	2.72	2.78	2.45	2.49	2.47	2.38	2.56	2.23	2.22	2.35	2.71	1.81
K_2O	0.84	0.41	0.63	0.40	0.37	0.62	0.35	0.38	0.37	0.42	0.37	0.59	0.52
TiO_2	3.75	2.60	2.40	2.59	2.53	3.68	2.56	2.63	2.84	2.89	2.97	3.24	2.30
P2O5	0.79	0.39	0.35	0.32	0.29	0.59	0.40	0.38	0.49	0.45	0.47	0.55	0.71
Rb	18.10	6.81	9.49	7.18	6.71	11.85	5.12	5.85	5.93	8.14	6.77	9.68	13.73
Ba	267.90	138.27	216.10	165.89	220.74	264.25	153.39	127.30	167.23	187.68	151.82	189.53	188.80
Th	3.02	0.91	1.30	0.93	0.93	1.65	0.76	0.92	1.08	1.28	1.27	1.42	1.85
U	0.88	0.26	0.39	0.34	0.36	0.63	0.24	0.28	0.46	0.54	0.46	0.41	0.78
Nb	44.15	16.71	16.45	14.37	13.67	25.94	17.78	20.20	18.09	19.35	19.51	22.44	17.62
Ta	3.28	1.35	1.30	1.19	1.15	2.07	1.42	1.52	1.47	1.54	1.56	1.73	1.41
La	38.50	15.31	18.23	14.20	13.13	24.44	15.15	16.83	17.36	18.83	19.11	21.82	19.81
Ce	88.13	36.13	42.69	32.97	30.59	56.27	36.14	40.19	39.72	43.22	44.09	51.62	42.34
Pb	3.84	1.58	2.65	9.51	3.53	3.68	1.65	1.78	2.03	2.57	2.34	2.07	3.99
Pr	11.71	5.10	5.66	4.70	4.43	7.79	5.13	5.43	5.45	5.97	6.06	6.45	5.79
Sr	298.50	292.25	349.40	281.25	280.76	271.05	307.96	297.60	246.61	258.03	246.70	263.73	237.15
Nd	50.26	23.16	24.92	21.37	20.30	34.66	23.60	24.40	24.93	26.78	27.25	28.62	25.30
Sm	11.85	5.79	6.00	5.48	5.26	8.60	5.90	6.00	6.24	6.74	6.87	7.02	6.14
Zr	384.50	146.06	175.80	127.21	122.34	223.72	144.91	166.40	165.51	176.87	180.43	193.94	161.81
Eu	3.72	2.08	2.07	1.97	1.87	2.80	2.10	2.11	2.09	2.22	2.27	2.33	1.93
Gd	11.67	6.04	5.84	5.88	5.64	8.75	5.93	6.06	6.43	6.83	6.96	7.06	6.12
Dy	11.13	6.13	5.85	6.20	5.89	8.90	5.87	6.00	6.64	7.08	7.18	7.35	6.21
Y	61.50	33.56	31.21	33.81	32.16	48.07	30.57	32.24	35.77	37.73	38.62	39.40	34.18
Ho	2.18	1.28	1.23	1.31	1.26	1.86	1.21	1.28	1.40	1.49	1.50	1.54	1.31
Yb	5.83	3.06	2.89	3.17	3.00	4.48	2.77	2.96	3.40	3.57	3.67	3.73	3.15
Tb	1.85	0.99	0.93	0.99	0.94	1.42	0.96	0.95	1.06	1.12	1.14	1.17	0.99
Er	5.99	3.40	3.15	3.52	3.35	4.97	3.14	3.26	3.73	3.96	4.01	4.09	3.48
Tm	0.88	0.49	0.43	0.51	0.49	0.73	0.45	0.45	0.54	0.57	0.58	0.60	0.50
Lu	0.88	0.47	0.42	0.48	0.46	0.67	0.42	0.44	0.52	0.55	0.56	0.56	0.48
Ni	13.20	53.90	22.14	82.65	61.80	90.88	156.23	93.83	66.18	61.69	67.04	95.12	69.96
Cr	5.77	65.30	72.00	186.70	139.61	201.03	409.65	217.80	144.73	133.78	142.17	176.37	159.27

Table S4.1 continued

V	343.80	368.94	361.30	404.29	376.43	454.09	321.77	398.80	388.75	394.38	402.29	386.35	309.02
Ga	23.30	20.84	20.47	20.16	19.77	22.45	19.08	20.38	19.09	19.90	20.22	21.22	18.19
Cu	77.16	165.04	41.77	158.78	95.46	268.28	140.60	109.20	208.07	185.01	202.26	194.29	181.38
Zn	183.50	131.65	119.60	128.53	114.98	169.95	121.09	134.10	139.26	140.91	163.49	144.26	132.01
Cs	0.20	0.09		0.11	0.11	0.14	0.07		0.09	0.14	0.13	0.10	0.39
Sc	39.37	38.77	39.51	42.56	42.02	43.41	39.17	40.92	40.12	41.01	42.62	37.65	34.53
As				1.13	2.85	1.04			0.71	0.97	0.68	0.50	1.90
Mo	2.23	0.77	1.29	1.27	1.04	2.50	1.84	0.80	1.36	1.21	1.05	1.58	0.96
Cd	0.46	0.11	0.25	0.16	0.15	0.22	0.16	0.18	0.16	0.25	0.24	0.15	0.93
Sb		0.10		0.16	0.06	0.08	< L,D,		< L,D,	0.06	0.07		0.12
W	0.62	< L.D.		< L,D,	< L,D,	< L,D,	< L,D,		< L,D,	< L,D,	< L,D,	1.02	< L,D,
Sn	3.11	1.35	1.76	2.64	1.28	2.11	1.31	1.77	1.71	1.48	1.87	1.62	3.47
Ge	1.92	1.51	1.72	1.55	1.51	1.68	1.48	1.75	1.49	1.55	1.58	1.56	1.48
In	0.16	0.09	0.10	0.09	0.09	0.12	0.09	0.10	0.09	0.10	0.11	0.10	0.12
Be	1.93	0.92	1.05	0.84	0.85	1.35	0.82	0.92	1.06	1.01	1.02	1.21	1.09
Co	39.13	47.72	40.55	49.07	46.66	50.34	49.18	50.80	46.29	47.88	49.47	48.16	43.51
Hf	8.50	3.64	4.32	3.48	3.28	5.68	3.70	4.05	4.24	4.40	4.47	4.68	4.03
Sample ID	**AF23_30**	**AF23_31**	**AF23_32**	**AF23_33**	**AF23_34**	**AF23_35**	**AF23_36B**	**AF23_37**	**AF23_38**	**AF23 - 41**	**AF23_42**	**AF23_43**	**AF23_44**
Latitude (°N)	**12.0241**	**12.018**	**12.018**	**12.024**	**12.027**	**12.027**	**12.002**	**11.972**	**11.953**	**11.848**	**11.849**	**11.852**	**11.848**
Longitude (°E)	**40.8729**	**40.888**	**40.888**	**40.892**	**40.897**	**40.900**	**40.910**	**40.922**	**40.922**	**40.810**	**40.814**	**40.818**	**40.884**
SiO_2	46.50	46.05	45.20	45.76	46.63	45.27	45.53	44.73	45.47	46.36	44.80	45.56	45.60
Al_2O_3	14.55	11.56	12.26	11.97	13.46	13.00	13.43	10.70	12.53	13.90	13.36	13.76	13.63
Fe_2O_3	13.62	19.56	18.27	18.47	14.85	15.21	15.33	20.30	18.86	14.65	13.65	14.07	13.96
MnO	0.21	0.29	0.27	0.28	0.23	0.23	0.23	0.30	0.28	0.22	0.23	0.22	0.22
MgO	8.73	4.76	5.53	5.65	6.58	7.27	6.58	4.81	5.55	8.24	7.26	7.80	8.02
CaO	11.53	10.25	10.57	10.23	11.30	11.64	11.24	10.54	10.33	10.80	12.24	11.54	12.06
Na_2O	2.33	2.64	2.51	2.52	2.33	2.22	2.20	2.42	2.70	2.43	2.37	2.46	2.38
K_2O	0.23	0.60	0.57	0.59	0.44	0.38	0.38	0.38	0.45	0.50	0.48	0.47	0.39
TiO_2	2.17	4.11	3.69	3.74	2.59	2.54	2.70	3.89	3.22	2.78	2.64	2.61	2.59
P2O5	0.39	0.63	0.61	0.63	0.52	0.48	0.45	0.59	0.49	0.41	0.42	0.41	0.42
Rb	2.71	10.06	9.87	9.79	7.46	6.49	7.01	5.80	6.92	6.94	6.39	6.61	5.10
Ba	120.64	210.75	222.80	228.90	155.96	148.02	156.96	180.70	175.19	185.14	315.27	189.28	232.46
Th	0.57	1.62	1.68	1.69	1.12	1.04	1.14	1.40	1.27	1.11	1.05	1.06	1.02
U	0.14	0.51	0.52	0.66	0.38	0.47	0.40	0.78	0.36	0.25	0.28	0.27	0.44
Nb	12.92	26.69	26.21	26.19	18.14	16.93	18.05	23.75	21.11	21.11	19.23	19.36	18.23
Ta	1.01	2.05	2.01	2.06	1.39	1.37	1.46	1.89	1.63	1.61	1.49	1.54	1.43
La	12.33	25.59	25.28	24.96	17.53	16.57	17.23	22.59	20.29	16.93	16.75	16.72	16.17
Ce	30.29	60.76	59.83	59.98	42.02	37.55	39.73	52.53	49.75	42.31	39.96	40.09	38.74
Pb	1.24	2.29	2.47	2.62	1.89	2.01	4.55	2.36	2.08	1.51	1.63	1.48	1.50
Pr	3.96	7.75	7.50	7.50	5.30	5.17	5.45	7.34	6.35	5.34	5.07	5.08	4.93
Sr	272.87	239.75	251.80	250.71	244.41	244.43	248.74	238.87	259.83	317.17	325.58	333.63	330.77
Nd	18.24	35.06	33.19	33.56	23.65	23.40	24.68	33.59	29.04	24.01	22.58	22.56	22.28
Sm	4.63	8.78	8.12	8.22	5.88	5.82	6.11	8.54	7.29	5.99	5.57	5.56	5.47

Table S4.1 continued

Zr	111.17	238.95	226.38	228.80	163.83	156.97	165.36	220.50	192.63	147.05	138.47	142.66	148.68
Eu	1.69	2.82	2.62	2.67	1.99	1.95	2.04	2.78	2.49	2.09	1.98	2.01	1.93
Gd	4.69	8.89	8.20	8.37	6.08	5.99	6.28	8.76	7.48	5.82	5.48	5.48	5.42
Dy	4.75	9.34	8.45	8.67	6.30	6.20	6.52	9.17	7.87	5.71	5.47	5.47	5.42
Y	25.09	51.38	46.13	46.71	34.16	32.84	34.17	48.03	42.07	29.34	28.75	28.51	28.31
Ho	0.97	1.94	1.76	1.81	1.30	1.30	1.35	1.92	1.63	1.18	1.11	1.11	1.11
Yb	2.28	4.80	4.34	4.43	3.21	3.19	3.28	4.65	4.02	2.68	2.59	2.62	2.61
Tb	0.76	1.48	1.36	1.37	0.99	0.99	1.03	1.43	1.24	0.92	0.88	0.88	0.87
Er	2.57	5.24	4.72	4.76	3.41	3.46	3.60	5.11	4.30	3.02	2.89	2.89	2.88
Tm	0.37	0.77	0.69	0.69	0.50	0.50	0.52	0.74	0.62	0.43	0.41	0.42	0.41
Lu	0.34	0.72	0.65	0.66	0.48	0.49	0.50	0.71	0.59	0.41	0.39	0.39	0.39
Ni	147.39	37.70	83.67	69.84	90.16	135.47	79.93	31.85	66.63	130.66	122.55	133.53	135.05
Cr	354.12	101.94	201.21	162.20	219.57	310.45	192.21	49.36	106.46	335.73	342.45	338.24	348.95
V	293.95	530.61	447.12	446.15	352.29	350.00	365.26	509.53	449.44	351.40	353.36	337.69	323.41
Ga	16.91	22.91	21.65	21.29	19.02	18.45	19.16	22.25	22.00	19.13	17.88	18.11	17.66
Cu	107.35	288.62	235.86	244.31	167.25	182.81	164.19	267.34	191.23	104.33	98.49	112.21	102.78
Zn	104.95	174.00	157.77	160.43	126.23	132.59	135.17	181.61	156.28	120.09	111.96	114.46	113.30
Cs	0.04	0.11	0.12	0.11	0.11	0.11	0.13	0.09	0.08	0.10	0.07	0.07	0.05
Sc	38.53	49.06	43.64	43.72	40.02	39.28	39.90	46.84	44.34	37.91	39.02	36.87	37.51
As		0.56	0.69	0.61	0.80	0.80	1.01	0.73	0.61	0.80	1.20	1.32	0.72
Mo	0.88	1.36	1.66	1.55	1.18	1.73	1.16	1.31	1.42	0.95	1.40	1.11	1.35
Cd	0.21	0.18	0.29	0.26	0.31	0.26	0.19	0.23	0.23	0.11	0.21	0.13	0.13
Sb				0.13	0.15	0.10	0.08	0.09	0.13	0.17	0.16	0.18	0.14
W	0.86	0.95	0.98		< L,D,	< L,D,	< L,D,	< L,D,	< L,D,	< L.D.	< L,D,	< L,D,	< L,D,
Sn	0.94	2.05	1.76	1.90	1.63	1.98	1.36	2.39	1.56	1.15	1.03	1.29	1.04
Ge	1.39	1.77	1.67	1.66	1.46	1.48	1.54	1.76	1.63	1.51	1.41	1.40	1.34
In	0.08	0.13	0.12	0.12	0.09	0.09	0.09	0.13	0.12	0.09	0.09	0.08	0.08
Be	0.68	1.39	1.34	1.30	0.94	0.89	0.98	1.27	1.05	0.93	0.85	0.91	0.86
Co	51.75	46.99	48.31	48.52	47.78	51.14	46.81	49.85	54.25	51.65	48.48	50.20	49.91
Hf	2.70	5.78	5.46	5.62	3.95	3.93	4.18	5.65	4.73	3.79	3.47	3.55	3.54
Sample ID	**AF23_45**	**AF23-46**	**AF23-47**	**AF23-48B**	**AF23-49**	**AF23-50**	**AF23-51**	**AF23-68**	**AF23-69**	**AF23-70**	**AF23-74**	**AF23-75**	**AF23_87B**
Latitude (°N)	**11.816**	**12.088**	**12.087**	**12.086**	**12.086**	**12.053**	**12.052**	**11.809**	**11.807**	**11.806**	**11.815**	**11.864**	**12.132**
Longitude (°E)	**40.933**	**40.960**	**40.960**	**40.961**	**40.961**	**40.954**	**40.954**	**41.021**	**41.022**	**41.016**	**41.077**	**41.036**	**40.860**
SiO_2	45.98	47.50	46.07	45.93	45.50	46.30	46.04	47.96	49.10	48.59	46.15	47.77	46.90
Al_2O_3	14.11	12.85	12.74	12.69	12.95	12.84	12.99	15.13	12.47	12.29	14.24	15.52	13.63
Fe_2O_3	14.31	18.43	18.09	18.40	17.81	17.88	17.86	13.73	16.94	17.31	13.20	13.07	16.05
MnO	0.22	0.28	0.26	0.27	0.27	0.27	0.26	0.21	0.28	0.27	0.20	0.23	0.23
MgO	7.73	5.40	5.96	5.60	5.79	5.59	5.85	6.89	4.38	4.47	7.13	4.75	6.48
CaO	11.61	9.84	9.90	10.15	10.31	10.29	10.10	11.07	8.78	8.85	12.76	11.39	11.21
Na_2O	2.47	3.00	2.55	2.63	2.48	2.60	2.64	2.66	3.08	2.97	2.27	2.75	2.50
K_2O	0.45	0.55	0.63	0.62	0.54	0.63	0.56	0.43	0.84	0.94	0.36	0.61	0.41
TiO_2	2.69	3.10	3.54	3.69	3.60	3.66	3.52	2.35	3.82	3.84	2.38	2.41	2.84
P2O5	0.40	0.37	0.59	0.63	0.66	0.56	0.52	0.35	0.77	0.75	0.42	0.76	0.49

Table S4.1 continued

Rb	4.57	9.36	10.64	10.80	8.79	10.34	8.45	6.74	15.64	17.22	5.66	10.51	6.37
Ba	172.05	152.16	214.15	213.90	205.03	212.58	189.77	140.83	252.32	257.32	134.99	224.28	137.26
Th	1.10	1.23	1.59	1.66	1.68	1.62	1.52	1.12	2.71	2.58	0.83	1.76	1.05
U	0.24	0.36	0.45	0.49	0.47	0.44	0.41	0.31	0.69	0.69	0.33	0.58	0.34
Nb	19.46	18.11	24.67	25.01	25.09	24.94	23.35	17.16	39.87	39.10	17.61	27.81	17.67
Ta	1.55	1.43	1.95	2.03	2.00	1.98	1.89	1.37	3.02	3.05	1.40	2.11	1.43
La	17.65	16.58	23.91	24.42	25.06	24.84	22.91	17.06	36.38	35.04	16.12	27.21	17.13
Ce	40.11	42.16	54.73	55.49	57.32	56.90	52.14	38.27	78.38	81.54	37.17	62.95	39.21
Pb	1.52	1.70	2.16	2.46	2.39	2.21	1.95	1.58	2.98	3.24	1.65	2.43	1.67
Pr	5.16	5.40	6.96	7.56	7.25	7.20	6.67	4.77	10.28	10.80	5.20	7.86	5.47
Sr	301.42	257.28	250.72	258.72	264.93	252.68	246.42	324.50	266.27	267.73	294.54	376.62	243.39
Nd	23.07	24.60	31.26	33.75	32.66	32.28	29.89	21.33	44.94	47.10	23.63	35.01	24.72
Sm	5.67	6.49	7.72	8.22	8.00	8.01	7.39	5.13	10.69	11.19	5.82	8.34	6.22
Zr	147.38	160.57	217.74	227.73	220.21	223.20	206.13	145.29	328.40	346.76	151.09	229.81	165.22
Eu	2.00	2.24	2.53	2.69	2.61	2.61	2.47	1.79	3.33	3.53	2.02	2.73	2.14
Gd	5.52	6.70	7.81	8.45	8.05	8.00	7.51	5.19	10.42	11.09	5.78	8.01	6.43
Dy	5.58	7.24	8.07	8.67	8.35	8.43	7.82	5.35	10.48	11.02	5.68	7.91	6.78
Y	29.04	39.08	43.09	46.58	43.96	44.35	40.98	27.66	54.10	57.19	29.60	41.79	35.85
Ho	1.16	1.54	1.71	1.79	1.78	1.78	1.66	1.12	2.19	2.25	1.16	1.65	1.40
Yb	2.68	3.72	4.12	4.38	4.22	4.27	4.02	2.62	5.28	5.46	2.72	3.82	3.41
Tb	0.90	1.12	1.28	1.39	1.32	1.33	1.25	0.84	1.70	1.79	0.92	1.29	1.06
Er	2.99	4.02	4.44	4.81	4.58	4.61	4.33	2.90	5.68	5.99	3.07	4.24	3.74
Tm	0.42	0.59	0.65	0.67	0.66	0.67	0.62	0.42	0.82	0.84	0.43	0.60	0.53
Lu	0.40	0.57	0.62	0.65	0.64	0.64	0.60	0.40	0.79	0.80	0.41	0.57	0.51
Ni	122.24	30.08	86.53	103.87	78.63	65.67	115.94	88.04	111.85	76.24	106.24	69.35	79.04
Cr	313.06	18.31	170.77	224.78	157.87	153.93	264.17	239.55	251.81	155.54	296.93	334.94	199.81
V	340.15	457.09	428.81	446.09	427.54	435.65	410.03	320.48	340.07	368.14	312.60	229.47	393.22
Ga	18.30	22.64	21.39	22.11	21.45	21.38	20.96	18.38	21.80	22.92	18.30	20.66	20.10
Cu	115.36	216.02	177.05	257.06	173.92	206.63	299.01	129.40	73.46	92.52	135.83	76.50	182.71
Zn	114.78	150.53	154.64	170.68	156.62	154.94	152.32	107.60	164.08	178.07	118.37	129.30	139.94
Cs	0.05	0.11	0.13	0.13	0.15	0.11	0.08	0.07	0.16	0.18	0.08	0.15	0.08
Sc	37.57	45.31	41.81	42.41	40.65	42.34	41.05	36.96	38.60	39.29	38.30	31.29	42.85
As		< L,D,	0.56	< L,D,	0.73	0.72	0.60	0.62	0.60	0.54	0.65	0.76	< L,D,
Mo	0.81	1.07	1.83	2.21	1.61	1.47	1.92	1.12	3.14	3.01	1.02	1.75	1.21
Cd	0.11	0.12	0.15	0.19	0.15	0.14	0.14	0.10	0.17	0.21	0.12	0.18	0.11
Sb	< L.D.	0.16	0.07	0.07	0.09	< L,D,	0.16	0.14	0.17	0.08	0.06	0.09	0.25
W	< L.D.	< L,D,	< L,D,	< L,D,	< L,D,	< L,D,	< L,D,	< L.D.	< L.D.	< L.D.	< L,D,	< L.D.	< L,D,
Sn	1.28	1.48	1.95	1.83	1.92	1.90	1.66	1.17	2.34	2.49	1.13	1.69	1.34
Ge	1.44	1.62	1.63	1.67	1.62	1.67	1.54	1.43	1.82	1.87	1.43	1.60	1.51
In	0.08	0.11	0.11	0.11	0.11	0.11	0.11	0.08	0.13	0.14	0.08	0.10	0.10
Be	0.87	1.04	1.29	1.35	1.26	1.32	1.28	0.89	1.84	1.80	0.85	1.24	0.94
Co	49.61	52.62	50.34	50.66	49.13	46.94	49.04	45.62	39.81	42.75	46.76	33.74	49.18
Hf	3.71	4.25	5.34	5.48	5.43	5.51	5.16	3.57	7.89	8.10	3.67	5.47	4.06

Table S4.1 continued

Sample ID	AF23_88	AF23_89	AF23_90	AF23_91	AF23_92	AF23_93B	AF23_94	AF23_95	AF23-96	AF23-98	AF23-100	AF23-107	AF23-108
Latitude (°N)	**12.099**	**12.043**	**12.016**	**11.994**	**11.989**	**11.963**	**11.961**	**11.955**	**11.942**	**11.932**	**11.873**	**11.855**	**11.919**
Longitude (°E)	**40.867**	**40.897**	**40.907**	**40.912**	**40.914**	**40.926**	**40.923**	**40.923**	**40.916**	**40.923**	**40.952**	**40.829**	**41.198**
SiO_2	45.25	45.18	44.88	44.29	45.50	44.34	46.17	45.66	45.14	46.82	46.61	45.53	46.68
Al_2O_3	12.20	12.69	12.72	11.78	12.31	12.12	12.64	12.76	13.01	13.01	14.27	14.06	14.69
Fe_2O_3	15.22	14.53	14.80	18.73	19.56	21.37	18.96	19.07	18.97	18.07	14.32	13.99	14.67
MnO	0.24	0.23	0.22	0.28	0.29	0.30	0.28	0.29	0.28	0.27	0.22	0.22	0.22
MgO	6.30	7.03	6.74	5.37	5.36	5.24	5.60	5.65	5.72	5.85	6.83	7.72	7.08
CaO	11.72	12.15	12.43	10.64	10.20	9.48	9.98	10.18	10.16	10.09	11.49	11.51	11.23
Na_2O	2.10	2.13	2.11	2.33	2.72	2.67	2.77	2.67	2.46	2.70	2.45	2.34	2.41
K_2O	0.45	0.39	0.31	0.38	0.48	0.34	0.51	0.44	0.35	0.47	0.42	0.43	0.32
TiO_2	2.79	2.60	2.62	3.35	3.51	3.92	3.30	3.30	3.35	3.05	2.81	2.61	3.04
P2O5	0.53	0.46	0.48	0.52	0.51	0.54	0.48	0.47	0.46	0.51	0.48	0.41	0.41
Rb	7.84	6.35	5.09	5.50	7.67	4.34	7.71	6.64	5.89	6.90	5.79	5.83	3.19
Ba	181.42	176.86	154.41	168.46	175.43	159.69	175.70	161.97	142.01	155.40	168.38	505.87	148.22
Th	1.33	1.22	1.08	1.36	1.36	1.40	1.24	1.26	1.47	1.14	0.98	1.02	0.70
U	0.54	0.57	0.38	0.52	0.43	0.32	0.35	0.36	0.35	0.38	0.29	0.32	0.19
Nb	19.06	18.07	17.67	20.89	21.86	23.86	20.22	20.13	21.29	18.93	20.30	18.38	14.79
Ta	1.51	1.47	1.40	1.67	1.77	1.97	1.64	1.61	1.73	1.47	1.59	1.49	1.24
La	19.72	18.78	17.11	21.36	22.00	22.30	20.45	20.21	21.71	18.45	18.23	16.48	14.76
Ce	45.50	43.21	39.26	49.55	51.27	53.06	48.18	47.12	49.98	43.50	43.45	38.21	36.56
Pb	2.15	2.11	1.92	2.35	2.43	2.16	2.09	1.98	2.40	1.93	1.57	1.76	1.58
Pr	5.77	5.41	5.39	6.35	6.59	7.36	6.17	6.07	6.66	5.63	5.66	4.90	4.84
Sr	249.99	243.28	250.88	251.83	251.97	251.81	246.94	245.38	251.08	248.46	280.90	342.26	367.68
Nd	25.75	24.40	24.11	28.85	29.83	33.27	28.00	27.59	29.92	25.82	25.54	22.23	22.45
Sm	6.35	5.99	6.03	7.22	7.49	8.44	7.12	6.97	7.57	6.54	6.34	5.36	5.64
Zr	172.77	162.96	160.29	189.65	197.08	225.78	187.02	186.11	195.77	172.32	174.36	128.81	150.48
Eu	2.11	1.99	2.04	2.39	2.52	2.82	2.40	2.35	2.52	2.22	2.15	1.93	2.04
Gd	6.41	6.10	6.19	7.34	7.72	8.52	7.20	7.12	7.64	6.63	6.30	5.30	5.63
Dy	6.77	6.39	6.38	7.84	8.10	8.91	7.66	7.54	7.97	6.97	6.32	5.19	5.64
Y	36.89	33.82	34.20	41.34	42.70	46.88	40.37	40.05	41.70	37.39	32.53	26.68	28.77
Ho	1.44	1.37	1.34	1.67	1.74	1.87	1.62	1.61	1.69	1.48	1.30	1.08	1.16
Yb	3.47	3.30	3.20	4.00	4.19	4.53	3.96	3.83	4.08	3.59	3.08	2.50	2.64
Tb	1.07	1.02	1.01	1.23	1.27	1.41	1.21	1.19	1.28	1.11	1.04	0.85	0.93
Er	3.78	3.56	3.53	4.35	4.55	4.97	4.30	4.20	4.45	3.92	3.40	2.78	2.97
Tm	0.55	0.52	0.49	0.63	0.66	0.69	0.62	0.61	0.65	0.57	0.50	0.41	0.42
Lu	0.53	0.49	0.48	0.60	0.63	0.67	0.59	0.58	0.60	0.53	0.45	0.37	0.39
Ni	73.62	79.81	83.73	38.55	62.53	42.98	71.96	135.61	48.01	108.56	109.23	135.76	113.79
Cr	161.21	162.16	203.91	41.44	96.25	48.10	114.52	270.68	72.99	211.36	278.80	341.93	295.20
V	371.86	342.77	365.93	444.50	452.88	534.53	428.27	428.49	459.63	428.23	343.39	317.72	349.39
Ga	18.68	17.82	18.73	21.06	21.74	23.85	21.38	20.94	21.77	21.15	18.77	17.49	18.78
Cu	166.87	162.06	165.39	203.44	210.77	189.25	192.82	185.97	160.09	184.01	127.79	100.88	115.38
Zn	130.89	120.42	129.47	154.05	160.60	187.48	154.34	151.46	152.80	145.62	117.14	109.64	120.60

Table S4.1 continued

Cs	0.13	0.09	0.08	0.09	0.09	0.06	0.08	0.08	0.11	0.09	0.07	0.07	0.06
Sc	39.81	38.18	39.22	42.38	43.74	46.04	43.83	44.60	47.00	43.79	39.52	35.97	38.10
As	0.89	0.71	0.61	0.94	0.63	0.51	< L,D,	0.57	0.65	< L,D,	< L.D.	0.89	< L,D,
Mo	1.13	0.89	1.09	1.05	1.44	1.18	1.45	2.27	0.89	1.91	1.38	1.19	1.00
Cd	0.20	0.30	0.22	0.67	0.27	0.14	0.13	0.16	0.15	0.18	0.12	0.18	0.14
Sb	0.06	0.19	0.16	0.16	0.17	0.10	0.16	0.21	0.22	0.23	0.24	0.22	0.24
W	< L,D,	< L,D,	< L,D,	< L,D,	< L,D,	< L,D,	< L,D,	< L,D,	< L,D,	< L,D,	< L.D.	< L,D,	< L,D,
Sn	1.49	1.54	1.28	1.83	1.69	1.93	1.57	1.62	1.80	1.57	1.32	1.16	1.32
Ge	1.48	1.43	1.46	1.61	1.63	1.75	1.54	1.60	1.67	1.53	1.42	1.40	1.45
In	0.10	0.10	0.09	0.12	0.13	0.13	0.11	0.11	0.12	0.11	0.09	0.08	0.09
Be	1.01	0.97	0.87	1.17	1.22	1.17	1.12	1.09	1.03	1.08	0.98	0.85	0.79
Co	46.40	44.42	47.33	49.89	52.70	58.10	52.98	53.89	53.99	53.99	45.80	49.71	48.95
Hf	4.27	4.15	3.90	4.89	5.15	5.82	4.80	4.74	5.05	4.38	4.34	3.36	3.80
Sample ID	**AF23-109**	**AF23-110**	**AF23-111**	**AF23-112**	**AF23-113**	**AF23_114**	**AF23_115**	**AF23_116**	**AF23_117**	**AF23_118**	**AF23_119**	**AF23_120**	**AF23_121B**
Latitude (°N)	**11.921**	**11.927**	**11.914**	**11.843**	**11.850**	**11.850**	**11.859**	**11.859**	**11.859**	**11.857**	**11.855**	**11.851**	**11.822**
Longitude (°E)	**41.197**	**41.213**	**41.183**	**41.037**	**41.043**	**41.043**	**41.057**	**41.056**	**41.050**	**41.048**	**41.046**	**41.028**	**41.080**
SiO_2	46.73	47.38	46.53	47.51	46.66	46.98	47.73	46.85	46.70	68.48	48.84	46.35	46.48
Al_2O_3	14.89	14.70	15.20	14.51	13.22	15.10	18.12	17.23	16.23	12.89	15.65	13.83	14.01
Fe_2O_3	15.03	14.27	13.87	13.39	16.57	12.61	10.60	10.65	12.04	7.35	13.57	15.76	13.65
MnO	0.22	0.21	0.21	0.24	0.26	0.20	0.16	0.17	0.19	0.22	0.24	0.24	0.21
MgO	6.38	7.20	6.95	4.78	5.72	6.40	5.20	5.32	7.25	0.11	4.46	6.69	6.71
CaO	10.69	11.19	11.24	10.69	11.24	11.48	12.86	13.18	12.26	2.81	10.31	10.87	12.14
Na_2O	2.72	2.54	2.58	2.74	2.55	2.21	2.48	2.38	2.35	4.77	3.02	2.57	2.42
K_2O	0.42	0.37	0.35	0.67	0.50	0.53	0.33	0.35	0.34	2.99	0.73	0.45	0.42
TiO_2	3.36	2.74	2.54	2.42	3.21	2.32	1.74	1.77	2.02	0.45	2.39	2.74	2.56
P2O5	0.40	0.33	0.40	0.96	0.48	0.39	0.25	0.26	0.39	0.10	0.75	0.42	0.45
Rb	4.07	4.26	3.98	10.87	8.59	9.18	5.10	6.26	4.67	60.82	12.38	7.64	6.25
Ba	146.04	125.21	156.66	286.81	187.76	151.12	101.57	118.34	127.07	706.86	214.69	172.15	138.69
Th	0.68	0.67	0.82	1.91	1.32	1.36	0.74	0.88	0.70	9.59	1.91	1.12	0.87
U	0.20	0.19	0.36	0.83	0.39	0.35	0.22	0.33	0.25	2.55	0.53	0.36	0.44
Nb	16.53	14.22	16.48	29.07	20.04	18.42	11.33	12.28	14.80	90.18	29.26	17.58	18.64
Ta	1.35	1.15	1.32	2.26	1.62	1.48	0.90	0.98	1.18	6.57	2.25	1.39	1.48
La	15.56	14.12	17.01	27.93	19.44	17.35	11.17	12.27	14.00	80.40	26.72	16.76	16.77
Ce	38.12	34.07	40.76	65.60	47.07	41.29	25.53	27.42	33.83	175.71	64.20	40.44	38.47
Pb	1.50	1.35	1.55	2.36	2.01	2.04	1.27	1.52	1.28	8.68	2.06	1.77	1.52
Pr	5.11	4.51	5.26	8.41	6.04	5.23	3.48	3.72	4.34	21.53	8.14	5.24	5.41
Sr	368.92	327.39	334.59	335.22	256.70	290.35	305.58	307.27	300.39	166.83	327.85	259.22	283.60
Nd	23.74	20.78	23.63	37.42	27.33	23.29	15.74	16.80	19.69	87.22	35.88	23.81	24.83
Sm	6.11	5.21	5.71	8.80	6.92	5.59	3.84	4.04	4.81	19.43	8.52	5.97	6.05
Zr	167.01	141.61	156.39	248.96	181.81	158.71	101.68	108.30	127.27	1155.98	254.05	160.00	159.53
Eu	2.18	1.92	2.03	2.88	2.28	1.90	1.43	1.46	1.73	5.13	2.86	2.02	2.09
Gd	6.09	5.31	5.67	8.71	7.06	5.58	3.95	4.16	4.84	18.84	8.43	6.18	6.10
Dy	6.04	5.27	5.55	8.46	7.44	5.48	4.06	4.25	4.80	20.40	8.28	6.38	6.07

Table S4.1 continued

Y	30.46	27.16	28.50	44.25	39.12	28.35	21.86	22.86	25.21	109.23	43.45	34.62	31.79
Ho	1.23	1.10	1.17	1.78	1.58	1.15	0.86	0.89	1.00	4.44	1.73	1.34	1.26
Yb	2.81	2.57	2.67	4.16	3.79	2.69	1.99	2.09	2.30	12.37	4.05	3.25	2.91
Tb	0.99	0.87	0.90	1.36	1.16	0.89	0.64	0.68	0.78	3.17	1.34	1.04	0.97
Er	3.13	2.82	2.96	4.55	4.14	2.97	2.25	2.34	2.59	12.22	4.44	3.53	3.30
Tm	0.46	0.41	0.42	0.66	0.60	0.43	0.32	0.34	0.38	1.89	0.65	0.53	0.47
Lu	0.41	0.37	0.40	0.62	0.57	0.40	0.30	0.32	0.35	1.89	0.61	0.49	0.43
Ni	85.36	94.66	92.99	49.00	74.01	70.77	77.50	57.92	157.76	90.91	62.46	84.27	88.77
Cr	184.01	255.90	196.01	228.15	224.58	226.85	244.51	194.12	390.33	218.19	285.64	191.03	283.22
V	359.64	332.46	317.41	204.02	419.33	266.18	264.44	268.25	253.52	2.68	193.23	387.60	332.94
Ga	19.71	18.57	18.82	20.06	20.48	18.04	19.13	18.99	17.47	27.59	20.87	20.02	18.90
Cu	133.64	124.83	115.21	65.04	202.17	122.26	127.21	130.66	123.02	18.99	77.86	161.49	148.11
Zn	124.10	113.38	113.63	137.67	143.16	104.33	88.26	90.08	96.07	210.99	134.63	131.22	118.72
Cs	0.04	0.05	0.05	0.12	0.11	0.18	0.06	0.10	0.08	0.70	0.17	0.23	0.08
Sc	35.84	38.05	35.16	31.37	44.45	36.18	32.84	33.20	32.99	8.80	31.27	39.81	41.20
As	< L,D,	< L,D,	< L,D,	0.98	< L.D.	< L,D,	< L,D,	< L,D,	< L,D,	1.44	0.53	0.57	< L,D,
Mo	0.79	0.73	1.27	1.68	1.74	0.70	1.08	0.75	1.55	5.99	1.90	1.16	1.13
Cd	0.11	0.12	0.11	0.19	0.17	0.14	0.12	0.14	0.14	0.40	0.14	0.14	0.11
Sb	0.25	0.31	0.28	0.21	0.20	0.16	0.08	0.09	0.20	0.35	0.21	0.17	0.08
W	< L,D,	< L,D,	< L,D,	< L,D,	< L.D.	< L,D,	< L,D,	< L,D,	< L,D,	1.48	< L,D,	< L,D,	< L,D,
Sn	1.77	1.16	1.15	2.16	1.94	1.26	0.83	0.87	1.21	6.12	1.76	1.45	1.31
Ge	1.43	1.43	1.45	1.64	1.63	1.42	1.26	1.29	1.31	2.58	1.63	1.53	1.49
In	0.09	0.09	0.08	0.11	0.11	0.08	0.06	0.06	0.07	0.20	0.10	0.10	0.08
Be	0.94	0.80	0.87	1.42	1.08	1.00	0.63	0.69	0.73	4.73	1.38	0.98	0.92
Co	46.14	47.75	47.07	31.49	45.05	39.95	37.42	37.39	44.18	3.21	30.94	50.43	45.66
Hf	4.12	3.57	3.85	5.93	4.71	3.95	2.56	2.71	3.05	26.53	6.06	4.02	3.86
Sample ID	**AF23_122**	**AF23_123B**	**AF23_126**	**AF23_127**	**AF23_128**	**AF23_129**	**AF23_130**	**AF23_131B**	**AF23_132B**	**AF23_133**	**AF23_134**	**AF23_135**	**AF23_136B**
Latitude (°N)	**11.822**	**11.818**	**12.073**	**12.073**	**12.072**	**12.068**	**12.067**	**12.065**	**12.058**	**12.050**	**12.146**	**12.145**	**12.143**
Longitude (°E)	**41.081**	**41.070**	**40.905**	**40.905**	**40.903**	**40.903**	**40.903**	**40.902**	**40.903**	**40.899**	**40.848**	**40.849**	**40.848**
SiO_2	45.14	46.87	44.24	43.52	43.38	44.35	45.12	44.40	44.44	45.52	46.50	44.94	46.21
Al_2O_3	14.78	13.71	13.23	12.04	11.04	11.96	12.73	12.62	12.59	13.41	13.79	13.41	13.50
Fe_2O_3	12.24	14.29	17.72	16.25	17.54	17.46	17.81	17.62	17.99	14.90	14.42	14.62	15.19
MnO	0.20	0.22	0.27	0.25	0.27	0.26	0.27	0.26	0.27	0.23	0.22	0.22	0.23
MgO	6.65	6.44	6.04	6.05	5.36	5.61	5.60	5.60	5.55	6.75	5.77	6.71	6.54
CaO	13.03	11.87	10.51	12.02	11.64	11.05	10.58	10.81	10.71	11.62	11.01	11.73	11.32
Na_2O	2.21	2.47	2.49	2.17	2.22	2.30	2.48	2.48	2.52	2.30	2.38	2.24	2.45
K_2O	0.39	0.44	0.43	0.37	0.44	0.54	0.60	0.47	0.50	0.36	0.57	0.40	0.40
TiO_2	2.18	2.76	3.39	3.12	3.67	3.54	3.59	3.51	3.66	2.58	2.60	2.54	2.68
P2O5	0.49	0.48	0.52	0.53	0.62	0.69	0.56	0.54	0.56	0.45	0.50	0.42	0.41
Rb	6.55	6.44	6.64	6.26	7.64	10.55	11.56	8.10	8.40	5.95	12.64	10.57	6.26
Ba	159.84	148.34	191.93	218.50	233.54	246.80	214.42	202.65	202.05	146.07	179.67	139.48	147.28
Th	0.95	0.92	1.49	1.44	1.66	1.72	1.67	1.61	1.68	1.07	1.46	1.10	1.02
U	0.41	0.28	0.40	0.68	0.75	0.70	0.52	0.46	0.44	0.39	0.46	0.37	0.33

Table S4.1 continued

Nb	16.86	20.62	22.63	20.92	25.80	25.36	24.87	24.06	25.76	16.70	17.79	16.20	17.11
Ta	1.34	1.63	1.80	1.70	2.08	2.07	1.96	1.97	2.08	1.35	1.44	1.33	1.39
La	17.33	18.25	21.56	20.91	25.32	24.56	23.67	23.39	24.18	16.35	17.84	15.80	16.51
Ce	37.00	42.55	49.17	47.29	57.22	55.63	56.73	52.87	55.19	37.25	42.36	38.16	37.90
Pb	1.78	1.51	2.41	2.47	2.65	2.61	2.74	2.32	2.39	1.85	2.38	1.69	1.64
Pr	5.29	5.97	6.84	6.52	7.84	7.68	7.28	7.34	7.58	5.20	5.42	4.97	5.30
Sr	303.22	288.75	271.78	276.38	270.25	271.89	252.90	278.00	277.90	251.42	228.66	243.29	249.43
Nd	23.96	27.31	30.73	29.01	35.27	34.15	32.41	32.38	34.21	23.51	24.05	22.35	23.98
Sm	5.68	6.59	7.43	7.09	8.65	8.33	7.81	8.01	8.44	5.91	5.89	5.54	6.02
Zr	145.77	176.54	201.74	188.37	232.20	228.34	218.99	219.80	231.58	156.69	162.84	150.21	160.34
Eu	1.97	2.30	2.48	2.36	2.76	2.72	2.57	2.62	2.76	2.02	1.96	1.90	2.10
Gd	5.81	6.71	7.62	7.28	8.86	8.70	7.93	8.21	8.69	6.23	6.07	5.76	6.31
Dy	5.67	6.58	7.83	7.38	9.12	8.82	8.23	8.43	8.82	6.48	6.23	6.02	6.51
Y	30.85	34.74	42.14	39.79	47.27	46.22	44.39	44.16	47.15	34.26	33.04	31.75	34.58
Ho	1.19	1.38	1.66	1.55	1.89	1.88	1.74	1.76	1.87	1.36	1.31	1.27	1.38
Yb	2.73	3.19	3.97	3.70	4.56	4.48	4.22	4.27	4.46	3.24	3.26	3.09	3.30
Tb	0.91	1.07	1.24	1.17	1.43	1.41	1.33	1.32	1.41	1.01	1.01	0.96	1.02
Er	3.08	3.59	4.42	4.15	5.02	4.96	4.57	4.65	4.92	3.60	3.47	3.36	3.63
Tm	0.45	0.51	0.64	0.60	0.72	0.72	0.67	0.68	0.73	0.53	0.52	0.49	0.53
Lu	0.41	0.48	0.60	0.57	0.68	0.66	0.64	0.64	0.66	0.49	0.49	0.47	0.50
Ni	103.39	106.15	78.97	79.23	75.87	87.90	168.05	64.56	57.93	98.39	97.45	82.68	78.13
Cr	288.16	332.90	144.49	150.61	187.64	187.84	389.30	128.40	123.08	239.89	242.04	187.17	187.65
V	287.52	359.20	414.18	385.01	450.28	441.75	429.75	435.86	465.91	369.52	332.30	341.24	384.07
Ga	18.32	19.54	21.37	20.04	21.14	22.43	21.43	22.05	22.77	19.48	18.78	18.31	19.78
Cu	130.20	160.49	214.72	219.57	271.02	300.04	244.28	238.40	224.24	166.28	186.44	189.28	172.27
Zn	108.59	128.01	160.38	145.79	163.41	165.54	152.79	161.00	169.59	132.31	122.10	119.01	134.38
Cs	0.11	0.08	0.09	0.11	0.10	0.18	0.48	0.11	0.10	0.10	0.97	1.61	0.08
Sc	35.28	43.49	39.89	36.48	42.07	40.88	41.74	40.43	42.88	40.68	38.77	38.87	41.55
As	0.76	< L,D,	0.58	1.11	0.98	0.94	0.66	0.69	0.51	0.53	0.81	0.50	0.65
Mo	1.09	1.61	1.32	1.38	1.75	1.88	3.08	1.33	1.34	1.31	1.56	1.01	1.18
Cd	0.15	0.13	0.27	0.33	0.29	0.28	0.25	0.23	0.21	0.25	0.21	0.15	0.13
Sb	0.11	0.09	0.09	0.11	0.11	0.13	0.22	0.09	< L,D,	0.06	0.33	0.28	< L,D,
W	< L,D,	< L,D,	< L,D,	< L,D,	< L,D,	< L,D,	< L,D,	< L,D,	< L,D,	< L,D,	< L,D,	< L.D.	< L,D,
Sn	1.06	1.29	1.58	1.50	1.88	2.56	3.05	1.93	1.82	1.38	2.38	1.90	1.20
Ge	1.39	1.59	1.56	1.47	1.62	1.64	1.70	1.58	1.71	1.46	1.48	1.43	1.45
In	0.08	0.09	0.11	0.11	0.12	0.12	0.12	0.11	0.12	0.10	0.10	0.08	0.09
Be	0.82	0.98	1.16	1.11	1.31	1.30	1.33	1.25	1.22	0.87	1.06	0.92	0.92
Co	44.68	46.73	52.08	48.49	47.18	49.74	51.07	48.80	50.09	49.67	43.76	46.70	48.90
Hf	3.53	4.22	4.97	4.67	5.69	5.68	5.46	5.38	5.73	3.87	4.14	3.81	3.93
Sample ID	**AF23_137B**	**AF23_138B**	**AF23_139B**	**AF23_140**	**AF23_141B**	**AF23_142B**	**AF23_143**	**AF23_144**	**AF23_145**	**AF23_146**	**AF23_147**	**AF23_148**	**AF23_149**
Latitude (°N)	**12.138**	**12.138**	**12.121**	**12.069**	**12.059**	**12.037**	**11.833**	**11.833**	**11.830**	**11.832**	**11.830**	**11.826**	**40.981**
Longitude (°E)	**40.844**	**40.848**	**40.853**	**40.886**	**40.892**	**40.898**	**41.008**	**41.008**	**41.006**	**41.003**	**40.984**	**11.826**	**40.981**
SiO_2	46.65	46.47	46.42	45.79	45.01	45.21	47.26	47.05	47.55	47.72	47.76	47.64	46.91

Table S4.1 continued

Al_2O_3	13.69	13.40	12.79	11.72	13.63	12.50	14.65	14.50	17.52	16.62	16.11	16.57	15.66
Fe_2O_3	15.71	15.59	16.28	15.26	16.00	18.90	13.69	13.68	11.91	12.46	13.22	12.69	12.93
MnO	0.24	0.23	0.25	0.24	0.24	0.28	0.21	0.21	0.18	0.19	0.20	0.19	0.20
MgO	6.45	6.20	6.02	6.43	6.52	5.31	7.00	6.95	4.96	4.80	5.31	4.95	4.99
CaO	10.88	10.93	10.40	11.05	10.79	10.24	10.98	10.88	11.26	11.46	11.18	10.91	11.82
Na_2O	2.57	2.55	2.42	2.11	2.30	2.60	2.60	2.59	2.84	2.85	2.84	2.89	2.80
K_2O	0.45	0.48	0.42	0.34	0.28	0.52	0.44	0.42	0.40	0.44	0.45	0.44	0.50
TiO_2	2.78	2.81	2.98	2.80	2.77	3.94	2.32	2.33	2.17	2.33	2.46	2.37	2.47
P2O5	0.44	0.44	0.53	0.47	0.45	0.61	0.35	0.36	0.35	0.38	0.36	0.35	0.37
Rb	7.41	8.39	7.39	5.70	4.24	8.76	7.85	7.59	6.25	7.71	7.47	8.58	9.09
Ba	146.78	170.38	176.60	170.09	125.05	190.51	142.30	159.38	154.79	171.15	151.91	154.30	165.23
Th	1.16	1.18	1.13	1.11	1.10	1.65	1.22	1.26	1.15	1.32	1.29	1.30	1.46
U	0.33	0.38	0.39	0.46	0.34	0.45	0.34	0.39	0.29	0.39	0.33	0.37	0.42
Nb	18.20	18.83	18.95	17.80	17.57	25.85	18.67	19.32	17.22	19.10	19.61	19.85	20.72
Ta	1.48	1.53	1.55	1.45	1.43	2.10	1.40	1.45	1.34	1.46	1.46	1.57	1.57
La	17.65	18.76	18.71	17.65	16.95	24.54	16.86	17.79	15.89	18.06	17.85	18.91	19.87
Ce	41.01	42.32	42.59	40.27	38.76	56.44	40.29	42.24	37.91	42.71	41.92	44.31	45.48
Pb	1.78	1.92	1.79	1.91	1.74	2.39	1.54	1.66	1.43	1.73	1.60	1.60	1.82
Pr	5.66	5.88	5.94	5.57	5.38	7.78	5.04	5.31	4.75	5.32	5.29	5.64	5.81
Sr	248.74	254.79	247.02	247.70	239.44	254.05	277.81	288.14	328.84	321.34	295.07	316.72	310.81
Nd	25.27	26.30	26.94	25.29	24.19	34.74	22.42	23.37	21.03	23.48	23.21	24.54	25.65
Sm	6.39	6.67	6.69	6.29	6.12	8.55	5.42	5.65	5.07	5.69	5.58	6.02	6.14
Zr	172.27	181.81	178.97	166.26	166.60	237.75	156.58	157.63	145.98	161.52	161.05	165.42	174.48
Eu	2.17	2.24	2.30	2.14	2.10	2.79	1.90	1.96	1.83	1.99	1.96	2.09	2.09
Gd	6.63	6.95	7.00	6.58	6.40	8.77	5.39	5.54	4.95	5.44	5.48	5.96	6.04
Dy	6.95	7.16	7.16	6.80	6.54	8.92	5.65	5.80	5.14	5.73	5.72	5.98	6.19
Y	36.35	38.44	38.05	35.57	34.88	47.82	30.15	30.99	27.88	30.71	30.75	31.83	33.56
Ho	1.47	1.52	1.51	1.42	1.38	1.85	1.17	1.21	1.06	1.19	1.20	1.25	1.29
Yb	3.47	3.61	3.64	3.39	3.33	4.52	2.75	2.86	2.50	2.79	2.81	3.02	3.02
Tb	1.07	1.13	1.15	1.07	1.04	1.42	0.89	0.93	0.83	0.91	0.91	0.98	0.99
Er	3.84	4.03	4.01	3.76	3.67	4.95	3.01	3.14	2.81	3.09	3.12	3.29	3.36
Tm	0.56	0.58	0.58	0.55	0.53	0.72	0.44	0.46	0.41	0.45	0.46	0.48	0.49
Lu	0.52	0.55	0.55	0.53	0.50	0.68	0.43	0.44	0.38	0.43	0.43	0.45	0.46
Ni	87.59	74.37	65.32	92.50	72.72	55.43	94.08	97.24	61.17	52.85	50.59	45.18	46.18
Cr	213.00	188.02	145.38	205.66	154.73	156.12	281.67	255.70	101.62	98.15	108.09	96.40	94.76
V	390.10	399.36	405.89	390.05	384.80	488.00	351.20	353.39	305.44	323.31	347.29	328.48	361.81
Ga	20.59	20.93	20.33	18.91	19.75	22.35	19.54	20.10	20.90	21.13	20.95	21.22	21.43
Cu	148.02	159.55	190.20	195.51	161.58	242.34	119.02	141.54	125.83	153.36	157.32	165.00	147.20
Zn	138.45	141.71	148.59	135.61	137.44	171.24	121.25	117.40	105.83	111.94	113.86	113.90	117.36
Cs	0.09	0.09	0.10	0.09	0.08	0.09	0.08	0.09	0.08	0.10	0.09	0.10	0.12
Sc	42.09	42.33	43.10	40.58	42.03	45.91	39.35	37.07	31.23	33.00	37.64	33.91	36.61
As	< L,D,	0.56	< L,D,	0.74	< L,D,	0.69	0.41	0.82	0.51	0.80	0.59	0.64	0.75
Mo	1.39	1.21	1.16	1.57	0.86	1.39	1.09	1.21	0.88	1.17	0.89	0.94	0.94

Table S4.1 continued

Cd	0.15	0.14	0.14	0.22	0.12	0.13	0.11	0.13	0.11	0.13	0.10	0.12	0.13
Sb	< L,D,	< L,D,	< L,D,	0.06	< L,D,	0.08	0.19	0.17	0.18	0.20	0.18	0.19	0.23
W	< L,D,	< L,D,	< L,D,	< L,D,	< L,D,	< L,D,	0.36	0.39	0.34	0.40	0.37	0.44	0.43
Sn	1.45	1.40	1.65	1.73	1.26	1.76	1.65	1.33	1.33	1.35	1.75	1.62	1.59
Ge	1.56	1.58	1.57	1.48	1.50	1.74	1.50	1.51	1.36	1.45	1.43	1.40	1.51
In	0.09	0.10	0.10	0.10	0.09	0.12	0.09	0.09	0.08	0.08	0.09	0.09	0.09
Be	0.98	1.01	1.04	0.99	0.94	1.32	0.87	0.85	0.82	0.91	0.96	0.94	0.96
Co	49.23	49.89	49.58	48.28	50.42	48.48	49.05	49.70	38.93	39.44	40.73	39.99	40.72
Hf	4.30	4.44	4.48	4.17	4.09	5.73	3.76	3.91	3.55	3.86	3.84	4.14	4.10

Sample ID	**AF23_159**	**AF23_160**	**AF23_161**	**AF23_162**	**AF23_163**	**AF23_164**	**AF23_165**	**AF23_166**	**AF23_175**
Latitude (°N)	**11.908**	**11.907**	**11.905**	**11.905**	**11.901**	**11.902**	**11.882**	**11.883**	**11.877**
Longitude (°E)	**41.094**	**41.094**	**41.095**	**41.095**	**41.099**	**41.098**	**41.055**	**41.044**	**40.936**
SiO_2	47.63	47.44	51.08	47.61	47.02	47.41	47.23	48.19	45.57
Al_2O_3	12.52	17.26	12.91	17.16	14.28	14.59	16.79	17.65	14.59
Fe_2O_3	17.00	12.37	15.82	12.43	13.95	13.41	11.02	11.23	14.61
MnO	0.28	0.19	0.29	0.19	0.22	0.21	0.18	0.17	0.22
MgO	4.46	4.50	3.52	4.46	6.98	6.80	5.42	5.61	6.80
CaO	9.05	11.70	7.90	11.45	11.80	11.54	12.34	12.37	11.29
Na_2O	2.83	2.86	3.39	2.90	2.55	2.57	2.37	2.57	2.39
K_2O	0.87	0.40	1.09	0.41	0.44	0.42	0.48	0.33	0.30
TiO_2	3.72	2.35	3.03	2.36	2.38	2.33	1.87	1.86	2.87
P2O5	0.76	0.35	1.03	0.36	0.43	0.37	0.30	0.26	0.47
Rb	16.21	6.03	23.66	7.57	7.66	7.16	10.34	5.54	4.94
Ba	335.05	185.62	350.41	175.44	182.82	163.30	153.28	109.61	165.40
Th	2.88	1.27	3.83	1.32	1.27	1.17	1.52	0.82	1.14
U	0.74	0.34	1.01	0.37	0.45	0.36	0.47	0.24	0.30
Nb	40.34	18.78	53.21	19.33	19.20	18.23	16.62	12.93	23.38
Ta	3.00	1.43	3.82	1.43	1.45	1.39	1.27	1.01	1.81
La	36.21	17.82	47.50	18.15	18.72	17.14	16.99	12.31	20.02
Ce	82.86	41.56	109.56	42.20	42.83	39.52	37.82	29.20	49.54
Pb	3.34	1.68	4.14	2.03	1.74	1.46	2.28	1.29	1.78
Pr	10.95	5.25	14.30	5.35	5.51	5.09	4.85	3.80	6.54
Sr	290.87	329.76	304.89	344.82	290.76	296.47	318.71	309.06	319.85
Nd	47.58	23.28	62.23	23.47	24.36	22.65	21.15	17.07	29.70
Sm	11.32	5.50	14.48	5.67	5.87	5.52	5.05	4.27	7.28
Zr	339.94	161.47	447.90	164.27	162.25	157.24	143.82	115.98	202.82
Eu	3.50	1.94	4.37	1.96	1.94	1.87	1.67	1.53	2.47
Gd	10.92	5.50	14.04	5.56	5.83	5.51	4.95	4.25	7.22
Dy	10.97	5.63	13.98	5.70	6.00	5.70	5.04	4.50	7.29
Y	59.75	30.49	75.08	31.38	32.30	30.18	28.18	24.37	38.74
Ho	2.29	1.17	2.86	1.17	1.23	1.17	1.06	0.93	1.50
Yb	5.46	2.77	6.91	2.80	2.92	2.75	2.54	2.21	3.47
Tb	1.77	0.91	2.25	0.91	0.94	0.90	0.81	0.71	1.19

Table S4.1 continued

Er	6.03	3.12	7.66	3.13	3.26	3.09	2.81	2.45	3.87
Tm	0.86	0.44	1.10	0.45	0.47	0.44	0.41	0.35	0.56
Lu	0.81	0.41	1.04	0.42	0.44	0.41	0.38	0.34	0.53
Ni	97.41	53.12	85.91	49.59	94.56	81.58	68.68	59.02	97.84
Cr	200.29	99.38	198.99	91.60	277.34	276.64	224.50	204.88	251.41
V	392.07	318.92	226.86	325.62	357.55	342.54	281.45	286.47	389.07
Ga	23.04	21.35	25.39	21.50	19.57	19.47	19.78	19.06	20.65
Cu	113.77	148.81	41.63	142.94	144.19	162.88	144.93	134.67	148.71
Zn	179.50	109.28	187.69	114.59	121.36	115.83	99.59	94.35	131.23
Cs	0.18	0.08	0.26	0.09	0.11	0.14	0.23	0.07	0.08
Sc	39.05	31.81	32.42	31.84	38.40	39.02	33.42	34.86	40.47
As	0.65	0.46	0.75	0.53	0.62	1.45	0.85	0.43	0.83
Mo	3.21	1.15	3.65	1.19	1.17	1.10	0.97	0.68	1.17
Cd	0.24	0.12	0.24	0.15	0.16	0.12	0.15	0.09	0.17
Sb	0.25	0.21	0.26	0.22	0.21	0.22	0.24	0.23	0.20
W	0.73	0.38	0.82	0.41	0.41	0.40	0.50	0.35	0.36
Sn	2.64	1.90	3.30	1.52	1.37	1.34	3.12	1.16	1.70
Ge	1.95	1.44	2.11	1.44	1.53	1.63	1.50	1.36	1.63
In	0.14	0.08	0.15	0.09	0.09	0.09	0.08	0.07	0.11
Be	1.78	0.92	2.36	0.90	0.89	0.82	0.82	0.60	1.00
Co	44.53	38.02	32.92	37.55	49.88	47.72	39.97	39.12	48.99
Hf	7.95	3.84	10.28	3.81	3.86	3.68	3.43	2.82	4.84

Table S4.2: *Sr, Nd, and Pb Isotopic compositions of lava flows from central Afar sub-segments*

Sample Name	$^{87}Sr/^{86}Sr$	Err (2 sigma)	$^{143}Nd/^{144}Nd$	Err (2 sigma)	$^{206}Pb/^{204}Pb$	Err (2 sigma)
AF 13_317	0.703828	0.000008	0.512885	0.000010	18.446091	0.0011
AF 13_348	0.704160	0.000005	0.512904	0.000008	18.387475	0.0013
AF 13_351	0.703788	0.000008	0.512883	0.000006	18.460841	0.0014
AF 18_01	0.703999	0.000010	0.512908	0.000054	18.399563	0.0018
AF 23_25B	0.704248	0.000010	0.512882	0.000006	18.486171	0.0016
AF 23_30	0.703871	0.000006	0.512887	0.000008	18.460168	0.0018
AF 23_37	0.704120	0.000008	0.512842	0.000052	18.405960	0.0013
AF 23_41	0.703853	0.000005	0.512896	0.000019	18.521727	0.0014
AF 23_46	0.703811	0.000008	0.512894	0.000007	18.467464	0.0014
AF 23_50	0.703821	0.000012	0.512910	0.000021	18.454163	0.0013
AF 23_97B	0.704201	0.000011	0.512905	0.000006	18.220266	0.0009
AF 23_110	0.703726	0.000008	0.512893	0.000006	18.408254	0.0012
AF 23_115	0.703664	0.000008	0.512901	0.000008	18.510555	0.0015
AF 23_118	0.703686	0.000006	0.512883	0.000012	18.501169	0.0009
AF 23_128	0.704282	0.000008	0.512882	0.000019	18.505709	0.0014
AF 23_137B	0.703870	0.000008	0.512893	0.000008	18.456132	0.0010
AF 23_147	0.703677	0.000008	0.512897	0.000010	18.569918	0.0011
AF 23_161	0.703750	0.000011	0.512922	0.000015	18.515673	0.0014
AF 23_168	0.703904	0.000008	0.512911	0.000020	18.222043	0.0029
AF 23_170	0.703856	0.000008	0.512855	0.000026	18.331229	0.0017
AF 23_175	0.703974	0.000010	0.512892	0.000016	18.441405	0.0010
AF 23_176	0.704089	0.000008	0.512902	0.000019	18.168146	0.0015

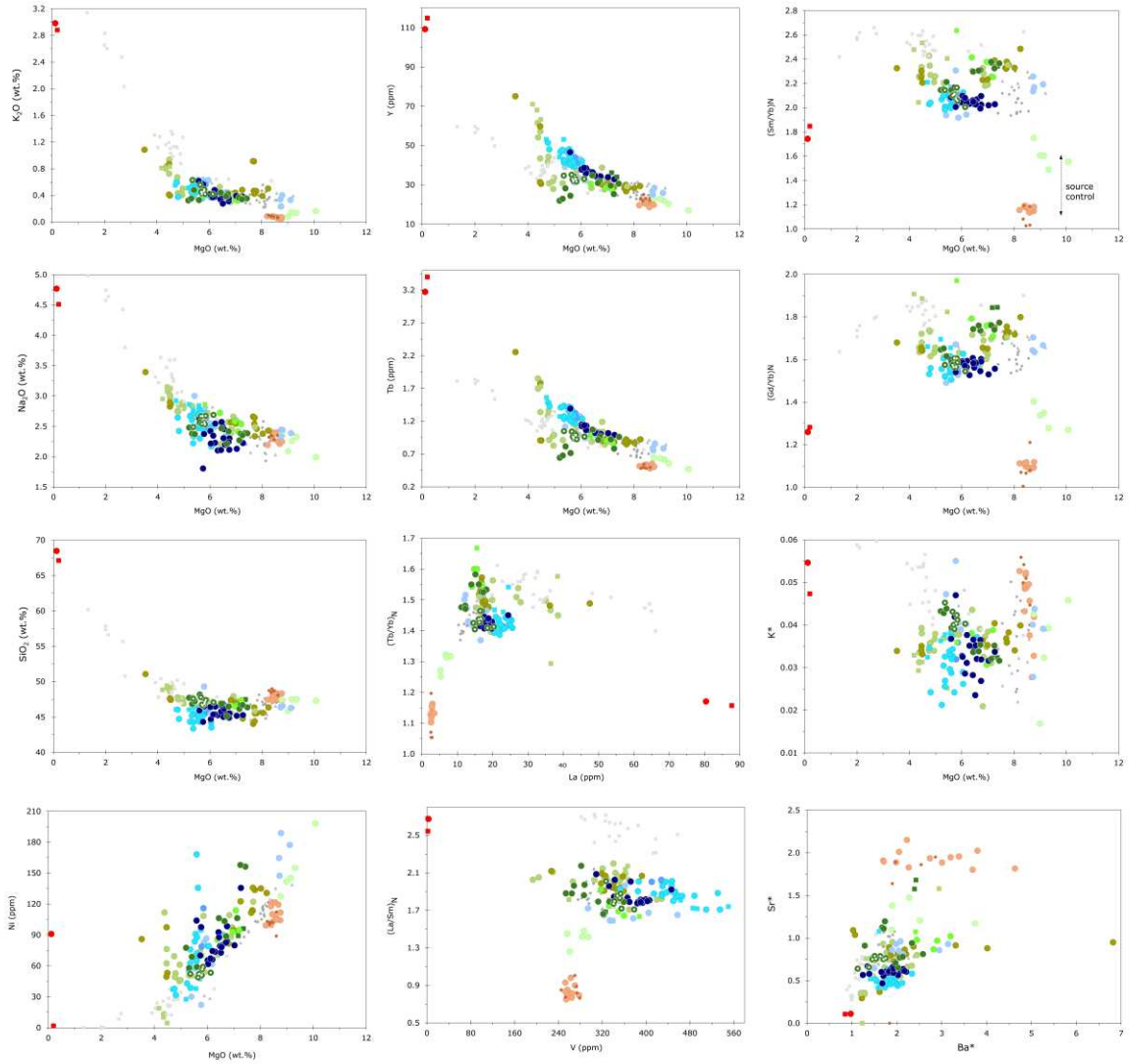

Figure S4.1: *Major and trace elements variations of the central Afar lava series in the binary diagrams. The legend is same as for the Figure 4.7*

Appendix IV (Chapter 5)

Table S5.1: *Major (in wt.%) and trace element (in ppm) concentrations in bulk rock samples after corrections for Plageoclase accumulation. Analysis performed at Service d'Analyse des Roches et des Minéraux (SARM-CRPG, Nancy, France).*

Sample ID	22DJ01	22DJ02	22DJ03	22DJ04	22DJ05	22DJ06	22DJ07	22DJ09	22DJ11	22DJ15	22DJ18	22DJ21	22DJ23
Latitude (°N)	11.623	11.622	11.621	11.619	11.618	11.616	11.616	11.612	11.608	11.581	11.568	11.627	11.628
Longitude (°E)	42.464	42.465	42.467	42.470	42.470	42.471	42.471	42.479	42.482	42.502	42.506	42.436	42.439
SiO_2	48.21	47.98	47.12	47.39	47.69	46.39	48.06	47.27	48.06	47.79	47.49	46.31	47.64
Al_2O_3	12.88	13.27	12.86	12.39	12.92	15.28	14.98	15.40	15.11	14.65	13.60	14.83	13.61
Fe_2O_3	15.38	13.92	13.62	13.57	13.84	11.99	13.31	12.59	13.40	12.66	13.39	11.70	12.95
MnO	0.24	0.22	0.21	0.21	0.22	0.20	0.21	0.19	0.22	0.19	0.21	0.18	0.20
MgO	5.98	7.01	8.48	8.75	7.87	5.94	6.14	7.34	5.76	7.06	6.10	7.18	7.70
CaO	9.83	10.89	11.86	12.26	11.63	12.41	11.20	12.14	11.09	11.88	11.53	12.54	12.27
Na_2O	3.07	2.90	2.59	2.52	2.70	2.61	2.94	2.75	3.01	2.68	2.79	2.45	2.62
K_2O	0.45	0.35	0.27	0.25	0.30	0.46	0.42	0.33	0.49	0.34	0.41	0.34	0.31
TiO_2	2.72	2.22	2.01	2.06	2.13	2.21	2.49	2.04	2.55	2.09	2.57	1.88	2.09
P_2O_5	0.35	0.24	0.22	0.22	0.25	0.33	0.36	0.26	0.40	0.26	0.35	0.21	0.24
Total	97.60	97.62	97.88	98.28	98.17	97.84	100.11	100.30	100.09	99.60	98.43	97.62	99.63
Rb	8.77	7.39	5.82	5.54	6.08	10.68	7.52	5.72	9.54	5.91	6.96	6.01	5.76
Ba	123.41	105.46	81.08	78.89	87.81	152.10	116.78	90.76	134.02	90.10	408.78	92.18	99.01
Th	1.34	1.15	0.89	0.84	0.95	1.53	1.14	0.84	1.36	0.88	1.16	0.95	0.96
U	0.36	0.31	0.24	0.23	0.25	0.60	0.33	0.27	0.42	0.25	0.36	0.29	0.27
Nb	18.35	14.90	11.37	11.12	12.14	16.49	17.31	12.50	18.11	12.40	15.74	10.91	11.29
Ta	1.39	1.10	0.86	0.85	0.94	1.32	1.39	1.03	1.47	1.02	1.30	0.91	0.95
La	15.64	12.81	9.75	9.52	10.60	15.46	14.72	11.02	16.08	10.93	14.17	10.04	10.51
Ce	37.42	30.53	23.82	23.44	25.78	34.88	34.15	25.52	36.77	25.13	32.25	22.80	24.17
Pb	1.61	1.71	1.74	1.84	1.39	3.78	1.29	3.92	2.83	3.06	1.73	1.63	2.11
Pr	4.96	4.11	3.19	3.14	3.49	4.80	4.79	3.63	5.11	3.53	4.53	3.21	3.42
Sr	250.07	244.99	190.76	188.16	202.52	302.47	281.39	266.35	279.75	277.21	301.61	272.81	261.05
Nd	23.02	18.91	15.02	15.00	16.19	21.50	21.88	16.83	23.32	16.52	20.65	14.78	15.81
Sm	5.95	5.05	4.13	4.04	4.34	5.30	5.61	4.33	5.85	4.29	5.33	3.86	4.18
Zr	165.68	137.70	110.40	106.18	117.10	142.77	147.30	121.35	159.58	116.49	143.63	100.11	105.85
Eu	2.07	1.78	1.47	1.50	1.58	1.81	1.95	1.59	1.99	1.56	1.84	1.41	1.50
Gd	6.25	5.26	4.38	4.26	4.65	5.60	5.97	4.69	6.06	4.64	5.56	4.08	4.43
Dy	6.83	5.83	4.94	4.83	5.14	5.78	6.09	4.96	6.35	4.88	5.77	4.28	4.72
Y	37.79	32.64	27.34	26.55	29.04	30.94	32.77	26.49	34.03	26.28	30.65	22.64	25.10
Ho	1.45	1.25	1.05	1.04	1.11	1.20	1.28	1.04	1.33	1.02	1.20	0.90	0.98
Yb	3.59	3.08	2.58	2.52	2.77	2.85	3.10	2.53	3.25	2.49	2.88	2.17	2.36
Tb	1.06	0.91	0.76	0.75	0.80	0.91	0.98	0.78	1.01	0.77	0.92	0.68	0.74
Er	3.87	3.36	2.85	2.77	2.97	3.19	3.45	2.78	3.52	2.72	3.15	2.38	2.62
Tm	0.57	0.48	0.41	0.40	0.44	0.46	0.50	0.40	0.51	0.40	0.46	0.35	0.38
Lu	0.55	0.47	0.39	0.39	0.42	0.44	0.47	0.39	0.50	0.38	0.43	0.33	0.36
Ni	44.90	66.13	87.89	93.51	75.71	60.19	57.81	90.07	64.38	90.45	59.67	73.27	83.96

Table S5.1 continued

Cr	58.90	112.43	176.08	227.51	141.74	125.56	123.94	187.50	136.50	223.06	123.89	233.94	269.12
V	390.39	358.17	348.61	354.08	349.34	301.88	342.61	317.66	337.67	324.38	359.17	294.21	334.12
Ga	27.18	29.79	34.39	33.43	32.72	22.58	23.40	29.78	24.86	20.70	19.27	25.97	21.51
Cu	142.19	149.98	159.26	162.51	155.86	102.60	120.31	131.14	110.59	160.22	146.38	158.21	164.11
Zn	139.26	122.91	112.88	111.04	116.15	109.09	117.99	96.02	109.79	95.42	104.87	87.22	92.90
Cs	0.10	0.11	0.09	0.10	0.09	0.28	0.09	0.07	0.17	0.09	0.11	0.16	0.12
Sc	42.14	43.64	50.05	51.39	49.03	35.75	40.61	41.81	37.96	42.47	42.05	42.28	48.13
As	0.39					0.98	0.00	0.00	0.62	0.00	0.00	0.00	0.00
Mo	1.00	0.89	0.76	0.76	0.75	0.95	1.17	0.87	1.24	0.92	0.97	0.74	0.83
Cd	0.15	0.16	0.15	0.14	0.12	0.18	0.13	0.11	0.15	0.10	0.18	0.12	0.12
Sn	1.34	1.21				1.27	1.46	1.04	1.44	1.01	1.23	0.89	0.97
Ge	1.81	1.84	2.05	1.91	1.86	1.57	1.66	1.76	1.63	1.49	1.48	1.68	1.63
In	0.10	0.09	0.08	0.08	0.08	0.08	0.09	0.07	0.09	0.07	0.09	0.07	0.07
Be	0.93	0.79	0.67	0.64	0.68	0.84	0.90	0.67	1.01	0.68	0.84	0.65	0.67
Co	47.88	49.69	53.55	52.39	50.93	39.09	42.94	46.10	41.11	45.72	42.46	41.96	46.47
Hf	4.23	3.43	2.80	2.73	2.99	3.59	3.83	3.10	4.08	2.99	3.63	2.63	2.77
Sample ID	**22DJ25**	**22DJ26**	**22DJ31**	**22DJ32**	**22DJ34**	**22DJ37**	**22DJ42**	**22DJ44**	**22DJ46**	**22DJ48**	**22DJ51**	**22DJ53**	**22DJ54**
Latitude (°N)	**11.621**	**11.614**	**11.557**	**11.557**	**11.542**	**11.582**	**11.605**	**11.609**	**11.604**	**11.595**	**11.568**	**11.569**	**11.575**
Longitude (°E)	**42.442**	**42.444**	**42.526**	**42.526**	**42.528**	**42.519**	**42.474**	**42.466**	**42.465**	**42.491**	**42.525**	**42.526**	**42.510**
SiO_2	47.50	47.52	46.99	47.42	47.92	48.96	46.52	47.42	48.02	52.47	48.19	47.82	47.89
Al_2O_3	14.82	13.58	13.98	15.08	15.73	13.93	16.91	13.41	13.97	13.83	14.99	15.31	13.96
Fe_2O_3	11.85	13.17	12.84	12.33	12.01	14.63	9.65	13.24	13.28	14.10	13.75	13.36	13.88
MnO	0.18	0.20	0.21	0.19	0.18	0.23	0.14	0.20	0.20	0.27	0.21	0.20	0.22
MgO	6.90	7.70	7.74	7.66	6.72	4.89	9.32	7.97	6.89	3.42	5.69	5.89	5.84
CaO	12.60	12.45	12.45	12.48	12.20	9.50	13.03	12.67	12.22	7.32	10.48	11.10	10.89
Na_2O	2.41	2.67	2.50	2.59	2.72	3.50	2.05	2.66	2.67	4.45	3.23	3.06	2.87
K_2O	0.35	0.31	0.31	0.31	0.36	0.66	0.24	0.30	0.35	0.94	0.51	0.47	0.52
TiO_2	1.91	2.12	2.04	1.92	2.02	3.12	1.23	2.09	2.26	2.75	2.78	2.60	2.67
P_2O_5	0.22	0.23	0.28	0.26	0.30	0.57	0.15	0.23	0.26	0.87	0.43	0.39	0.38
Total	98.75	99.96	99.34	100.24	100.16	99.99	99.24	100.20	100.12	100.42	100.27	100.21	99.12
Rb	7.61	5.50	5.86	5.75	6.13	11.93	4.75	5.08	6.23	16.92	8.82	8.12	10.27
Ba	101.23	85.96	120.82	88.86	94.91	167.08	64.22	88.89	95.91	224.84	129.42	120.73	141.37
Th	1.05	0.79	0.94	0.84	0.90	1.75	0.64	0.76	0.92	2.45	1.28	1.19	1.51
U	0.30	0.22	0.30	0.24	0.25	0.48	0.19	0.28	0.25	0.67	0.35	0.33	0.45
Nb	11.35	11.42	12.90	11.99	13.72	26.90	7.79	10.95	12.47	35.07	19.54	17.61	18.11
Ta	0.92	0.93	1.03	0.97	1.11	2.10	0.62	0.91	1.03	2.77	1.58	1.42	1.46
La	10.63	10.07	12.44	10.92	12.13	22.26	7.32	9.80	11.17	30.68	16.54	15.25	16.53
Ce	24.18	23.43	28.41	25.35	28.29	51.75	16.84	22.77	25.62	73.00	38.26	35.03	37.57
Pb	1.47	2.60	3.57	1.34	1.05	1.55	1.12	1.22	1.47	2.26	1.32	2.62	2.45
Pr	3.40	3.36	4.01	3.55	3.96	7.08	2.34	3.26	3.64	9.74	5.33	4.85	5.18
Sr	274.00	252.72	245.23	244.72	261.61	283.07	238.90	253.86	273.23	295.81	278.07	269.98	277.11
Nd	15.34	15.51	18.20	16.42	17.84	32.15	10.82	15.16	16.87	44.10	24.44	22.06	23.20
Sm	3.98	4.10	4.75	4.30	4.74	8.03	2.82	4.08	4.45	10.81	6.11	5.62	5.86

Table S5.1 continued

Zr	102.77	102.14	121.93	114.88	125.46	232.31	76.68	100.91	114.45	322.65	173.79	158.26	164.42
Eu	1.42	1.51	1.65	1.52	1.64	2.53	1.03	1.52	1.60	3.42	2.05	1.91	1.97
Gd	4.14	4.38	4.93	4.59	4.91	8.16	3.02	4.32	4.73	11.13	6.44	5.93	6.10
Dy	4.33	4.59	5.19	4.84	5.17	8.41	3.22	4.64	5.01	11.48	6.67	6.08	6.27
Y	23.68	24.96	28.53	26.15	27.88	45.83	17.62	24.55	26.74	61.35	35.39	32.90	34.25
Ho	0.91	0.96	1.09	1.01	1.08	1.75	0.67	0.97	1.05	2.41	1.40	1.29	1.32
Yb	2.23	2.31	2.64	2.48	2.67	4.32	1.64	2.31	2.53	5.78	3.38	3.12	3.20
Tb	0.70	0.73	0.83	0.76	0.82	1.36	0.51	0.73	0.79	1.83	1.05	0.96	1.00
Er	2.40	2.56	2.88	2.68	2.89	4.71	1.81	2.58	2.77	6.35	3.71	3.37	3.52
Tm	0.36	0.37	0.42	0.40	0.43	0.68	0.26	0.37	0.40	0.92	0.54	0.49	0.51
Lu	0.34	0.35	0.40	0.38	0.40	0.65	0.25	0.35	0.38	0.88	0.51	0.47	0.49
Ni	74.00	79.23	79.62	83.18	77.06	142.18	152.11	82.22	63.89	94.93	62.86	61.73	173.05
Cr	244.95	263.75	199.05	207.70	198.08	319.57	387.28	281.36	204.40	226.74	112.06	114.37	394.81
V	304.00	343.86	317.98	307.41	298.61	376.14	210.53	338.19	343.51	166.46	354.60	339.36	361.80
Ga	21.50	26.59	27.23	28.73	24.18	21.99	23.90	27.77	20.29	23.90	24.45	24.86	19.76
Cu	155.16	161.62	140.74	144.09	126.09	97.39	100.56	177.22	174.97	19.02	113.08	116.02	138.61
Zn	87.70	93.81	99.14	91.91	92.15	127.58	70.41	94.50	99.02	147.33	111.37	106.82	111.59
Cs	0.20	0.11	0.16	0.14	0.13	0.16	0.15	0.10	0.12	0.20	0.12	0.12	0.24
Sc	43.32	48.76	46.03	44.71	41.52	37.92	36.20	49.81	47.25	26.81	39.44	39.05	41.29
As	0.00	0.00	0.00	0.00	0.00	0.00	0.00	0.00	0.00	0.65	0.00	0.00	0.85
Mo	0.76	0.79	0.75	0.00	0.96	3.23	0.00	0.80	0.75	3.14	1.29	1.14	2.97
Cd	0.14	0.10	0.13	0.15	0.10	0.15	0.08	0.10	0.12	0.17	0.14	0.15	0.18
Sn	0.95	0.96	1.15	1.08	1.04	1.85	0.67	0.92	0.99	2.49	1.45	1.30	1.46
Ge	1.54	1.75	1.79	1.82	1.62	1.70	1.47	1.80	1.50	1.85	1.62	1.61	1.53
In	0.07	0.08	0.08	0.07	0.07	0.11	0.05	0.07	0.08	0.13	0.09	0.09	0.09
Be	0.63	0.62	0.67	0.70	0.74	1.22	0.50	0.69	0.64	1.70	0.99	0.93	0.97
Co	42.90	47.87	47.77	46.04	41.69	41.12	44.69	47.91	45.09	27.66	39.98	40.02	44.52
Hf	2.67	2.61	3.02	2.91	3.12	5.62	1.94	2.65	2.94	7.44	4.33	3.88	4.09
Sample ID	**22DJ55**	**22DJ59**	**22DJ61**	**22DJ63**	**22DJ65**	**22DJ66**	**22DJ68**						
Latitude (°N)	**11.575**	**11.594**	**11.595**	**11.596**	**11.589**	**11.589**	**11.590**						
Longitude (°E)	**42.510**	**42.464**	**42.467**	**42.471**	**42.477**	**42.477**	**42.481**						
SiO_2	48.43	46.27	48.16	47.78	45.10	46.73	48.15						
Al_2O_3	14.07	14.54	13.80	14.55	15.57	14.05	13.89						
Fe_2O_3	14.25	13.32	13.20	12.65	10.20	12.47	14.06						
MnO	0.22	0.20	0.20	0.19	0.17	0.19	0.22						
MgO	5.84	7.58	6.98	7.31	7.29	8.93	5.74						
CaO	10.74	11.88	12.27	12.52	14.42	13.37	10.38						
Na_2O	3.15	2.86	2.68	2.56	2.06	2.48	3.17						
K_2O	0.49	0.32	0.35	0.33	0.33	0.26	0.52						
TiO_2	2.76	2.15	2.24	2.05	1.46	1.77	2.82						
P_2O_5	0.39	0.25	0.26	0.24	0.20	0.22	0.41						
Total	100.32	99.36	100.13	100.18	96.79	100.48	99.35						
Rb	8.29	5.65	6.27	6.50	9.07	4.35	9.36						

Table S5.1 continued

Ba	120.27	90.13	100.44	97.81	167.07	76.64	133.19
Th	1.21	0.84	0.90	0.94	1.36	0.68	1.36
U	0.33	0.25	0.26	0.28	0.48	0.31	0.39
Nb	18.34	12.33	12.94	11.60	10.17	10.26	19.42
Ta	1.44	1.00	1.04	0.94	0.81	0.81	1.54
La	15.37	10.83	11.26	10.64	11.65	9.40	16.46
Ce	35.40	24.96	25.94	24.22	25.12	21.59	37.75
Pb	4.02	1.04	1.39	2.92	3.45	2.67	4.86
Pr	5.02	3.58	3.70	3.44	3.48	3.10	5.28
Sr	278.79	244.06	291.65	291.71	268.15	227.14	281.79
Nd	22.95	16.37	17.10	15.80	15.29	14.42	24.05
Sm	5.85	4.30	4.46	4.16	3.78	3.78	6.12
Zr	159.55	112.01	114.58	105.46	98.19	102.25	173.18
Eu	1.96	1.60	1.62	1.50	1.29	1.43	2.07
Gd	6.02	4.62	4.79	4.35	3.97	4.14	6.34
Dy	6.36	4.96	5.11	4.63	4.17	4.52	6.72
Y	34.32	26.43	27.22	25.26	22.56	24.52	36.23
Ho	1.34	1.06	1.06	0.96	0.87	0.96	1.40
Yb	3.19	2.52	2.54	2.32	2.11	2.29	3.39
Tb	1.00	0.77	0.79	0.72	0.66	0.70	1.05
Er	3.52	2.74	2.80	2.51	2.31	2.51	3.69
Tm	0.51	0.40	0.41	0.37	0.34	0.37	0.54
Lu	0.49	0.37	0.39	0.35	0.32	0.35	0.51
Ni	123.03	95.19	82.82	82.67	76.04	95.12	60.88
Cr	273.20	228.57	249.02	260.51	195.62	254.29	119.12
V	387.78	346.10	354.70	325.28	243.87	305.69	380.58
Ga	20.61	35.57	19.26	24.29	26.38	34.99	20.59
Cu	146.90	178.32	186.44	177.86	112.90	163.66	143.33
Zn	113.51	100.70	101.23	93.19	79.78	90.17	113.77
Cs	0.11	0.09	0.09	0.14	0.37	0.07	0.14
Sc	42.81	45.12	47.22	46.91	39.21	50.24	42.00
As	0.00	0.00	0.00	0.00	1.21	0.00	0.00
Mo	2.35	1.09	1.03	0.85	0.00	0.00	1.25
Cd	0.16	0.18	0.13	0.14	0.18	0.09	0.08
Sn	1.41	1.06	1.06	0.98	0.92	1.14	1.56
Ge	1.52	1.92	1.52	1.59	1.68	1.92	1.55
In	0.10	0.08	0.08	0.07	0.07	0.07	0.09
Be	0.93	0.79	0.71	0.68	0.66	0.61	0.97
Co	44.10	48.28	46.37	45.68	40.00	48.90	41.71
Hf	3.97	2.90	2.96	2.74	2.52	2.54	4.26

Table S5.2: *Concentrations of the ^{36}Cl target elements, measured in splits taken from the samples after the chemical pre-treatment. Analysis performed at the SARM-CRPG, Nancy, France.*

Samples	SiO_2 (%)	Al_2O_3 (%)	Fe2O3 (%)	MnO (%)	MgO (%)	CaO (%)	Na_2O (%)	K_2O (%)	TiO_2 (%)	P_2O_5 (%)	LOI
22DJ08	51.19±1.01	28.88±0.58	0.53±0.01		0.18±0.04	15.16±0.30	1.59±0.16		0.034±0.020		1.77
22DJ14	50.55±1.01	28.28±0.57	1.10±0.02		0.61±0.09	15.20±0.30	1.65±0.17	0.04±0.03	0.14±0.03		1.78
22DJ18	52.69±1.01	11.71±0.23	12.43±0.25	0.19±0.04	4.86±0.49	10.18±0.20	2.49±0.25	0.40±0.10	2.94±0.29	0.17±0.10	0.95
22DJ20	51.63±1.01	28.78±0.58	0.60±0.01		0.20±0.04	15.01±0.30	1.61±0.16		0.043±0.020		1.84
22DJ22	52.20±1.01	28.34±0.57	0.61±0.01		0.20±0.04	14.76±0.30	1.61±0.16		0.046±0.020		2.01
22DJ24	53.90±1.01	27.18±0.54	0.53±0.01		0.16±0.03	14.19±0.28	1.52±0.15		0.035±0.020		2.36
22DJ27	52.26±1.01	27.63±0.55	0.90±0.02		0.36±0.07	14.67±0.29	1.60±0.16	0.03±0.03	0.11±0.03		2.38
22DJ31	53.01±1.01	27.63±0.55	0.48±0.01		0.18±0.04	14.45±0.29	1.48±0.15		0.028±0.020		1.93
22DJ47	55.39±1.11	14.31±0.29	11.02±0.22	0.20±0.04	2.31±0.23	7.11±0.36	4.42±0.44	0.87±0.17	2.82±0.28	0.60±0.09	0.00
22DJ50	50.59±1.01	20.13±0.40	7.57±0.15	0.11±0.023	3.05±0.31	12.17±0.24	2.35±0.24	0.30±0.03	1.61±0.16	0.23±0.10	0.87
22DJ62	50.64±1.01	24.56±0.49	3.54±0.07	0.048±0.015	2.00±0.20	14.36±0.29	1.88±0.19	0.09±0.02	0.57±0.11		1.11
22DJ65	53.50±1.01	26.84±0.54	0.50±0.01		0.20±0.04	14.13±0.28	1.43±0.14		0.032±0.020		2.34

Table S5.3: *Interpolated ages for the Lava surface samples at the Asal-Ghoubbet rift segment.*

Sample Name	Volcanic centres	Lava morphology and petrology	Interpolated ages (ka)
22DJ06	Axial chain	Pahoehoe, Porphyritic	3.5
22DJ10	Axial chain	A'a, Porphyritic	2.8
22DJ33	Ghoubbet	Pahoehoe, Porphyritic	3.5
22DJ36	Armae Koma	A'a, Aphyric	2.6
22DJ41	Axial chain	A'a, Porphyritic	2.8
22DJ43	Manda area	A'a, Porphyritic	2.25
22DJ45	Manda	Pahoehoe, Porphyritic	2.2
22DJ52	Ghoubbet	Pahoehoe, Porphyritic	2.2
22DJ54	Armae Koma	Pahoehoe, Porphyritic	2.6
22DJ58	Manda	Pahoehoe, Porphyritic	2.15
22DJ60	Manda	Pahoehoe, Porphyritic	2.17
22DJ67	Secondary Chain	A'a, Aphyric	2.4

Table S5.4: *Bulk rock composition of the Aphyric lava flows of the axial zone of Asal rift and olivine-hosted melt inclusions.*

Sample ID	Petrology	Correction	SiO2	TiO2	Al2O3	Fe2O3	FeO	MnO	MgO	CaO	Na2O	K2O	P2O5	Cr_2O_3	H2O	FeOt	Total	T_°C	Fo
22DJ18	aphyric	none	47.49	2.57	13.60	13.39		0.21	6.10	11.53	2.79	0.41	0.35			12.06	97.10		
22DJ37	aphyric	none	48.96	3.12	13.93	14.63		0.23	4.89	9.50	3.50	0.66	0.57			13.18	98.54		
22DJ48	aphyric	none	52.47	2.75	13.83	14.10		0.27	3.42	7.32	4.45	0.94	0.87			12.70	99.02		
22DJ55	aphyric	none	48.43	2.76	14.07	14.25		0.22	5.84	10.74	3.15	0.49	0.39			12.83	98.91		
22DJ68	aphyric	none	48.15	2.82	13.89	14.06		0.22	5.74	10.38	3.17	0.52	0.41			12.66	97.96		
22DJ03	MI-ol	Petrolog3	50.89	3.37	14.87	2.24	8.78	0.18	3.51	10.52	3.90	0.43	0.32	0.00	1.01	10.80	98.77	1060.00	70.25
22DJ03	MI-ol	Petrolog3	50.89	3.37	14.87	2.24	8.78	0.18	3.51	10.52	3.90	0.43	0.32	0.00	1.01	10.80	98.77	1060.00	70.25
22DJ03	MI-ol	Petrolog3	50.87	3.37	14.86	2.24	8.78	0.18	3.51	10.51	3.90	0.43	0.32	0.00	1.03	10.80	98.75	1060.00	70.25
22DJ04	MI-ol	Petrolog3	48.19	1.65	14.52	1.18	9.34	0.11	8.78	13.04	2.16	0.24	0.23	0.00	0.57	10.40	99.32	1208.00	84.60
22DJ04	MI-ol	Petrolog3	48.19	1.65	14.52	1.18	9.34	0.11	8.78	13.04	2.16	0.24	0.23	0.00	0.57	10.40	99.32	1208.00	84.60
22DJ04	MI-ol	Petrolog3	48.80	1.22	14.47	1.14	9.38	0.17	9.00	12.82	2.17	0.15	0.09	0.00	0.58	10.41	99.31	1214.00	84.87
22DJ04	MI-ol	Petrolog3	48.81	1.22	14.47	1.14	9.38	0.17	9.00	12.82	2.17	0.15	0.09	0.00	0.57	10.41	99.32	1214.00	84.87
22DJ04	MI-ol	Petrolog3	48.77	1.25	14.30	1.16	9.37	0.19	8.99	13.00	2.21	0.13	0.07	0.00	0.58	10.41	99.31	1213.00	84.87
22DJ03	MI-ol	Petrolog3	50.21	2.17	13.75	1.47	9.50	0.17	6.72	11.97	2.99	0.37	0.21	0.00	0.48	10.81	99.38	1163.00	80.61
22DJ01	MI-ol	Petrolog3	49.42	2.81	13.60	2.33	11.31	0.14	5.08	10.47	3.13	0.38	0.31	0.00	1.01	13.41	98.75	1129.00	72.56
22DJ01	MI-ol	Petrolog3	49.60	2.92	13.86	2.39	11.32	0.20	5.09	10.26	3.33	0.46	0.37	0.00	0.21	13.47	99.55	1131.00	72.56
22DJ04	MI-ol	Petrolog3	48.74	1.27	14.63	1.15	9.37	0.13	8.74	13.01	2.20	0.18	0.12	0.00	0.46	10.41	99.42	1207.00	84.51
22DJ01	MI-ol	Petrolog3	49.28	2.64	13.67	2.23	11.41	0.14	5.44	10.21	3.32	0.38	0.28	0.00	1.00	13.42	98.78	1144.00	73.71
22DJ01	MI-ol	Petrolog3	49.31	2.64	13.68	2.23	11.40	0.14	5.44	10.22	3.32	0.38	0.28	0.00	0.98	13.41	98.80	1144.00	73.71
22DJ01	MI-ol	Petrolog3	49.31	2.64	13.68	2.23	11.40	0.14	5.44	10.22	3.32	0.38	0.28	0.00	0.97	13.41	98.81	1144.00	73.71
22DJ01	MI-ol	Petrolog3	49.22	2.66	13.93	2.23	11.41	0.17	5.32	10.19	3.21	0.40	0.29	0.00	1.00	13.42	98.78	1139.00	73.28
22DJ01	MI-ol	Petrolog3	49.24	2.66	13.94	2.23	11.40	0.17	5.32	10.20	3.21	0.40	0.29	0.00	0.96	13.41	98.82	1139.00	73.28
22DJ01	MI-ol	Petrolog3	49.46	2.60	13.63	2.25	11.38	0.21	5.30	10.17	3.31	0.38	0.32	0.00	0.99	13.41	98.79	1140.00	73.26
22DJ01	MI-ol	Petrolog3	49.27	2.71	13.62	2.23	11.39	0.23	5.43	10.12	3.27	0.39	0.27	0.00	1.07	13.40	98.70	1144.00	73.71
22DJ01	MI-ol	Petrolog3	49.25	2.71	13.61	2.24	11.41	0.23	5.44	10.11	3.26	0.39	0.27	0.00	1.10	13.42	98.68	1144.00	73.71
22DJ01	MI-ol	Petrolog3	49.25	2.65	13.72	2.31	11.33	0.23	5.08	10.50	3.19	0.39	0.24	0.00	1.11	13.42	98.66	1130.00	72.52
22DJ01	MI-ol	Petrolog3	49.26	2.65	13.72	2.31	11.33	0.23	5.08	10.50	3.19	0.39	0.24	0.00	1.10	13.42	98.67	1130.00	72.52
22DJ03	MI-ol	Petrolog3	48.13	1.27	14.52	1.21	9.72	0.23	9.35	12.13	2.19	0.27	0.40	0.00	0.59	10.80	99.29	1230.00	84.89
22DJ03	MI-ol	Petrolog3	48.14	1.27	14.52	1.21	9.72	0.23	9.35	12.13	2.19	0.27	0.40	0.00	0.58	10.80	99.30	1230.00	84.89
22DJ03	MI-ol	Petrolog3	49.12	2.00	13.88	1.29	9.64	0.21	9.23	10.75	2.91	0.38	0.20	0.00	0.40	10.81	99.47	1236.00	84.83
22DJ01	MI-ol	Petrolog3	48.44	2.25	13.51	1.92	11.71	0.22	6.74	10.80	2.82	0.29	0.28	0.00	1.03	13.44	98.78	1178.00	77.15
22DJ03	MI-ol	Petrolog3	49.83	2.10	14.34	1.38	9.56	0.20	7.04	11.85	2.79	0.35	0.16	0.00	0.38	10.81	99.48	1170.00	81.19
22DJ03	MI-ol	Petrolog3	49.99	2.23	13.44	1.46	9.52	0.17	7.01	12.55	2.79	0.32	0.19	0.00	0.33	10.83	99.52	1167.00	81.19
22DJ03	MI-ol	Petrolog3	50.23	2.40	13.82	1.43	9.52	0.23	7.00	11.55	2.87	0.35	0.22	0.00	0.39	10.81	99.46	1171.00	81.18
22DJ01	MI-ol	Petrolog3	48.90	2.57	13.50	2.21	11.56	0.22	5.61	10.70	3.00	0.37	0.27	0.00	1.11	13.54	98.67	1146.00	74.05
22DJ01	MI-ol	Petrolog3	49.03	2.51	13.53	2.18	11.55	0.21	5.58	10.69	2.98	0.33	0.29	0.00	1.12	13.52	98.66	1145.00	73.96
22DJ01	MI-ol	Petrolog3	49.74	3.10	13.06	2.37	11.28	0.24	5.31	10.19	3.21	0.43	0.30	0.00	0.79	13.41	98.98	1138.00	73.45
22DJ01	MI-ol	Petrolog3	49.66	3.08	12.98	2.34	11.39	0.24	5.50	10.13	3.19	0.43	0.30	0.00	0.78	13.49	98.99	1145.00	73.94
22DJ03	MI-ol	Petrolog3	49.71	2.04	14.35	1.40	9.55	0.20	7.12	11.54	3.05	0.36	0.23	0.00	0.45	10.81	99.41	1177.00	81.38
22DJ03	MI-ol	Petrolog3	49.66	1.76	14.52	1.34	9.67	0.15	7.15	11.78	2.77	0.27	0.17	0.00	0.77	10.88	99.10	1175.00	81.27
Table S5.4 continue																			
22DJ03	MI-ol	Petrolog3	49.64	1.76	14.52	1.34	9.67	0.15	7.15	11.77	2.77	0.27	0.17	0.00	0.80	10.87	99.07	1175.00	81.27
22DJ04	MI-ol	Petrolog3	48.71	1.41	14.41	1.16	9.36	0.15	8.93	12.78	2.19	0.16	0.17	0.00	0.58	10.40	99.31	1213.00	84.79
22DJ04	MI-ol	Petrolog3	48.71	1.41	14.41	1.16	9.36	0.15	8.93	12.78	2.19	0.16	0.17	0.00	0.59	10.40	99.30	1213.00	84.79
22DJ01	MI-ol	Petrolog3	49.31	2.73	13.63	2.28	11.35	0.23	5.31	10.13	3.33	0.43	0.23	0.00	1.04	13.41	98.74	1140.00	73.33

22DJ01	MI-ol	Petrolog3	49.31	2.73	13.63	2.28	11.35	0.23	5.31	10.13	3.33	0.43	0.23	0.00	1.04	13.41	98.74	1140.00	73.33
22DJ01	MI-ol	Petrolog3	49.31	2.73	13.63	2.28	11.35	0.23	5.31	10.13	3.33	0.43	0.23	0.00	1.04	13.41	98.74	1140.00	73.33
22DJ01	MI-ol	Petrolog3	49.32	2.73	13.63	2.28	11.35	0.23	5.31	10.13	3.33	0.43	0.23	0.00	1.03	13.41	98.75	1140.00	73.33
22DJ01	MI-ol	Petrolog3	49.31	2.74	13.73	2.25	11.41	0.22	5.30	9.98	3.22	0.39	0.27	0.00	1.17	13.44	98.61	1140.00	73.22
22DJ01	MI-ol	Petrolog3	49.32	2.74	13.73	2.26	11.41	0.22	5.31	9.98	3.22	0.39	0.27	0.00	1.15	13.44	98.63	1140.00	73.22
22DJ01	MI-ol	Petrolog3	49.30	2.74	13.73	2.25	11.41	0.22	5.30	9.98	3.22	0.39	0.27	0.00	1.18	13.44	98.60	1140.00	73.22
22DJ03	MI-ol	Petrolog3	50.37	2.31	13.95	1.43	9.52	0.20	7.05	11.21	3.09	0.39	0.20	0.00	0.29	10.81	99.57	1176.00	81.29
22DJ01	MI-ol	Petrolog3	49.30	3.18	12.82	2.11	11.58	0.27	6.65	9.18	3.33	0.57	0.35	0.00	0.65	13.48	99.14	1188.00	77.11
22DJ01	MI-ol	Petrolog3	49.04	3.22	12.75	2.15	11.49	0.25	6.59	9.39	3.47	0.57	0.43	0.00	0.66	13.42	99.13	1187.00	77.11
22DJ01	MI-ol	Petrolog3	49.04	3.22	12.75	2.15	11.49	0.25	6.59	9.39	3.47	0.57	0.43	0.00	0.66	13.42	99.13	1187.00	77.11
22DJ01	MI-ol	Petrolog3	49.10	3.93	11.96	2.28	11.35	0.25	6.52	9.74	3.19	0.55	0.51	0.00	0.62	13.40	99.15	1179.00	77.11
22DJ01	MI-ol	Petrolog3	49.62	2.70	13.86	2.28	11.44	0.18	5.30	10.34	3.21	0.46	0.32	0.00	0.30	13.50	99.48	1137.00	73.14
22DJ01	MI-ol	Petrolog3	49.13	2.80	13.77	2.33	11.46	0.26	5.36	10.63	3.17	0.46	0.28	0.00	0.37	13.55	99.40	1138.00	73.35
22DJ01	MI-ol	Petrolog3	49.04	2.09	13.98	1.98	11.63	0.20	6.00	10.96	2.79	0.33	0.23	0.00	0.79	13.41	99.02	1154.00	75.19
22DJ01	MI-ol	Petrolog3	49.04	2.09	13.98	1.98	11.63	0.20	6.00	10.96	2.79	0.33	0.23	0.00	0.79	13.41	99.02	1154.00	75.19
22DJ01	MI-ol	Petrolog3	49.10	2.65	13.66	2.29	11.48	0.21	5.30	10.31	3.23	0.35	0.31	0.00	1.10	13.54	98.67	1139.00	73.09
22DJ01	MI-ol	Petrolog3	49.10	2.65	13.66	2.29	11.48	0.21	5.30	10.31	3.23	0.35	0.31	0.00	1.10	13.54	98.67	1139.00	73.09
22DJ01	MI-ol	Petrolog3	49.07	2.86	13.67	2.32	11.32	0.21	5.25	10.18	3.34	0.39	0.31	0.00	1.09	13.41	98.68	1138.00	73.17
22DJ01	MI-ol	Petrolog3	49.06	2.86	13.66	2.32	11.32	0.21	5.25	10.18	3.34	0.39	0.31	0.00	1.11	13.41	98.66	1138.00	73.17
22DJ03	MI-ol	Petrolog3	50.05	2.37	14.00	1.42	9.53	0.24	7.08	11.55	2.84	0.39	0.24	0.00	0.28	10.81	99.58	1174.00	81.33
22DJ01	MI-ol	Petrolog3	49.50	3.09	12.22	2.12	11.52	0.24	6.90	9.91	3.24	0.65	0.32	0.00	0.30	13.43	99.49	1191.00	77.83
22DJ01	MI-ol	Petrolog3	49.66	2.83	14.11	2.39	11.26	0.20	4.80	10.25	3.20	0.45	0.32	0.00	0.53	13.41	99.23	1120.00	71.51
22DJ01	MI-ol	Petrolog3	49.31	2.75	13.88	2.32	11.31	0.23	5.14	10.41	3.30	0.41	0.33	0.00	0.62	13.40	99.15	1133.00	72.79
22DJ01	MI-ol	Petrolog3	49.09	2.79	14.06	2.32	11.32	0.20	5.14	10.41	3.28	0.41	0.27	0.00	0.72	13.41	99.05	1132.00	72.74
22DJ01	MI-ol	Petrolog3	50.91	3.98	12.07	2.57	11.10	0.24	5.36	9.21	3.38	0.65	0.53	0.00	0.26	13.41	99.74	1146.00	73.94
22DJ03	MI-ol	Petrolog3	50.96	2.23	14.26	1.46	9.50	0.26	6.40	11.23	3.09	0.38	0.24	0.00	0.00	10.81	99.86	1157.00	79.83
22DJ03	MI-ol	Petrolog3	51.36	2.11	14.17	1.49	9.54	0.15	6.43	10.60	3.49	0.44	0.24	0.00	0.00	10.88	99.85	1165.00	79.83
22DJ03	MI-ol	Petrolog3	50.62	2.35	14.54	1.46	9.50	0.29	6.40	11.16	3.08	0.36	0.26	0.00	0.00	10.81	99.86	1156.00	79.83
22DJ03	MI-ol	Petrolog3	51.02	2.36	13.96	1.48	9.48	0.19	6.39	11.47	2.99	0.42	0.26	0.00	0.00	10.81	99.85	1154.00	79.83
22DJ01	MI-ol	Petrolog3	50.10	2.88	13.30	2.31	11.33	0.24	5.46	10.04	3.51	0.47	0.37	0.00	0.00	13.41	99.77	1147.00	73.94
22DJ03	MI-ol	Petrolog3	50.63	2.14	14.12	1.47	9.48	0.20	6.39	11.94	3.06	0.36	0.21	0.00	0.00	10.81	99.85	1153.00	79.83
22DJ03	MI-ol	Petrolog3	50.53	2.16	13.96	1.48	9.48	0.17	6.38	12.34	2.93	0.34	0.23	0.00	0.00	10.81	99.85	1150.00	79.83
22DJ03	MI-ol	Petrolog3	50.83	2.11	13.79	1.48	9.57	0.17	6.45	12.17	2.85	0.38	0.22	0.00	0.00	10.90	99.85	1152.00	79.83

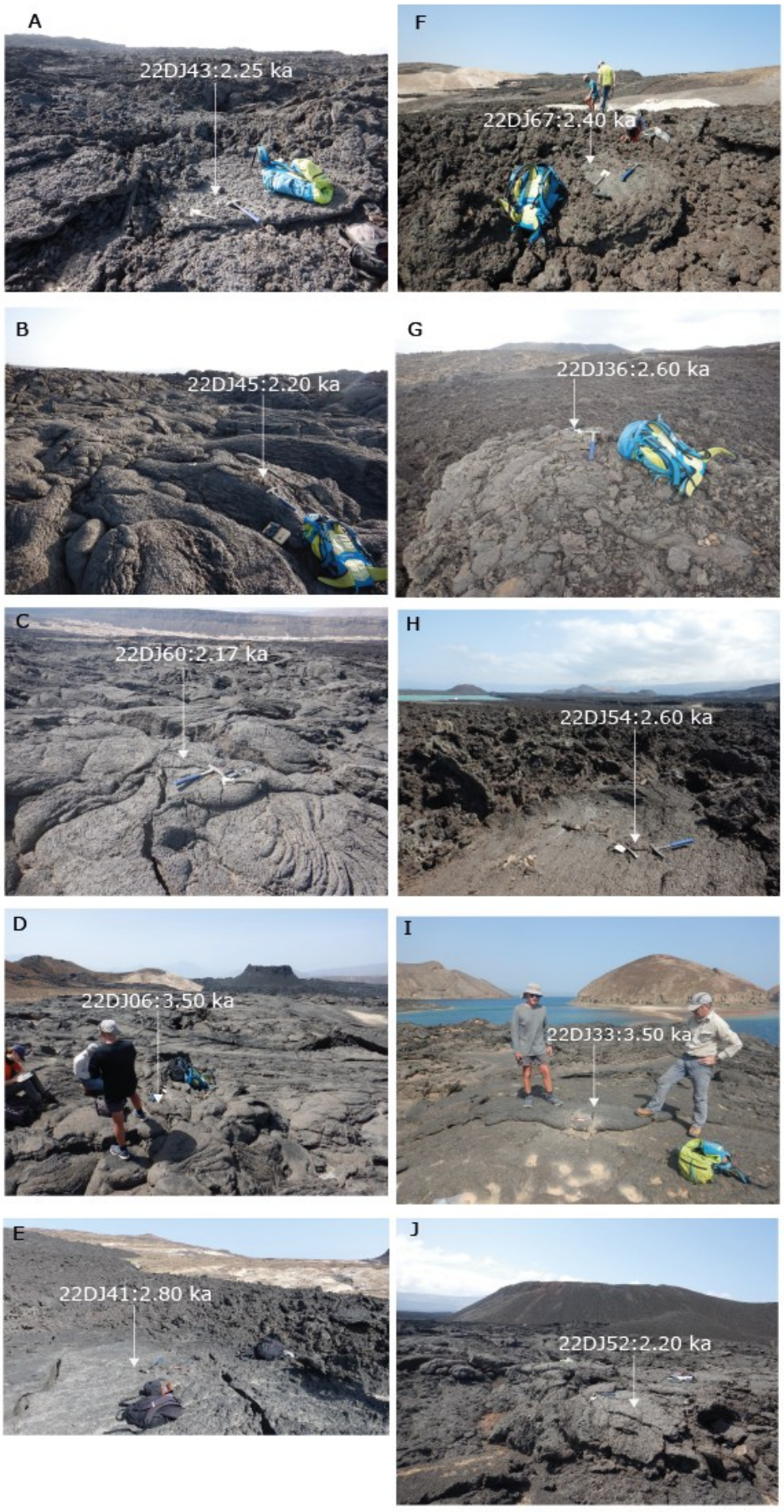
A
22DJ43:2.25 ka
F
22DJ67:2.40 ka
B
22DJ45:2.20 ka
G
22DJ36:2.60 ka
C
22DJ60:2.17 ka
H
22DJ54:2.60 ka
D
22DJ06:3.50 ka
I
22DJ33:3.50 ka
E
22DJ41:2.80 ka
J
22DJ52:2.20 ka

Figure S5.1: *Locations and field photographs of the volcanic features and ^{36}Cl CRE ages of various lava flow fields at the axial volcanic centres of the Asal-Ghoubbet rift. A'a-type lava surfaces at the Manda volcanic centre (A – C). A pahoehoe lava surface (D) and A'a-type lava surface (E) at the Axial chain volcanic centre. A'a-type lava surface at the Secondary Chain volcanic centre (F). Pahoehoe lava surface samples from the Armae Koma volcanic centre (G and H). Pahoehoe lava surface sample at the Ghoubbet volcanic centre (I). A Strombolian cone composed of scoria overlies the pahoehoe lava surface (J).*

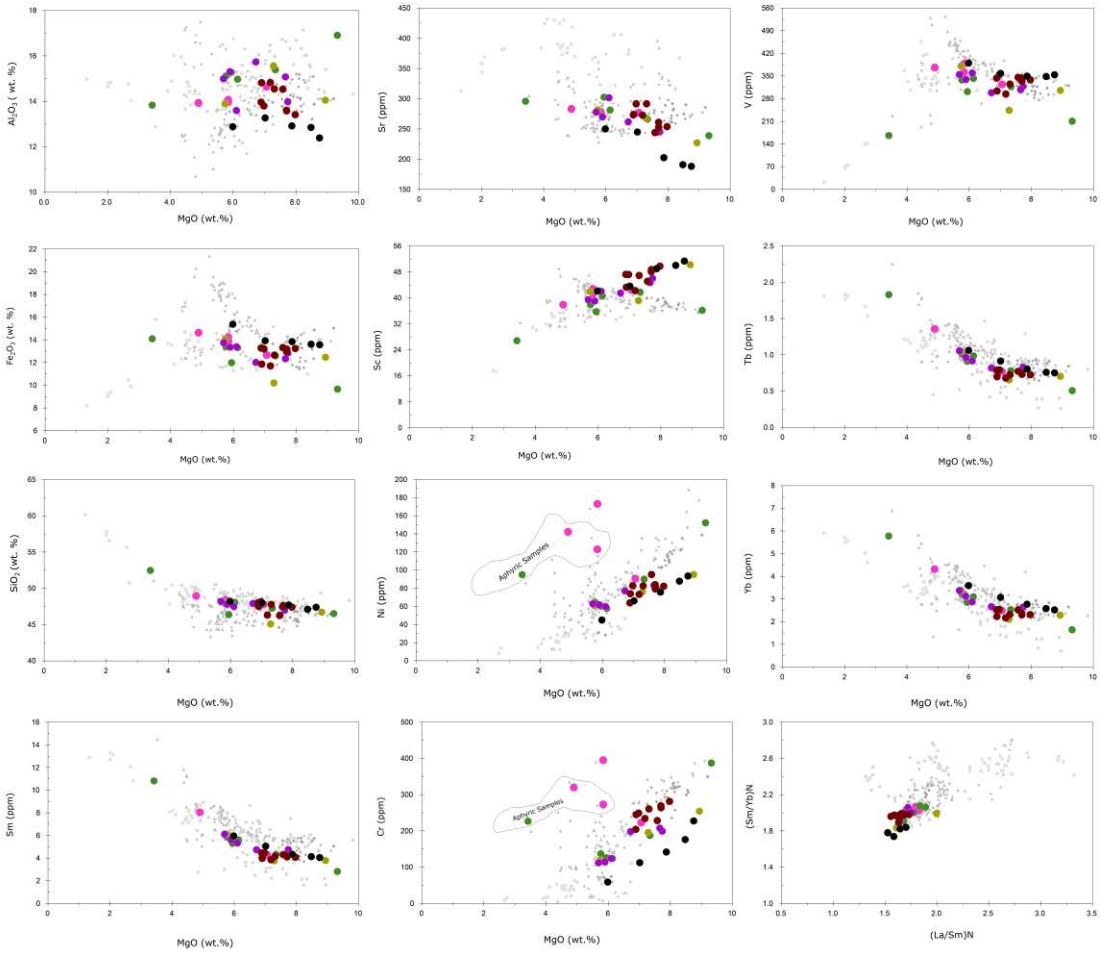

Figure S5.2: *Major and trace elements variations of the Asal-Ghoubbet lava series in the binary diagrams. The legend is same as for the Figure 5.7.*

Appendix V (Conference abstracts)

EGU23-3935, updated on 22 Feb 2023
https://doi.org/10.5194/egusphereegu233935

EGU General Assembly 2023

© Author(s) 2023. This work is distributed under the Creative Commons Attribution 4.0 License.

Detailed Architecture of the Manda Hararo Magmatic Segment in Afar, Ethiopia:

Yafet Gebrewold Birhane et al.

The Afar depression at the northern end of the East African Rift system is the only analog on earth where magmatic continental rifting and associated ongoing break-up processes are exposed onshore. This unique active system presents the key advantage to expose extensional structures related to ocean-continent transition, with magmatic rift segments characterized by contrasted morphologies, and magmato-tectonic styles. The main goal of this study is to identify the location and investigate the functioning and persistence of magma reservoirs at the active magmatic segments in the central Afar depression (Manda Hararo, northern Tendaho grabben), in order to (i) highlight their relationships and potential control with the first- and second-order local segmentation, and (ii) understand the interplay between magmatic and tectonic processes during the generation of such magmatic crust. We combine remote sensing, field investigations, precise and comprehensive mapping of volcanic and tectonic structures, cosmogenic (^{36}Cl) exposure dating of lava surfaces, and geochemical analysis to constrain the temporal frame and the dynamics of magmatic and tectonic processes. The first result of remote sensing analysis allows us to identify two active and self-consistent axial rift subsegments within this extensional system, map detailed lava flow fields which form these segment surfaces and investigate their relationships with caldera formation and focussed fissural activity. Geochemical analysis and dating of lava flow from this Manda Hararo rift system will be conducted to test the integrity of this model of contiguous subsegments.

How to cite: Birhane, Y. G., Pik, R., Bellahsen, N., France, L., Flahaut, J., Schimmelpfennig, I., Ayalew, D., and Yirgu, G.: Detailed Architecture of the Manda Hararo Magmatic Segment in Afar, Ethiopia: EGU General Assembly 2023, Vienna, Austria, 24–28 Apr 2023, EGU23-3935, https://doi.org/10.5194/egusphere-egu23-3935, 2023.

The EGU General Assembly 2024
Vienna, Austria | 14–19 April 2024

ABSTRACT

The Last Fissural Eruptions of the Manda Hararo Magmatic Segment, Central Afar (Ethiopia), Constrained from New cosmogenic Ages:

Yafet Gebrewold Birhane[1*], Raphael Pik[1], Nicolas Bellahsen[2], Irene Schimmelpfennig[3], Lydéric France[1], Simon Daout[1], Jessica Flahaut[1], Dereje Ayalew[4], and Gezahegn Yirgu[4]

[1]CRPG, CNRS, Universite´ de Lorraine, UMR 7358, Vandoeuvre-les-Nancy, France, [2]Sorbonne Universités, UPMC Université Paris 06, CNRS, Institut des Sciences de la Terre de Paris (iSTeP), Paris, France, [3]Aix-Marseille Université, CNRS, Coll France, IRD, INRAE, CEREGE, Aix en Provence, France, [4]School of Earth Sciences, Addis Ababa University, Addis Ababa, Ethiopia

Yafet.birhane@univ-lorraine.fr

The Afar depression at the northern end of the East African Rift system is presently experiencing the final stage of continental break-up and progressive onset of steady magmatic spreading. The Magmatic Rift Segments in Afar broadly analogous to those observed within the mid oceanic ridges, offer the opportunity to study both mantle and crustal processes. Investigating the crustal architecture of those magmatic segments represents a key aspect to decipher fundamental parameters that control focussing of magmatic and tectonic activity during the generation of magmatic crust. Here, we present the typical organization of a 32 km long subsegment of the Manda Hararo magmatic rift system, with fissural activities symmetrical to an apparent mid segment magmatic reservoir and establish geochronology of the last eruptive history. We combine field investigations, precise mapping of volcanological and tectonic features, cosmogenic ^{36}Cl exposure dating and geochemical analysis of lavas to constrain the temporal frame and the dynamics of magmatic processes. Our results show that the recent historical volcanic events (~ 500 to 2000 years) are sourced from calderas and fissures representing an alternating sequence of effusive and explosive (block fields) activities related to a coherent rifting episode along a single self-consistent magmatic sub-segment. Those recent fissural flows resurfaced a large portion of the segment and emplaced on older thick pahoehoe flows with a rather long lag-time of about 75 kyr separating the two episodes. Strongly contrasted geochemical signatures are also observed between those two volcanic episodes, with more differentiated and trace elements enriched basalts for the recent one, compared to the older one which are characterized by a unusual depleted signature. These new results for the Central Afar Manda Hararo rift have important implications for: (i) the local hazards along the segments, and (ii) the volcano-tectonic organization of the segment with coexistence of contrasted melt reservoirs on the underlying transcrustal plumbing system.

Theme: 1. Production of magma and assembly of volcanic plumbing systems

Session 1.3: Timing and duration of magmatic processes

Allocated presentation: Talk

New Cosmogenic Exposure Dating of Fissural Volcanic Episodes in Afar: Implications for Magmatic Processes and Plumbing System Organisation

Yafet Gebrewold Birhane*[1,7], Raphael Pik[1], Nicolas Bellahsen[2], Irene Schimmelpfennig[3], Lydéric France[1,4], Juliette Pin[1,5], Dereje Ayalew[6], and Gezahegn Yirgu[6]

[1]CRPG, CNRS, Universite´ de Lorraine, UMR 7358, Vandoeuvre-les-Nancy, France, [2]Sorbonne Universités, UPMC Université Paris 0C, CNRS, Institut des Sciences de la Terre de Paris (iSTeP), Paris, France, [3]Aix-Marseille Université, CNRS, Coll France, IRD, INRAE, CEREGE, Aix en Provence, France, [4]France, Institut Universitaire de France (IUF), [5]Laboratoire Géo-Océan (LGO), Institut Universitaire Européen de la Mer (IUEM), Université de Bretagne Occidentale (UBO), Brest, [C]School of Earth Sciences, Addis Ababa University, Addis Ababa, Ethiopia, [7]Department of Geology, College of Natural and Computational Sciences, Hawassa University, Ethiopia

*Yafet.yy@gmail.com

Divergent plate boundaries offer prime sites to study crustal extension and volcanic processes. The Afar depression, where active continental break-up and the transition from continental to oceanic rifting, provides a unique natural laboratory for these investigations. The magmatic segments within Afar (Erta Ale, Dabbahu-Manda Hararo and Asal) share structural organisation analogies to those in mid-ocean ridges. These segments offer insights into the mantle and crustal processes that control magma transfer, storage, and eruption. This study focuses on the dynamics of magma transfer through the crust, the organization of the plumbing system, and the processes controlling these mechanisms.

We combine high-resolution multispectral orthoimages and digital elevation model, precise geological mapping, field investigations, cosmogenic ^{36}Cl exposure dating, and lava geochemistry to constrain the timing and evolution of magmatic events. Due to the systematic axial resurfacing along the segments, only the very last volcano-tectonic cycles are preserved and documented with exposure ages. Our results document the last rifting episodes for each segment: Gumat Mali-Manda Hararo (~ 0.5 to 35 ka), and Asal (~1 to 8 ka). The recent exposure ages reveal

periodic recharge of shallow magma reservoirs that ultimately feed lateral dyke injections and surface eruptions. Our findings reveal the dynamic magma storage and transfer within the Afar axial rift, where segments are at different rifting stages. Variations in reservoir recharge and differentiation highlight distinct storage zones and potential connections between subsegments. These insights show how periodic magma transfer and differentiation cycles shape the rift magmatic evolution, with important implications for local hazards.

Résumé étendu en Français

Le rifting continental est un processus complexe qui s'étend du début de l'extension jusqu'à la fragmentation continentale, et dans lequel le magmatisme joue un rôle fondamental. La manière dont les magmas se forment, sont transférés du manteau vers la croûte et finissent par atteindre la surface fournit des informations essentielles sur la dynamique de l'extension, en particulier lors de la transition entre les phases continentale et océanique, c'est-à-dire la transition océan-continent (OCT). Dans la région d'Afar, qui représente une jonction triple entre deux dorsales océaniques, le golfe d'Aden et la mer Rouge, et un rift continental correspondant au rift est-africain, l'extension est actuellement accommodée par de nombreux segments magmatiques. Ces segments présentent des morphologies contrastées, allant de rides axiales à des dépressions axiales, et diffèrent par leur taux d'extension, l'épaisseur de la croûte, les sources des magmas, ainsi que par l'intensité et la fréquence de l'activité tectonique et volcanique. Une telle variabilité soulève des questions fondamentales quant aux raisons pour lesquelles le rifting s'exprime différemment dans chaque segment, quant à savoir si ces variations reflètent des différences de maturité ou des styles distincts de rifting, et quant à la manière dont le magmatisme a évolué depuis les phases volcaniques antérieures vers l'activité axiale actuelle.

Depuis environ 0,4 Ma, la déformation dans la région d'Afar s'est concentré le long de segments de rifts magmatiques en échelon, d'une longueur de 60 à 100 km et d'une largeur de 20 à 40 km, qui ressemblent fortement à ceux observés sur les dorsales lentes. Du nord au sud, les segments d'Erta Ale, de Dabbahu–Manda Hararo et d'Asal–Ghoubbet présentent de forts contrastes en termes de morphologie et d'apport magmatique. Le segment d'Erta Ale se caractérise par une activité magmatique récente nettement plus importante et par le développement d'une ride axiale proéminente, tandis que les segments de Dabbahu–Manda Hararo et d'Asal–Ghoubbet présentent un magmatisme récent comparativement moins volumineux, ainsi qu'une topographie volcanique moins développée. Ces variations spatiales ont été interprétées soit comme des différences de maturité du rift, soit comme des styles de rifting distincts, bien que les modèles existants reposent souvent sur des ensembles de données qui ne documentent pas les systèmes à des échelles spatiales et temporelles comparables. Malgré des études géophysiques et volcanologiques approfondies, l'architecture interne des segments magmatiques, en particulier l'organisation des systèmes de conduits magmatiques et

leur interaction avec les réseaux de failles, reste mal comprise tant dans le temps que dans l'espace.

Dans ce contexte, la présente étude porte sur deux segments de rift actifs de la dépression d'Afar, à savoir le segment de Manda Hararo, en Afar Central (Ethiopie), et le segment d'Asal-Ghoubbet, dans le sud de l'Afar (République de Djibouti), afin de comprendre les facteurs de contrôle et les causes potentielles de l'accrétion magmatique. L'étude vise à localiser les réservoirs magmatiques et à étudier leur fonctionnement et leur persistance, dans le but de déterminer l'organisation verticale et latérale des systèmes de conduits, leurs interconnexions potentielles, leur interaction avec les processus d'extension et leur rôle dans le contrôle de la segmentation à grande échelle. Ces objectifs sont abordés à l'aide d'approches complémentaires combinant la télédétection, les investigations sur le terrain, la cartographie géologique précise, la datation par ^{36}Cl cosmogénique et la géochimie des laves, ce qui permet de contraindre à la fois le cadre temporel et la dynamique des processus magmatiques.

La télédétection, les études de terrain et la géochronologie des surfaces de lave constituent un élément fondamental de ce travail. L'imagerie multispectrale enregistre l'énergie électromagnétique réfléchie ou émise, chaque matériau présentant des profils d'absorption et de réflexion caractéristiques. Dans les zones volcaniques, la réflectance spectrale des coulées de lave est significative dans les régions du spectre visible et du proche infrarouge, ce qui permet d'identifier les champs de coulées de lave, de déterminer leurs directions d'écoulement et de localiser les appareils volcaniques associés. La cartographie géologique par télédétection utilise ces propriétés spectrales pour distinguer les lithologies et délimiter les structures. Afin de cartographier l'étendue et la diversité des unités volcaniques au sein des sous-segments magmatiques de l'Afar central, plusieurs ensembles de données ont été utilisés, notamment des images Landsat 8 OLI de niveau 2, des images multispectrales Sentinel-2 et des images stéréoscopiques haute résolution Pléiades. Ces ensembles de données permettent d'élaborer des cartes détaillées des structures volcaniques et des coulées de lave, qui ont ensuite été validées par des observations sur le terrain. Les investigations sur le terrain fournissent des contraintes sur les relations stratigraphiques et les caractéristiques structurales, garantissant ainsi la fiabilité des interprétations issues de la télédétection.

Le cadre chronologique de l'activité volcanique est établi à l'aide de datations d'exposition par ^{36}Cl cosmogénique. Cette méthode est basée sur la production de nucléides cosmogéniques,

qui résulte de l’interactions entre le rayonnement cosmique et la matière distribuée dans les quelques premiers mètres de la surface terrestre. La production n'a lieu qu'à proximité de la surface, et l'accumulation de nucléides cosmogéniques commence lorsque des matériaux auparavant protégés sont exposés, comme par exemple lors d'une éruption volcanique. La concentration de ^{36}Cl accumulée dans les surfaces est proportionnelle à la durée d'exposition, et permets de dater les coulées de lave sur des échelles de temps allant de quelques centaines à quelques dizaines de milliers d'années. La dépression d'Afar, caractérisée par un climat aride et de faibles taux d'érosion, offre des conditions particulièrement favorables pour l’utilisation de cette méthode. Dans le cadre de cette étude, un total de 56 échantillons de surface de lave a été prélevé dans le centre de l'Afar et dans le rift d'Asal lors de campagnes de terrain menées en 2013, 2018, 2022 et 2023. Les surfaces de lave du centre de l'Afar sont généralement dépourvues de phénocristaux ; les analyses ont donc été réalisées sur des échantillons de roche totale, tandis que les laves du rift d'Asal, riches en phénocristaux, ont permis des analyses sur des fractions de plagioclase. La préparation des échantillons a comporté des étapes de broyage, de tamisage, de purification et de traitement chimique visant à extraire le 36Cl cosmogénique, y compris des étapes de dissolution séquentielle pour réduire les concentrations totales de chlore et concentrer les signaux cosmogéniques.

Les analyses géochimiques des coulées de lave fournissent des contraintes supplémentaires sur les sources magmatiques et les processus magmatiques. Les compositions en éléments majeurs et en éléments traces, ainsi que les compositions isotopiques, sont utilisées pour caractériser les types de magma et déduire les conditions de fusion du manteau. Les résultats indiquent que la variabilité géochimique régionale observée dans les segments centraux et méridionaux du rift d’Afar peut s’expliquer par l’incorporation de petits volumes de magmas mantelliques appauvris dans des magmas majoritairement enrichis provenant du panache mantellique d’Afar. Cette observation implique que les interprétations des profils d'éléments de terres rares doivent être considérées avec prudence, en particulier lorsqu'il s'agit de déterminer les profondeurs de fusion ou d'identifier les composants de sources mantelliques. Les laves enrichies du centre et du sud de l'Afar diffèrent des autres séries de laves régionales ou plus anciennes, qui nécessitent soit une fusion plus profonde avec davantage de grenat dans la source, soit des fractions de fusion plus faibles, soit un composant plus enrichi, ce qui souligne la complexité des processus mantelliques sous le rift.

L'intégration de la cartographie géologique, de la géochronologie et de la géochimie apporte un éclairage nouveau sur la dynamique et l'organisation de l'activité volcanique dans l'Afar. Les résultats révèlent que l'activité volcanique est épisodique et s'organise spatialement au sein de sous-segments magmatiques. Dans le centre de l'Afar, la cartographie détaillée et les datations cosmogéniques des coulées de lave permettent de mettre en évidence très précisément la chronologie des événements éruptifs et montrent que les différents sous-segments présentent des histoires volcaniques distinctes. L'organisation des coulées de lave, combinée à leurs signatures géochimiques, impliques la présence de multiples réservoirs de magma avec des évolutions temporelle différentes au sein de la croûte. Dans les sous-segments du centre de l'Afar, l'évolution temporelle des magmas au cours des 20 000 dernières années suggère que les magmas stockés à différentes profondeurs dans la croûte et à différents stades de différenciation ont été mobilisés, différenciés et ont interagi de manière répétée sur des échelles de temps caractéristiques de quelques milliers d'années. Dans le sous-segment de Gumat Mali, l'intégration d'âges d'exposition cosmogéniques à haute résolution et de données géochimiques permet d'identifier 4 épisodes volcaniques distincts (0,6–1,2 ka). Dans le segment Asal–Ghoubbet, l'intégration d'âges d'exposition cosmogéniques à haute résolution avec les données géochimiques permet de reconstituer les cycles magmatiques au sein de la zone axiale, mettant en évidence les variations de l'apport en magma et de l'activité éruptive au cours des 10 000 dernières années.

Les résultats démontrent en outre que les systèmes magmatiques du rift d'Afar se caractérisent par des réseaux de conduits et réservoirs transcrustaux organisés verticalement et latéralement. Plutôt que d'être stocké dans une seule chambre magmatique, le magma est réparti dans plusieurs réservoirs situés à différentes profondeurs de la croûte, formant ainsi des systèmes complexes et dynamiques. Ces systèmes évoluent au fil du temps sous l'effet de la recharge magmatique, de la cristallisation fractionnée et des interactions entre magmas. Dans les stades plus avancés de l'évolution de ces sous-segments de rift d'Afar central, les systèmes magmatiques deviennent plus riches en cristaux et plus dynamiques, avec de multiples réservoirs interconnectés et des conditions de stockage variables. Cette évolution contraste avec les stades plus précoces de la formation du rift, où le stockage du magma peut être plus stable et localisé à la base de la croûte.

Le magmatisme et la tectonique sont étroitement liés dans le processus d'accommodation de l'extension. Les injections répétées de dykes sont considérées comme un moteur fondamental

de l'accrétion crustale, transportant le magma depuis les réservoirs crustaux vers la surface par le biais de fissures. Ces processus jouent un rôle clé dans le développement des segments de rift et dans la formation de nouvelle croûte. Dans les environnements de rift continental, l'extension est souvent dominée par la failles, tandis que dans les systèmes riches en magma, tels que ceux se rapprochant des conditions d'expansion océanique, l'intrusion de dykes devient le principal mode d'extension. La transition entre ces modes se produit dans les systèmes de rift matures tels que l'Afar, où les deux processus interagissent. Les résultats de cette étude soulignent l'importance des intrusions magmatiques dans l'accommodation de l'extension, en particulier dans le centre de l'Afar, où l'extension est largement contrôlée par l'injection de magma plutôt que par la seule formation de failles.

La segmentation tectonique exerce une influence déterminante sur les voies de remontée du magma et la localisation des réservoirs. La répartition des structures volcaniques et des réseaux de failles indique que la segmentation influence l'organisation des systèmes magmatiques à plusieurs échelles. Parallèlement, les conditions environnementales locales, telles que la présence d'eaux souterraines peu profondes, peuvent influencer les processus éruptifs. Dans le segment de Gumat au Mali, la présence d'une nappe phréatique relativement constante facilite les interactions entre le magma ascendant et les eaux souterraines, conduisant à des éruptions phréatomagmatiques. De telles éruptions représentant un danger important pour les populations locales.

Les résultats de cette thèse contribuent à la compréhension des interactions magmato-tectoniques au cours des dernières phases de la fragmentation continentale. En intégrant plusieurs ensembles de données, cette étude démontre que l'extension dans la dépression d'Afar est en grande partie compensée par des processus magmatiques, et que l'organisation et l'évolution des systèmes magmatiques transcrustaux jouent un rôle central dans le contrôle de la segmentation du rift et de l'activité volcanique. Les différences observées entre les segments du rift sont principalement interprétées comme des styles distincts de rifting, contrôlés par la disponibilité du magma et par l'interaction à long terme entre la lithosphère continentale et le panache mantellique d'Afar.

Cette thèse met également en évidence le rôle central des systèmes magmatiques transcrustaux, organisés verticalement et latéralement, dans l'accommodation de l'extension lors de la transition océan-continent. Ces résultats ouvrent plusieurs pistes pour les recherches futures.

Des études pétrologiques axées sur la chimie des minéraux et de leurs inclusions magmatiques permettraient d'établir des contraintes quantitatives sur les profondeurs de stockage des magmas et l'évolution des réservoirs magmatiques. Des études tectoniques combinant une cartographie détaillée des réseaux de failles avec des données géodésiques et sismiques aideraient à quantifier la répartition des déformations entre les processus tectoniques et magmatiques. L'extension de cette approche intégrée (cartographie-géochronologie-géochimie) à d'autres segments de rift en d'Afar (i.e. Erta Ale) permettrait d'évaluer dans quelle mesure l'organisation des systèmes magmatique identifiée dans cette étude peut être généralisée à l'ensemble du système de rift.